

**Towards Understanding the Microscopic Structural
Organization of Some Mono and Dicationic Room
Temperature Ionic Liquids through Various
Spectroscopic Techniques**

By

**DEBASHIS MAJHI
CHEM 11201304001**

**National Institute of Science Education and Research
Bhubaneswar, Odisha**

*A thesis submitted to the
Board of Studies in Chemical Sciences
In partial fulfillment of requirements
For the degree of*

**DOCTOR OF PHILOSOPHY
of
HOMI BHABHA NATIONAL INSTITUTE**



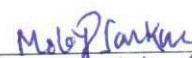
May, 2018

Homi Bhabha National Institute¹

Recommendations of the Viva Voce Committee

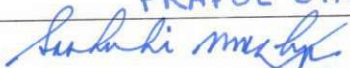
As members of the Viva Voce Committee, we certify that we have read the dissertation prepared by Mr. Debashis Majhi entitled "Towards Understanding the Microscopic Structural Organization of Some Mono and Dicationic Room Temperature Ionic Liquids Through Various Spectroscopic Techniques" and recommend that it may be accepted as fulfilling the thesis requirement for the award of Degree of Doctor of Philosophy.

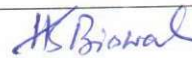
Chairman - <Name>  Prof. A. Srinivasan Date: 21.08.2018

Guide / Convener - <Name>  Dr. Moloy Sankar Date: 21.08.2018

Co-guide - <Name> (if any) Date: 21.08.2018

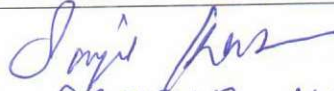
Members

Examiner - <Name>  PRAFUL SINGRU Date: 21/8/18
SAPTARSHI MUKHERJEE

Member 1- <Name>  Date: 21/08/2018

HIMANSU SEKHAR BISWAL

Member 2- <Name>

 Date: 21/08/2018
Dr. SAONJIB KAR

Final approval and acceptance of this thesis is contingent upon the candidate's submission of the final copies of the thesis to HBNI.

I/We hereby certify that I/we have read this thesis prepared under my/our direction and recommend that it may be accepted as fulfilling the thesis requirement.

Date: 21.08.2018

Place: Bhubaneswar,
NISER, Jatni campus

<Signature>

Co-guide (if applicable)


<Signature>

Guide

¹ This page is to be included only for final submission after successful completion of viva voce.

STATEMENT BY AUTHOR

This dissertation has been submitted in partial fulfillment of requirements for an advanced degree at Homi Bhabha National Institute (HBNI) and is deposited in the Library to be made available to borrowers under rules of the HBNI.

Brief quotations from this dissertation are allowable without special permission, provided that accurate acknowledgement of source is made. Requests for permission for extended quotation from or reproduction of this manuscript in whole or in part may be granted by the Competent Authority of HBNI when in his or her judgment the proposed use of the material is in the interests of scholarship. In all other instances, however, permission must be obtained from the author.

Debashis Majhi

Debashis Majhi

DECLARATION

I, hereby declare that the investigation presented in the thesis has been carried out by me. The work is original and has not been submitted earlier as a whole or in part for a degree / diploma at this or any other Institution / University.

Debashis Majhi

Debashis Majhi

List of Publications

1. *Probing the aggregation behavior of 4-aminophthalimide and 4-(N, N-dimethyl) amino-N-methylphthalimide: A combined photophysical, crystallographic, microscopic and theoretical (DFT) study. **Majhi, D.**; Das, S. K.; Sahu, P. K.; Pratik, Md. S.; Kumar, A. and Sarkar, M. *Phys. Chem. Chem. Phys.*, **2014**, *16*, 18349-18359.
2. Analyte interactions with a new dansylamide-nitrobenzoxadiazole dyad: A combined photophysical, NMR and theoretical (DFT) study. Bhoi, A. K.; Das, S. K.; **Majhi, D.**; Sahu, P. K.; Nijamudheen, A.; Anoop, N.; Rahaman, A. and Sarkar, M. *J. Phys. Chem. B*, **2014**, *118*, 9926-9937.
3. Investigating the influence of alkyl side chain length on the fluorescence response of C153 in a series of room temperature ionic liquids. Das, S. K.; **Majhi, D.**; Sahu, P. K. and Sarkar, M. *RSC Adv.*, **2015**, *5*, 41585–41594.
4. *Probing the aggregation behavior of neat imidazolium-based alkyl Sulfate (alkyl= ethyl, butyl, hexyl and octyl) ionic liquids through time resolved fluorescence anisotropy, NMR and fluorescence correlation spectroscopy (FCS) study. **Majhi, D.**; Pabbathi, A. and Sarkar, M. *J. Phys. Chem. B*, **2016**, *120*, 193–205.
5. *Probing the interactions of structurally similar but chemically distinguishable organic solutes with 1-ethyl-3-methylimidazolium alkylsulfate(alkyl = ethyl, hexyl and octyl) ionic liquids through fluorescence, NMR and fluorescence correlation spectroscopy (FCS) study. **Majhi, D.**; Sahu, P. K.; Seth, S. and Sarkar, M. *Phys. Chem. Chem. Phys.*, **2016**, *18*, 22343-22354.
6. *Linking diffusion-viscosity decoupling and jump dynamics in a hydroxyl-functionalized ionic liquid: Realization of microheterogeneous nature of the medium. Das, S. K.; **Majhi, D.**; Sahu, P. K. and Sarkar, M. *Chem. Phys. Chem.* **2017**, *18*, 198-207.

7. Easy access to new anthracenyl π -conjugates: Generation of distinct AIE-active materials. Baig, M. Z. K.; **Majhi, D.**; Tulichala, R. N. P.; Sarkar, M.; Chakravarty, M. *J. Mater. Chem. C*, **2017**, *5*, 2380-2387.
8. *Probing the microscopic structural organization of neat ionic liquids (ILs) and ionic liquid-based gel through resonance energy transfer (RET) studies. **Majhi, D.**; Sarkar, M. *Phys. Chem. Chem. Phys.*, **2017**, *19*, 23194-23203.
9. *Difference in the behavior of dicationic and monocationic ionic liquids as revealed by time resolved-fluorescence, electron paramagnetic resonance (EPR) and fluorescence correlation spectroscopy. **Majhi, D.**; Seth, S.; Sarkar, M. *Phys. Chem. Chem. Phys.*, **2018**, *20*, 7844-7856.
10. Evidence of Homo-FRET in quantum dot-dye hetrostructured assembly. Saha, S.; **Majhi, D.**; Bhattacharyya, K.; Preeyanka, N.; Datta, A.; Sarkar, M. *Phys. Chem. Chem. Phys.*, **2018**, *20*, 9523-9535.
11. Striking Similarities in the Fluorescence Behavior Between Carbon Dots and Ionic Liquids: Towards Understanding the Fluorescence Behavior of Carbon Dots. Roy, S.; Preeyanka, N.; **Majhi, D.**; Seth, S.; Sarkar, M. *J. Phys. Chem. C*, **2018**, *23*, 12384–12394.

*pertaining to the thesis

Conferences

1. Trombay symposium on radiation and photochemistry (TSRP-2016), January 05-09, 2016, organised by “Indian society for radiation and photochemical sciences” (ISRAPS), Mumbai, India. Presented a poster entitled “Probing the aggregation behavior of 4-Aminophthalimide and 4-(N, N-dimethyl) amino-N-methylphthalimide: A combined photophysical, crystallographic, microscopic and theoretical (DFT) study.”
2. Symposium on “Radiation and photochemistry” (NSRP – 2017), March 02- 04, 2017, organised by “Indian society for radiation and photochemical sciences (ISRAP), Manipal university, Manipal, India. Presented a poster entitled “Probing the aggregation behavior of neat imidazolium-based alkyl Sulfate (alkyl= ethyl, butyl, hexyl and octyl) ionic liquids through time resolved fluorescence anisotropy, NMR and fluorescence correlation spectroscopy (FCS) study”.
3. The Inter IISER & NISER Chemistry Meet (IINCM-2017), December 22-24, 2017, NISER, Bhubaneswar, India. Delivered a talk entitled “Probing the microscopic structural organization of neat ionic liquids (ILs) and ionic liquid-based gel through resonance energy transfer (RET) studies”.

Debashis Majhi

Debashis Majhi

Dedicated to.....

My Beloved Parents

ACKNOWLEDGEMENTS

I humbly express my deep sense of gratitude to my supervisor Dr. Moloy Sarkar for his enormously helpful guidance and constant encouragement throughout the program of my research work. I have learned a lot from him not only about research but also many things which eventually helped me to be a better human being. It was really a great experience working under the guidance of Dr. Moloy Sarkar.

It gives me great gratification to thank my thesis committee members Dr. Sanjib Kar, Dr. Himansu Sekhar Biswal, Dr. Arindam Ghosh and Dr. Praful Singru for their suggestions and useful advices during my research work. I would like to thank to Dr. N. K. Sharma, Chairman, PGCS NISER. I wish to extend my warmest thanks to Prof. A. Srinivasan, Chairperson, School of Chemical Sciences, NISER. I am thankful to all faculties of my department for providing me a healthy atmosphere. I acknowledge my indebted to all nonteaching staff of my department for their constant support.

In last five years many people have helped and encouraged me to continue with the present work. I am thankful to all of them. I wish to thank my seniors Dr. S. K. Das and Dr. P.K. Sahu for their help and suggestions during my PhD work. I would like to acknowledge my past and present lab members Abhas, Shiba, Gaurav, Avinash, Samya, Abhilash, Ranu, Shubhasis, Muhaiminul, Somnath, Manjari, Preeyanka, Sahadev and Aman with whom working in the lab was a enjoyment. I also express my heartfelt thanks to all my friends in NISER for their help and support and making my life more cheerful.

I would like to take this occasion to express my respect and love to my parents. From the very beginning of my life they instilled me a wish for dreaming about scientific research. They

provided every type of opportunities and supports that helped me to step forward on this way. I express my love to my brother Ashis who is always with me, and love to all my near and dear ones for their contribution that helped me to touch my dream of my life. I extended my respect to my late grandfather. Finally, I yield to gratify my wife Rajnandini for her cooperation, encouragement and mental support in the present work without which it would not have been achievable for me to devote all my time in the present study.

Debashis

CONTENTS

	Page No
SYNOPSIS	16
List of Schemes	27
List of Figures	28
List of Tables	39
Glossary of Acronyms	43
 <i>Chapter 1</i>	
Introduction	48
1.1. Room Temperature Ionic Liquids	48
1.1.1. <i>Properties of RTILs</i>	51
1.1.2. <i>Structural and Dynamic Heterogeneity of RTILs</i>	56
1.1.3. <i>Applications of RTILs</i>	58
1.1.4. <i>Photophysical Studies in RTILs</i>	59
1.1.5. <i>NMR Investigations on RTILs</i>	64
1.1.6. <i>Fluorescence Correlation Spectroscopy (FCS) and Electron Paramagnetic Resonance (EPR) Studies</i>	65
1.2. Objective Behind the Thesis	67
 <i>Chapter 2</i>	
Instrumentations and Methods	70
2.1. Purification and Characterization of RTILs	70

2.2. Sample Preparation for Spectroscopic Measurements	70
2.3. Instrumentations	71
2.3.1. Instruments Used for Chemical Characterisation of Samples	71
2.3.2. Instrumental Techniques for Absorption and Steady State Emission Measurements	71
2.3.2.1. <i>Absorption Measurements</i>	71
2.3.2.2. <i>Steady State Fluorescence Measurements</i>	72
2.3.3. <i>Instrumental Techniques for Time-resolved Studies</i>	72
2.3.3.1. <i>Fluorescence Lifetime Measurements</i>	72
2.3.3.2. <i>Basic Principle of TCSPC Technique</i>	74
2.3.3.3. <i>Important Components of a TCSPC Setup</i>	76
2.3.4. Other Instrumentations	78
2.4. Methods	79
2.4.1. <i>Analysis of the Fluorescence Decay Curves</i>	79
2.4.1.1. <i>Data Analysis</i>	79
2.4.1.2. <i>Reduced Chi-square (χ^2) Values</i>	80
2.4.1.3. <i>Distribution of Weighted Residuals</i>	81
2.4.2. <i>Time-resolved Fluorescence Anisotropy Measurements</i>	81
2.5. NMR Measurements	84
2.6. Fluorescence Correlation Spectroscopy (FCS) and Electron Paramagnetic Resonance (EPR) Measurements	84
2.7. Quantum Yield Calculations	86
2.8. Theoretical Calculations	86

2.9. Standard Error Limits	87
----------------------------	----

Chapter 3

Investigation of Solute-Solvent Interaction in Imidazolium-Based Room Temperature Ionic Liquids Using Spectroscopic Methods

Part A

3A.1. Introduction	88
3A.2. Experiment Section	91
3A.2.1. Synthesis of HNBD and ANBD	91
3A.3. Result and Discussion	93
3A.3.1. Steady State Absorption and Emission of HNBD and ANBD	93
3A.3.2. Rotational Dynamic Study	97
3A.4. Conclusion	111

Part B

3B.1. Introduction	112
3B.2. Experiment Section	114
3B.3. Result and Discussion	115
3B.3.1. Thermophysical Properties of RTILs	115
3B.3.2. Steady-State Studies	118
3B.3.3. Time Resolved Studies	120
3B.4. Conclusion	129

Chapter 4

Time Resolved-Fluorescence, Electron Paramagnetic Resonance (EPR), NMR, and Fluorescence Correlation Spectroscopy (FCS) Studies in Some Dicationic and Monocationic Room Temperature Ionic Liquids

4.1. Introduction	130
4.2. Experiments and Methods	133
4.2.1. Materials	133
4.2.2. Synthesis of DILs	134
4.3. Result and Discussion	136
4.3.1. Steady State Absorption, Emission and EPR Studies	136
4.3.2. Studies on Rotational Diffusion through EPR and Time-Resolved Fluorescence	
Anisotropy Study	142
4.3.2.1. EPR Studies	143
4.3.2.2. Time-Resolved Fluorescence Anisotropy Study	145
4.3.3. FCS Studies	159
4.4. Conclusion	161

Chapter 5

Effect of Anion Chain Length on the Aggregation Behavior of Neat Imidazolium-Based Alkyl Sulfate Room Temperature Ionic Liquids: A Combined Time Resolved Fluorescence Anisotropy, NMR and Fluorescence Correlation Spectroscopy (FCS) Study

5.1. Introduction	163
5.2. Experiments and Methods	167
5.3. Result and Discussion	168
5.3.1. Steady State Absorption and Emission of Neat RTILs	169
5.3.2. Rotational Dynamic Study of Neat RTILs	170
5.3.3. NMR Spectroscopic Studies	176
5.3.4. FCS Studies	183

5.4. Conclusion	186
-----------------	-----

Chapter 6

Effect of Anion Chain Length and Nature of Cation on the Microscopic Structural Organization of Neat 1-Ethyl-3-Methyl Imidazolium Alkyl Sulfate, Ammonium and Pyrrolidinium Based Ionic Liquids: A Resonance Energy Transfer (RET) Study

6.1. Introduction	187
6.2. Experiment Section	190
6.3. Result and Discussion	191
6.3.1. Fluorescence Behavior of Neat RTILs	191
6.3.2. Investigation of RET Process through Steady State Measurements	193
6.3.3. Investigation of RET Process through Time-Resolved Measurements	195
6.4. Conclusion	210

Chapter 7

Influence of Ionic Liquids on the Aggregation Behavior of 4-Aminophthalimide (AP) and 4-(N,N-Dimethyl) Amino-N-Methylphthalimide (DMP)

7.1. Introduction	212
7.2. Experiment Section	215
7.2.1. Materials	216
7.2.2. Synthesis and Characterization of DMP	216
7.2.3. Preparation of AP and DMP Solution	217
7.2.4. Preparation and Characterization of AP and DMP Aggregate	217
7.3. Result and Discussion	217

7.3.1. Optical Studies of AP and DMP in Molecular Form	217
7. 3. 2. Microscopic Analysis of AP and DMP Aggregates	220
7. 3. 3. Spectroscopic Studies on AP and DMP Aggregates	221
7.3.4. Crystal Structures of AP and DMP	231
7.3.5. Theoretical Calculation of the Experimental Results	235
7.3.6. Effect of Ionic Liquids on Aggregates	238
7.4. Conclusion	243
Summery and Future Prospects	245
REFERENCES	247
APPENDIX	272

SYNOPSIS

In recent times, room temperature ionic liquids (RTILs) have emerged as the promising material in several chemical, biological and industrial applications.^{1,2} This surge has been mainly driven by the fact that RTILs possess some interesting physicochemical properties.^{3,4} Interestingly, it has also been observed that the properties of RTILs can be tuned by appropriate choice of cationic and anionic constituents.³ However, understanding of the behavior of RTILs in terms of intermolecular interactions, structure and dynamics is still inadequate. The main objective of the present thesis is to understand the kinship among intermolecular interactions, structure and dynamical behavior of several imidazolium-based RTILs through time-resolved fluorescence anisotropy, NMR, fluorescence correlation spectroscopy (FCS) and electron paramagnetic resonance (EPR) spectroscopic studies.

Organization of thesis

The present thesis has been organized in seven chapters. The contents of the different chapters of the thesis are briefly mentioned below.

Chapter 1: Introduction

This chapter initially provides a brief introduction about ionic liquids (ILs) and their physicochemical properties. The applications of RTILs both in chemical, biological and material sciences have also been outlined. In this chapter, studies on excitation wavelength dependent emission behavior, solute rotation, solvation dynamics, NMR and FCS investigation of several RTILs are discussed by illustrating several literature reports. Finally, the current challenges in ionic liquids research and objective of the present thesis work have been discussed at the end of this chapter.

Chapter 2: Instrumentation and Method

Basic principles of different experimental techniques used in the present study, such as absorption spectroscopy, steady-state and time-resolved emission spectroscopy have been demonstrated briefly in this chapter. The working principle of time-correlated single photon counting (TCSPC) techniques has also been discussed. Principles of time resolved fluorescence anisotropy and Pulsed-Field-Gradient NMR (PFG-NMR) measurements are described in detail. Methodologies used to obtain the rotational relaxation time and analysis of time resolved fluorescence anisotropy data by using several hydrodynamic models have also been demonstrated. In this chapter, the basic principles of FCS and EPR techniques are discussed. The error limits corresponding to different experimental parameters are also provided at the end of this chapter.

Chapter 3. Investigation of Solute-Solvent Interaction in Imidazolium-Based Room Temperature Ionic Liquids Using Spectroscopic Methods

This chapter is divided into two part, *Part A* and *Part B*.

In part A, the solute-solvent interaction between organic solutes and RTILs (solvent) has been investigated with the aim of understanding intermolecular interactions among solute and solvent molecules. Primarily, solute-solvent interaction has been examined by employing two structurally similar and chemically distinguishable organic solutes, 4-(azetidene-1-yl)-7-nitrobenzo[1,2,5]oxadi-azole (ANBD) and 7-nitrobenzo[1,2,5]oxadiazole-4-amine (HNBD), in 1-ethyl-3-methylimidazolium alkyl sulfate (alkyl = ethyl, hexyl and octyl) (Chart 1). The investigation has been carried out by exploiting fluorescence, NMR and FCS. In this study the RTILs having a fixed cationic moiety are chosen so as to monitor the roles of the alkyl chain length on the anions during the rotational diffusion of the solutes in the given RTILs. The rotational diffusion data for both the solutes have been analyzed in light of hydrodynamic⁵ and quasi hydrodynamic^{6, 7} theories. Interestingly, the rotational dynamics of ANBD is observed to

be relatively fast and shows slip hydrodynamics, whereas HNBD exhibits hindered rotation with superstick behavior (Figure 1). The hindered rotation of HNBD as compared to that of ANBD in both ILs has been explained by considering the strong hydrogen bonding interactions between the two N–H groups of HNBD and sulfate anions of RTILs. The presence of a specific hydrogen bonding interaction between solute (HNBD) and solvent (RTILs) molecules has been confirmed by $^1\text{H-NMR}$ experiments. FCS measurements have independently demonstrated the relatively strong association of HNBD with the present RTILs as compared to that of ANBD. The faster rotation of ANBD with the increasing anion chain length has been explained by invoking the quasi hydrodynamic theory.⁸

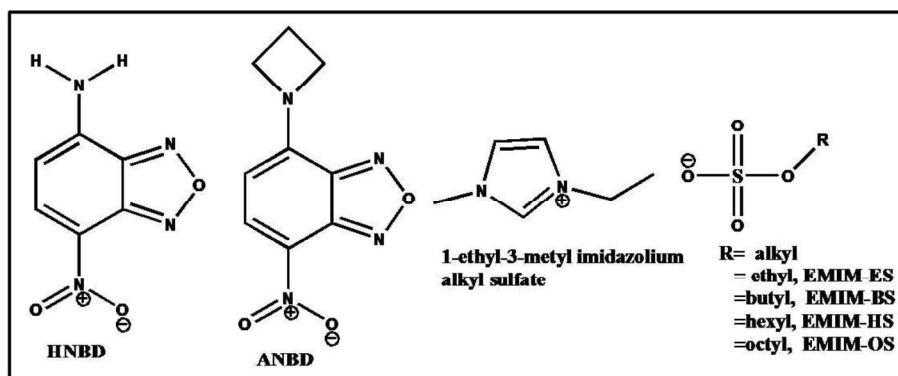


Chart 1: Molecular structure of HNBD, ANBD and RTILs

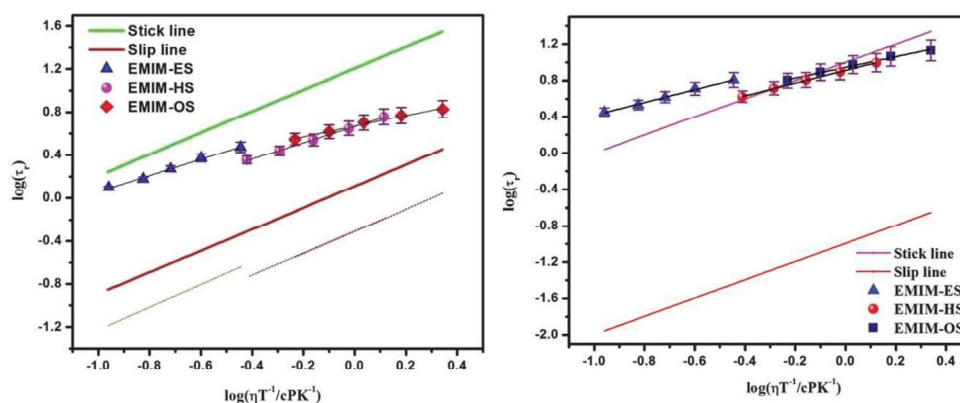


Figure 1. $\log(\tau_r)$ vs. $\log(\eta/T)$ plot of (a) ANBD (b) HNBD in 1-ethyl-3-methyl alkyl sulfate RTILs. The solid black lines indicate fit to the data points. [Dotted lines correspond to DKS lines in figure (a)].

In part B, the microscopic behavior of hydroxyl-functionalized RTIL has been investigated by monitoring solute-solvent interaction between coumarin 153 (C153) and 1-hydroxyethyl-3-methylimidazolium fluoroalkylphosphate ([OH-Emim][FAP]) RTIL (Chart 2). Additionally, the non-hydroxyl-functionalized RTIL, 1-ethyl-3-methylimidazolium fluoroalkylphosphate ([Emim][FAP]), ([Emim][FAP]) is also chosen in the present study so that the effect of OH-functionalization into the cationic moiety is exclusively monitored. The investigation has been carried out by using steady state, time-resolved fluorescence and NMR experiments. Analysis of time-resolved fluorescence anisotropy data in light of the Stokes–Einstein–Debye hydrodynamic (SED) description reveals significant decoupling of rotational motion of the solute and the viscosity of the medium for a hydroxyl-functionalized RTIL. Diffusion experiments through NMR measurements have also indicated the diffusion-viscosity decoupling behavior in hydroxyl-functionalized RTIL. These observations suggest that the hydroxyl-functionalized RTIL is more heterogeneous than other structurally similar imidazolium-based RTIL.⁹

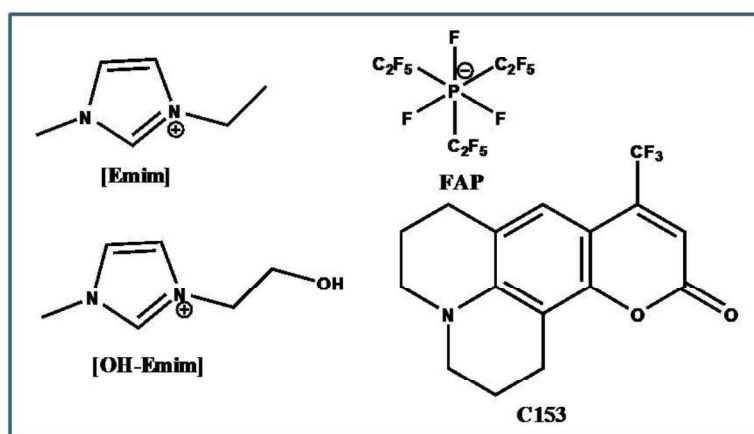


Chart 2: Molecular structure of C153 and RTILs

Chapter 4. Time Resolved-Fluorescence, Electron Paramagnetic Resonance (EPR), NMR, And Fluorescence Correlation Spectroscopy (FCS) Studies in Some Dicationic and Monocationic Room Temperature Ionic Liquids.

This chapter describes the micro-polarity, intermolecular interactions, structure and dynamics of some dicationic and monocationic RTILs. Specifically, two imidazolium-based dicationic ionic liquids (DILs), 1,8-bis-(3-methylimidazolium-1-yl)octane bis-(trifluoromethylsulfonyl)amide ($[\text{C}_8(\text{mim})_2][\text{NTf}_2]_2$), 1,9-bis-(3-methylimidazolium-1-yl)nonane bis-(trifluoromethylsulfonyl)amide ($[\text{C}_9(\text{mim})_2][\text{NTf}_2]_2$) and one monocationic ionic liquid (MIL), 1-butyl-3-methyl imidazolium bis(trifluoromethylsulfonyl)amide ($[\text{C}_4(\text{mim})][\text{NTf}_2]$) (Chart 3), have been investigated through combined fluorescence, EPR, NMR and FCS studies. Steady state absorption, emission and EPR spectroscopic data reveal that DILs are less polar as compared to MIL. Microscopic behavior of DILs and MIL have been investigated by studying the rotational diffusion of two organic solutes, perylene and 8-methoxypyrene-1,3,6-sulfonate (MPTS) in DILs and MIL. The rotation of perylene in DILs has been observed to be relatively faster than that in MIL, and it goes beyond the limit predicted by SED theory (Figure 2(a)). The observed rotational behavior of perylene has been explained by considering the fact that larger solvent molecule (DILs) induces lower friction to the rotating solute. Interestingly, unlike perylene, rotations of MPTS in both ILs are observed to be much hindered. More interestingly, rotation of MPTS is observed to be faster in DILs than that in MIL despite the fact that DILs is more viscous than MIL (Figure 2(b)). Relatively faster rotation of MPTS in DILs has been explained by resorting to NMR and FCS studies. Outcome of NMR and FCS studies have revealed that DIL in the experimental condition exists in folded form. Because of this structural restriction of DIL it becomes difficult for bulky MPTS to make stronger hydrogen bonding interaction with DIL, which eventually makes rotation of MPTS in DIL faster. The out come of

present investigation demonstrated that the structural organization of (DILs) are significantly different than the corresponding MIL.¹⁰

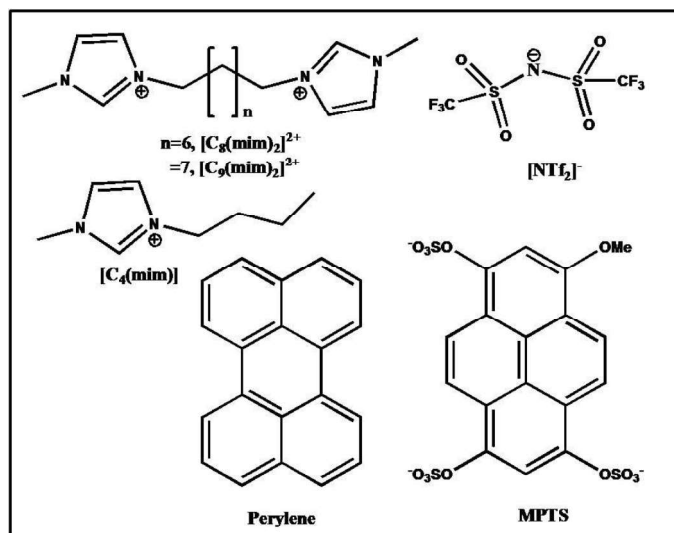


Chart 3: Molecular structure of DILs, MIL, Perylene and MPTS.

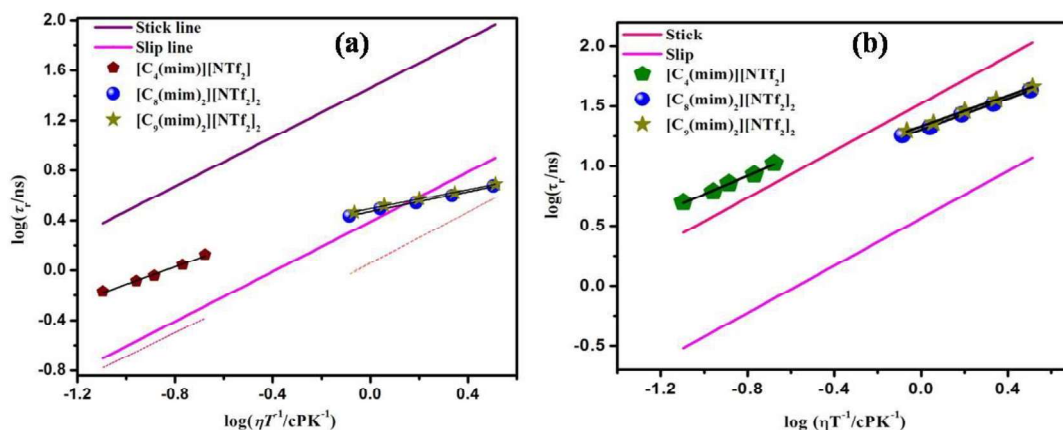


Figure 2. $\log(\tau_r)$ vs. $\log(\eta/T)$ plot of (a) Perylene (b) MPTS in DILs and MIL with stick and slip boundary condition limits. The solid black lines indicate fit to the data points. [Dotted lines correspond to DKS lines in figure (a)].

Chapter 5. Effect of Anion Chain Length on the Aggregation Behavior of Neat Imidazolium-Based Alkyl Sulfate Room Temperature Ionic Liquids: A Combined Time Resolved Fluorescence Anisotropy, NMR and Fluorescence Correlation Spectroscopy (FCS) Study.

This chapter discusses the aggregation behavior of a series of neat 1-ethyl 3-methylimidazolium alkyl sulfate (alkyl = ethyl, butyl, hexyl, and octyl) RTILs (Chart 4) through combined time-resolved fluorescence, 1-D and 2-D NMR, and FCS studies. Interestingly, the experimentally measured rotational relaxation times (τ_r) for ethyl, butyl, hexyl and octyl systems are found to be 2.25, 1.64, 1.36, and 1.32 times higher than the theoretically estimated ones (using SED theory) for these systems respectively (Table 1). This indicates that the emitting species is not the monomeric imidazolium moiety rather an associated species. More interestingly, while calculating the volume of the rotating fluorescence species, it can be observed that the volume of the rotating fluorescing species decreases even though the length of the alkyl moiety on the anions is increased (Table 1). The ^1H -NMR experiments shows that the neat RTILs exist in the aggregated form. Further, 2D-ROESY experiment demonstrates that interaction between imidazolium and sulfate is relatively stronger in the ethyl system than that in the longer octyl system. Additionally, FCS measurements independently show that the hydrodynamic volume decreases with an increase in the anion chain length. The NMR and FCS results are consistent with the findings of the fluorescence anisotropy study. All these studies suggest that cation-anion interaction is relatively stronger in short alkyl chain RTIL than that in long alkyl chain RTIL.¹¹

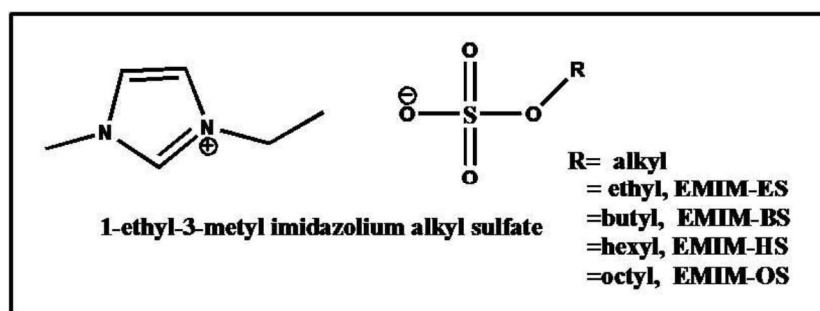


Chart 4: Molecular structure of neat 1-alkyl 3-methyl imidazolium alkyl sulfate.

Table 1. The $\tau_r^{\text{exp}}/\tau_r^{\text{thr}}$ and volume of the rotating species (using SED theory) of neat RTILs

Systems	$\tau_r^{\text{exp}}/\tau_r^{\text{thr}}$	Volume (\AA) ³
EMIM-ES	2.25	378
EMIM-BS	1.64	268
EMIM-HS	1.36	217
EMIM-OS	1.32	202

Chapter 6. Effect of Anion Chain Length and Nature of Cation on the Microscopic Structural Organization of Neat 1-Ethyl-3-Methyl Imidazolium Alkyl Sulfate, Ammonium and Pyrrolidinium Based Ionic Liquids: A Resonance Energy Transfer (RET) Study.

In this chapter, the resonance energy transfer (RET) studies from neat ionic liquids (donor) to rhodamine 6G (R6G) (acceptor) molecules have been investigated to understand the microscopic structural organization of neat RTILs. Basically, three different sets of RTILs are taken for this studies, where in the first set (1-ethyl-3-methyl imidazolium alkyl sulfate) the alkyl side chain length on the anionic moiety is systematically varied, in the second set variation is done on the cation (aromatic and nonaromatic) and in the three set, the branching on the cationic moiety of RTILs is varied (Chart 5). The data related to the RET events have been analyzed in light of Förster theory.^{12, 13} A clear rise time in the fluorescence intensity decay profile of the acceptor for all the systems has unequivocally established the RET process between the donor and acceptor. Interestingly, in case of set one, the donor–acceptor distance (R_{DA}) is observed to increase from 35.0 \AA to 47.5 \AA upon increasing the anion chain length from ethyl to octyl. However, for second set, R_{DA} is found to decrease (40.5 \AA to 34.9 \AA) upon going from 1-methyl-3-butylimidazolium to 1-butyl-1-methylpyrrolidinium cations. In case of other set, the R_{DA} increases with increasing the branching on the cationic moiety (Table 2). The variation of the relevant RET parameters for the three sets of RTILs has been rationalized by considering the change in the structural organization of the respective set of RTILs.¹⁴

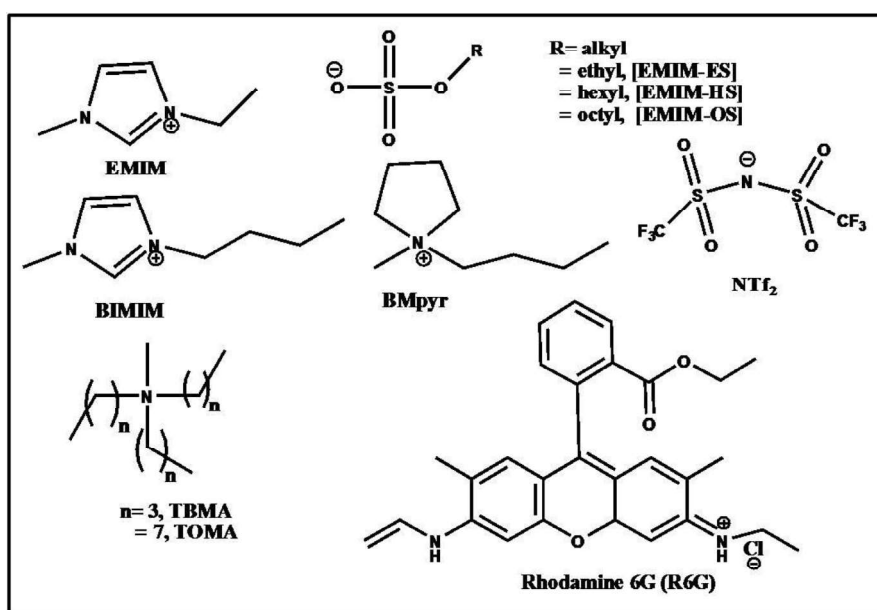


Chart 5. Molecular structure of RTILs and Rhodamine 6G (R6G).

Table 2. The magnitude of relevant RET parameters

Systems	Φ_D	$J(\lambda) (10^{16})$ ($M^{-1}cm^{-1}nm^4$)	τ_D^0 (ns)	τ_{rise} (ns)	R_0 (Å)	R_{DA} (Å)	E	K_{RET} ($10^8 s^{-1}$)
EMIM-ES	0.01	3.56	1.36	0.58	40.35	35.0	70	17.24
EMIM-HS	0.03	3.38	2.13	1.22	48.13	43.9	65	7.57
EMIM-OS	0.04	3.18	2.31	1.66	50.21	47.5	58	6.02
BMIM-NTf ₂	0.02	1.82	2.26	1.94	41.55	40.5	54	5.10
BMPyr-NTf ₂	0.01	1.58	1.42	1.12	36.27	34.9	56	8.92
TBMA-NTf ₂	0.07	2.17	1.58	1.06	52.77	49.0	60	9.43
TOMA-NTf ₂	0.13	1.89	2.46	1.86	57.88	54.8	57	5.37

Chapter 7. Influence of Ionic Liquids on the Aggregation Behavior of 4-Aminophthalimide (AP) and 4-(N,N-Dimethyl) Amino-N-Methylphthalimide (DMP).

In this chapter, the aggregation behavior of two fluorescent molecules, 4-aminophthalimide (AP) and 4-(N,N-dimethyl)amino-N-methylphthalimide (DMP) has been investigated to get an idea about the effect of intermolecular hydrogen bonding interactions (N–H) on the aggregation behavior of these molecules. The influence of ILs on their aggregation behavior of the fluorescence dye molecules has also been demonstrated. The molecular structure of AP, DMP and ILs are provided in Chart 6. Photophysical behavior of these well characterized systems has

been investigated in molecular as well as aggregated forms. Interestingly, the AP-aggregates exhibit a blue-shifted absorption band (as compared to AP in its molecular form), while DMP-aggregates exhibit a red shifted absorption band (as compared to DMP in its molecular form). These absorption data indicate the formation of H and J aggregates for AP and DMP respectively. X-ray crystallography data and theoretical studies (DFT and TD-DFT) also support the formation of H and J aggregates for AP and DMP respectively.¹⁵ Interestingly it can be observed that, the dissociation of colloidal aggregates takes place in presence of long alkyl chain ionic liquid such as 1-dedocyl-3-methyl imidazolium bromide ($[C_{12}(mim)Br]$). However, no effect on the colloidal aggregates has been observed in presence of short alkyl chain ionic liquids such as 1-butyl-3-methyl imidazolium bromide ($[C_4(mim)Br]$). The dissociation of colloidal aggregates upon addition of long alkyl chain IL in aqueous medium can be attributed due to formation of micelles of $[C_{12}(mim)Br]$. The future projections of the present thesis work are also outlined at the end of the last chapter.

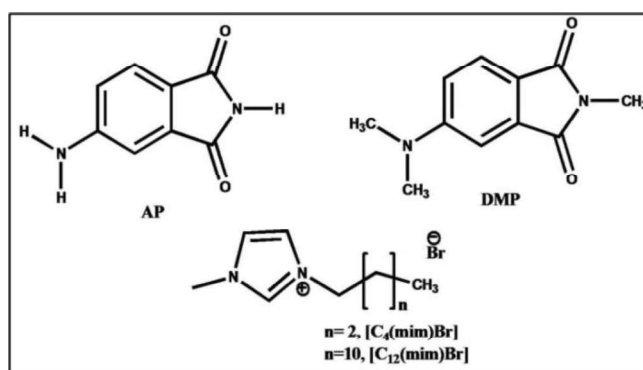


Chart 6: Molecular structure of AP, DMP and ionic liquids.

References

- (1) Hallett, J. P.; Welton, T. *Chem. Rev.* **2011**, *111*, 3508.
- (2) Plechkova, N. V.; Seddon, K. R. *Chem. Soc. Rev.* **2008**, *37*, 123.
- (3) Rogers, R.D.; Seddon, K.R. *Science* **2003**, *302*, 792
- (4) Castner, E. W., Jr.; Wishart, J. F. *J. Chem. Phys.* **2010**, *132*, 120901.
- (5) Hu, C. M.; Zwanzig, R. J. *Chem. Phys.* 1974, *60*, 4354
- (6) Gierer, A.; Wartz, K. *Z. Naturforsch A* **1953**, *8*, 532.
- (7) Dote, J. L.; Kivelson, D.; Schwart, R. N. *J. Phys. Chem.* **1981**, *85*, 2169.
- (8) Majhi, D.; Sahu, P. K.; Seth, S.; Sarkar, M. *Phys. Chem. Chem. Phys.*, **2016**, *18*, 22343.
- (9) Das, S. K.; Majhi, D.; Sahu, P. K.; Sarkar, M. *Chem. Phys. Chem.* **2017**, *18*, 198.
- 10
- (11) Majhi, D.; Pabbathi, A.; Sarkar, M. *J. Phys. Chem. B*, **2016**, *120*, 193.
- (12) Förster, T. *Ann. Phys.* **1948**, *2*, 55.
- (13) Lakowicz, J. R. *Principles of Fluorescence Spectroscopy*, 3rd ed.; Plenum Press: New York, 1999.
- (14) Majhi, D.; Sarkar, M. *Phys. Chem. Chem. Phys.*, **2017**, *19*, 23194.
- (15) Majhi, D.; Das, S. K.; Sahu, P. K.; Pratik, Md. S.; Kumar, A.; Sarkar, M. *Phys. Chem. Chem. Phys.*, **2014**, *16*, 18349.

List of Schemes		Page No
1.	Scheme 1.1. Excitation wavelength dependent phenomanan.	60
2.	Scheme 2.1. A schematic diagram for the working principle of TCSPC setup.	75
3.	Scheme 2.2. A pictorial representation of fluorescence anisotropy measurements.	82
4.	Scheme 3.1. Synthetic route of HNBD molecule.	92
5.	Scheme 3.2. Synthetic route of ANBD molecule.	92
6.	Scheme 4.1. Schematic representation of long linker chain DILs in folded form. The blue dots represent the anions, red lines are the alkyl linker chains and black rings are the cations.	156
7.	Scheme 6.1. Schematic representation of RET between donor (RTIL) and acceptor (R6G) (a) Lemellar type structure of BMPyr-NTf ₂ . (b) Bilayer structure of BMIM-NTf ₂ .	205
8.	Scheme 7.1. Synthetic route of DMP molecule.	216

List of Figures		Page No
1.	Figure 3.1. (a) Normalized absorption and (b) emission spectra ($\lambda_{exc} = 405$ nm) of HNBD in EMIM-ES and EMIM-OS.	94
2.	Figure 3.2. (a) Normalized absorption and (b) emission spectra ($\lambda_{exc} = 405$ nm) of ANBD in EMIM-ES and EMIM-OS.	94
3.	Figure 3.3. Plot of λ_{em}^{max} vs. λ_{exc} of HNBD and ANBD in EMIM-ES and EMIM-OS.	96
4.	Figure 3.4. Change of FWHM values of the excitation wavelength dependent emission spectra of HNBD and ANBD in EMM-ES and EMIM-OS	97
5.	Figure 3.5. Variation of the viscosity of neat (a) EMIM-ES and (b) EMIM-OS with temperatures. The blue lines indicate the error bar from the data points.	98
6.	Figure 3.6. Anisotropy decay of (a) ANBD in EMIM-ES and (b) ANBD in EMIM-OS, ($\lambda_{exc} = 405$ nm). The solid black lines indicate the fit to the data points.	99
7.	Figure 3.7. $\log(\tau_r)$ vs $\log(\eta/T)$ plot of ANBD in RTILs with stick and slip boundary condition limit along with their DKS line. Dotted dark yellow, pink and violet line corresponds to DKS line for EMIM-ES, EMIM-HS and EMIM-OS respectively. The black lines indicate fit to the data points. The purple lines indicate the error bar from the data points.	101

8. **Figure 3.8.** Anisotropy decay of (a) HNBD in EMIM-ES and (b) HNBD in EMIM-OS, at 293 K and 313 K where $\lambda_{exc} = 405$ nm and $\lambda_{em} = 534$ nm. The solid black lines indicate fit to the data points. 104
9. **Figure 3.9.** $\log(\tau_r)$ vs $\log(\eta/T)$ plot of HNBD in RTILs with stick and slip boundary condition limit. The black lines indicate fit to the data points. The purple lines indicate the error bar from the data points. 107
10. **Figure 3.10.** $^1\text{H-NMR}$ spectra of HNBD, IL and IL+HNBD mixture in DMSO- d_6 . 108
11. **Figure 3.11.** Zoomed in FTIR spectrum of (a) HNBD and (b) HNBD in presence of EMIM-ES. 109
12. **Figure 3.12.** Autocorrelation functions of (a) HNBD and (b) ANBD in EMIM-ES. Solid red lines indicate fit to the data points. 110
13. **Figure 3.13.** (a) Viscosities and (b) densities of [Emim][FAP] and [OH-Emim][FAP] as a function of temperature. 116
14. **Figure 3.14.** Plot of $\ln(\eta)$ vs. $1/T$ of neat (a) [Emim][FAP] and (b) [OH-Emim][FAP] with temperatures. The solid black lines indicate the fitting to the data points. 117
15. **Figure 3.15.** Steady state absorption spectra of C153 in [Emim][FAP] and [OH-Emim][FAP]. Spectra are normalized at their corresponding peak maxima. 119
16. **Figure 3.16.** Steady state emission spectra of C153 in [Emim][FAP] and 119

[OH-Emim][FAP]. All emission spectra are normalized at their corresponding peak maxima. Emission spectra of neat RTILs are also shown in the same figure.

- | | | | |
|-----|---------------------|--|-----|
| 17. | Figure 3.17. | Time resolved fluorescence anisotropy decay (TRFAD) for C153 in [Emim][FAP] and [OH-Emim][FAP] at 298 K. The solid black lines indicate fit to the data points. | 121 |
| 18. | Figure 3.18. | Steady state emission spectra normalized to the peak of the monomer fluorescence band [$I_M(380\text{nm}) = 1.00$] for BPP in [Emim][FAP], [OH-Emim][FAP] and ethanol; ($\lambda_{exc} = 330\text{ nm}$). | 123 |
| 19. | Figure 3.19. | log-log plots of rotational relaxation time of C153 vs. η/T in [Emim][FAP] and [OH-Emim][FAP] with slip and stick boundary condition parameters. | 124 |
| 20. | Figure 3.20. | The NMR 2D ROSEY spectra of neat [Emim][FAP]. | 126 |
| 21. | Figure 3.21. | The NMR 2D ROSEY spectra of neat [OH-Emim][FAP]. | 127 |
| 22. | Figure 3.22. | Plot of diffusion coefficient (D) against T/η for neat [Emim][FAP] and [OH-Emim][FAP]. | 128 |
| 23. | Figure 4.1. | Normalized (a) absorption and (b) emission ($\lambda_{exc} = 375\text{ nm}$) spectra of C153 in $[\text{C}_8(\text{mim})_2][\text{NTf}_2]_2$ and $[\text{C}_4(\text{mim})][\text{NTf}_2]$. | 137 |
| 24. | Figure 4.2. | EPR spectra of TEMPO (red solid line) in (a) $[\text{C}_4(\text{mim})][\text{NTf}_2]$, (b) $[\text{C}_8(\text{mim})_2][\text{NTf}_2]_2$ and (c) $[\text{C}_9(\text{mim})_2][\text{NTf}_2]_2$. The blue dotted lines indicate the | 139 |

- simulated spectra.
25. **Figure 4.3.** Plot of a_N/G vs. E_T (30) values for TEMPO in 140
 $[C_8(mim)_2][NTf_2]_2$, $[C_9(mim)_2][NTf_2]_2$ and
 $[C_4(mim)][NTf_2]$. The stars indicate the values
corresponding to the known solvents.
 26. **Figure 4.4.** Excitation wavelength dependent emission behavior of 142
ANF in $[C_8(mim)_2][NTf_2]_2$ and $[C_4(mim)][NTf_2]$.
 27. **Figure 4.5.** Variation of the viscosity of $[C_8(mim)_2][(NTf_2)_2]$, 146
 $[C_8(mim)_2][(NTf_2)_2]$ and $[C_4(mim)][NTf_2]$ with
temperature and fitting with the VFT equation.
 28. **Figure 4.6.** Anisotropy decay of perylene in (a) $[C_4(mim)][NTf_2]$ and 147
(b) $[C_8(mim)_2][NTf_2]_2$.
 29. **Figure 4.7.** $\log(\tau_r)$ vs. $\log(\eta/T)$ plot of perylene in DILs and MIL with 149
stick and slip boundary condition limits. Dotted pink,
orange and violet line corresponds to DKS line for
 $[C_4(mim)][NTf_2]$, $[C_8(mim)_2][NTf_2]_2$ and
 $[C_9(mim)_2][NTf_2]_2$ respectively. The solid black lines
indicate fit to the data points.
 30. **Figure 4.8.** $\log(\tau_r)$ vs. $\log(\eta/T)$ plot of perylene in $[C_8(mim)][NTf_2]$ 150
with stick and slip boundary condition limits.
 31. **Figure 4.9.** $\log(\tau_r)$ vs. $\log(\eta/T)$ plot of MPTS in DILs and MIL with 154
stick and slip boundary condition limits. The solid black
lines indicate fit to the data points.

32.	Figure 4.10.	$\log(\tau_r)$ vs. $\log(\eta/T)$ plot of MPTS in $[\text{C}_8(\text{mim})][\text{NTf}_2]$ with stick and slip boundary condition limits.	156
33.	Figure 4.11.	Plot of diffusion coefficient (D) vs. T/η for $[\text{C}_8(\text{mim})_2][\text{NTf}_2]_2$ and $[\text{C}_4(\text{mim})][\text{NTf}_2]$. The solid black lines indicate fit to the data points.	158
34.	Figure 4.12.	FCS plot for $[\text{C}_8(\text{mim})_2][\text{NTf}_2]_2$ and $[\text{C}_4(\text{mim})][\text{NTf}_2]$.	160
35.	Figure 5.1.	(a) Absorption and (b) normalized emission spectra ($\lambda_{exc} = 375$ nm) of neat EMIM-ES and EMIM-OS.	169
36.	Figure 5.2.	Normalized emission spectra of neat EMIM-ES at different excitation wavelengths.	169
37.	Figure 5.3.	Emission spectra of neat (a) EMIM-ES and (b) EMIM-OS with addition of different mole fraction of water. $\lambda_{exc} = 375$.	170
38.	Figure 5.4.	Anisotropy decay of (a) EMIM-ES, (b) EMIM-BS, (c) EMIM-HS and (d) EMIM-OS, respectively, at 293 and 313 K where $\lambda_{exc} = 375$ nm and $\lambda_{em} = 450$ nm. The solid black lines indicate fit to the data points.	172
39.	Figure 5.5.	$\log(\tau_r)$ vs. $\log(\eta/T)$ plot with stick and slip boundary condition limits. The solid black lines indicate fit to the data points.	175
40.	Figure 5.6.	^1H NMR spectra of (a) neat EMIM-ES, (b) EMIM-ES+DMSO- d_6 (1:1) mixture, (c) EMIM-ES+DMSO- d_6 (1:2), (d) EMIM-ES+DMSO- d_6 (1:4), (e) EMIM-	177

- ES+DMSO-d₆ (1:8) and (f) EMIM-ES+DMSO-d₆ (1:16).
41. **Figure 5.7.** ¹H NMR spectra of (a) neat EMIM-OS, (b) EMIM-OS+ DMSO-d₆ (1:1) mixture, (c) EMIM-OS+ DMSO-d₆ (1:2) mixture, (d) EMIM-OS+DMSO-d₆ (1:4) mixture, (e) EMIM-OS+DMSO-d₆ (1:8) mixture and (f) EMIM-OS+ DMSO-d₆(1:16) mixture. 178
42. **Figure 5.8.** NMR 2D ROSEY spectra of neat EMIM-ES at 298 K. The box inside the figure indicates the common interaction with EMIM-OS RTIL in same condition. 180
43. **Figure 5.9.** NMR 2D ROSEY spectra of neat EMIM-OS at 298 K. The box inside the figure indicates the common interaction with EMIM-ES RTIL in same condition. 181
44. **Figure 5.10.** FCS results for neat (a) EMIM-ES and (b) EMIM-OS RTILs. Solid red lines indicate fit to the data points. 184
45. **Figure 6.1.** (a) Absorption spectrum of neat EMIM-ES and (b) normalized absorption and emission spectra of R6G and EMIM-ES. The highlighted region in figure 1(b) is the overlap region. 192
46. **Figure 6.2.** Normalized emission spectra of EMIM-ES at different excited wavelength (λ_{exc} = 360-450 nm). 192
47. **Figure 6.3.** Variation of emission intensity of EMIM-ES (λ_{ex} = 375 nm) upon gradual increase in the concentration of R6G. The inset indicates that the emission intensity of EMIM-ES 194

- decreases with increase in the acceptor concentration (from 0 μm to 231 μm).
48. **Figure 6.4.** Stern-Volmer plot showing the concentration variation change in the fluorescence of the donor (EMIM-ES). The blue lines denote the error bars from the data points. 194
49. **Figure 6.5.** Fluorescence decay curves of EMIM-ES without and in the presence of acceptor ($\lambda_{ex} = 375$ nm and $\lambda_{em} = 450$ nm). The solid black lines denote fit to the data points. 195
50. **Figure 6.6.** Stern-Volmer plot of τ^0/τ vs. concentration for EMIM-ES and R6G system. The blue lines denote the error bars from the data points. 196
51. **Figure 6.7.** Fluorescence decay curve of the acceptor (R6G) ($\lambda_{ex} = 375$ nm and $\lambda_{em} = 580$ nm; concentration of acceptor = 231 μM) in presence of donor (EMIM-ES). A clear rise has been shown in the inset. The solid black line indicates fit to the data points. 199
52. **Figure 6.8.** Thermogravimetric analysis (TGA) spectrum of RTIL (EMIM-OS) /guar gum gel. 208
53. **Figure 6.9.** Emission spectra of EMIM-OS/guar gum and EMIM-OS/guar gum/R6G gel ($\lambda_{ex} = 375$ nm). 209
54. **Figure 6.10.** Fluorescence decay curve of the acceptor (R6G) ($\lambda_{ex} = 375$ nm and $\lambda_{em} = 580$ nm) in EMIM-OS/guar gum/R6G gel system. The solid black line denotes fit to the data points. 210

55. **Figure 6.11.** Image of (a) EMIM-OS/guar gum/R6G gel in presence of UV- irradiation and (b) Fluorescence microscopic images of EMIM-OS/guar gum/R6G gel when excited at 488 nm. 210
56. **Figure 7.1.** Absorption spectra of AP and DMP in molecular form in DMSO (5×10^{-6} M) solution at room temperature. Spectra are normalized at respective lowest energy peak maxima. 218
57. **Figure 7.2.** Emission spectra of AP and DMP in molecular form in DMSO (5×10^{-6} M) solution at room temperature. $\lambda_{exc.} = 375$ nm. 219
58. **Figure 7.3.** Fluorescence decay profiles of AP and DMP in molecular form at room temperature. $\lambda_{exc.} = 375$ nm. Solid black lines indicate the single exponential fit to the experimental data points. Chi-square (χ^2) values for AP and DMP are 1.19 and 1.07 respectively. 219
59. **Figure 7.4.** FESEM images of (a) AP and (b) DMP aggregates at room temperature. 220
60. **Figure 7.5.** FESEM images of (a) AP and (b) DMP aggregates at higher temperature ($T = 65^{\circ}$ C). 220
61. **Figure 7.6.** Absorption spectra of AP in molecular form in DMSO (5×10^{-6} M) solution and in aggregated form in 99% water-DMSO medium at room temperature. Spectra are normalized corresponding to second peak maxima. 221

62. **Figure 7.7.** Normalized absorption spectra of DMP in molecular form in DMSO (5×10^{-6} M) solution and in aggregated form in 99% water-DMSO medium at room temperature. Spectra are normalized corresponding to second peak maxima. 223
63. **Figure 7.8.** Absorption spectra in aggregated form of AP in different 99% water-solvent medium at room temperature. Spectra are normalized corresponding to second peak maxima. 224
64. **Figure 7.9.** Schematic diagram illustrating allowed transition for H- and J- aggregates. Here ‘m’ represents transition moment integral, which must be greater than zero for allowed transitions. 224
65. **Figure 7.10.** Emission spectra of AP and DMP in aggregated form in 99% water-DMSO medium at room temperature. $\lambda_{exc} = 375$ nm. 226
66. **Figure 7.11.** Emission spectra of (a) AP and (b) DMP in molecular form in DMSO (5×10^{-6} M) solution and in aggregated form in 99% water-DMSO medium at room temperature. $\lambda_{exc.} = 375$ nm. 227
67. **Figure 7.12.** Fluorescence decay profiles of AP and DMP in aggregated forms at room temperature. $\lambda_{exc.} = 375$ nm. Solid black lines indicate the single exponential fit to the experimental data points. Chi-square (χ^2) values for AP and DMP aggregates are 1.23 and 1.12 respectively. 228

68.	Figure 7.13.	Wavelength dependent fluorescence decay profiles of AP in aggregated forms at room temperature. $\lambda_{exc.} = 375$ nm.	229
69.	Figure 7.14.	Emission spectra of AP aggregate at different excitation wavelength ($\lambda_{exc.}$).	229
70.	Figure 7.15.	Absorption spectra of 5-amino-2-methylisoindolne-1, 3-dione in molecular form in DMSO (5×10^{-6} M) solution and in aggregated form in 99% water-DMSO medium at room temperature. Spectra are normalized corresponding to second peak maxima.	229
71.	Figure 7.16.	Emission spectra of 5-amino-2-methylisoindolne-1, 3-dione in molecular form in DMSO (5×10^{-6} M) solution and in aggregated form in 99% water-DMSO medium at room temperature. Spectra are normalized corresponding to second peak maxima.	230
72.	Figure 7.17.	The absorption maxima of 1:1 AP-DMP aggregate, along with AP and DMP aggregate.	230
73.	Figure 7.18.	ORTEP diagram (50% displacement thermal ellipsoids) with atomic numbering scheme of (a) AP and (b) DMP.	232
74.	Figure 7.19.	Interplay of N-H---O hydrogen bonding interactions involving the bifurcated oxygen acceptor O1 in building 3D crystal lattice of AP.	233
75.	Figure 7.20.	The parallel aryl rings of AP molecules form channelized π --- π stacking.	233

76.	Figure 7.21.	Role of C-H...O interactions in head to tail interlinking of molecules in repeating anti-parallel chains and 2D supramolecular array of DMP.	234
77.	Figure 7.22.	Ground State optimized structures (at M06-2X/6-31+G (d ,p) level in gas phase) for (a) AP monomer, (b) AP linear dimer, (c) AP π -stacked dimer, (e) DMP monomer, (f) DMP linear dimer, (g) DMP π -stacked dimer and (h) AP-DMP parallel.	236
78.	Figure 7.23.	The computed λ_{max} for AP and DMP and their homo and hetero aggregation at TD-B3LYP/6-31+G (d, p) level of theory.	238
79.	Figure 7.24.	(a) Absorption and (b) emission spectra of AP aggregates in presence and absence of [C ₄ (mim)]Br.	239
80.	Figure 7.25.	Variation of (a) absorption and (b) emission spectra of the colloidal solution of AP with the increasing concentration of the [C ₁₂ (mim)]Br.	240
81.	Figure 7.26.	Variation of (a) absorption and (b) emission spectra of the colloidal solution of DMP with the increasing concentration of the [C ₁₂ (mim)]Br.	241
82.	Figure 7.27.	Fluorescence decay of AP aggregates in presence and absence of [C ₁₂ (mim)]Br.	242
83.	Figure 7.28.	The colloidal particle size of (a) AP and (b) DMP aggregates in presence and absence of [C ₁₂ (mim)]Br.	243

List of Tables			Page No
1.	Table 1.1.	Physical properties of some common imidazolium-based RTILs	53
2.	Table 3.1.	Absorption ($\lambda_{\max.}^{\text{abs.}}$) and emission ($\lambda_{\max.}^{\text{flu.}}$) maxima of HNBD and ANBD in EMIM-ES and EMIM-OS	95
3.	Table 3.2.	Reorientation times (τ_r) of ANBD in EMIM-ES, EMIM-HS and EMIM-OS at different temperatures ($\lambda_{\text{exc}} = 405$)	99
4.	Table 3.3.	Dimensions and van der Waals volumes of HNBD and ANBD along with shape factors and boundary condition parameters (calculated using SED theory)	100
5.	Table 3.4.	Reorientation times (τ_r) of ANBD in BIMIMFAP and HIMIMFAP at different temperatures ($\lambda_{\text{exc}} = 405$)	103
6.	Table 3.5.	Reorientation times (τ_r) of HNBD with viscosity of RTILs at different temperatures ($\lambda_{\text{exc}} = 405$ nm)	105
7.	Table 3.6.	Reorientation times (τ_r) of HNBD in BIMIMFAP and HIMIMFAP at different temperatures ($\lambda_{\text{exc}} = 405$)	106
8.	Table 3.7.	The obtained physical parameters for HNBD and ANBD in EMIM-ES from FCS measurements	110
9.	Table 3.8.	Viscosity (η) and density (ρ) of [Emim][FAP] and [OH-Emim][FAP] at different temperatures	115
10.	Table 3.9.	Fitting parameters for viscosity and density according to equations 3.2 and 3.3	117

11.	Table 3.10.	Thermal expansion coefficient values of present RTILs as a function of temperature	118
12.	Table 3.11.	Absorption, emission maxima and steady-state Stokes' shifts ($\Delta\gamma$) of C153 in [Emim][FAP] and [OH-Emim][FAP] at 298 K	119
13.	Table 3.12.	Reorientation times of C153 in [Emim][FAP] and [OH-Emim][FAP] as a function of temperature	121
14.	Table 3.13.	Calculation of translational diffusion coefficient through NMR spectroscopy	128
15.	Table 4.1.	The a_N/G value of TEMPO in RTILs and molecular solvents and the estimated $E_T(30)$ values	140
16.	Table 4.2.	Rotational correlation time (τ_r) and rotational diffusion coefficient (D) for TEMPO in [C ₈ (mim) ₂][NTf ₂] ₂ , [C ₉ (mim) ₂][NTf ₂] ₂ and [C ₄ (mim)][NTf ₂]	142
17.	Table 4.3.	Reorientation time (τ_r) and viscosity (η) of perylene and MPTS in [C ₄ (mim)][NTf ₂], [C ₈ (mim) ₂][NTf ₂] ₂ and [C ₉ (mim) ₂][NTf ₂] ₂	143
18.	Table 4.4.	Van der Waals volumes (V), shape factors (f) and boundary condition parameter (C_{slip}) of perylene and MPTS	144
19.	Table 4.5.	Reorientation time (τ_r) and viscosity (η) of perylene and MPTS in [C ₈ (mim)][NTf ₂]	149
20.	Table 4.6.	Translational diffusion coefficient (D) for [C ₈ (mim) ₂][NTf ₂] ₂ and [C ₄ (mim)][NTf ₂] through NMR spectroscopy	158
21.	Table 4.7.	The obtained physical parameters through FCS for [C ₈ (mim) ₂][NTf ₂] ₂ and [C ₄ (mim)][NTf ₂] at 298 K	160

22.	Table 5.1.	Reorientation time (τ_r) and viscosity (η) of all four neat RTILs at different temperatures	171
23.	Table 5.2.	Calculation of volume of rotating species at different systems using Stokes-Einstein equation	175
24.	Table 5.3.	FWHM values corresponding to relevant proton NMR signals of neat EMIM-ES and EMIM-OS and their mixtures with co-solvent (RTIL+ DMSO-d ₆ (1:16) mixture)	178
25.	Table 5.4.	Integrated peak volume of all observed $\{^1\text{H}-^1\text{H}\}$ ROSEY cross peak of neat EMIM-ES and EMIM-OS. $n_{\text{H}1}$ and $n_{\text{H}2}$ are the number of proton in solution and $N = n_{\text{H}1} + n_{\text{H}2}$. Integrated volume is the analyzed integral value by top spin NMR software. The corrected volume is the integrated volume divided by the normalization factor $(n_{\text{H}1}n_{\text{H}2}/N)$ for EMIM-ES and $(n_{\text{H}1}n_{\text{H}2}/N)(0.08/0.14)$ for EMIM-OS {the factor (0.08/0.14) is multiplied with corrected volume in EMIMOSU due to normalized the volume with respect to EMIM-ES}	181
26.	Table 5.5.	Calculation of translational diffusion coefficient through NMR spectroscopy	182
27.	Table 5.6.	Hydrodynamic radius of molecule in different RTILs	183
28.	Table 5.7.	The physical parameters obtained from FCS measurement	184
29.	Table 6.1.	Time constants of fluorescence decay of the donor (RTILs) in the presence of acceptor (R6G) at different concentration (where $\lambda_{\text{ex}} =$	197

375 nm and $\lambda_{em} = 450$ nm)

30.	Table 6.2.	Time constants of fluorescence decay of the acceptor (R6G) in difference concentration	200
31.	Table 6.3.	The magnitude of relevant FRET parameters	202
32.	Table 7.1.	Absorption $\lambda_{max}^{abs.}$ (nm) and emission maxima $\lambda_{max}^{flu.}$ (nm) of AP and DMP in molecular form in DMSO (5×10^{-6} M) solution and in aggregated form in 99% water-DMSO (5×10^{-5} M) solution	225
33.	Table 7.2.	Hydrogen bond parameters obtained from crystal structures of AP and DMP	235
34.	Table 7.3.	The computed λ_{max} for AP and DMP, in monomer, homo and hetero dimmers form	237
35.	Table 7.4.	Absorption ($\lambda_{max}^{abs.}$) and emission ($\lambda_{max}^{em.}$) maxima of AP and DMP aggregates in presence of [C ₁₂ (mim)]Br	241
36.	Table 7.5.	Fluorescence lifetime (τ) of AP and DMP aggregates in presence of [C ₁₂ (mim)]Br	242

Glossary of Acronyms

ILs	ionic liquids
RTILs	room temperature ionic liquids
HF	hydrofluoric acid
MILs	monocationic ionic liquids
DILs	dicationic ionic liquids
NTF ₂ ⁻	bis(trifluoromethanesulfonyl)imide
BF ₄ ⁻	tetrafluoroborate
PF ₆ ⁻	hexafluorophosphate
FAP	fluoroalkylphosphate
Cl ⁻	chloride ion
Br ⁻	bromide ion
I ⁻	iodide ion
T _d	thermal decomposition
T _g	glass transition temperature
<i>n_D</i>	refractive index
<i>ρ</i>	Density
<i>η</i>	Viscosity
<i>σ</i>	specific conductivity
<i>E_T</i> (30)	solvent polarity parameters
EMIMCl	1-ethyl-3-methylimidazolium chloride
BIMIMCl	1-butyl-3-methylimidazolium chloride

EMIMPF ₆	1-ethyl-3-methylimidazolium hexafluorophosphate
BMIMPF ₆	1-butyl-3-methylimidazolium hexafluorophosphate
EMIMNTf ₂	1-ethyl-3-methylimidazolium bis(trifluoromethanesulfonyl)imide
BMIMNTf ₂	1-butyl-3-methylimidazolium bis(trifluoromethanesulfonyl)imide
[C ₄ (mim) ₂][NTf ₂] ₂	1,4-bis-(3-methylimidazolium-1-yl)butane bis-(trifluoromethylsulfonyl)amide
[C ₆ (mim) ₂][NTf ₂] ₂	1,6-bis-(3-methylimidazolium-1-yl)hexane bis-(trifluoromethylsulfonyl)amide
[C ₈ (mim) ₂][NTf ₂] ₂	1,8-bis-(3-methylimidazolium-1-yl)octane bis (trifluoromethylsulfonyl)-amide
[C ₉ (mim) ₂][NTf ₂] ₂	1,9-bis-(3-methylimidazolium-1-yl)nonane bis-(trifluoromethylsulfonyl)amide
C ₂ mim[X]	1-ethyl-3-methylimidazolium halide
C ₄ mim[Tf ₂ N]	1-butyl-3-methylimidazolium bis(trifluoromethylsulfonyl)imide
EPR	electron paramagnetic resonance
FT-IR	Fourier transform infrared spectroscopy
DFT	density functional theory
TD-DFT	time dependent density functional theory
EAN	ethyl ammonium nitrate
NMR	nuclear magnetic resonance
OHD-RIKES	Optical heterodyne-detected Raman induced Kerr effect spectroscopy
MD	molecular dynamics

TSILs	task specific ionic liquids
REE	red edge effect
ANS	8-anilinonaphthalene-1-sulfonate
RET	Förster resonance energy transfer
PFG-NMR	Pulsed field gradient nuclear magnetic resonance
[BMIM][TF2N]	1-butyl-3-methylimidazolium bis(trifluoromethylsulfonyl)imide
[EMIM][SCN]	1-ethyl-3-methylimidazolium thiocyanate
[BMIM][BF4]	1-butyl-3-methylimidazolium tetrafluoroborate
NOE	Nuclear Overhauser Effect
ROESY	Rotating frame Overhauser Effect Spectroscopy
FCS	Fluorescence correlation spectroscopy
TEMPO	2,2,6,6-tetramethylpiperidine-1-oxyl
TEMPAMINE	4-amino-2,2,6,6-tetramethylpiperidine-1-oxyl
HNBD	7-nitrobenzo[1,2,5]oxadiazole-4-amine
ANBD	4-(azetidino-1-yl)-7 nitrobenzo[1,2,5]oxadiazole
R6G	rhodamine 6G
AP	4-aminophthalimide
DMP	4-(N,N-dimethyl)amino-N-methylphthalimide
C153	coumarin153
PMT	photomultiplier tube
TCSPC	time-correlated single photon counting
CFD	Constant Fraction Discriminator
TAC	Time to Amplitude Converter

MCA	Multichannel Analyzer
ADC	Analog-to-Digital Converter
FWHM	full width at half maximum
IRF	instrument response function
NLLS	nonlinear least squares
DFT	density functional theory
DLS	dynamic light scattering
D	diffusion coefficient
EMIM-ES	1-ethyl-3-methylimidazolium ethyl sulfate
EMIM-BS	1-ethyl-3-methylimidazolium butyl sulfate
EMIM-HS	1-ethyl-3-methylimidazolium hexyl sulfate
EMIM-OS	1-ethyl-3-methylimidazolium octyl sulfate
[EMIM][FAP]	1-ethyl-3-methylimidazolium fluoroalkylphosphate
[OH-EMIM][FAP]	1-hydroxyethyl-3-methylimidazolium fluoroalkylphosphate
ANF	2-amino-7-nitrofluorene
[C ₄ (mim)][NTf ₂]	1-butyl-3-methyl imidazolium bis(trifluoromethylsulfonyl)amide
[C ₈ (mim)][NTf ₂]	1-octyl-3-methyl imidazolium bis(trifluoromethylsulfonyl)amide
CT	charge transfer
VTF	Vogel-Tammann-Fulcher
MPTS	sodium 8-methoxypyrene-1,3,6-sulfonate
DMDPP	2, 5-dimethyl-1, 4-dioxo-3, 6-diphenylpyrrolo [3,4-c] pyrrole
BMIM-NTf ₂	1-methyl-3-butylimidazolium bis(trifluoromethane)sulfonimide
BMPyr-NTf ₂	1-butyl-1-methylpyrrolidinium bis(trifluoromethane)sulfonamide

TBMA-NTf ₂	tributylmethylammoniumbis- (trifluoromethane)sulfonamide
TOMA-NTf ₂	trioctylmethylammonium bis(trifluoro- methane)sulfonamide
SAILs	surface active ionic liquids
SDS	sodium dodecyl sulfate
CTAB	cetyltrimethylammonium bromide
[C ₁₂ (mim)]Br	1-dodecyl-3-methylimidazolium bromide
[C ₄ (mim)]Br	1-butyl-3-methylimidazolium bromide
[Bmim][C ₈ SO ₄].	1-butyl-3-methylimidazolium octyl sulfte
NaBH ₃ CN	sodium cyanoborohydride
DMSO	dimethyl sulfoxide
FESEM	field emission scanning electron microscope
EDA	electron donor acceptor
ICT	intra molecular charge transfer
TICT	twisted intra molecular charge transfer

Chapter 1

Introduction

This chapter initially provides a brief introduction about room temperature ionic liquids (RTILs) and their physicochemical properties. The applications of RTILs in chemical, biological and material sciences have also been outlined. In this chapter, studies on excitation wavelength dependent emission behavior, solute rotation, resonance energy transfer (RET), NMR, fluorescence correlation spectroscopy (FCS) and electron paramagnetic resonance (EPR) on several RTILs are discussed by illustrating several literature reports. Finally, the current challenges in RTILs research and objective of the present thesis work have been discussed at the end of this chapter.

1.1. Room Temperature Ionic Liquids

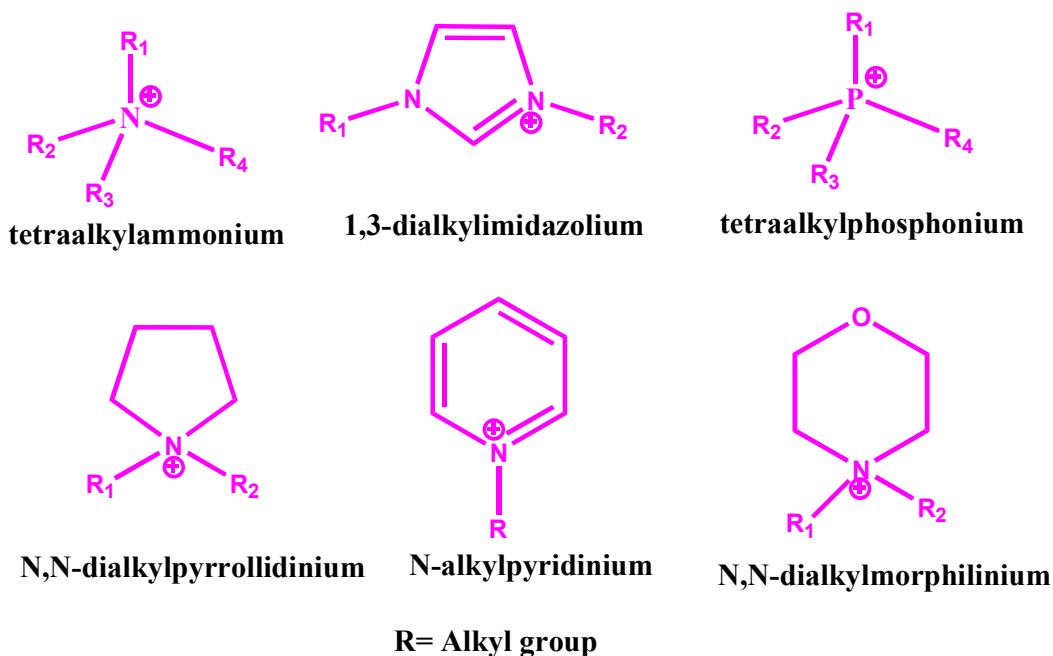
Ionic liquids (ILs) are molten salts having melting temperature less than 100⁰ C.¹ Room temperature ionic liquids (RTILs) are the group of ILs, which are liquids at ambient temperature and pressure.¹ ILs usually consist of large organic cation and organic or inorganic anions. The organic cations generally include organic moieties such as imidazolium, ammonium, pyridinium, pyrrolidinium etc. and the anions are usually bromide, chloride, sulfate, hexafluorophosphate, tetrafluoroborate etc. Since, the charge on the constituent ions (cations and anions) of RTILs is diffused due to their larger size, the charge density over the constituent ions becomes low.² Moreover, the large size of constituent ions makes the lattice packing inefficient.² The large size of constituent ions of RTILs and the small charge densities on them help to decrease the Coulombic interactions among the constituents leading to interruption of the lattice packing, which eventually prevents them to form a regular crystalline structure. The inefficient packing of

the molecules and low charge densities over the constituents of RTILs make these materials liquid at ambient temperature and pressure. We would like to mention that these liquids are very different from “molten salts” in a sense that they exist in liquid state at room temperature but retain the non volatility which is inherent to salts.^{3, 4} Moreover, the physiochemical properties of RTILs are also significantly different from that of the conventional organic solvent.⁵⁻⁹ The RTILs possess some interesting physiochemical properties such as extremely low vapor pressures, high viscosity, low toxicity, high ionic conductivity, extremely high thermal stability and capability to dissolve a wide range of inorganic, organic compounds.¹¹⁻¹⁹ These unique properties of RTILs are highly advantageous for their applications toward chemical, biological and material sciences.²⁰⁻³⁴

Though the first RTIL (ethylammonium nitrate) was discovered by Paul Walden in 1914³⁵, but it's achieved considerable attentions to the scientific community in 1960, when used as a promising electrolytic material in batteries.³¹ In 1980s the alkylimidazolium halogenoaluminate RTILs were developed by simple mixing of imidazolium with the aluminum halides.^{36, 37} After that, many cations such as imidazolium, pyrrolidinium, pyridinium, ammonium, phosphonium, etc. were used along with different anions such as hexafluorophosphate (PF_6^-), tetrafluoroborate (BF_4^-), nitrate etc. to obtain RTILs (Chart 1.1). Both the anions and cations play a vital role in determining the hydrophobic or hydrophilic character of RTILs.³⁸ RTILs are mainly classified into three generations. In the 1970s–80s, the first generation RTILs were developed, which were based on aluminum halides anions.^{37, 38} However, these RTILs were very hygroscopic which limited their practical usage. To overcome the drawback of first generation RTILs, the second generations RTILs were developed in 1990s.^{26, 39} These RTILs were composed of air-stable anions⁴¹ such as BF_4^- , PF_6^- etc. Though, these liquids were extremely viscous but produced

noticeable amount of HF acid in presence of small amount of water.²⁶ To address the problems of second generation RTILs, after 1990s, the third generations RTILs have been developed.^{27, 28} They were consists of perfluorinated anions such as NTf₂, FAP etc. These RTILs are mainly hydrophobic in nature and processing low viscosity, low melting points and low conductivity.^{27,}
²⁸ But there are also some problems with these RTILs as these were more expensive and have a high tendency to bind with metal ions. Again they were toxic and harmful due to the presence of fluorine.^{27, 28}

Cations



Anions

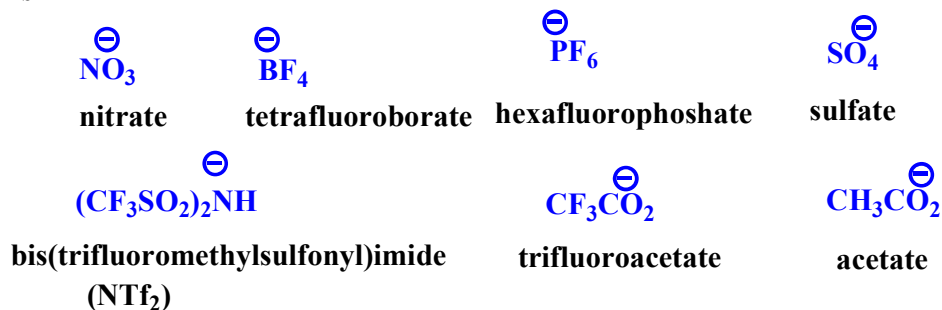


Chart 1.1. Molecular structure of some cations and anions of RTILs

Later on non-fluorinated (such as carborane orthoborate, sulfate) anion containing RTILs were developed, which were cheaper and low coordinating.^{29, 30}

In recent times, some task specific RTILs are also developed for a particular task⁴⁰⁻⁴³, such as thiol functionalized RTILs are being extensively used for the synthesis of nanocrystal quantum dots.⁴³ Amino acid based RTILs are also developed, these RTILs widely used for different biological applications.^{44, 45} Moreover, many other new families of RTIL such as, germinal dicationic, tricationic etc. have also been developed in recent times.⁴⁶⁻⁵²

1.1.1. Properties of RTILs

In last few years, a great deal of effort has been devoted to the study of RTILs due to their interesting physicochemical properties.¹⁰⁻¹⁹ Physicochemical properties of RTILs are very different from conventional organic solvents. These liquids are treated as specialized media primarily because of the fact that they possess unique properties, such as extremely low vapor pressures, low toxicity, high ionic conductivity, and extremely high thermal stability.^{2, 10-19} Since, properties of the RTILs are also found to depend on the nature of cations and anions that they are composed of, they are designated as “designer solvents”.² Molecular diagrams of some imidazolium-based RTILs are provided in Chart 1.2. Some important physical properties of imidazolium-based RTILs are depicted in Table 1.1.

Melting point: Melting point is an important parameter of a compound. Wide liquidus range of RTILs is characterized by their low melting and high decomposition points. The compounds melt, when the molecules or ions fall out of their crystal lattice and the crystal structure disrupts. The melting points of majority of the RTILs are not sharp as they can undergo supercooling.³⁸ Since the physicochemical properties of the RTILs depend on the nature of consistent ions, attempts have been made to link the melting point of the RTILs to the nature of their constituent

ions.^{53, 54} It has been pointed out that the symmetric cation containing RTILs shows the highest melting point. Moreover, the melting points of RTILs are found to decrease with increasing the alkyl chainlength on the cationic or anionic moiety of RTILs.^{53, 54} It has also been observed that the melting point of RTILs decrease with increasing the radius of the anion.⁵⁵

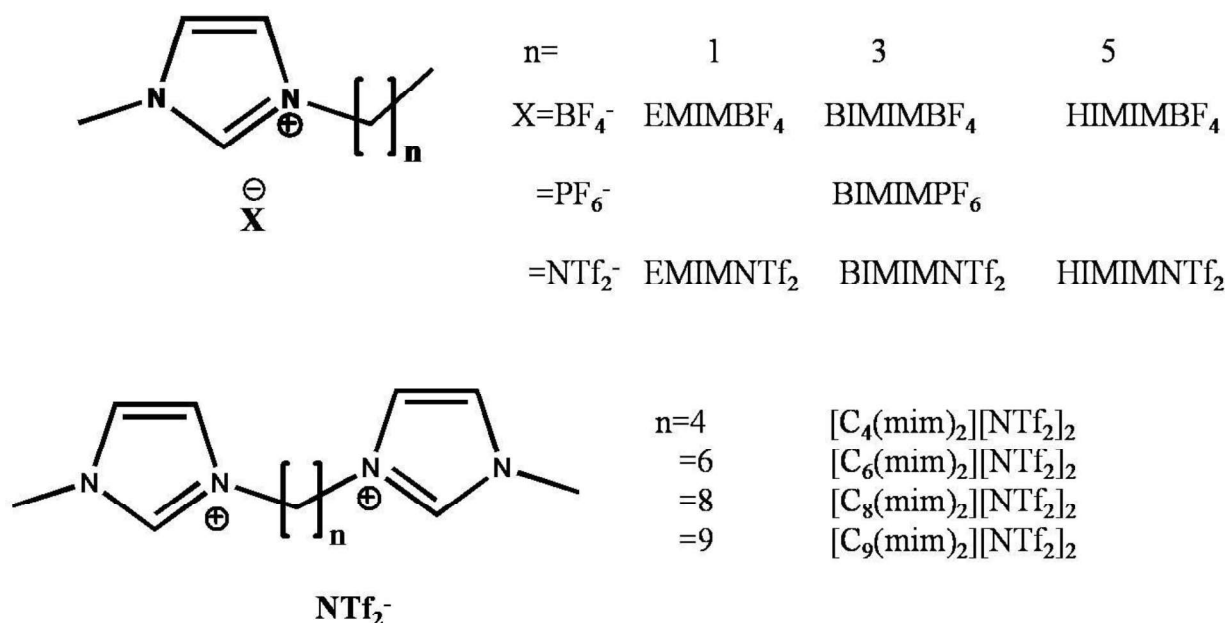


Chart 1.2. Molecular diagram and abbreviation of some imidazolium-based RTILs.

Glass transition temperature:

The glass transition temperature (T_g) provides an idea about the strength of cohesive forces in a given salt. The electron repulsion decrease cohesive interactions while, attractive Coulomb and van der Waals interactions increases the same.⁵⁶ The T_g depends on the various interaction (such as cation-anion interaction) that are present within the RTILs. Therefore, the T_g changes with changing the cation-anion combination in a particular RTIL. It can be seen that the T_g values decrease with both lowering the cation size and increase in asymmetry of the cation.⁶² This is due to decrease in the packing and cohesive energy of the RTILs.⁵⁷

Table 1.1. Physical properties of some common imidazolium-based RTILs

RTILs	T _{mp} (° C)	T _d (° C)	η (cP)	ρ (g/cc)	σ (ms/Cm)	E _T (30)
EMIMCl	86 ^a	-	solid	solid	-	-
BIMIMCl	65 ^a	-	solid	solid	-	-
EMIMPF ₆	60 ^b	-	solid	solid	5.2 ^c	-
BMIMPF ₆	-61 ^d	-	371 ^e	1.37 ^e	1.5 ^f	52.3 ^g
EMIMNTf ₂	-3 ^h	-	34 ^h	1.52 ^h	8.8 ^h	47.7 ⁱ
BMIMNTf ₂	-4 ^h	>400 ^j	52 ^k	1.43 ^k	3.9 ^k	47.2 ⁱ
BMIMBF ₄	-81 ^d	435 ^j	154 ^e	1.2 ^e	3.5 ^j	48.9 ^l
[C ₄ (mim) ₂][NTf ₂] ₂	59.5 ^m	433.4 ^m	-	-	-	-
[C ₆ (mim) ₂][NTf ₂] ₂	-	427.1 ^m	649 ^m	1.54 ^m	-	-
[C ₈ (mim) ₂][NTf ₂] ₂	-	423.2 ^m	661 ^m	1.48 ^m	-	-
[C ₉ (mim) ₂][NTf ₂] ₂	-	421.3 ^m	678 ^m	1.47 ^m	-	-

T_{mp}: melting point, T_d: decomposition temperature, η: viscosity, ρ: density, σ: specific conductivity, E_T: solvent polarity parameters. (a) ref 19; (b) ref 58; (c) ref 54; (d) ref 59; (e) at 20^o C ref 18; (f) ref 60; (g) ref 61; (h) ref 62; (i) at 20^o C ref 63; (j) ref 64; (k) ref 65; (l) ref 66; (m) ref 46.

Thermal stability: Thermal decomposition of the RTILs is highly dependent on the structures of RTILs and it varies with the constituents of RTILs.³⁸ RTILs are generally thermally stable up to 440^o C. It has been seen that usually the thermal decomposition temperature of RTILs decreases with an increase of hydrophobicity of anion.⁶⁷ The thermal stability of RTILs changes with changing the anion and it follows the order PF₆⁻ > NTf₂⁻ > BF₄⁻ > halides.^{38, 67} And for cations, the following trend is observed, phosphonium > imidazolium > tetraalkyl ammonium > pyrrolidinium.⁶⁷

Density: The Density values of RTILs depend on how closely the ionic constituents are packed and the shape and size of the ions. Therefore, the density of RTILs also depends on the nature of anions and cations. Usually, the densities of RTILs range between 1.0 to 1.6 g cm⁻³. The density depends on the nature of cations and it decreases in the order of pyridinium RTILs > imidazolium RTILs > piperidinium RTILs.^{68, 69} It has also been seen that the density decrease with increasing alkyl chainlength on the cation moiety of imidazolium, ammonium and sulfonium-based RTILs.^{70, 71} The density also depends on the nature of anion of RTILs. Like cationic moiety, the density also decreases with increasing alkyl chainlength on the anion of RTILs. Again, the density varies with varying the anionic moiety of RTILs. For example, for 1-ethyl-3-methylimidazolium-based RTILs, the density follows the order: CH₃SO₃⁻ < BF₄⁻ < CF₃SO₃⁻ < (CF₃SO₂)₂N⁻ < (C₂F₅SO₂)₂N⁻.^{18, 62, 69} Interestingly, the density is found to decrease with increasing the ring carbon number of the cation for lactum-based RTILs with fluorinated anions.⁷² This has been rationalized to the change in the cation-anion interaction due to the increase in the cation size.⁷²

Viscosity: Viscosity of a fluid depends on the various intra and inter molecular interaction (such as Coulombic, van der Waals and hydrogen bonding interactions etc.) prevailing within the constituents of the fluid. Naturally, the viscosity of RTILs is significantly affected by the nature of cations and anions of the RTILs. Interestingly, the viscosities of RTILs are estimated to be considerably higher than that of conventional organic solvents.⁶² It has been seen that viscosity increases with increasing the alkyl chainlength on the cationic or anionic moiety of RTILs.⁶² This is due to the increase the van der Waals interactions within the RTILs.⁶² Again, the viscosity of the RTIL is also dependent on the nature of the anion. The viscosity of the RTIL is also influenced by the basicity and the ability of the anion to form hydrogen bonding interaction with

the cation.^{73, 74} H-bonding is the main cause for the higher viscosities of alcohol functionalized RTILs than their alkylated counterparts.^{73, 74} Viscosity variation also happens due to variation in the shape, size, and molar mass of anion. It is important to note that the viscosities of RTILs significantly decrease in presence of water and halide impurity.⁷⁵ Again, the viscosity of RTILs decreases with increasing the temperature due to lowering of viscosity of the medium.⁷⁶

Ionic conductivity: Ionic conductivity or specific conductivity is a fundamental and important property of a given medium. It is of vital important, for many electrochemical applications. The ionic conductivity (specific conductivity) of RTILs originates from the mobility of the constituent of ions. Thus, the ionic mobility of a medium depends on the number of charge carriers and the viscosity of the medium.^{62, 71, 74} Moreover, any association/aggregation between ionic species can reduce the ionic conductivity of the medium.⁷⁷ Generally, RTILs have relatively larger ionic conductivities compared to conventional organic solvents. The ionic conductivity of alkyimidazolium and alkylammonium-based RTILs decreases with increasing the alkyl chainlength on the cation. However, more change in conductivity is seen for short alkyl chains (C1-C4) and small change for longer alkyl chains (C4-C10) containing RTILs.^{54, 60}

Polarity: Polarity is an important parameter of a medium. The polarity of RTILs is determined through various experimental methods such as EPR spectroscopy,^{78, 79} fluorescence spectroscopy^{66, 80} and microwave spectroscopy.⁸¹ FT-IR combined with theoretical DFT (density functional theory) methods⁸² are also employed to estimate the polarity of some RTILs. The polarity of different RTILs is generally found to be more than acetonitrile but less than methanol. Some studies have revealed that the polarity of some imidazolium-based RTILs is close to short chain alcohols.^{61, 83} The polarity of the RTILs has been found to decrease with increasing the alkyl chainlength on the anionic or cationic moiety.

Other properties: Other important properties of RTILs are refractive index and surface tension. The refractive index (n_D) of a compound can provide the knowledge about its polarity. Similar to other properties of RTILs, the n_D values of RTILs depend on the nature of anion or cation. From n_D values of RTILs, it can be considered to be moderately polar medium like acetonitrile but less polar than short chain alcohol. Interestingly, the n_D values decrease with increasing the alkyl chainlength on the cationic or anionic moiety of RTILs. However, hydroxyl-group containing RTILs possess higher n_D value.⁸⁴

Another very important property of RTILs is surface tension. It has been seen that variation in either the cationic or the anionic moieties has a similar effect on surface tension.⁸⁴ The surface tension is found to decrease with increase in packing efficiency while increase in hydrogen bonding interaction or ionic interactions.

1.1.2. Structural and Dynamic Heterogeneity of RTILs

To have a proper understanding on complex physical, chemical and dynamical behavior of RTILs, it is extremely important to understand the structural organization of RTILs. Studies have shown that RTILs are not homogeneous in nature. RTILs are micro-heterogeneous in nature.⁸⁵⁻⁹¹ Several experimental and theoretical studies have been carried out to understand the structural organization of RTILs.⁹²⁻¹⁰⁷ Some experimental and theoretical studies have demonstrated that structures of RTILs vary from ion pairs, ion clusters (supramolecular assemblies) to H-bond networks (mesoscopic) pattern.¹⁰⁸⁻¹¹²

The structural information of some RTILs has been determined through X-ray diffraction methods.⁹² These studies have demonstrated the presence of an extended network in RTILs where, the cations and anions linked through hydrogen bonding interactions.⁹² The evidence of hydrogen bonded extended network of ionic constituents of RTILs has also been established

through neutron diffraction,⁹³ NMR,⁹⁴ mass spectrometry^{95, 96} and Raman spectroscopy⁹⁷ studies. Some X-ray diffraction measurements on RTILs have also revealed that some RTILs can exist in micellar and reverse micellar structure.^{98, 99}

The ion pair structure of ethylammonium nitrate (EAN) has been established by Weingärtner and coworker¹⁰⁰ through conductivity measurements. Some multinuclear NMR studies have also revealed that C₂mim[X] (where X=Cl⁻, Br⁻ and Γ) exist as contact ion pairs formation.¹⁰¹ In another study, Every et. al.¹⁰² have demonstrated the formation of ion pair in dialkylimidazolium RTILs through transport property measurements. However, some recent studies based on dielectric spectroscopic measurements on RTILs have demonstrated no evidence in support of ion pair formation.¹⁰²⁻¹⁰⁶ Similarly, NMR experiments also do not support ion-pair formation of RTILs.¹⁰⁷

Several fluorescence studies in RTILs have demonstrated that neat RTILs are micro-heterogeneous in nature.^{89, 88, 113, 114} Among these the studies by Samanta and coworkers⁸⁸ are noteworthy where they have investigated the micro-heterogeneous behavior of several RTILs by exploiting excitation wavelength dependent fluorescence study. Some experimental and theoretical studies revealed that RTILs are both structurally and dynamically heterogeneous in nature.^{90, 91} Bhattacharyya⁹¹ and Maroncelli⁹⁰ through excitation wavelength dependent solvation dynamics study on RTILs were independently shown that RTILs are not only structurally heterogeneous but also dynamically heterogeneous. Some recent investigations through IR spectroscopy have also shown the dynamic heterogeneity of ammonium-based RTILs.¹¹⁵ The micro-heterogeneous behavior of RTILs has also investigated by Hu and Margulis⁸⁹ through MD simulation studies. Recently, the heterogeneous behavior of RTILs are also evident through optical heterodyne-detected Raman induced Kerr effect (OHD-RIKES) studies.⁸⁷ Nevertheless,

as RTILs are complex media, additional studies based on experimental and theoretical investigations are essential to understand the kinship among structural variation of ions and micro-heterogeneous behavior of RTILs.

1.1.3. Applications of RTILs

RTILs have many unique properties that conventional fluids do not have, these unique properties of RTILs are highly advantageous for their applications toward chemical, biological and material sciences.²⁰⁻³⁴ The RTILs have the potential to dissolve a wide range of compounds (inorganic and organic), which can make them useful in various kinds of applications like drug delivery process, ion diffusion devices etc.^{116, 117} RTILs have shown great promise in replacing the volatile organic solvents in numerous chemical reactions including catalysis.¹¹⁸⁻¹²¹ RTILs have also been used in bioseparation processes of active compounds and in separation technology, such as, as a mobile phase in liquid chromatography.¹²² The RTILs are also used as solvents or co-catalysts in protein activity, stability, and crystallization.^{123, 124} Among several real and future applications of RTILs, it is importance to notice their role in energy-related applications. Due to the favorable electrochemical properties such as wide electrochemical window, non-flammability and high thermal stability, RTILs are indeed exploited as electrolytes for capacitors,¹²⁵ solar cells¹²⁶ and in various metal ion batteries such as lithium-ion batteries,¹²⁷ Li-sulfur batteries¹²⁸ etc. Recently, RTILs have been used as electrolytes in conducting polymer-based electrochemical devices.¹²⁹ RTILs have also been used in a variety of other industrial applications such as rocket propellants and lubricants.¹³⁰ In the last decades, different type of “task-specific” ionic liquids (TSILs) have been developed, which has been used in organic synthesis,⁵ catalysis,¹³¹ synthesis of nanomaterials,⁴² and ion conductive materials¹³² etc.

Geminal dicationic ionic liquids (DILs), composed of one dication and two monoanions^{46, 47} have also been developed recently. These systems offer more cation-anion combinations than monocationic ionic liquids (MILs). This can be helpful to achieve greater tunability and variability of the properties of RTILs. In fact, some literature reports have suggested that physicochemical properties such as surface tension, density, thermal stability etc. corresponding to DILs are superior to those of MILs.^{46, 47} Recent studies have demonstrated that DILs, can be used effectively as catalysts,¹³³⁻¹³⁶ lubricants,^{137, 138} solvents for chemical reaction,¹³⁹ and high temperatures electrolytes in metal ion-batteries.^{140, 141}

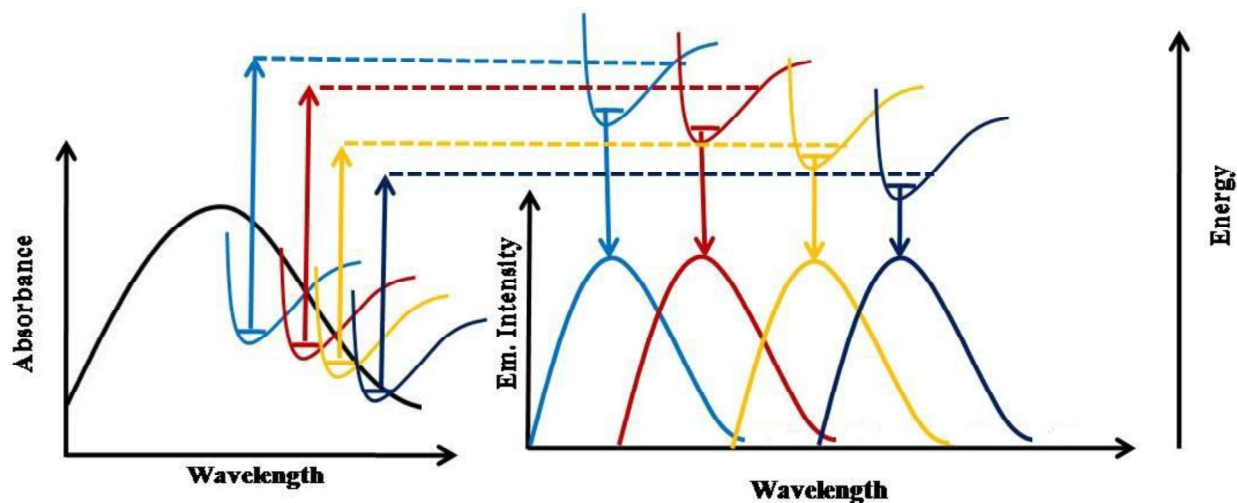
1.1.4. Photophysical Studies in RTILs

A molecular level understanding in terms of interaction, structure and dynamics of new solvent system is required for their effective utilization in various applications. Therefore, considerable efforts have been made towards understanding the structure-property relationship^{63, 85-91} of RTIL-based solvent systems through both theoretical¹⁴²⁻¹⁵⁷ and experimental studies.^{63, 88, 91, 158-229} Among experimental work, photophysical²³⁰⁻²³⁵ and photochemical²³⁶ investigation are found to be widely exploited in recent times. Several studies have suggested that RTILs are not homogeneous in nature like conventional organic solvents. They are micro-heterogeneous in nature.⁸⁵⁻⁹¹ Some of the useful photophysical studies in RTILs relevant to the present work are described below.

Excitation wavelength dependent fluorescence study

According to Kasha's rule²³⁷, emission maximum of a fluorescent molecule is thought to be independent of excitation wavelength. However, under certain conditions, emission maximum of a fluorophore can shift towards the low energy (red) region with an increase in the excitation wavelength.²³⁸⁻²⁴⁴ This type of behaviour is known as the red- edge- effect (REE).^{238, 239} REE is

usually observed under a particular situation.²³⁹⁻²⁴¹ Firstly, if there are distribution of energetically different solvated species in the ground state. This situation leads to inhomogeneous broadening of the absorption spectrum. Secondly, rate of energy transfer among different species is slow. Under these conditions REE effect can be observed. This study though can not predict exact length scale of heterogeneity but certainly provide qualitative idea about micro-heterogeneous nature of the medium. Some organic fluorescent molecules shows the REE in RTILs.⁹⁴ REE also gives an indirect idea on the presence of specific solute-solvent interactions between fluorophore and RTILs. It has been reported that specific H-bonding interactions between 8-anilinonaphthalene-1-sulfonate (ANS) and anion of the RTIL contribute to the REE observed in [bmim][PF₆].¹⁶¹ The molecular basis of this phenomenon is illustrated through a schematic diagram which is provided in Scheme 1.1.



Scheme 1.1. Excitation wavelength dependent phenomenon.

Time-resolved fluorescence anisotropy, Rotational relaxation dynamics:

Rotational relaxation dynamics of a fluorescent molecule in a given media has been investigated through time-resolved fluorescence anisotropy measurements of the molecule in the said medium. Fluorescence anisotropy is the extent of emission depolarization of a fluorescent probe that absorbed polarized light. Rotational diffusion in the excited state of the molecule is the cause of emission depolarization.²⁴⁵ In a homogeneous solution, the isotropic arrangement of the molecules is disturbed by polarized light beam. The molecules are selectively excited whose dipole moment vectors are aligned with the electric vector of the polarized light. This introduces an anisotropic distribution of molecules in the system. The average angular displacement of dipole of the molecule between the absorption and subsequent emission due to rotational diffusion is determined through anisotropy measurements. The rotational diffusion of a molecule not only depends upon its size and shape but also on the local microenvironment (viscosity) of the medium. Interestingly, as the rotational motion of a solute molecule, dissolved in a solvent is also dependent on the solute-solvent interaction (such as electrostatic, H-bonding interaction etc.), on the solute-solvent, solvent-solvent interaction investigations on solute rotation in a given media can provide valuable information of liquids and solutions.²⁴⁶

The data obtained from fluorescence anisotropy are usually analyzed in light of hydrodynamic^{239, 247} and quasi-hydrodynamic^{248, 249} theories. The Stock-Einstein-Debye (SED) theory can successfully explain the rotational motion of solute when the size of solute and solvent are comparable. According to the SED theory the rotational times (τ_r) is related with the viscosity (η) of the medium. The SED theory is provided by the following equation^{239, 247}

$$\tau_r = \left(\frac{\eta V f C}{kT} \right) \quad (1.1)$$

where η = viscosity of the medium and V is the van der Waals volume. f and C are the shape factor and the boundary condition parameter respectively. The parameter f takes into consideration of the non spherical nature of the solute molecule and the magnitude of C indicates the degree of coupling between solute and solvent, and it has two limit stick ($C=1$) and slip ($0 < C < 1$). k is the Boltzmann constant and T is the absolute temperature. According to SED theory, solvent is considered as a structure less continuum, which is featured by the viscosity. For a specific η/T , the reorientation time is independent on the nature of the solvent. SED theory is useful for the estimation of rotational coupling constants (C_{rot}) which measure the departure from the normal hydrodynamic behavior.

However, the SED theory often fails to explain the rotational dynamical behavior of a given solute molecule when the solvent size is larger than the solute molecule. In that scenario, to explain solvent size dependent rotational behavior of fluorescence molecule, quasi hydrodynamic theories, such as Gierer-Wirtz (GW)²⁴⁸ and Dote-Kivelson-Schwartz (DKS)²⁴⁹ theory are exploited. According to GW theory, the solvent is made up of concentric shells of spherical particles surrounding the spherical solute molecule at the center and the boundary condition parameter (C_{GW}) is estimated by considering the decrease in the angular velocity of the solvent molecules in successive shells surrounding the solute.²⁴⁸ While, DKS theory takes into consideration both the size of solvent and solute molecule as well as the free space created between solute and the solvent molecule.²⁴⁹ According to DKS theory, when the size of the solute is comparable to the free spaces in the solvents, the coupling between the solute and the solvent will become weak. This results in reduced friction experienced by the solute molecule.

Understanding of various interactions of the constituents of RTILs and their interactions with the added solutes are crucial for their further use. Viscosity, temperature and specific solute-solvent

interactions, of the surrounding solvent medium are the key factor, which control the dynamics of solute rotation. Rotational dynamic studies of fluorescent organic solutes in RTILs can provide information on the solute-solvent interactions and the solvent properties of the medium. In recent times, a number of studies have been investigated by several groups towards attaining this goal.¹⁸³⁻²⁰⁵ These investigations have demonstrated that the solute rotation not only depends on the medium viscosity but also depends on the specific solute-solvent interactions. The presence of specific solute-solvent hydrogen bonding interactions makes the rotation of solute molecules significantly hindered in a given RTIL.^{168, 184, 195, 205, 206} Moreover, the solute rotation is also influenced by size of solvent molecule in absence of any specific interaction.^{184, 195} Since RTILs consist of ions, it is expected that electrostatic (charge-charge) interaction of the constituents ions will influence the rotational dynamics of charged probes molecules.^{7, 189} However, rotational dynamics studies have demonstrated that the rotational times of charged probe in RTILs depend only on the viscosity of the medium, no significant influence of charge-charge interactions on the rotational dynamics has been observed.^{7, 189} Rotational relaxation dynamic of neat RTILs have also been studied recently. Recently Dutt and co-workers²⁰¹ have investigated the rotational dynamic of several RTILs in their neat condition and concluded that the emission of neat RTILs originates from the associated species rather than the monomeric moiety. However, a systematic study on the rotational dynamics of RTILs in their neat condition is not available. Therefore, studies on rotational dynamics of neat RTILs with a systematic variation in the constituents of RTILs are very essential.

Förster resonance energy transfer studies:

Förster resonance energy transfer (RET) is a phenomenon in which the excitation energy of the donor is non-radiatively transferred to the acceptor.²⁴⁵ More importantly, efficiency of RET

process dependent on the distance between donor and the acceptor (10 to 100 Å), and by virtue of this, it has been used as a “spectroscopic ruler” in molecular biology.^{245, 250, 251} Perhaps one of the greatest advantage of RET process is to monitor events in heterogeneous environments such as cells, protein assemblies, polymer matrices etc., in noninvasive manner.^{245, 250} RET being a distance dependent phenomenon, a small change in the donor-acceptor distance of the concerned system can affect the RET efficiency.²⁴⁵

Some studies have demonstrated the usefulness of RET studies towards understanding the behavior of RTILs.^{168-173, 212, 213} Bhattacharya and coworkers¹⁷¹ have demonstrated that excitation wavelength (λ_{ex}) dependent FRET study can provide information about the different regions of an ionic liquid based micellar system. Stricoli and co-workers²²⁷ have also demonstrated the aggregation behavior of several RTILs by exploring RET studies. The RET studies from neat RTILs to organic fluorophore molecule are limited. Among these the studies by Ghosh et. al.^{212, 213} are noteworthy where RET studies have been investigated by employing RTILs having different alkyl groups on the cations, and different types of anions. However, more RET studies are needed to obtain further physical insights into the RET process in RTILs.

1.1.5. NMR Investigations on RTILs

NMR spectroscopy is a powerful technique and is primarily used to characterize the molecules. Simple ¹H and ¹³C-NMR chemical shift measurements are carried out to characterize the RTILs. However, ¹H-NMR technique has also been used to understand the solute-RTILs interactions. For example, the solute-solvent hydrogen bonding interactions between the imidazolium alkyl sulfate RTILs and 4-aminophthalimide have been confirmed through ¹H-NMR chemical shifts measurements by Das et. al.¹⁹⁵ In recent times, multinuclear NMR techniques have been widely

used for measuring the translational diffusion coefficient, cation-anion interaction, spin-spin and spin-lattice relaxation time, and many other physiochemical properties of RTILs.²⁵²

In this context, the Pulsed field gradient NMR (PFG-NMR) method has been used quite effectively to determine the translational diffusion coefficients of constituent's ions of a RTIL.²⁵³

Self-diffusion coefficient measurement of RTILs is extremely important, as it directly related with the transport properties of the medium. Therefore by measuring the self-diffusion coefficient one can get the idea about the transport properties of RTILs. Rossler and coworkers²⁵⁴ have calculated the self-diffusion coefficients of the cationic moiety of [BMIM][BF₄] and [EMIM][SCN] respectively by using ¹H relaxation data, whereas diffusion coefficients of anions (BF₄⁻) for [BMIM][BF₄] is determined by using ¹⁹F-NMR relaxation data.

Moreover, the nuclear overhauser effect (NOE) is also used to understand the cation-anion interaction in RTILs.²¹⁵⁻²¹⁹ Castner and coworkers²¹⁹ have used the NMR NOE technique to obtain an idea on the structure and interactions between ions in RTILs. Recently, several studies have been reported to understand the inter or intra molecular interactions among the constituents of RTILs.²¹⁵⁻²¹⁹

1.1.6. Fluorescence Correlation Spectroscopy (FCS) and Electron Paramagnetic Resonance (EPR) Studies

Fluorescence correlation spectroscopy (FCS) is an advanced and powerful fluorescence technique at the single molecule level for the investigation of molecular diffusion, chemical reactions, binding studies, protein dynamics etc.²⁴⁵ This technique is based on the fluctuations of fluorescence intensity of a dilute fluorophore solution in a small confocal volume. Studies on diffusion of organic fluorophores by FCS technique eventually help to understand the microscopic structural organization of the RTILs. Baker and coworkers¹⁶² were first used this

technique to investigate the translational diffusion of charged and neutral fluorophores in RTILs. They have also reported the biphasic diffusion behavior of rhodamine 6G in N-alkyl-N-methylpyrrolidinium-based RTILs.¹⁶² Both the fast and slow diffusion coefficients decrease with increase in the alkyl chain length on the cation. They have demonstrated the observation of self-aggregation of the alkyl chains of the cationic ring.¹⁶² The diffusion of neutral and anionic dyes in two imidazolium-based RTILs has been investigated by Bhattacharyya and coworkers.²²⁰ A wider distribution of the diffusion coefficients of a dye in RTILs is attributed to the heterogeneity of the media. Diffusion coefficients of neutral and anionic dyes are found to be very similar in water.²²⁰ But the anionic dye diffuses ~1.7 times slower than the neutral dye in RTILs due to presence of electrostatic interactions, indicating that FCS experiments are useful to understand the electrostatic/specific interactions between fluorescent probe and RTILs.²²⁰ Satyajit et. al.¹⁵⁹ have compared the results of FCS and fluorescence lifetime data to explain the heterogeneity and existence of polar and non-polar regions of the RTILs. Recently, Kim and co-workers,^{202, 203} have used the FCS techniques to calculate the diffusion coefficient and the number density of the fluorescing species of neat RTILs. They have shown that the fluorescence of neat RTILs is originating from different anion-cation associated species.²⁰² However, the FCS study in neat RTILs is very limited. Therefore a thorough FCS study of neat RTILs is very much essential.

Electron paramagnetic resonance (EPR) spectroscopy is another valuable technique which can be used to investigate the microscopic behavior of RTILs. Basically, in this technique EPR active free radical probes such as 2,2,6,6-tetramethylpiperidine-1-oxyl (TEMPO) and 4-amino-2,2,6,6-tetramethylpiperidine-1-oxyl (TEMPAMINE) are used for studies. EPR technique can be used to calculate the micro-polarity of RTILs.^{78, 79, 221, 222} The hyperfine coupling constant of EPR active

probe can be correlated to the polarity of the medium. Shibuya and coworkers have calculated the polarity of several RTILs using EPR techniques.^{78, 79} Noel et al.²²³ investigated the solvation of two EPR active probe in RTILs. They have demonstrated that the solvation properties of RTILs are similar to those of polar organic solvents.²²³ Additionally, several researchers have investigated the rotational diffusion of EPR active spin probes in RTILs.²⁵⁵⁻²⁵⁹ Evans et al.²⁵⁵ has investigated the rotational and translational diffusion of EPR active probe TEMPO in five RTILs and has determined the activation energy for the same. In three of these RTILs, they have observed that the activation energies of viscosity, translation and rotation are similar. However, in the remaining two RTILs, the rotational activation energies are found to be lower than the translational activation energies and activation energies for viscous flow. They have suggested that these two RTILs have more ordered structures.²⁵⁵ Recently, Mladenova et al.²⁵⁸ have studied the rotational correlation time of several EPR active probes in a series of imidazolium-based RTILs in a wide range of temperatures. However, the EPR studies in RTILs are observed to be very limited.

1.2. Objective Behind the Thesis

Though considerable progress in studying of RTILs by theory and experimental work has been undertaken, kinship among intermolecular interaction, structure and dynamics of monocationic and dicationic RTILs are not yet properly understood. Moreover, combined studies on RTILs by involving steady-state and time-resolved fluorescence, NMR, EPR and FCS study are very limited. It is expected that outcome of the combined fluorescence, NMR, EPR and FCS studies would be helpful to understand this complex media in much better fashion. Some of the important issues regarding RTILs that require proper attention are;

- Nature of various interactions (solvent-solvent and solute-solvent) existing in RTILs which affect their physicochemical properties.
- Appropriate understanding of the micro-heterogeneous behavior of various RTILs.
- Understanding the nano structural organization of RTILs.
- Understanding the relationship among intermolecular interactions, structure and dynamics of mono cationic and dicationic RTILs.

The present thesis work has been carried out mainly to address the above mentioned issues. The main objective of the present thesis is to understand the kinship among intermolecular interactions, structure and dynamical behavior of several mono and dicationic RTILs through time-resolved fluorescence anisotropy, NMR, fluorescence correlation spectroscopy (FCS) and electron paramagnetic resonance (EPR) spectroscopic studies.

Solute-solvent interaction has been examined by employing two structurally similar and chemically distinguishable organic solutes, 4-(azetidino-1-yl)-7 nitrobenzo[1,2,5]oxadiazole (ANBD) and 7-nitrobenzo[1,2,5]oxadiazole-4-amine (HNBD), in 1-ethyl-3-methylimidazolium alkyl sulfate (alkyl = ethyl, hexyl and octyl) with an aim to understand the intermolecular interactions among solute and solvent molecules. Additionally, the microscopic behavior of hydroxyl-functionalized RTIL has been investigated by monitoring solute-solvent interaction between coumarin 153 (C153) and 1-hydroxyethyl-3-methylimidazolium fluoroalkylphosphate ([OH-Emim][FAP]) RTIL (Chapter 3).

With an aim to understand the behavior in terms of intermolecular interactions, structure and dynamics of dicationic and monocationic ionic liquids (ILs), two imidazolium-based dicationic ionic liquids (DILs) and one monocationic ionic liquid (MIL) has been investigated through

combined fluorescence, electron paramagnetic resonance (EPR), NMR and fluorescence correlation spectroscopy (Chapter 4).

Chapter 5 describes the aggregation behavior of a series of neat 1-ethyl 3-methylimidazolium alkyl sulfate (alkyl = ethyl, butyl, hexyl, and octyl) RTILs through combined time-resolved fluorescence spectroscopy, 1-D, 2-D NMR spectroscopy, and fluorescence correlation spectroscopy.

The resonance energy transfer (RET) studies have been investigated from neat ionic liquids (donor) to rhodamine 6G (R6G) (acceptor) molecules to understand the microscopic structural organization of neat RTILs. Basically, three different sets of RTILs are taken for this studies, where in first set (1-ethyl-3-methyl imidazolium alkyl sulfate) the alkyl side chain length on the anionic moiety is systematically varied, in second set variation is done on the cation (aromatic and nonaromatic) and in another set, the branched chainlength on the cationic moiety of RTILs is varied (Chapter 6).

In last chapter, the aggregation behavior of two fluorescent molecules, 4-aminophthalimide (AP) and 4-(N,N-dimethyl)amino-N-methylphthalimide (DMP) and the influence of ILs on their aggregation behavior has been investigated (Chapter 7). Summery and future prospects of the present investigation are also outlined at the end of this chapter.

Chapter 2

Instrumentations and Methods

This chapter demonstrates the details of different experimental techniques used in the present thesis work. This chapter also describes the different methodologies that are adopted to analyse the experimental data.

2.1. Purification and Characterization of RTILs

The RTILs used in the present thesis work were obtained from Merck (Germany), Iolitech (USA) and Frontier Scientific (USA). The RTILs were purified by active charcoal treatment and purity of the RTILs were checked by using different conventional analytical techniques such as NMR and mass spectrometry. The dicationic RTILs (DILs) were synthesized in our laboratory by following a literature procedure.⁴⁶ The synthetic routes, purification and characterization of the DILs are provided in details in chapter 4.

2.2. Sample Preparation for Spectroscopic Measurements

For the steady state and time-resolved fluorescence measurements, the RTILs have been taken in long-necked quartz cuvette having a path length of 1cm. Necessary amount of fluorescence probe was dissolved in the RTILs so that the optical density of the probe was maintained below 0.4. During sample preparation the proper precaution was taken to avoid moisture absorption by the samples. The cuvettes were sealed by using the parafilm and rubber septum to avoid the moisture absorption.

2.3. Instrumentations

2.3.1. Instrumentations Used for Characterization of Samples

The samples were characterized by using Bruker Avance 400 MHz NMR spectrometer. The ESI-MS (Electrospray ionization mass spectrometry) spectra were collected by using Bruker micrOTOF-QII mass spectrometer. Cone and Plate viscometer (Brookfield LVDV-III Ultra) was used to record the dynamic viscosity of the RTILs. The temperature dependent viscosity measurements were performed by using a Julabo water circulator bath.

2.3.2. Instrumental Techniques for Absorption and Steady State Emission Measurements

2.3.2.1. Absorption Measurements

The UV-visible spectroscopy measurements of all the samples were investigated by using Perkin Elmer (Lambda 750) spectrophotometer with a wavelength resolution of 0.15 nm. Absorption spectroscopy mainly provides the idea about the ground electronic states of systems. From absorption measurements, one can get the information about the nature of electronic transitions possible in the ground state of the chromophore of the concerned samples usually by looking at the wavelength of different absorption bands and molar extinction coefficient. This essentially helps to characterize the various types of chromophoric systems and their neighboring micro-environments.²⁶⁰⁻²⁶² Moreover, absorption spectrum of an absorbing species is also influenced by polarizability, solvent polarity or hydrogen bonding interaction in the ground state. Therefore, UV-visible absorption spectroscopy is also capable of providing useful insights into the interactions between the chromophoric species and its surrounding micro-environment in the ground electronic state.

The UV-Visible absorption spectroscopy follows the Lambert Beer's law, according to which the absorbance (A_λ) of an absorbing species in a solution at an wavelength λ , is directly proportional

to the concentration (C) of the species in the solution and its molar extinction coefficient (ϵ_λ) at that particular wavelength. It can be expressed by the following relation²⁶⁰⁻²⁶²

$$A_\lambda = \log\left(\frac{I_o}{I}\right) = \epsilon_\lambda Cl \quad (2.1)$$

where I_o = Intensity of the incident light and I = Intensity of the transmitted light. l = path length of the sample.

2.3.2.2. Steady State Fluorescence Measurements

All the steady state fluorescence measurements of the present work were carried out by using a Perkin Elmer (LS55) fluorescence spectrometer. A high pressure xenon lamp and a R-928F (Hamamatsu) photomultiplier tube (PMT) was used as the excitation source and photodetector respectively. Perkin Elmer, PTP1 peltier temperature programmer was used for controlling the temperature of the sample holder.

Fluorescence spectroscopy is a powerful and sensitive tool to examine various types of photochemical and photophysical processes of the fluorescing species in the excited state. Slight changes in the environment or interactions of the fluorphore molecules in the excited state can cause change in the emission maxima, intensity and shape of the emission spectra of the respective species.²⁶⁰⁻²⁶² Therefore, this technique can provide a better understanding on the micro-environment of the emitting species.

2.3.3. Instrumental Techniques for Time-Resolved Studies

2.3.3.1. Fluorescence Lifetime Measurements

Time-resolved fluorescence techniques are very useful in giving insightful information about the kinetics and dynamics of various photochemical and photophysical process. In this technique, a very short pulse light is used to excite the fluorescent molecule that results an initial population

(n_o) of fluorescent molecule in the excited state. The excited state population decays with a rate (k_r+k_{nr}) according to the following relation²⁶⁰⁻²⁶⁴

$$-\frac{dn(t)}{dt} = (k_r + k_{nr})n(t) \quad (2.2)$$

where $n(t)$ = number of excited molecule at time t following the excitation of fluorophore molecule with the very short pulse light. The k_r and k_{nr} denotes the radiative and nonradiative rate constant respectively. Moreover, in a given period of time, the possibility of emission from every excited fluorophore is same. And the excited state population decays with an exponential manner with the following equation is provided below;

$$n(t) = n_o \exp\left(-\frac{t}{\tau}\right) \quad (2.3)$$

It can be seen from equation 2.3, that the fluorescence intensity is directly proportional to the number of excited molecules present in the solution. Therefore the equation 2.3 can be simply be written in terms of the time dependent intensity $I(t)$ and the integration of the resulting equation provide the following equation

$$I(t) = I_o \exp\left(-\frac{t}{\tau_f}\right) \quad (2.4)$$

where I_o = intensity at zero time, τ_f = fluorescence lifetime of the sample that is related to the radiative and nonradiative decay rate constants as per the following equation

$$\tau_f = \frac{1}{k_r+k_{nr}} \quad (2.5)$$

The excited state fluorescence lifetime is estimated through time-correlated single photon counting (TCSPC) technique. In this context, it should be noted that different molecules spend different span of time in the excited states. Therefore, in the excited state, some molecules may emit at longer time whereas others may take very short time. Therefore, the time distribution of these emitted photons appears as the measured fluorescence decay of the fluorescent sample

under examination. Thus, the estimated lifetime denotes the statistical average of the times that the fluorophore molecules spend in the excited state.

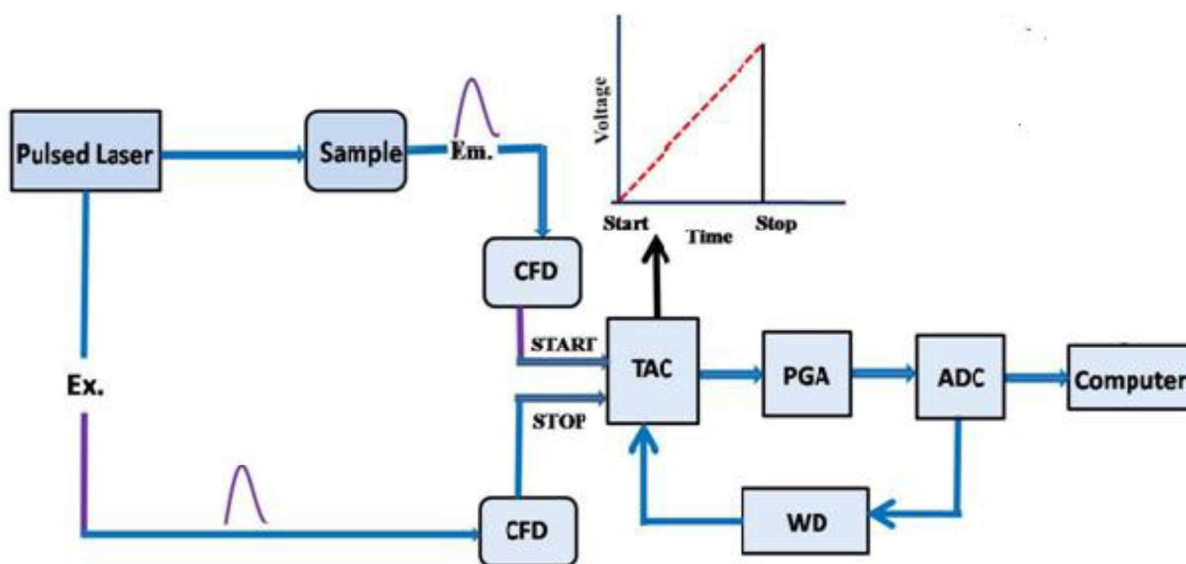
In the present investigation, all the time-resolved measurements have been carried out by using Edinburgh OB920 TCSPC instrument. The fundamental working principles and important components correlated to the TCSPC setup are described below.

2.3.3.2. Basic Principle of TCSPC Setup

The working principle of TCSPC technique is unique. The working principle of TCSPC techniques is based on the single photon detection from a sample following a pulsed excitation.^{245, 263-266} The working principle of TCSPC technique is dependent on the time dependent probability distribution of the single photon emission from an excited fluorophore. Time dependent probability distribution of the single photon emission from the excited fluorophore is equivalent to the time dependent changes in the fluorescence intensity of the sample after its excitation through the short light pulse.^{245, 263-266} The working principle of TCSPC setup (in forward mode) is provided by a schematic diagramed in Scheme 2.1

As describe in Scheme 2.1, an excitation pulse is divided into two parts, the first part is used to excite the sample and the second part of the pulse excitation is directed towards the start PMT. The optical signal at the start PMT generates an electrical signal that corresponds to START pulse. The START pulse is then passed through the Constant Fraction Discriminator (CFD) which exactly measures the arrival time of the pulse. Then the signal arrives through START input to the Time to Amplitude Converter (TAC), which generates a voltage ramp which increases linearly with time. In another channel, after pulsed excitation, the photons emitted from the sample are then detected one by one by the stop PMT to generate electrical STOP pulses for each of the individual photons collected. Again, the STOP pulses generated in the stop PMT are

also passed through a CFD and variable delay line to the STOP input of the same TAC unit. The TAC unit stops to generate the voltage ramp once it detects the first STOP pulse. Essentially, the TAC contains a voltage that is proportional to the time delay (Δt) between the excitation and emission pulse. The TAC output pulse signal is then passed through PGA (Pulsed Gain Amplifier) to an ADC (Analog-to-Digital Converter). The ADC generates a numerical value, which is proportional to the height of the TAC output pulse signal. Finally, the data is stored in the multichannel analyser (MCA).



Scheme 2.1. A schematic diagram for the working principle of TCSPC setup.

The above cyclic process is repeated again and again for a large number of times. This results the collection of histogram of counts in the MCA channels. Scheme 2.1 has provided for a TCSPC technique that is worked in “forward mode”. But, in present times, almost all TCSPC measurements are done in the "reverse mode".²⁴⁵ For the present work, TCSPC setup is also used in “reverse mode”. This process is almost same as described above except that the emission pulse is used to start the TAC and the excitation pulse is used to stop the TAC. This procedure is used because of the high repetition rate of modern pulsed-light-based sources. The TAC has to be

reset and set to zero before each start pulse, which takes a finite amount of time. The TAC can be constantly in reset mode if the start signals arrive too rapidly. The emission signals occur about 1 per 100 excitation pulses, and hence much less frequently than the excitation pulses. These emission pulses are used to start the TAC, and the next laser pulse is used to stop the TAC. Present electronics for TCSPC setup only allow the detection of the first arrival photon. A brief description of important electronic components of TCSPC setup is described below. Analysis procedure for estimation of fluorescence lifetime from the measured fluorescence decay curves is also discussed in the later part of this chapter.

2.3.3.3. Important Components of a TCSPC Setup

The main components of the current TCSPC setup are appended below.

(i) Pulsed excitation source: The fluorophore molecule is excited by using the excitation sources. Different diode lasers (such as EPL 375 nm, 405 nm and 445 nm) are employed as the excitation sources. The instrument response function (IRF) is measured from full width at half height maximum (FWHM) of IRF pulse and the IRF values for this TCSPC setup is estimated to be ~100 ps. The repetition rate for excitation pulse was typically kept at 1 MHz.

(ii) Constant fraction discriminator (CFD): In TCSPC setup, the signals from both START and STOP PMTs are passed through two CFDs. The primary work of the CFD is to develop the signal to noise ratio (S/N) by removing the signals below a threshold height such that the counts recorded by the instrument are essentially due to the photons detected by the PMTs and not due to spurious electrical noises. Additionally, it also measures the actual arrival time for the START and STOP inputs to the TAC unit such that the timing jitter in the detection is minimized. Since, the leading edge discriminators are usually associated with considerable timing errors, the CFDs

are considered to be the most suitable discriminators for the TCSPC to get the precise time for the START and STOP signal.

(iii) Time-to-amplitude converter (TAC): In TCSPC setup, both the START and STOP pulse is passed through a time-to-amplitude converter (TAC). The TAC unit is the most important part of the instrument and can be considered as the heart of the setup. On receiving the START pulse, following the preset delay which is already set in the TAC itself, a timing capacitor in the TAC start charging linearly with time from a constant current source. When the charging is discontinued upon receiving a STOP pulse, the charging process is stopped and TAC unit generates an output pulse. The magnitude of the charge collected on the TAC capacitor is linearly proportional to the measure of time difference between the arrivals of START pulse and STOP pulse. In the current TCSPC setup, the TAC range can be varied from 2.5 ns to 50 μ s. A suitable TAC range was consciously chosen for a particular TCSPC experiment depending on the probable fluorescence lifetime of the sample used.

(iv) Multichannel analyzer (MCA): The MCA used in a TCSPC setup is operated in two modes i.e. Pulse Height Analysis (PHA) and Multichannel Scaling (MCS) mode. The Pulse Height Analysis (PHA) and Multichannel Scaling (MCS) mode are used to measure the fluorescence decays and time-resolved emission spectra respectively. The data collected in the MCA channels are transferred to a computer for additional processing and analysis.

(v) START and STOP PMTs: Though in a TCSPC instrument suitable start and stop PMTs are used to carry out the experiments, only a single PMT with very low transit time and high gain is used in the present Edinburgh OB920 instrument to detect the emission photons from the sample. Hence, the only photodetector used in the current instrument is a unique Hamamatsu (R3809U-50) PMT, used in grouping with a Quantum, North West (TC 125) temperature controller. The

detector is having a spectral response from ~300 to 800 nm. As in the present work TCSPC setup is used in the “reverse mode”. Therefore, the signal from the special PMT is used as a start pulse for the TAC unit and an electrical signal synchronized with the pulsed diode laser is used as the stop pulse. This “reverse mode” is adopted specially for faster data collection with high repetition rate of the excitation pulses. This “reverse mode” of detection is also very important to avoid unnecessary charging of the TAC unit through the high repetition rate excitation pulses. In Edinburgh OB920 model TCSPC set up a PC based TCC card is used which incorporates both TAC and MCA directly and has been used for the data collection. Moreover, PC monitor is used to display the experimental decay profile. For the present thesis work, appropriate analysis software (F900) is used to fit the experimental decay curves and get the fluorescence lifetimes of the samples.

2.3.4. Other Instrumentations

In the present work, the X-ray diffraction technique has also been used. For X-ray crystal analysis, a suitable single crystal was carefully selected under a polarizing microscope and mounted at the tip of the thin glass fibre using cyanoacrylate adhesive. X-ray data were collected from a Bruker CCD X-ray diffraction system with a graphite-monochromatized Mo K α radiation (2.4 kW sealed-tube X-ray source, $\lambda = 0.71073 \text{ \AA}$). Structures were solved with a direct method using SHELXS-97 and developed on F^2 by a full-matrix least-squares method using the SHELXTL-PLUS64 programs. The programs Mercury and DIAMOND were employed to draw the structures.

The particles size of the colloidal solution was measured by using dynamic light scattering (DLS). The particle size measurements were conducted by using a Beckman-Coulter N4 Plus particle analyser equipped with a 10 mW helium neon laser ($\lambda_{exc.} = 632.8 \text{ nm}$). The detector angle

was set as 90° to determine the particle size. The data were analysed by using the size distribution processor (SDP) analysis package. A STA-6000 Perkin-Elmer Simultaneous Thermal Analyzer was used for Thermogravimetric analysis (TGA). An Axio Imager.M2 at 40×magnification and an AF 488 filter were used for fluorescence microscopy imaging.

2.4. Methods

2.4.1. Analysis of the Fluorescence Decay Curves

2.4.1.1. Data Analysis

Reconvolution least squares method were used to determine the fluorescence lifetime values from the fluorescence decay curves.²⁶⁷ If the estimated decay time is higher than the pulse-width of the excitation source, then the excitation pulse can be expressed as a δ -function. Though, when the excited state lifetime is small, several factors (such as the finite decay time of the source pulse, response time of the photomultiplier tube (PMT) and related electronics) can distort the experimental data. Therefore, the instrument response function depends not only on the decay time of the lamp pulse but also depends on the response time of the detector (PMT) and associated electronics. As the measured decay function is convolution of the accurate fluorescence decay and IRF. Therefore, it is essential to deconvolute the IRF from the experimental decay to obtain the fluorescence lifetime. The method can be mathematically expressed as^{261, 262, 268-271}

$$I_m(t) = \int_0^t I_R(t-t')R(t')dt' \quad (2.6)$$

where $I_m(t)$ is the fluorescence intensity at time t , $I_R(t-t')$ is the response function of the experimental system and $R(t')$ is the intensity of the exciting pulse at time t' . Instrument response function (IRF) was estimated using a dilute Ludox solution and deconvolution algorithm was made through iterative reconvolution method.

Then, a nonlinear least squares (NLLS) data processing method is used to fit the ideal decay with some assumed functional form. This method is adopted to examination whether a selected mathematical method is consistent with the actual data points or not. The least square analysis is only useful if the data points fulfill certain assumptions. The main assumptions are that there should be sufficient independent data points. The uncertainties in the experimental data points are Gaussian distributed and there should be no systematic error in the experimental data points. Experimentally, both the $I_m(t)$ and $R(t')$ can be obtained from the TCSPC setup. During analysis, a decay function $G(t)$ is first assumed for the sample and this function is deconvoluted with the observed $R(t')$ according to equation 2.6 to get a calculated curve $Y(t)$. The $Y(t)$ is then compared with the experimentally observed decay curve $I_m(t)$.^{245, 261, 262, 268, 270} The variables in the function $G(t)$ is iteratively changed until a good comparison (best fit) between the $Y(t)$ and $I_m(t)$ is obtained. The function $G(t)$ is typically assumed to be a sum of exponentials in such a way that

$$G(t) = \sum_i B_i \exp\left(\frac{-t}{\tau_i}\right) \quad (2.7)$$

where B_i is the pre-exponential factor for the i th component and τ_i is the corresponding fluorescence lifetime. The success of an analysis and accordingly the acceptance of a fit to the observed decay curve are determined from the judicial judgments of the following statistical parameters.

2.4.1.2. Reduced Chi-square (χ^2) Values

Reduced χ^2 values are monitored to judge the goodness of an iterative analysis and its value approaches unity if the model does fit the data. The χ^2 is denoted as

$$\chi^2 = \frac{\sum_i W_i \{Y_i - I_i\}^2}{n-p} \quad (2.8)$$

where Y_i is the count of i th channel of the calculated curve, I_i is the count at the i th channel of the experimentally measured curve. W_i [$W_i = I/I_i$], is the weighting factor of the counts in the i th

channel, n is the number of channels used for the decay to be analyzed and p is the number of degrees of freedom in the decay function consider for the analysis which is equal to the number of variables in the function $G(t)$. For a good fit, the χ^2 values must be close to unity. Generally a χ^2 values between 1.0 to 1.2 is considered to be a good fit to the data.

2.4.1.3. Distribution of Weighted Residuals

The weighted residuals are the differences between the measured decay function and the fitted function. It is one of the vital parameters for the judgments of the achievement of an analysis of TCSPC data set and defined by the following equation

$$r_i = \sqrt{W_i}(Y_i - I_i) \quad (2.9)$$

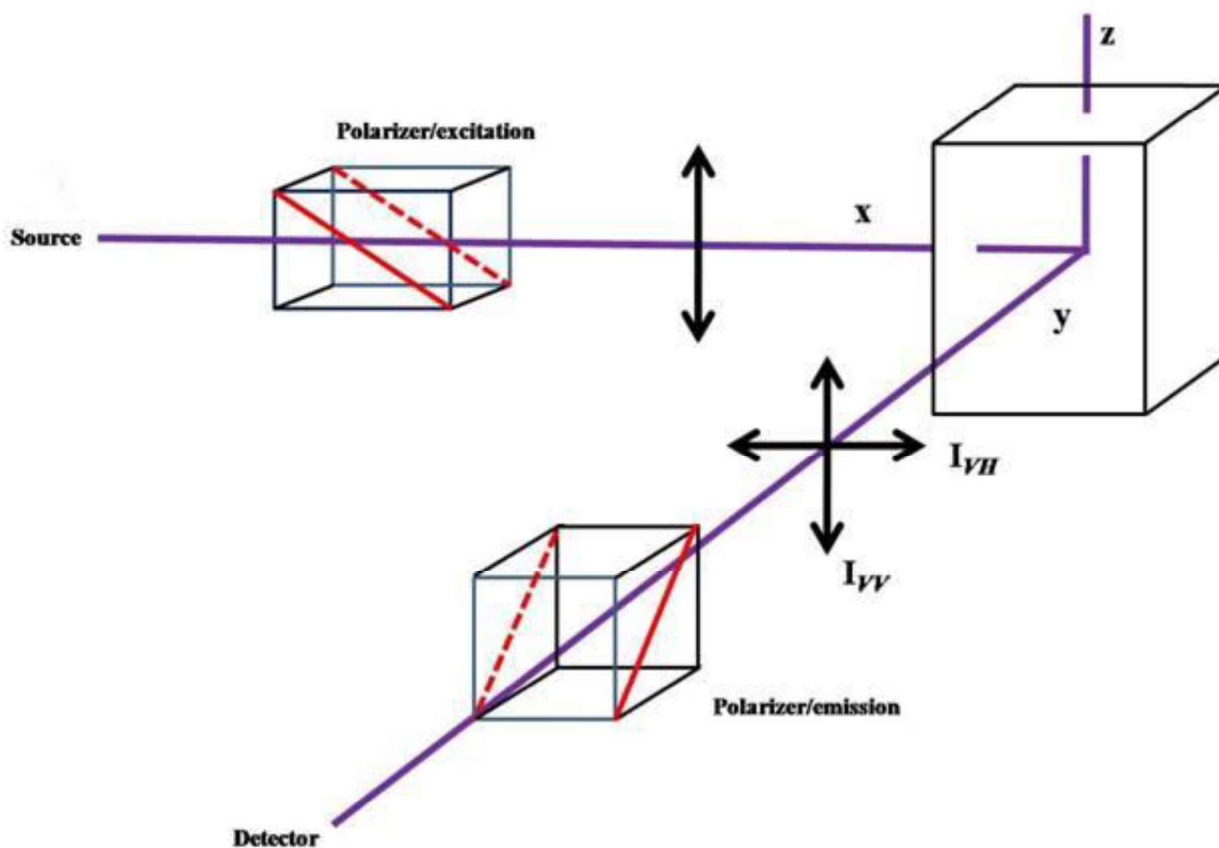
where W_i , Y_i and I_i are defined as previously. For a good fit, random distribution of the weighted residuals about the zero line for the entire data range of the data channels used in the analysis is expected to be obtained. The quality of the fit is judged by visually inspection of the residuals.

2.4.2. Time-resolved Fluorescence Anisotropy Measurements

The fluorescence anisotropy is defined as the extent of the average angular displacement of fluorphore that occurs between absorption and subsequent emission.²⁴⁵ A pictorial representation of the diagram corresponding to fluorescence anisotropy measurement is provided in Scheme 2.2.²⁴⁵ The orientation of the emission polarization is defined by the electric vector of the excitation pulse. I_{VV} indicates the emission intensity observed with parallel polarization (excitation and emission polarizer are in vertical position) and I_{VH} represents the intensity of perpendicularly polarized emission (excitation and emission polarizer are in vertical and horizontal position respectively). The ideal anisotropy $r(t)$ is defined as

$$r(t) = \frac{I_{VV}(t) - I_{VH}(t)}{I_{VV}(t) + 2I_{VH}(t)} \quad (2.10)$$

The anisotropy is a dimensionless quantity as the difference between parallel and perpendicular emission is normalized by the total emission intensity. Moreover, it is also independent of the fluorophore concentration as well as the total emission intensity.



Scheme 2.2. A pictorial representation of fluorescence anisotropy measurements.

Since, in TCSPC technique, sensitivity of experimental setup and electronics (such as monochromator) may influence, the actual anisotropy measurements, therefore, it is necessary to incorporate correction factor (G) while estimating the $r(t)$. This value of G represents the relative sensibility of the detection system to the different polarization. G varies with the emission wavelength and the band pass of the monochromator. It is expressed as

$$G = \frac{\sum I_{HH}(t)}{\sum I_{HV}(t)} \quad (2.11)$$

where I_{HV} and I_{HH} are the emission intensities when the excitation and emission polarizers are in horizontal-vertical and horizontal-horizontal position respectively. The G factor is estimated based on the intensity ratio between I_{HV} and I_{HH} . The measured anisotropy is then estimated by using the following relation

$$r(t) = \frac{G I_{VV}(t) - I_{VH}(t)}{G I_{VV}(t) + 2I_{VH}(t)} \quad (2.12)$$

In the present work, Edinburgh, OB920 TCSPC was used to measure time-resolved fluorescence anisotropy. Essentially through time-resolved fluorescence anisotropy measurements the dynamic of angular displacement between absorption and subsequent emission of a given fluorephore sample is monitored. An alternate collection of the emission intensity in perpendicular and parallel polarization (with respect to the vertically polarized excitation laser beam) for an equal interval of time had been carried out until the count difference between the two polarizations (at $t = 0$) is ~ 5000 . The same method was adopted for G -factor calculate but with 5 cycles and horizontal polarization of the exciting laser beam. The anisotropy data are fitted by the following equation to calculate rotational relaxation time

$$r(t) = r_0 \exp \frac{-t}{\tau_r} \quad (2.13)$$

where, r_0 is the initial anisotropy, and τ_r is the rotational relaxation time or reorientation time. It can be mentioned here that the r_0 values must be in the range of - 0.20 to 0.40 for any single-photon excitation.²⁴⁵ Therefore, the maximum value of r_0 is 0.4. The data corresponding to time-resolved anisotropy decay mesurments are again analyzed through hydrodynamic and quasi-hydrodynamic theories. These analysis are discuss in the working chapters of the current thesis.

2.5. NMR Measurements

NMR studies have been carried out by using a 9.4 Tesla Bruker Avance NMR spectrometer at Larmor frequencies of 400.1MHz for ^1H . Stimulated echo bipolar pulse-gradient pulse (stebpgp) sequence has been used for the measurements of translational diffusion coefficients (D) at different temperatures (298 K to 328 K). The echo heights were measured at 16 identical intervals, where the gradient pulse strength varies from 2 to 95% of the maximum gradient pulse strength (50 G/cm). The echo heights were then fit to the relation

$$S(g)=S(0)\exp[-D\gamma^2\delta^2g^2(\Delta-\delta/3)] \quad (2.14)$$

where $S(g)$ and $S(0)$ denote the echo height at the gradient strength g and 0 respectively. γ =gyromagnetic ratio of the proton, δ denotes the gradient pulse length. Δ =duration between the two gradient pulses.

Additionally, the NMR 2D ROESY experiments of neat RTILs were also carried out by using same instrument. From ROSEY spectra, the cross peak intensity of the interacting atom was calculated from volume intensity integration by using topspin software. The integrated ROESY intensity was corrected by $(n_{\text{H1}}n_{\text{H2}}/N)$, where n_{H} is the number of ^1H nuclei involved in the observed signal and $N = n_{\text{H1}} + n_{\text{H2}}$.

2.6. Fluorescence Correlation Spectroscopy (FCS) and Electron Paramagnetic Resonance (EPR) Measurements

A confocal fluorescence microscope, Micro-Time 200 (PicoQuant), was used to perform the fluorescence correlation spectroscopy (FCS) measurements. An excitation light of 485 nm was reflected by a dichroic mirror and focused onto the sample using a water immersion objective (60 \times /1.2 NA). The fluorescence from the sample was collected by the same objective and

passed through a filter and pinhole before entering the two detectors. The correlation curves were generated by cross-correlating the signal from the two detectors. The correlation data were fitted to the following equation 2.15, which consists of single-component diffusion along with intersystem crossing;

$$G(\tau) = \frac{1-T + T \exp(-\tau/\tau_T)}{N(1-T)} \left(1 + \frac{\tau}{\tau_D}\right)^{-1} \left(1 + \frac{\tau}{\kappa^2 \tau_D}\right)^{-\frac{1}{2}} \quad (2.15)$$

In the above equation, τ_D is the diffusion time, and κ is the structure parameter of the observation volume and is given by $\kappa = \omega_z/\omega_{xy}$, where ω_z and ω_{xy} are the longitudinal and transverse radii of the observation volume, respectively. τ_T is the lifetime of the molecule in the triplet state, and T is the associated amplitude. N is the number of molecules in the observation volume. The excitation volume was calibrated using rhodamine 6G (R6G) (diffusion coefficient $426 \mu\text{m}^2/\text{s}$ in water). The diffusion coefficient (D) of the molecule is estimated using the relation defined as

$$\tau_D = \frac{\omega_{xy}^2}{4D} \quad (2.16)$$

We have further explored the diffusion coefficient data to calculate the hydrodynamic radius of the diffusing species through the Stokes-Einstein relation²⁷¹

$$D = \frac{kT}{6\pi\eta R} \quad (2.17)$$

where D = translational diffusion coefficient, k = Boltzmann constant, T = temperature, η = viscosity of the medium and R = hydrodynamic radius of the molecule.

A Bruker Super QCW-EPR bridge (model A300) X band spectrometer was used to collect the electron paramagnetic resonance (EPR) spectra. For EPR measurements, the sample solutions were taken in a borosilicate glass capillary tube with an internal diameter of 2 mm. Then the EPR tube was placed centrally in the EPR cavity. Simulation of the EPR spectra was done by using WinEPRSymfonia software (version 1.26 beta).

2.7. Quantum Yield Calculations

The quantum yields (Φ_s) of neat RTILs used in the study were estimated by using anthracene (anthracene in ethanol 0.27),²⁷² as a reference standard and by using the following equation

$$\Phi_S = \frac{I_s}{I_r} \times \frac{n_s^2}{n_r^2} \times \Phi_r \quad (2.18)$$

where I_s and I_r are the integrated fluorescence emission of the sample and the reference, respectively. Φ_r is the quantum yields of the reference (anthracene, $\Phi_r = 0.27$). The n_s and n_r are the refractive indices of the sample and the reference respectively. The values of I_s and I_r are determined by integrating the emission intensity over the spectral range. The sample and reference are excited at optically method condition.

2.8. Theoretical Calculations

To obtain a clearer picture of the experimental finding, the theoretical studies have also been investigated in some cases. For most of the cases, structural parameters were calculated with the help of density functional theory (DFT), which is a more accurate method of calculations than Hartee-Fock theory in a sense that it includes both exchange energy and electron correlation.^{273,}
²⁷⁴ The ground state structures were optimized using the hybrid DFT functional M06-2X43–45 with 6-31+g(d,p) basis set as implemented in Gaussian 09. The hybrid meta exchange-correlation functional, M06-2X from Truhlar et al.²⁷⁵ has been successful in accounting for medium and long-range electron correlation in charge-transfer systems and correctly incorporates dispersion forces. Moreover, in some cases, time-dependent DFT (TD-DFT) calculations were also employed to obtain the computed absorption spectra.

2.9. Standard Error Limits

Standard error limits involved in the experimental results were

Viscosity (η)	$\pm 2\%$
Density	$\pm 2\%$
λ_{\max} (abs./flu.)	$\pm 1-2$ nm
$\tau_f (> 1\text{ ns})$	$\pm 5\%$
Rotational relaxation time	$\pm 5-10\%$
The energy transfer rate	$\pm 5\%$
Polarity (through EPR)	$\pm 2-5\%$
Diffusion coefficient (through NMR)	$\pm 5\%$
Diffusion coefficient (through FCS)	$\pm 5-10\%$

Chapter 3

Investigation of Solute-Solvent Interaction in Imidazolium-Based Room Temperature Ionic Liquids Using Spectroscopic Methods

This chapter describes the solute-solvent interaction between some fluorescent solutes molecules and several imidazolium-based RTILs. The chapter is divided into two parts such as *Part A* and *Part B*.

Part A

In *Part A*, basically, the solute-solvent hydrogen bonding interaction is investigated by taking two structurally similar but chemically distinguishable organic solutes, 4-(azetidino-1-yl)-7-nitrobenzo[1,2,5]oxadiazole (ANBD) and 7-nitrobenzo[1,2,5]oxadiazole-4-amine (HNBD), in 1-ethyl-3-methylimidazolium alkyl sulfate (alkyl = ethyl, hexyl and octyl) RTILs by employing fluorescence, NMR and FCS. The outcome of the present study demonstrates that solute-solvent specific hydrogen bonding interaction makes the rotation of solutes molecules significantly hindered. It has also been observed that the specific solute-solvent interaction decreases with increasing the alkyl chainlength on the anionic moiety.

3A.1. Introduction

Intermolecular interactions between solute and solvent molecules have profound role in determining the physicochemical properties of liquids and solutions.²⁴⁶ Understanding solute-solvent and solvent-solvent interactions in liquids and solutions has always been an interesting theme of research.^{175, 176, 192, 205, 276-281} It may also be noted that physicochemical properties of RTILs can also be influenced significantly due to their micro-heterogeneous nature.^{113, 114} Thus to understand structure-property correlation of these specialized media both the intermolecular

interaction and the micro-heterogeneity prevailing in the RTILs need to be realized in proper manner.

Recently, studies on molecular rotation in light of hydrodynamic description have been performed successfully to study the solute-solvent and solvent-solvent interactions in liquids.^{183,}

¹⁹⁸ In these studies, generally reorientation time is correlated with the viscosity of the medium.

One of the approaches by which the solute-solvent interaction in liquids can be studied is to measure the reorientation time of the solute molecule in polar and nonpolar medium in isoviscous condition, and if the reorientation time significantly differs then the variation can be rationalized in terms of solute-solvent interaction. However, this approach has some limitation as measured reorientation time will also depend on size and free volume of solvent systems.^{207, 208}

An alternate approach is to find/synthesize suitable structurally similar but chemically distinguishable solute molecules and study their rotational diffusion behavior in the solvents of interest and then the difference in the reorientation time can be ascribed to the solute-solvent interaction alone. Moreover, the idea of solute-solvent interaction will also help in understanding the solvent-solvent interaction in the liquids. Even though several literatures are available on rotational dynamic in conventional solvents, limited number of literature reports are available on the same aspect of RTILs.^{183, 195, 198, 200, 207, 208, 210}

It may also be noted here that RTILs are complex solvents due to the fact that their local microstructures are structurally heterogeneous unlike most non-hydrogen bonded conventional solvents.⁸⁵⁻⁹¹ Studies have shown that structural organisation within RTILs arises due to their polar and nonpolar subunits.^{86, 87, 166, 159} It may be noted here that an idea about the micro-heterogeneous nature of RTILs can be obtained by investigating the excitation wavelength dependent fluorescence behaviour of appropriate solute molecule in the RTILs.^{88, 160, 161} Solute-

solvent interaction may significantly contribute to the inhomogeneous broadening of the absorption spectrum of the solute in a given solvent.¹⁶⁰ Due to the ground state heterogeneity and slow excited state relaxation process in RTILs a gradual red-shift of the emission spectrum with a change in the excitation wavelength can be observed.^{88, 160} Even though these studies cannot comment on the exact length scale over which structural heterogeneity of the RTILs can occur, they can certainly provide qualitative information about the heterogeneous nature of the medium. Keeping the above facts in mind, two structurally similar but chemically distinguishable compounds 7-nitrobenzo[1,2,5]oxadiazole-4-amine (HNBD) and 4-(azetidene-1-yl)-7-nitrobenzo[1,2,5] oxadi-azole (ANBD) have been synthesized and their rotational relaxation behaviors have been investigated in 1-ethyl-3-methylimidazolium ethyl sulfate (EMIM-ES), 1-ethyl-3-methylimidazolium hexyl sulfate (EMIM-HS) and 1-ethyl-3-methylimidazolium octyl sulfate (EMIM-OS). These RTILs are purposefully chosen, so as to have appreciable variation in the alkyl chainlength on the anionic moiety. It may be noted here that alkyl chainlength plays important role in governing the physicochemical properties^{186, 282-284} and microheterogeneous^{89, 285, 286} behaviors of the RTILs. Out of the two solute molecules, HNBD can form hydrogen bond with the sulphate anion due to its acidic hydrogens (-NH), whereas ANBD cannot form such bond as in the later case the two hydrogen atoms are replaced by alkyl moiety. Molecular diagrams of the solutes and RTILs are provided in Chart 3.1.

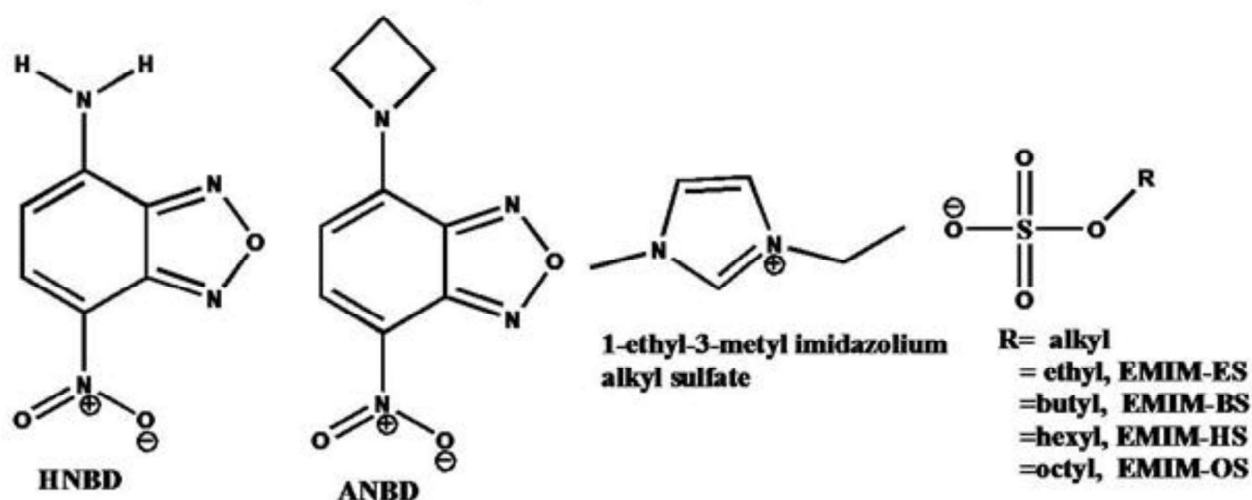


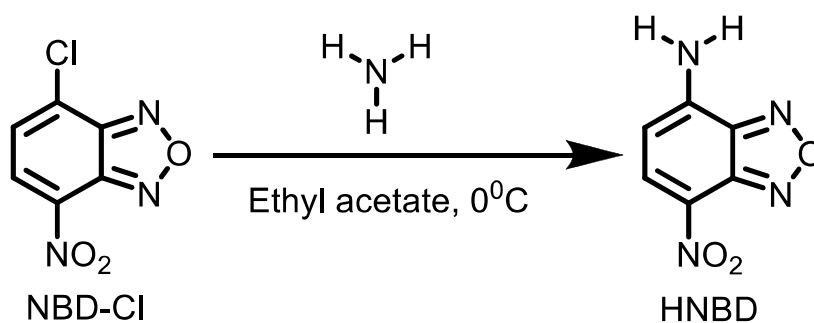
Chart 3.1. Molecular structure of probes and RTILs

3A.2. Experiment Section

The RTILs, EMIM-ES, EMIM-HS and EMIM-OS were procured from Merck Germany (>99% purity) with < 100 ppm halide and water. To avoid moisture, RTILs were kept in high vacuum before use. DMSO- d_6 (99.9%) and $CDCl_3$ were purchased from Across Chemical. Rhodamine 6G (Rh6G) was obtained from sigma Aldrich. The HNBD and ANBD are synthesized in our laboratory and the details synthesis procedure is provided in section 3A.2.1.

3A.2.1. Synthesis of HNBD and ANBD

Synthesis of HNBD: Synthesis of HNBD was carried out by following the synthetic procedure proposed by Satyen et.al.²⁸⁷ Ammonia (1.2 mmol) dissolved in ethyl acetate was added drop wise in an NBD-chloride (1 mmol) solution in ethyl acetate with rigorous stirring in an ice bath. After stirring for 40 min in the ice bath, the reaction mixture was then stirred for additional 2h at room temperature (Scheme 3.1). The compound has been purified through column chromatography technique using neutral alumina. Hexane and ethyl acetate (40/60) was used to separate the product. The compound was characterized by NMR and mass spectrometric study.

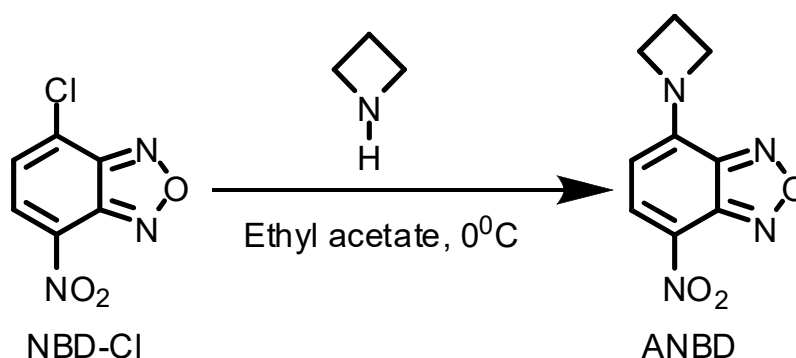


Scheme 3.1. Synthetic route of HNBD molecule.

¹H-NMR (DMSO-d₆): 2H(8.86 ppm, S), 1H(8.48 ppm, d), 1H (6.38 ppm, d)

Mass (M+Na⁺): 203. Yield: 84%

Synthesis of ANBD: ANBD was synthesized by following the literature procedure proposed by Satyen et.al.²⁸⁷ Azetidine (1.2 mmol) dissolved in ethyl acetate was added drop wise in an NBD-chloride (1 mmol) solution with constant stirring in an ice bath. After stirring for 40 min in ice bath, the reaction mixture was then stirred for additional 2 h at room temperature (Scheme 3.2). The compound was purified through column chromatography technique using neutral alumina. Hexane and ethyl acetate (40/60) was used to separate the product. The compound was characterized by NMR and mass spectrometric study.



Scheme 3.2. Synthetic route of ANBD molecule.

¹H-NMR (CDCl₃): 1H(8.72 ppm, d), 1H(5.84 ppm, d) 4H(4.96 ppm, b), 2H(2.88ppm, q)

Mass (M+H⁺): 221. Yield: 72%

3A.3. Result and Discussion

3A.3.1. Steady State Absorption and Emission of HNBD and ANBD

The absorption spectral profiles for HNBD and ANBD in EMIM-ES and EMIM-OS are provided in Figures 3.1 (a) and 3.2 (a) respectively. In EMIM-ES and EMIM-OS, both the NBD compounds exhibit a broad absorption band. The broad absorption band for NBD compounds arises due to the intramolecular charge transfer (amino to nitro) nature of the transition.²⁸⁷ For HNBD, the absorption maxima appears at 465 nm and 466 nm in EMIM-ES and EMIM-OS respectively (Table 3.1). However, for ANBD, the absorption maxima appear at 495 nm and 489 nm in EMIM-ES and EMIM-OS respectively (Table 3.1). These absorption data clearly demonstrate that the locations of the probes in these RTILs are different. Nearly the similar absorption maxima for HNBD in both EMIM-ES and EMIM-OS indicate that the microenvironment for HNBD in these RTILs is very similar. It is reasonable to expect that HNBD resides in more polar region (near sulphate group) due to the hydrogen bonding interaction between acidic hydrogen atoms of HNBD moiety and the sulphate group of RTILs. A nearly 6 nm blue shift of absorption for ANBD upon changing the solvent from ethyl to octyl derivatives indicates that the ANBD is located near the hydrophobic chain of the RTILs, and the blue shift of the absorption in case of longer chain containing system arises due to the increase in apolar character upon increase in alkyl chainlength.⁸¹

The emission maxima of HNBD and ANBD in EMIM-ES and EMIM-OS are provided in Figures 3.1 (b) and 3.2 (b) respectively. The emission maxima for HNBD are found to be very close (533 nm) in these RTILs (Table 3.1). However, the emission maximum of ANBD is observed to be blue shifted upon going from ethyl to octyl analogue (Figure 3.2 (b)). This observation reflects that the locations of HNBD and ANBD are different in these RTILs, and the

blue shift of emission band for ANBD arises due to the increase in apolar character upon increase in the alkyl chain length in the octyl derivative.

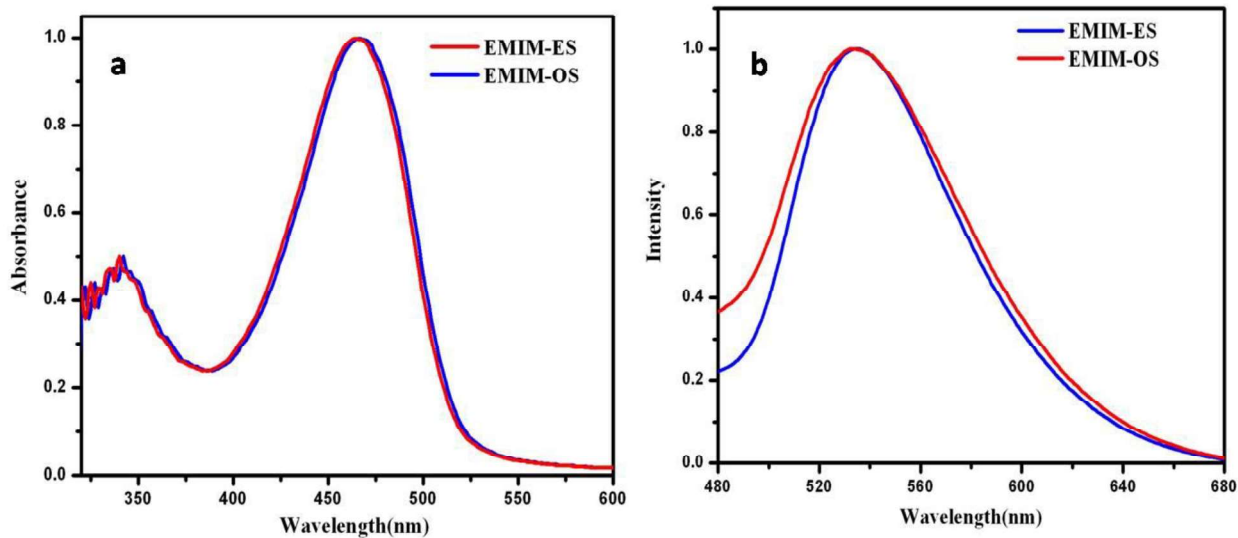


Figure 3.1. (a) Normalized absorption and (b) emission spectra ($\lambda_{exc} = 405$ nm) of HNBD in EMIM-ES and EMIM-OS.

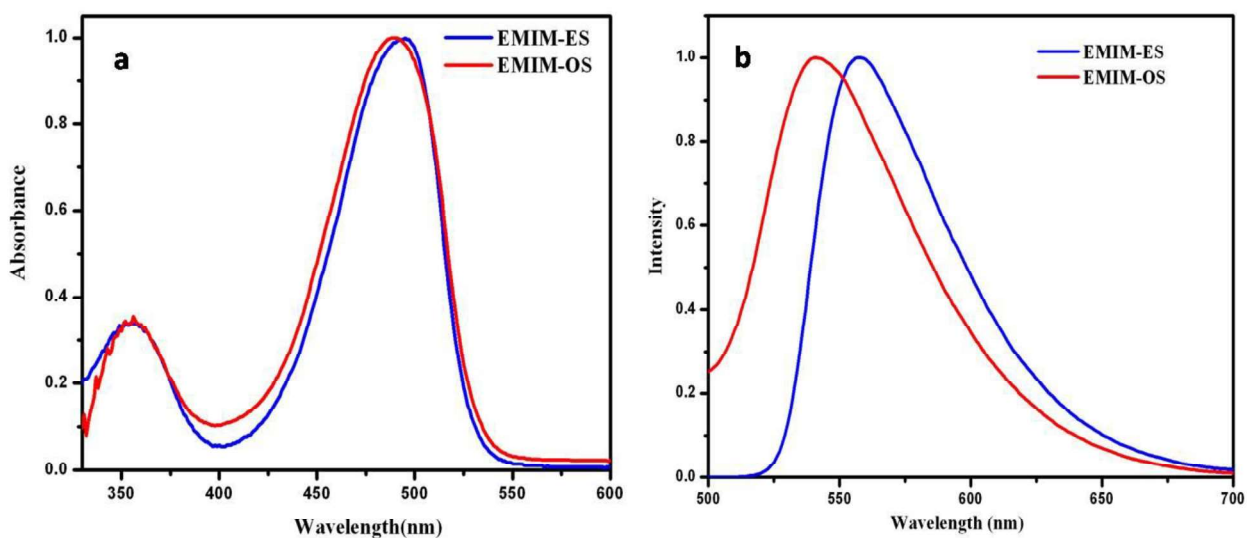


Figure 3.2. (a) Normalized absorption and (b) emission spectra ($\lambda_{exc} = 405$ nm) of ANBD in EMIM-ES and EMIM-OS.

Table 3.1. Absorption ($\lambda_{max}^{abs.}$) and emission ($\lambda_{max}^{flu.}$) maxima of HNBD and ANBD in EMIM-ES and EMIM-OS

Systems	RTILs	$\lambda_{max}^{abs.}$ (nm) ^a	$\lambda_{max}^{flu.}$ (nm) ^b
HNBD	EMIM-ES	467	533
	EMIM-OS	468	533
ANBD	EMIM-ES	495	557
	EMIM-OS	489	543

^{a,b} Experimental error = $\pm 2\%$

The excitation wavelength dependent fluorescence behaviour of a given solute in a particular medium often helps to get an idea about the heterogeneous behaviour of the medium.^{186, 238, 239} If there exists a distribution of energetically different solvated species in the ground state and the rate of energy transfer between them is slow then instead of obeying Kasha's rule,²³⁷ the emission spectrum of the fluorescent solute is observed to shift gradually towards low energy region. This type of behavior is known as red-edge-effect (REE).^{238, 239} Thus, this investigation at least can provide qualitative idea about micro-heterogeneous behavior of the given medium.^{238, 239} To investigate this aspect in the present case, excitation wavelength dependent emission spectra of HNBD and ANBD in EMIM-ES and EMIM-OS are monitored. The variation of emission maximum (λ_{em}^{max}) with excitation wavelength (λ_{exc}) for each system is provided in Figure 3.3. Interestingly, for HNBD, excitation wavelength dependent emission is found in both the RTILs, when the sample is excited at longer wavelength region (red region) of the absorption spectrum. However, no excitation wavelength dependent emission is found in ANBD in these RTILs (Figure 3.3). Again, for HNBD, the maximum fluorescence shift is observed to be larger (18 nm) in EMIM-ES but relatively smaller (~9 nm) in EMIM-OS (Figure 3.3). Here, we note that the solute-solvent interaction can play an important role in creating distribution of energetically different species in a medium like RTIL.¹⁶⁰ The observation in the present scenario suggests that the hydrogen bonding interaction between free amine moiety of HNBD and the

sulfate moiety of RTILs is playing an important role in creating energetically different species in the RTILs. Since ANBD is not capable of forming such interaction with RTILs, no excitation wavelength dependent fluorescence is observed for ANBD. The changes in full width at half maximum (FWHM) of the emission spectra for both the solutes in EMIM-ES and EMIM-OS are provided in Figure 3.4. Interestingly, the FWHM values are estimated to be $\sim 3500\text{ cm}^{-1}$ and $\sim 2650\text{ cm}^{-1}$ for HNBD and ANBD respectively. This also indicates that the probability of formation of energetically different species in the ground state is higher for HNBD than that for ANBD.

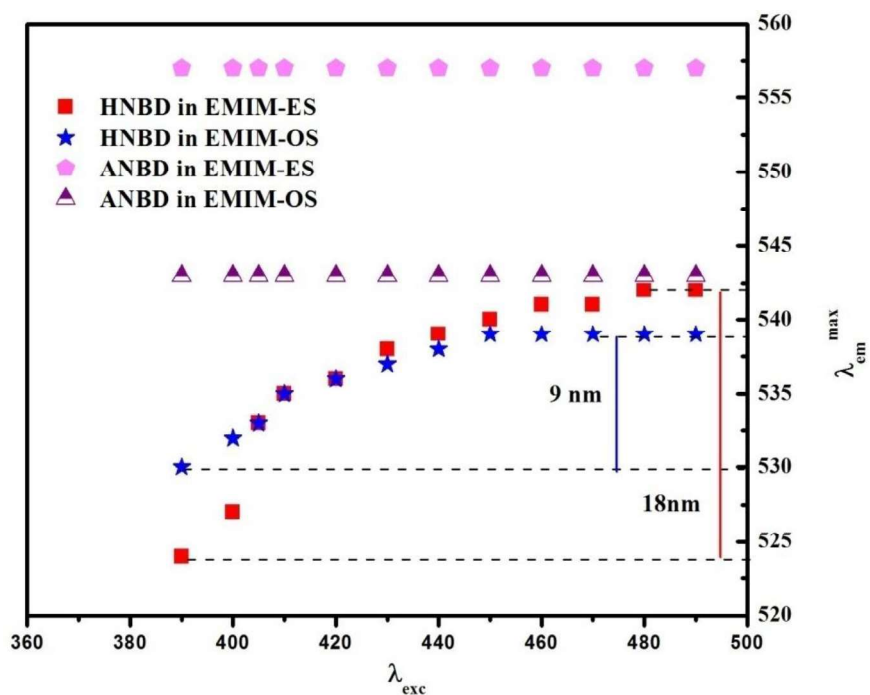


Figure 3.3. Plot of λ_{em}^{max} vs. λ_{exc} of HNBD and ANBD in EMIM-ES and EMIM-OS.

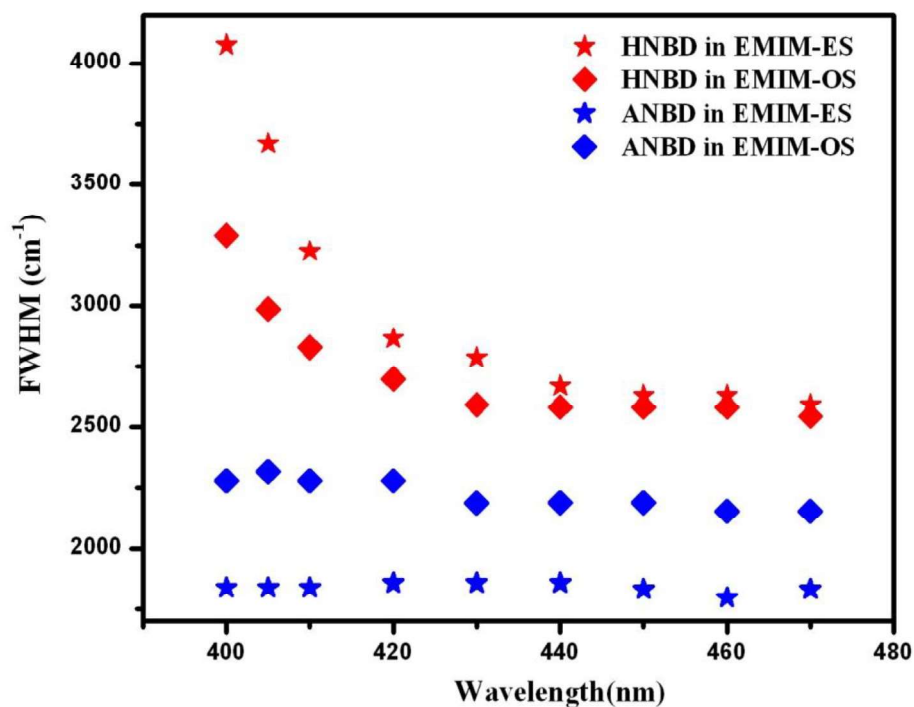


Figure 3.4. Change of FWHM values of the excitation wavelength dependent emission spectra of HNBD and ANBD in EMM-ES and EMIM-OS.

3A.3.2. Rotational Dynamic Study

ANBD. The temperature dependence viscosities of these RTILs are collected in the temperature range 293-313 K (Table 3.2). It is evident from Table 3.2 that viscosity increases with increase in the chainlength. The activation energies of the viscous flow in neat EMIM-ES and EMIM-OS are calculated by fitting the data points to Arrhenius type relation⁶² as shown in $\ln(\eta)$ vs. $1/T$ plots (Figure 3.5). The activation energies of the viscous flow for EMIM-ES and EMIM-OS are found to be 41.03 kJ/mol and 48.05 kJ/mol, respectively. The present data indicate that the structural organization of the two RTILs is not the same.

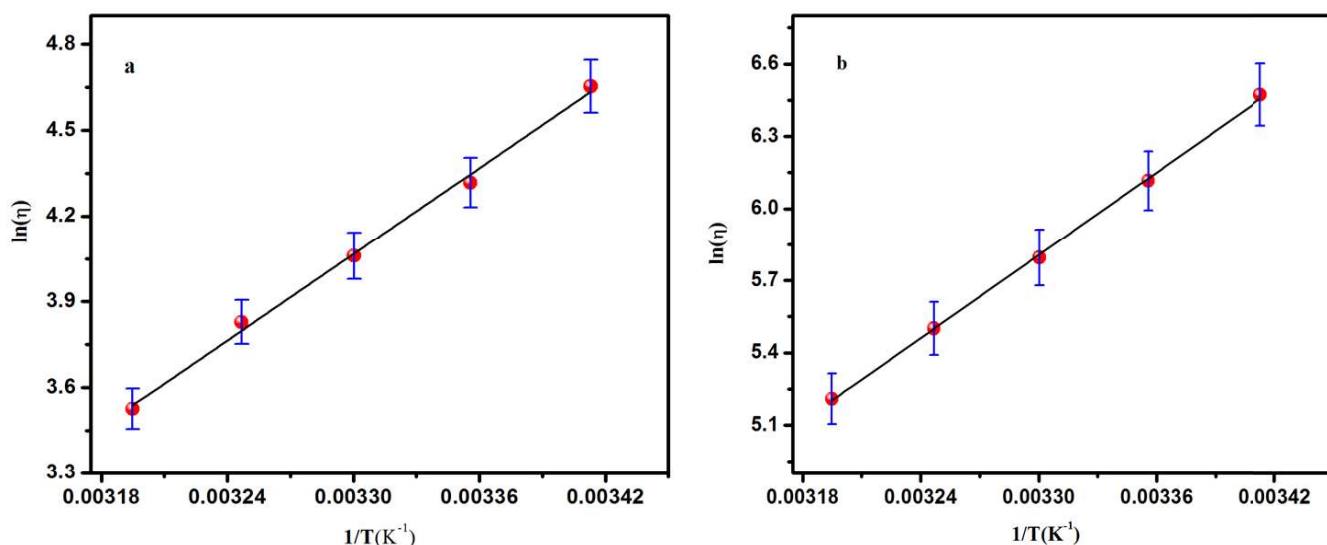


Figure 3.5. Variation of the viscosity of neat (a) EMIM-ES and (b) EMIM-OS with temperatures. The blue lines indicate the error bar from the data points.

The anisotropy decay profiles of ANBD in EMIM-ES and EMIM-OS are provided in Figure 3.6. The rotational relaxation parameters for ANBD are collected in Table 3.2. The anisotropy decay is fitted by single exponential decay function. It is evident from Figure 3.6 and Table 3.2 that faster rotation is observed upon increasing the temperature. This happens due to the lowering of the viscosity of the medium with increase in the temperature. Interestingly, the reorientation times (τ_r) of ANBD is observed to increase with an increase in the length of the alkyl chain (Table 3.2). The increase in τ_r values with increase in alkyl chainlengths seems to be reasonable since viscosity increases with increase in alkyl chainlength. However, upon more careful look, one can also see that even though the viscosity is increased six times from ethyl to octyl, τ_r increases only two times (Table 3.2). For example at 298 K, the viscosity values increase from 75 cP to 453 cP on going from ethyl to octyl, whereas τ_r increases from 2.95 ns to 6.65 ns for the same systems (Table 3.2). This observation indicates that rotational motion of ANBD is not that much hindered in octyl system as compared to ethyl derivative despite the fact that the

viscosity is much higher in the former. It is an interesting observation where size of the solvent molecule seems to be playing an important role.

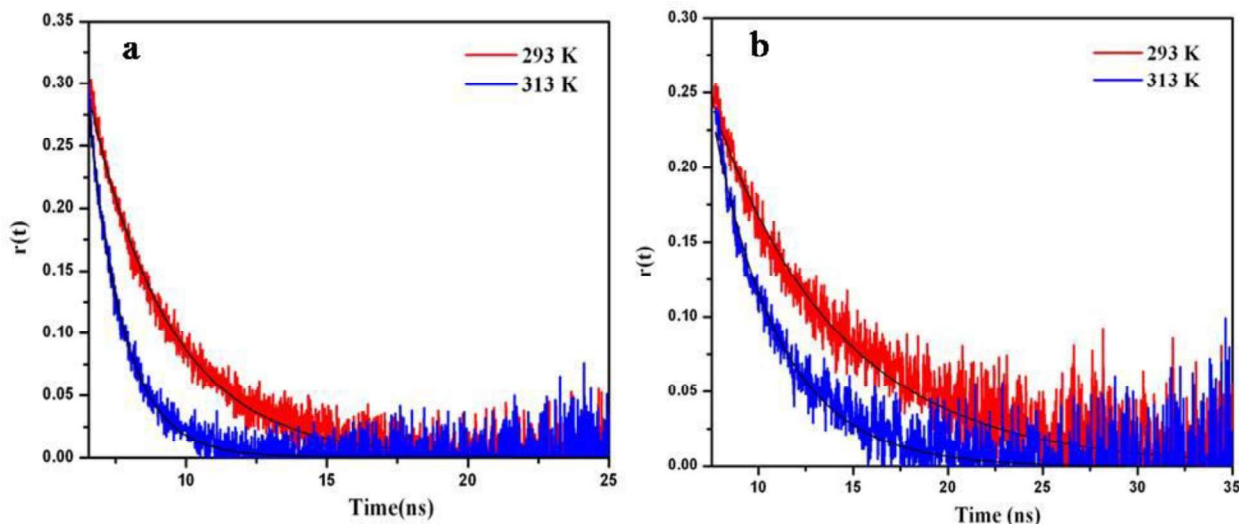


Figure 3.6. Anisotropy decay of (a) ANBD in EMIM-ES and (b) ANBD in EMIM-OS, ($\lambda_{exc} = 405$ nm). The solid black lines indicate the fit to the data points.

Table 3.2. Reorientation times (τ_r) of ANBD in EMIM-ES, EMIM-HS and EMIM-OS at different temperatures ($\lambda_{exc} = 405$)

RTILs	Temp. (K)	Vis. (cP) ^a	τ_r (ns) ^b	$C_{rot} = \tau_r^{exp} / \tau_r^{stk}$
EMIM-ES	293	105	2.95	0.49
	298	75	2.36	0.59
	303	58	1.86	0.60
	308	46	1.50	0.62
	313	34	1.25	0.72
EMIM-HS	293	381	5.67	0.26
	298	284	4.41	0.28
	303	211	3.45	0.30
	308	160	2.73	0.32
	313	122	2.26	0.37
EMIM-OS	293	646	6.69	0.18
	298	453	5.84	0.23
	303	329	5.02	0.28
	308	245	4.11	0.32
	313	183	3.48	0.36

^aExperimental error= $\pm 2\%$, ^bExperimental error= $\pm 5\%$

To get a better idea about rotational dynamic of ANBD in these RTILs, we have analyzed our result through the Stokes-Einstein-Debye (SED) hydrodynamic theory.^{239, 247} The probes property such as axial radii, van der Waals volumes (V), shape factors (f) and C_{slip} for HNBD and ANBD are estimated using literature data^{288, 289} and are provided in Table 3.3. From the values of C_{slip} and f , the theoretical τ_r^{slip} and τ_r^{stk} for ANBD in all these RTILs are determined. The experimental rotational times (τ_r) are correlated with theoretically estimated (from SED equation) values for the same.

Table 3.3. Dimensions and van der Waals volumes of HNBD and ANBD along with shape factors and boundary condition parameters (calculated using SED theory)

Solutes	axial radii/ A^3	V/A^3	f	C_{slip}
HNBD	3.32×3.14×2.75	130	1.075	0.01
ANBD	4.58×3.43×2.75	181	1.23	0.08

The $\log(\tau_r)$ vs $\log(\eta/T)$ plots is provided in Figure 3.7. It is evident from Figure 3.7 that the experimentally measured reorientation times of ANBD in all three RTILs lie between the theoretically obtained stick and slip lines. This observation indicates that no specific interaction like hydrogen bonding interaction is present between ANBD and the RTILs. However, upon careful look, a clear difference in the rotational diffusion behavior of the same solute molecule in these RTILs can be seen. As is depicted from Figure 3.7, the rotational motion of ANBD is observed to be relatively faster in octyl derivative as compared to the same in ethyl derivative. The experimental data for ANBD in octyl system is observed to be closer to slip line (Figure 3.7).

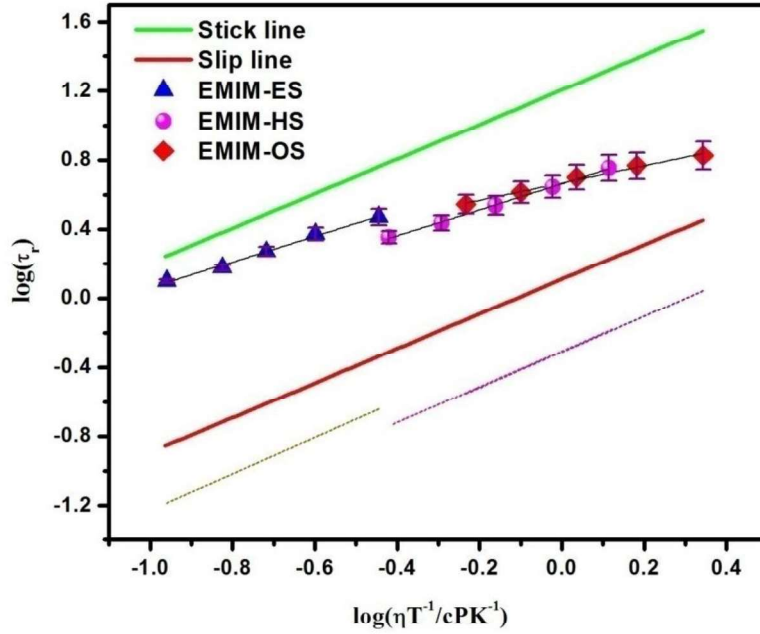


Figure 3.7. $\log(\tau_r)$ vs $\log(\eta/T)$ plot of ANBD in RTILs with stick and slip boundary condition limit along with their DKS line. Dotted dark yellow, pink and violet line corresponds to DKS line for EMIM-ES, EMIM-HS and EMIM-OS respectively. The black lines indicate fit to the data points. The purple lines indicate the error bar from the data points.

The faster rotation of ANBD can also be seen when we fit the τ_r and η/T data by using the relation $\tau_r = A (\eta/T)^n$. Where, $A = VfC/k$ and n are constant. The value of n indicates nonlinearity of τ_r vs. η/T plot. Deviation of n value from unity indicates viscosity-diffusion decoupling in the corresponding medium which in other words indicates the heterogeneous nature of the medium.^{192, 183} The present exponent (n) values for these RTILs indicate that the EMIM-OS is more heterogeneous than EMIM-ES.

ANBD in EMIM-ES

$$\tau_r = (6.30 \pm 0.031) (\eta/T)^{0.74 \pm 0.022} \quad (N=5, R=0.993)$$

ANBD in EMIM-OS

$$\tau_r = (4.57 \pm 0.006) (\eta/T)^{0.49 \pm 0.030} \quad (N=5, R=0.985)$$

The rotational coupling constant C_{rot} which is defined as $C_{rot} = \tau_r^{exp} / \tau_r^{stk}$ (τ_r^{exp} is the experimental and τ_r^{stk} is theoretically calculated rotational times) is also estimated by using equation 1.1. Interestingly, the decrease in C_{rot} values from ethyl to octyl derivative demonstrates the faster rotation of ANBD with increasing the anion chainlength. At this junction, it may be mentioned that SED theory is quite successful in explaining the experimental observation, when the size of solvent and solute molecules are comparable.^{239, 247} However, it fails to explain the rotational behavior of a solute molecule, when the size of solvent molecule is larger than that of the solute molecule. Actually SED theory takes into account the size of the solute molecule.^{239, 247} To explain solvent size dependent rotational behavior of the solute molecule in the present case, quasi hydrodynamic theory (DKS model) have been employed as it takes into consideration both the size of solute and solvent and the free space created in between solute and solvent molecule.²⁴⁹ The DKS theory is given by the following relation²⁴⁹

$$C_{DKS} = (1 + \gamma/\phi)^{-1} \quad (3.1)$$

where

$$\gamma = \frac{\Delta V}{V_p} \left[4 \left(\frac{V_p}{V_s} \right)^{2/3} + 1 \right] \quad \text{and} \quad \phi = f C_{slip}$$

where C_{slip} indicates the degree of coupling between solute and solvent under slip boundary condition. ΔV takes into consideration the smallest volume of free space per solvent molecule and it is defined as, $\Delta V = V_m - V_s$ where, V_m is the solvent molar volume divided by the Avogadro number. V_m of all three RTILs have been calculated by using the density of these RTILs. V_s and V_p are the van der Waals volume of the solvent and solute respectively. Edward increment method is used to calculate the van der Waals volumes of these RTILs.²⁹⁰

Figure 3.7, also provides the $\log(\tau_r)$ vs $\log(\eta/T)$ plots of ANBD in these RTILs with their modified boundary condition, obtained from the DKS theory. As can be seen, DKS theory is

quite successful in explaining the faster rotation of ANBD in the larger solvent system (EMIM-OS). Therefore, the present data shows that the rotational behavior of ANBD is largely affected by the size of the alkyl chainlength, and the faster rotation of ANBD can be attributed to larger size of the RTIL (octyl system) which offers lower friction to the rotating solute. However, when we go from EMIM-HS to EMIM-OS C_{rot} values for ANBD are found to be very close at a particular temperature (Table 3.2). This data indicates that rotational behavior of the solute molecules is quite similar in these longer chain containing systems. To have a better understanding on this aspect, we have also investigated the rotational behavior of ANBD in other two RTILs namely, 1-butyl-3-methylimidazolium tris-(pentafluoroethyl)trifluorophosphate (BIMIMFAP) and 1-hexyl-3-methylimidazolium tris-(pentafluoroethyl)trifluorophosphate (HIMIMFAP) RTILs (Table 3.4). Interestingly, C_{rot} values for ANBD in BIMIMFAP and HIMIMFAP are also observed to be very similar in a given temperature. These observations clearly indicate that the ANBD has located itself in the polar region of the RTILs and hence the effect on nonpolar alkyl chainlength has not been observed.

Table 3.4. Reorientation times (τ_r) of ANBD in BIMIMFAP and HIMIMFAP at different temperatures ($\lambda_{exc} = 405$)

RTILs	Temp. (K)	Vis. (cP) ^a	τ_r (ns) ^b	$C_{rot} = \tau_r^{exp} / \tau_r^{stk}$
BIMIMFAP	293	93.4	3.75	0.72
	298	72.3	3.08	0.78
	303	57.4	2.51	0.82
HIMIMFAP	293	112.7	4.48	0.71
	298	86.7	3.70	0.78
	303	67.9	2.90	0.80

^aExperimental error= $\pm 2\%$, ^bExperimental error= $\pm 5\%$

HNBD. The anisotropy decay behavior for HNBD is also investigated in EMIM-ES, EMIM-HS and EMIM-OS and the corresponding decay profiles are provided in Figure 3.8. The anisotropy

decay curves are fitted by single exponential function. Figure 3.9 represent the log-log plot of τ_r vs. η/T of HNBD along with the stick and slip boundaries. The rotational relaxation parameters for HNBD in these RTILs are given in Table 3.5. Like ANBD, the faster rotation of HNBD is also observed with increasing temperature due to the lowering of viscosity of the medium with increasing the temperature (Figure 3.8).

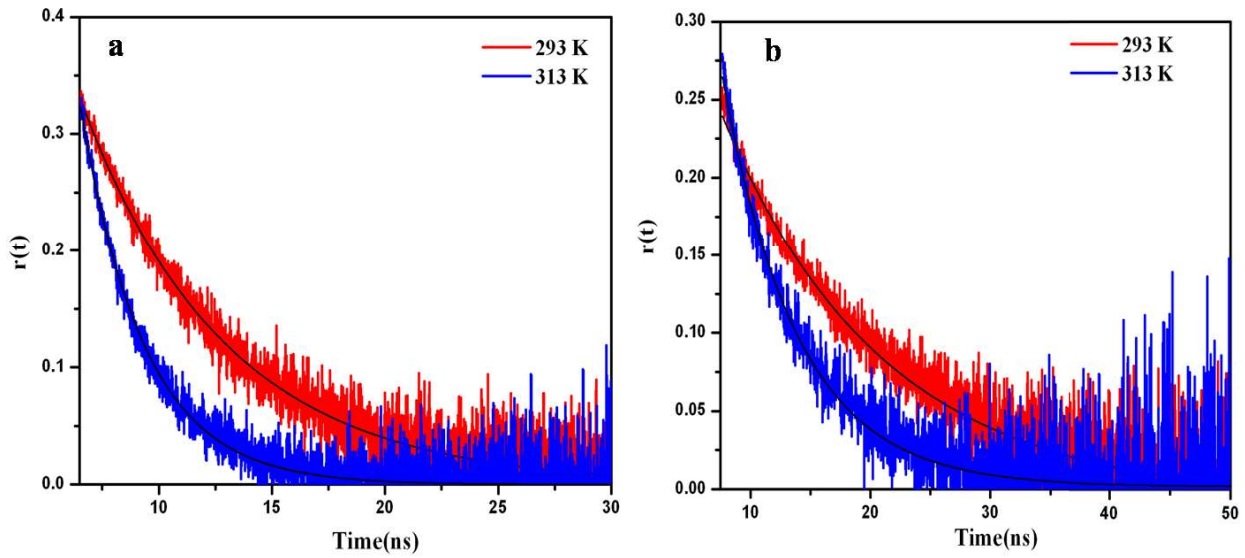


Figure 3.8. Anisotropy decay of (a) HNBD in EMIM-ES and (b) HNBD in EMIM-OS, at 293 K and 313 K where $\lambda_{exc} = 405$ nm and $\lambda_{em} = 534$ nm. The solid black lines indicate fit to the data points.

While analyzing the data in light of SED hydrodynamics theory it can be seen from Figure 3.9 that the rotational time of HNBD changes from superstick to stick with an increase in alkyl chainlength. This is also evident when the data are analyzed by employing an empirical relation $\tau_r = A(\eta/T)^n$, where the parameters A and n are constant,

HNBD in EMIM-ES

$$\tau_r = (13.1 \pm 0.010) (\eta/T)^{0.701 \pm 0.025} \quad (N=5, R=0.994)$$

HNBD in EMIM-OS

$$\tau_r = (8.70 \pm 0.007) (\eta/T)^{0.58 \pm 0.034} \quad (N=5, R=0.988)$$

Table 3.5. Reorientation times (τ_r) of HNBD with viscosity of RTILs at different temperatures ($\lambda_{exc} = 405$ nm)

Systems	Temp. (K)	Vis. (cP) ^a	τ_r (ns) ^b	$C_{rot} = \tau_r^{exp} / \tau_r^{stk}$
EMIM-ES	293	105	6.39	1.77
	298	75	5.12	2.01
	303	58	4.14	2.14
	308	46	3.38	2.23
	313	34	2.83	2.57
EMIM-HS	293	381	9.87	0.73
	298	284	7.88	0.81
	303	211	6.38	0.90
	308	160	5.18	0.98
	313	122	4.18	1.04
EMIM-OS	293	646	13.50	0.60
	298	453	11.56	0.75
	303	329	9.39	0.86
	308	245	7.75	0.96
	313	183	6.28	1.06

^aExperimental error= $\pm 2\%$, ^bExperimental error= $\pm 5\%$

Furthermore, rotational coupling constant (C_{rot}) values, which measure the extent of solute-solvent interaction, have also been estimated for HNBD in these RTILs (Table 3.5). The, C_{rot} value (Table 3.5) at a particular temperature, for HNBD is found to be significantly higher than that of ANBD indicating the rotation of HNBD is significantly hindered as compared to its alkylated analogue. As per hydrodynamic terminology, the hindered rotational behavior of HNBD in these RTILs is known as super-stick behavior. This super-stick behavior arises due to the strong association between the solute and solvent molecules. The fact that the specific solute solvent interaction can contribute to super-stick behavior has been documented in recent literature reports.^{160, 190, 193, 195, 198} The present observation clearly indicates that the hydrogen-bonding interaction between HNBD and the RTILs is responsible for the observed superstick behavior for HNBD. Interestingly, hindered rotation is observed for HNBD in both series of

ionic liquids, when we go from hexyl to octyl the C_{rot} values are very similar (Tables 3.5, 3.6). The relatively slower rotation for ANBD as compared to HNBD arises due to the absence of solute-solvent specific interaction in case of the former solute molecule. This indicates that in longer alkyl chain system e.g. hexyl and octyl a similar solute-solvent interaction is observed. Here we note that, Dutt while investigating the rotational behavior of 2,5-dimethyl-1,4-dioxo-3,6-diphenylpyrrolo[3,4-*c*]pyrrole (DMDPP) in several RTILs have demonstrated that that alkyl chainlength has no bearing on DMDPP rotation.¹⁹⁸

As discussed earlier, since ANBD is devoid of acidic hydrogens and thus can not participate in forming specific hydrogen bonding interaction with the sulfate anions, relatively faster rotation is observed for it.

Table 3.6. Reorientation times (τ_r) of HNBD in BIMIMFAP and HIMIMFAP at different temperatures ($\lambda_{exc} = 405$)

RTILs	Temp. (K)	Vis. (cP) ^a	τ_r (ns) ^b	$C_{rot} = \tau_r^{exp} / \tau_r^{stk}$
BIMIMFAP	293	93.4	3.88	1.20
	298	72.3	3.24	1.32
	303	57.4	2.65	1.38
HIMIMFAP	293	112.7	3.44	0.88
	298	86.7	2.78	0.94
	303	67.9	2.36	1.02

^aExperimental error= $\pm 2\%$, ^bExperimental error= $\pm 5\%$

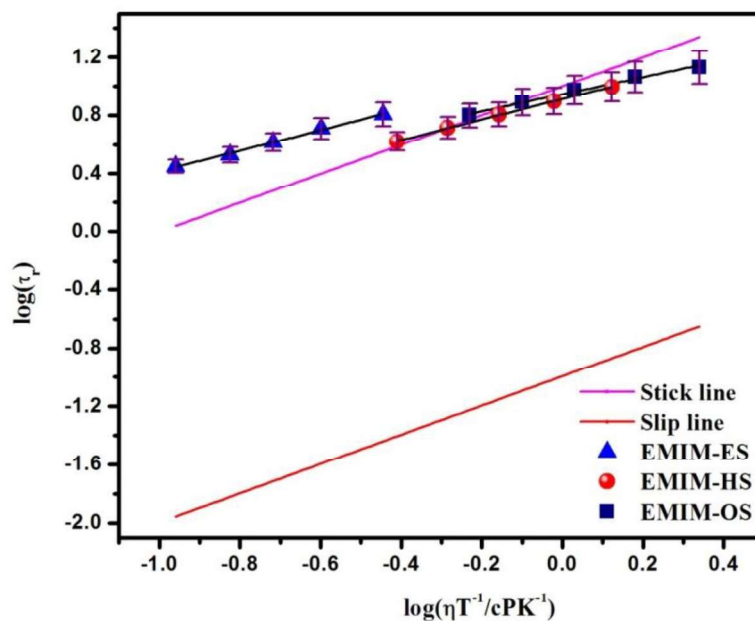


Figure 3.9. $\log(\tau_r)$ vs $\log(\eta/T)$ plot of HNBD in RTILs with stick and slip boundary condition limit. The black lines indicate fit to the data points. The purple lines indicate the error bar from the data points.

It may be mentioned here that Amendola and co workers²⁹¹ have demonstrated that acidic N-H fragment of an organic dye molecule is capable of forming hydrogen bonding interaction with the anions and can be used as the receptor for anion sensing event.^{210, 291} In the present system the charge density on the hydrogen atom (N-H moiety) is estimated to be fairly high (+0.345). This indicates that these hydrogen atoms are acidic in nature and can form hydrogen bond with the sulfate moiety. The hydrogen-bonding interaction between acidic hydrogens of HNBD and RTILs is further confirmed through ¹H NMR study. Figure 3.10, shows the ¹H -NMR spectrum of HNBD, EMIM-ES and HNBD in presence of EMIM-ES. It can be seen, the N-H proton signal of HNBD appears at 8.86 ppm. Upon addition of EMIM-ES to HNBD, N-H proton signal becomes broadened. The broadening of the N-H peak indicates the interaction between N-H and sulfate anion. Due to hydrogen bonding interaction the relaxation time (Δt) becomes very short, as compared to the NMR timescale, thereby uncertainty in energy (ΔE) and hence uncertainty in

frequency ($\Delta\nu$) becomes very large. This uncertainty results in broadening of N-H proton signal.²⁹² Solute-solvent hydrogen bonding interaction is further supported by FTIR experiments. FTIR experiments reveal that the characteristic N-H peak for HNBD appears at 3343 cm^{-1} . The peak is shifted to a lower frequency (3150 cm^{-1}) region in the presence of EMIM-ES (Figure 3.11). The observation indicates that the decrease in N-H peak frequency in the IR spectrum arises due to the hydrogen bonding interaction between the N-H of HNBD and the ionic liquid.

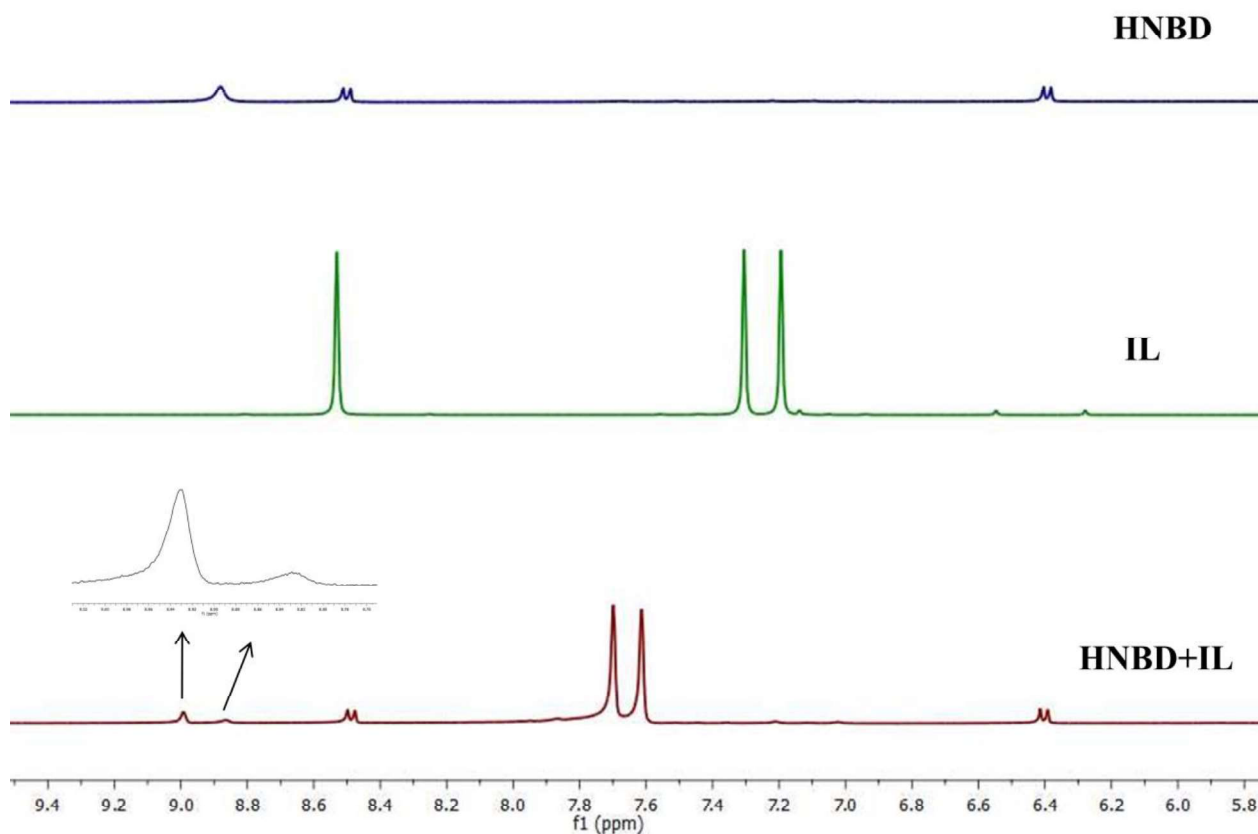


Figure 3.10. ^1H -NMR spectra of HNBD, IL and IL+HNBD mixture in DMSO-d_6 .

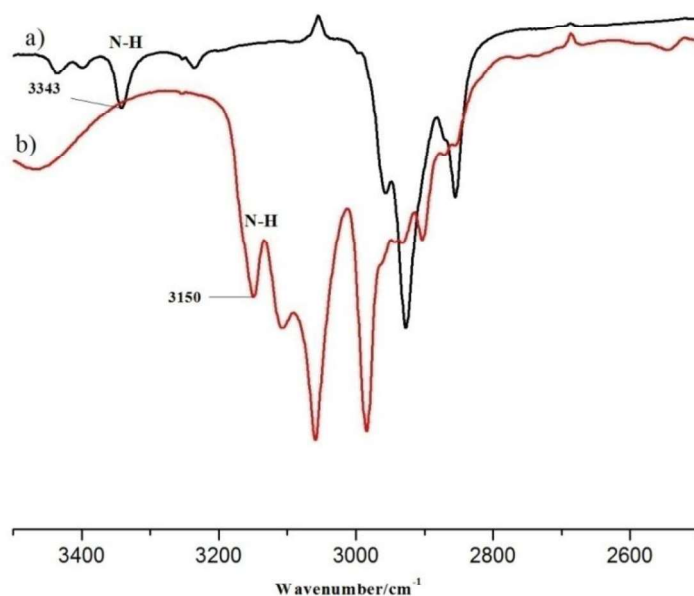


Figure 3.11. Zoomed in FTIR spectrum of (a) HNBD and (b) HNBD in presence of EMIM-ES.

The solute-solvent interactions have been investigated further by employing FCS technique. FCS is a powerful technique and capable of measuring the concentration and the diffusion coefficient of fluorescent molecules dissolved in a solvent.²⁴⁵ As diffusion coefficient depends on the molecular mass and shape of the diffusing fluorescent species, it would be possible to study the association/interaction between fluorescent solute molecule with the solvent molecules.^{162, 220, 202, 203} In the present FCS study, the interaction of both structurally similar NBD derivative with EMIM-ES has been investigated independently by measuring the translational diffusion coefficient (D) of the solutes in the given RTIL. The observed correlation curves of HNBD and ANBD in EMIM-ES are provided in Figures 3.12 (a) and (b) respectively. The parameters, obtained from FCS measurements are given in Table 3.7. Interestingly, the translational diffusion coefficient (D) of HNBD and ANBD are estimated to be $0.64 \times 10^{-11} \text{ m}^2/\text{s}$ and $2.75 \times 10^{-11} \text{ m}^2/\text{s}$ respectively in the neat RTIL at 298 K. The lower diffusion coefficient of HNBD

compared to ANBD in EMIM-ES indicates relatively stronger association of the former solute with the RTIL.

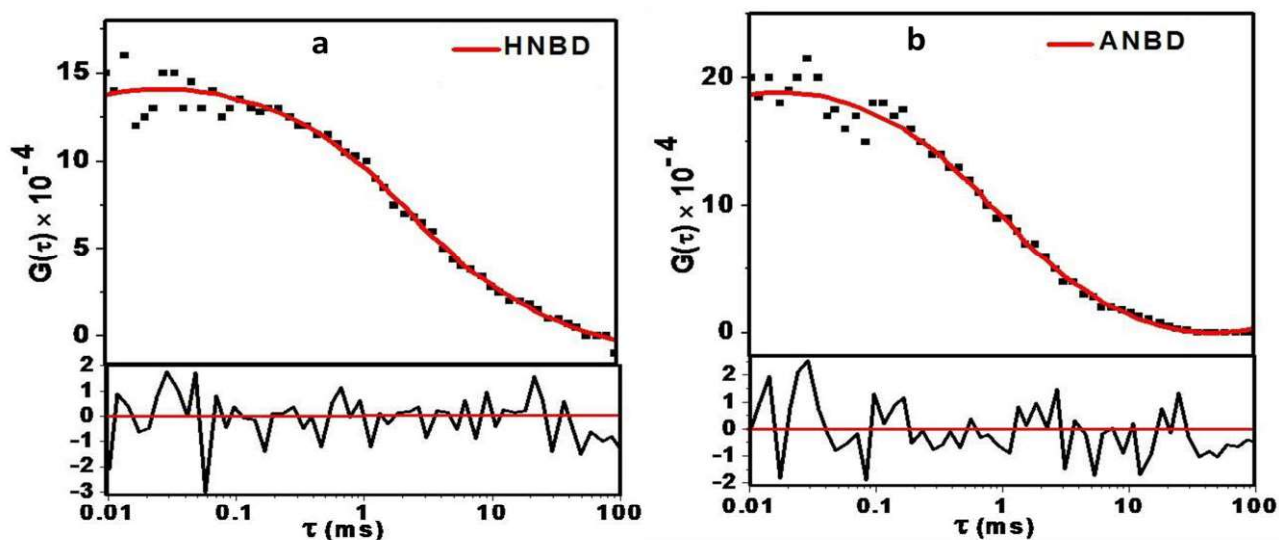


Figure 3.12. Autocorrelation functions of (a) HNBD and (b) ANBD in EMIM-ES. Solid red lines indicate fit to the data points.

Table 3.7. The obtained physical parameters for HNBD and ANBD in EMIM-ES from FCS measurements

System	$D(\mu\text{m}^2\text{s}^{-1})$	Concentration (nM)	Viscosity (cP)
HNBD	6.4 ± 1	1820 ± 80	75 ± 1.50
ANBD	27.5 ± 3	1020 ± 50	75 ± 1.50

Therefore, from the analysis of both NMR and the FCS data we can now conclude that the hydrogen bonding interaction between the acidic hydrogens of HNBD and the sulphate moiety of RTIL is primary responsible for stronger association between them. Since no such hydrogen bond is formed between ANBD and EMIM-ES a higher diffusion coefficient is estimated for ANBD.

3A.4. Conclusion

Interaction of two structurally similar but chemically distinguishable organic solutes HNBD and ANBD with 1-methyl-3-ethyl imidazolium alkyl sulfate (alkyl=ethyl, hexyl and octyl) RTILs has been investigated by fluorescence, NMR and FCS techniques. Steady state fluorescence measurements demonstrate that the location of the two solute molecules is quite different in two RTILs. Interestingly, for ANBD, faster rotation is observed upon moving from smaller to longer alkyl group containing RTIL despite the fact that longer system is more viscous than the smaller system. The faster rotation of ANBD upon increase in the alkyl chainlength of the RTIL can be attributed to larger size of the RTIL (octyl system) which offers lower friction to the rotating solute. Time resolved fluorescence anisotropy decay studies also indicate that the rotational diffusion of HNBD is considerably slower compared to that of ANBD in both RTILs. According to SED hydrodynamics description HNBD exhibits superstick behavior and ANBD lie between stick and slip limit. The observation indicates strong solute-solvent specific interaction between HNBD and sulfate moiety of RTILs. ¹H-NMR spectra confirm the hydrogen bonding interaction between the N-H hydrogen of HNBD and sulfate ion. The FCS studies have also demonstrated that association of HNBD is stronger with EMIM-ES as compared to ANBD. Interestingly, decoupling of rotational motion of solute with medium viscosity has been observed in case of longer alkyl chain derivative. The observation has been rationalized by considering the micro-heterogeneous behavior of the medium.

Part B

In *Part B*, the solute-solvent interaction also been investigated by taking coumarin 153 (C153) as a solute and 1-ethyl-3-methylimidazolium fluoroalkylphosphate ([Emim][FAP]), and 1-hydroxyethyl-3-methylimidazolium fluoroalkylphosphate ([OH-Emim][FAP]) RTILs as solvent by using fluorescence and NMR spectroscopy. The present investigation depicts that the diffusion-viscosity-decoupling is significantly higher for [OH-Emim][FAP]. This results indicate that the hydroxyl-functionalized RTIL is more micro-heterogeneous and structurally organized than the other non-hydroxylic RTIL.

3B.1. Introduction

In recent times, RTILs have drawn considerable attention from academia and industry, mainly because they can be used as customizable solvents for several synthetic applications.²¹ In this context functionalized and task specific ionic liquids are interesting as they are capable of performing a particular application.^{5, 11, 21, 42, 74} In particular, hydroxyl-functionalized RTILs have emerged as useful solvent systems in several applications.²⁹³⁻³⁰⁰ However, fewer studies are available towards understanding the physical chemistry of these media. Recently, Deng and coworkers³⁰⁰ have investigated the polarity of a series of hydroxyl functionalized RTILs. Palchowdhury and Bhargava²²⁴ have studied the self-assembly of cations in hydroxyl-functionalized RTILs. Paul and Samanta¹⁶⁰ observed the restricted rotation of solute molecule in a hydroxyl-functionalized RTIL. A recent study by Gholami and co-workers on thermodynamics properties of hydroxyl RTILs through molecular dynamics and ab initio calculations is noteworthy.¹⁵⁷ Nevertheless, experimental studies that focus on the structure, dynamics and micro-heterogeneous behavior of these RTILs are rather limited. It may also be noted here that RTILs are structurally and dynamically heterogeneous.^{88, 90, 91, 160} The heterogeneous behavior of

RTILs can influence many important physical attributes such as reaction rate, heat transfer process etc.^{88, 90, 301}

Since, it is also known that heterogeneity and hydrogen bonding interactions in RTILs are intricately related,³⁰² it is extremely important to have molecular-level understanding on intermolecular interaction, structure and dynamics of functionalized RTILs. In this context hydroxyl-functionalized RTIL could be a fascinating research targets by virtue of its interesting properties and wide range of applications.

Studies on solute and solvent dynamics in RTILs can be very useful in finding structure-dynamic correlation of these media.¹⁸³⁻²⁰² Understanding the interaction of dissolved solute and the time scale of solvent organization in such reaction media is crucially important for designing a solvent for carrying a specific reaction for a desired product. The micro-heterogeneous behavior of RTILs media can be investigated by means of the decoupling of solute and solvent dynamics from the viscosity of the medium.¹⁸³ Interestingly, it has recently been demonstrated that ion jump and angle jump in viscous media can contribute towards viscosity-diffusion decoupling behavior.¹⁷⁸ It has also been said that heterogeneity of the medium is primarily responsible for viscosity-diffusion decoupling.¹⁸³ Recently, Das et. al.¹⁷⁸ have shown by theoretical calculations that the jump dynamics and hydrogen bond fluctuation are closely related to each other. Hence, to investigate how the dynamics is decoupled with the viscosity in a viscous medium having hydrogen bond formation capability, such as the hydroxyl-functionalized RTILs, would be an interesting topic to study.

Keeping the above facts in mind, we have systematically carried out steady state and time-resolved fluorescence behavior of coumarin153 (C153) in 1-ethyl-3-methylimidazolium fluoroalkylphosphate [Emim][FAP] and 1-hydroxyethyl-3-methylimidazolium

fluoroalkylphosphate ([OH-Emim] [FAP]) RTILs. These RTILs are purposefully chosen so that the effect of -OH functionalization into the cationic moiety is exclusively monitored. Thermophysical properties such as viscosities, densities are estimated in these RTILs to get an idea about how the hydroxyl moiety can influence these properties. We chose C153 as fluorescence probe due to its suitable photophysical properties.²⁸³ We have also carried out 1D and 2D NMR experiments on the RTILs to identify the intermolecular interactions in the RTILs and the relationship between translational diffusion coefficient and the viscosity of the medium. The molecular structures of RTILs and C153 are provided in Chart 3.2.

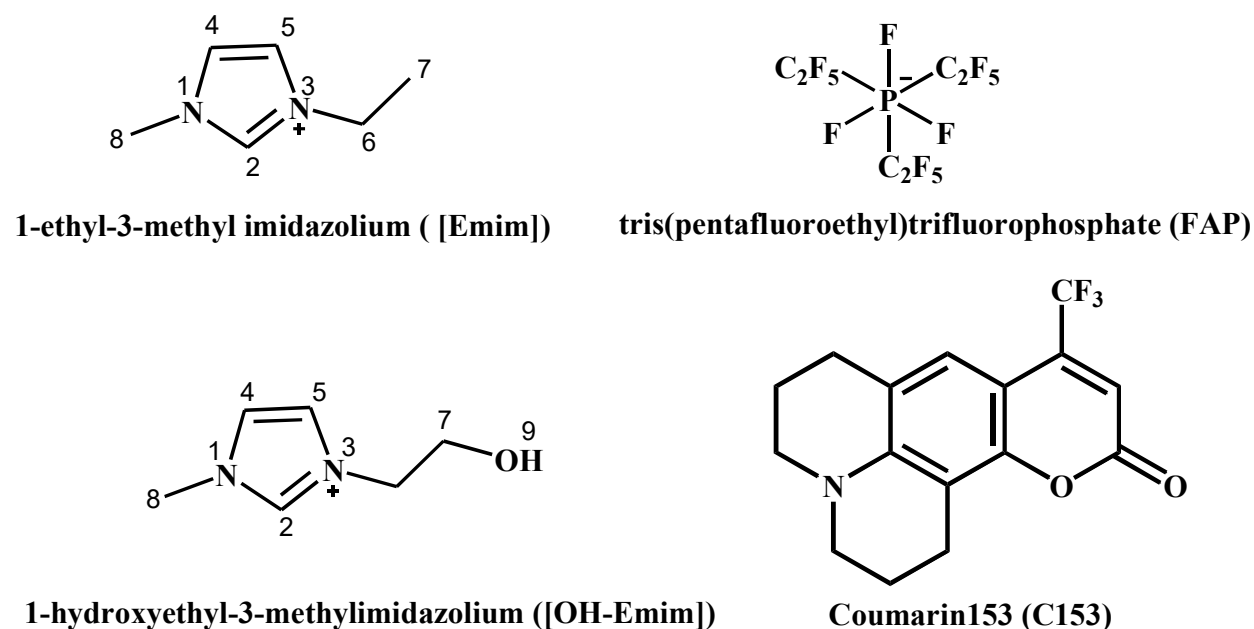


Chart 3.2. Molecular structure of C153 and RTILs.

3B.2. Experimental Section

Laser grade C153 was purchased from Exciton, USA and used without further purification. RTILs (Chart 3.2) were obtained from Merck, Germany (>99% purity) and used as received. 1, 3-bis (1-pyrenyl) propane (BPP) was purchased from Invitrogen. Acetone-d₆ was used as solvent for NMR experiments and obtained from Sigma-Aldrich. Proper precautions were maintained to

avoid moisture absorption by the medium during transferring the solute into the cuvette. The cuvettes were sealed with septum caps and Parafilm to avoid contamination by moisture from the environment.

3B.3. Results and Discussion

3B.3.1. Thermophysical Properties of RTILs

Physicochemical properties of RTILs depend on the ionic constituents, and hence RTILs are also known as designer solvents.² To investigate the effect of -OH functionalization of the cationic moiety in controlling the physicochemical properties of the RTILs, thermophysical studies on the present RTILs have been performed. Moreover, the knowledge about the physicochemical properties of RTILs is also expected to be helpful in explaining the new experimental findings that are obtained from fluorescence and NMR studies. The measured viscosities and densities of these RTILs at different temperatures are provided in the Tables 3.8. The variation of viscosity and density of these RTILs at different temperature are shown in Figures 3.13 (a) and 3.13 (b) respectively.

Table 3.8. Viscosity (η) and density (ρ) of [Emim][FAP] and [OH-Emim][FAP] at different temperatures

Temp. (K)	η (cP) ^a		ρ (gcm ⁻³) ^b	
	[Emim][FAP]	[OH-Emim] [FAP]	[Emim][FAP]	[OH-Emim][FAP]
293	73.1	265.5	1.714621	1.770211
298	58.5	185.1	1.708707	1.764392
303	47.6	132.8	1.702773	1.758647
308	39.2	98.1	1.696854	1.752835
313	32.5	73.2	1.690951	1.747005
318	27.1	56.9	1.685064	1.741174
323	22.9	44.5	1.679198	1.735345

^a Experimental errors are $\pm 2\%$, ^b Experimental errors are $\pm 2\%$

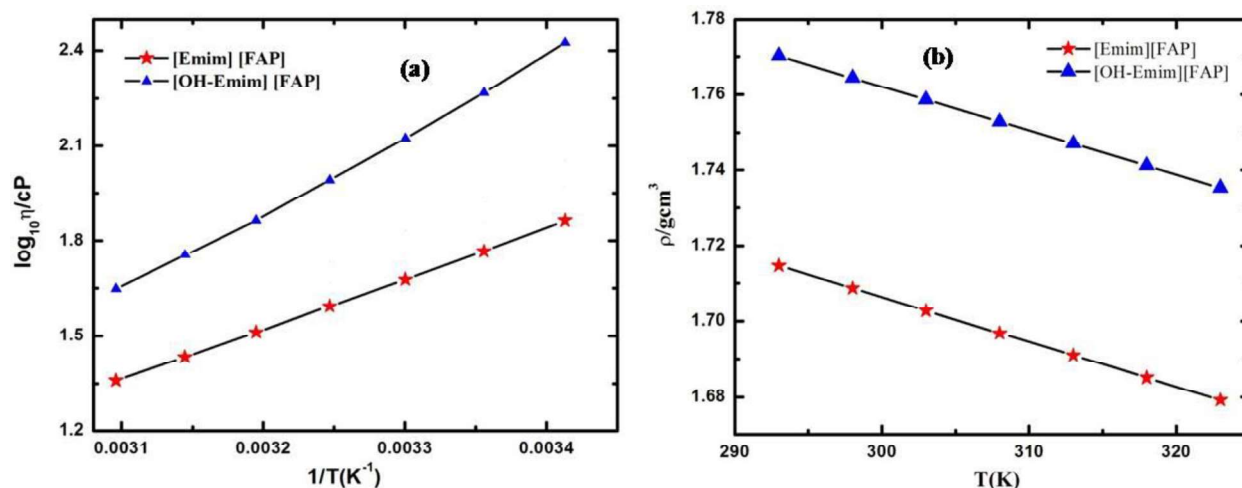


Figure 3.13. (a) Viscosities and (b) densities of [Emim][FAP] and [OH-Emim][FAP] as a function of temperature.

Figure 3.13 (a) shows that at any given temperature the viscosity of [OH-Emim][FAP] is higher than that of [Emim][FAP]. However, the activation energies of viscous flow of neat [OH-Emim][FAP] and [Emim][FAP] are calculated by plotting $\ln(\eta)$ versus $1/T$ to an Arrhenius type relation⁶² (Figure 3.14). The activation energies for [OH-Emim][FAP] and [Emim][FAP] are observed to be 30.84 kJ/mol and 49.0 kJ/mol, respectively. The present data indicate that the microscopic structural organizations of these two RTILs are different. Recently, Gholami and co-workers¹⁵⁷ reported that hydroxyl groups can play a significant role in the organization of anions around [OH-Emim]⁺. While the acidic hydrogen atom (C2-H) of imidazolium ring in conventional RTIL is the most probable site for hydrogen bonding interaction with anions,³⁰² the hydroxyl group in [OH-Emim][FAP] provides an additional hydrogen-bonding site for cation-anion interionic interactions. Gholami et. al.¹⁵⁷ also demonstrated that the stronger cation-cation interaction for hydroxyl-functionalized RTILs is possible with bulkier anions. In the present case, FAP is bulkier anion, and hence the present experimental observation of higher viscosities for OH-functionalized RTIL compared to the other RTIL indicates stronger cation-cation interactions. Similar behavior can also be evidenced through 2D ROSEY NMR spectroscopy

studies (*vide infra*).

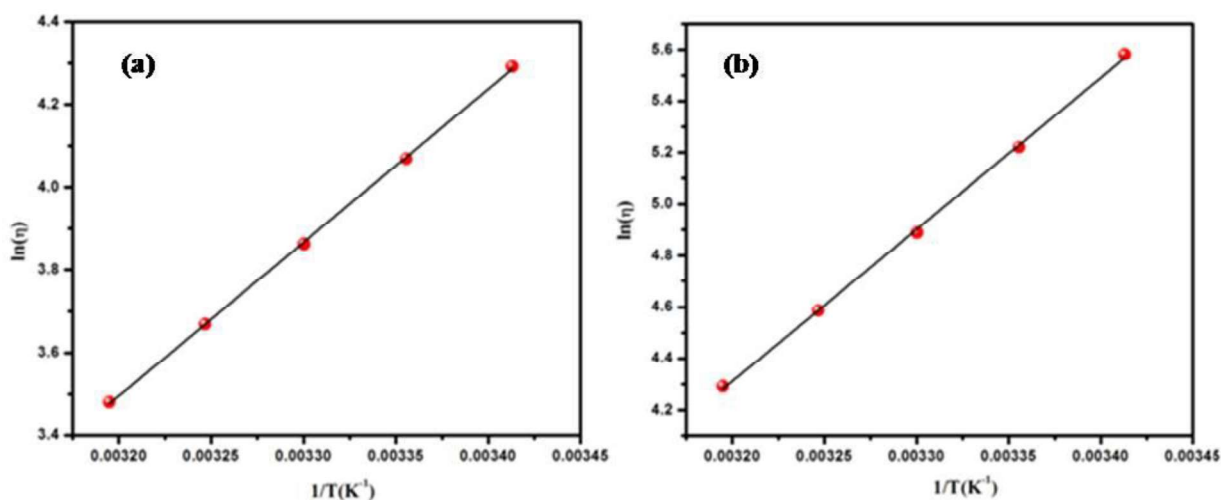


Figure 3.14. Plot of $\ln(\eta)$ vs. $1/T$ of neat (a) [Emim][FAP] and (b) [OH-Emim][FAP] with temperatures. The solid black lines indicate the fit to the data points.

At any given temperature, density of [OH-Emim][FAP] is slightly higher than that of the other RTIL (Figure 3.13b). The experimentally determined viscosity (η) and density (ρ) are fitted by the least-squares method (equation 3.2 and 3.3)^{304, 305}

$$\log \eta \text{ (cP)} = A_0 + (A_1/T) \quad (3.2)$$

$$\rho \text{ (g.cm}^{-3}\text{)} = A_2 + A_3 T \quad (3.3)$$

where η and ρ denote the viscosity and density of RTILs and A_0 , A_1 , A_2 and A_3 are the correlation coefficients and T is the temperature in Kelvin. The correlation coefficients are determined by a least squares fitting method using equations 3.2 and 3.3. All the fitting parameters in relation to the measurements of density and viscosity are provided in Table 3.9.

Table 3.9. Fitting parameters for viscosity and density according to equations 3.2 and 3.3

RTILs	A_0	A_1	R^2	A_2	$A_3 \times 10^{-3}$	R^2
[Emim][FAP]	-3.55	1583.93	0.999	2.06	-1.18	0.999
[OH-Emim][FAP]	-5.93	2444.70	0.999	2.11	-1.16	1.000

R^2 = regression coefficient

The experimentally determined density values are used again to estimate the thermal expansion coefficient (α) of these two RTILs by using the following equation³⁰⁵

$$\alpha_p = -\frac{1}{p} \left(\frac{\delta p}{\delta T} \right)_p = -\frac{A_3}{A_2 + A_3 T} \quad (3.4)$$

where A_2 , A_3 are the fitting parameters from equation 3.3 and α_p and T are the thermal expansion coefficient and absolute temperature respectively. The thermal expansion coefficients (α_p) of the RTILs are shown in Table 3.10. It can be seen from Table 3.10 that the coefficients of thermal expansion for -OH functionalized RTILs is lower than the other one due to the strong interionic interaction within [OH-Emim][FAP]. The observed α_p values in the present case are similar to those reported for imidazolium, pyridinium, phosphonium, and ammonium based RTILs, (4.8×10^{-4} to 6.5×10^{-4}) K^{-1} .^{306, 307}

Table 3.10. Thermal expansion coefficient values of present RTILs as a function of temperature

T/K	$\alpha \times 10^4 (K^{-1})$	
	[Emim][FAP]	[OH-Emim][FAP]
293	6.89	4.80
298	6.91	4.79
303	6.94	4.78
308	6.96	4.77
313	6.98	4.76
318	7.01	4.75
328	7.03	4.74

3B.3.2. Steady-State Studies

The steady state absorption and fluorescence spectra of C153 in [Emim][FAP] and [OH-Emim][FAP] are shown in Figures 3.15 and 3.16 respectively. Emission spectra of neat RTILs are also shown in Figure 3.16. The steady state spectral data of dissolved C153 in these RTILs are collected in Table 3.11 for comparison. It can be seen that both absorption and emission maxima of C153 appear at higher wavelengths region in [OH-Emim][FAP] than that in

[Emim][FAP]. This indicates that the polarity of [OH-Emim][FAP] is relatively higher than that of [Emim][FAP].

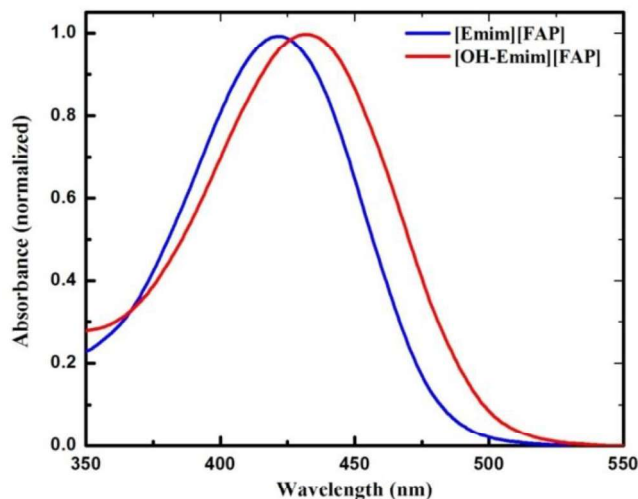


Figure 3.15. Steady state absorption spectra of C153 in [Emim][FAP] and [OH-Emim][FAP]. Spectra are normalized at their corresponding peak maxima.

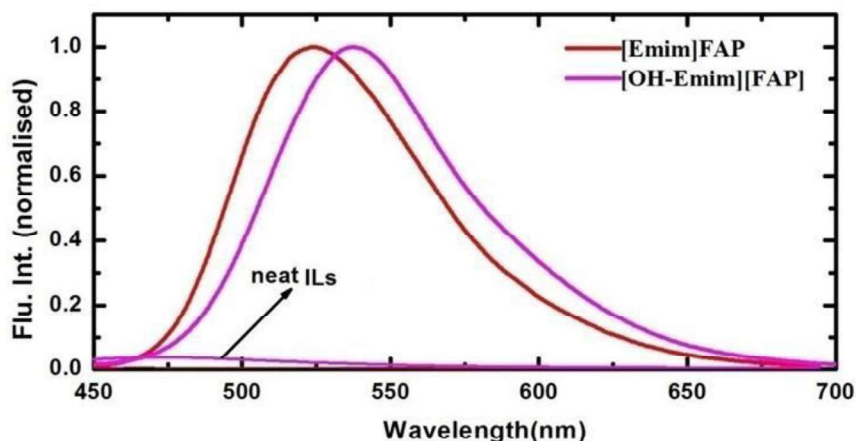


Figure 3.16. Steady state emission spectra of C153 in [Emim][FAP] and [OH-Emim][FAP]. All emission spectra are normalized at their corresponding peak maxima. Emission spectra of neat RTILs are also shown in the same figure.

Table 3.11. Absorption, emission maxima and steady-state stokes' shifts ($\Delta\gamma$) of C153 in [Emim][FAP] and [OH-Emim][FAP] at 298 K

RTILs	$\lambda_{\text{abs}}(\text{nm})^{\text{a}}$	$\lambda_{\text{flu.}}(\text{nm})^{\text{a}}$	$\Delta\gamma (\text{cm}^{-1})$
[Emim][FAP]	422	524	4613
[OH-Emim][FAP]	432	537	4526

^aexperimental error ± 1 nm

3B.3.3. Time Resolved Studies

The time-resolved fluorescence anisotropy decay profiles for C153 in the present RTILs are shown in Figure 3.17. The rotational relaxation parameters of C153 in these RTILs are provided in Table 3.12. The time resolved anisotropy decay profiles are fitted well by the biexponential decay function. It is known that solute rotation depends on the microviscosity of the local environment of the medium^{308, 309} In the present case, two distinct rotational component of C153 in the biexponential decay profile for C153 indicate the presence of two different types of domain for RTILs, whereby rotation is faster in one domain and slower in the other. It is pertinent to mention that RTILs are spatially heterogeneous in nature with distinctly different polar and nonpolar domains.³¹⁰ Nonpolar domains are believed to be formed mainly by aggregation of nonpolar alkyl chains, and polar domain forms by polar cationic and anionic moieties.³¹⁰ Moreover, polar domains are thought to be compact as they are formed due to columbic interaction between cation and anion, whereas the nonpolar domains are rather loose, and is formed mainly by hydrophobic interaction among the alkyl groups. Solute rotation is usually faster in loose domain and slower in compact domain.³¹⁰ Since, in both [OH-Emim][FAP] and [Emim][FAP], anionic moiety is hydrophobic FAP, it is reasonable to assume that nonpolar domains for the present RTILs are created by FAP moiety and polar domains by cationic moiety. Interestingly one can also see from Table 3.12 that the faster rotational relaxation component of C153 is almost constant at room temperature in both the RTILs, whereas values for slower component change. The present experimental findings also demonstrate that present RTILs form very similar nonpolar domains whereas formations of polar domains are different for different RTILs.

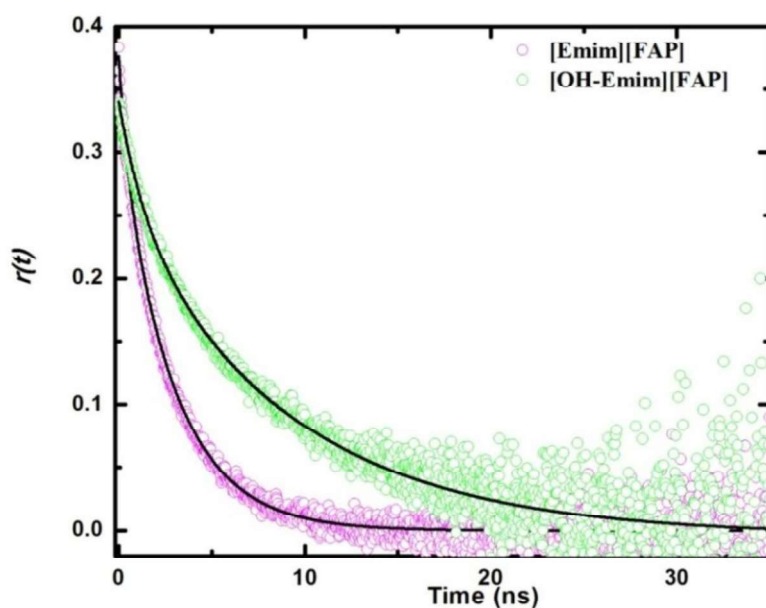


Figure 3.17. Time resolved fluorescence anisotropy decay (TRFAD) for C153 in [Emim][FAP] and [OH-Emim][FAP] at 298 K. The solid black lines indicate fit to the data points.

Table 3.12. Reorientation times of C153 in [Emim][FAP] and [OH-Emim][FAP] as a function of temperature

RTILs	Temp.(K)	Vis.(cP) ^a	^a r ₀	a ₁	τ _{1r}	a ₂	τ _{2r}	<τ _r > (ns) ^b	C _{rot}
[Emim][FAP]	293	73.1	0.38	0.22	0.94	0.78	4.12	3.42	0.52
	298	58.5	0.38	0.20	0.92	0.80	3.11	2.67	0.51
	303	47.6	0.37	0.23	0.89	0.77	2.58	2.19	0.53
	308	39.2	0.37	0.33	0.98	0.67	2.31	1.87	0.56
	313	32.5	0.38	0.70	1.18	0.30	2.57	1.60	0.58
[OH-Emim][FAP]	293	265.5	0.35	0.19	0.93	0.81	13.03	10.73	0.45
	298	185.1	0.34	0.20	0.85	0.80	10.67	8.71	0.53
	303	132.8	0.34	0.18	0.81	0.82	8.62	7.21	0.62
	308	98.1	0.34	0.18	1.06	0.82	7.24	6.13	0.73
	313	73.2	0.34	0.19	1.09	0.81	5.74	4.86	0.79

^aExperimental error= ±2%, ^bExperimental error= ±5%

The relatively higher average rotational relaxation time for C153 in [OH-Emim][FAP] than that in [Emim][FAP] indicates that microviscosity experienced by the solute molecule is

higher in the former RTIL. Microviscosity of the medium has been investigated further by carrying out the steady state emission behavior of a well-known microviscosity probe, namely, 1,3-bis(1-pyrenyl) propane (BPP), which is specifically very sensitive towards microheterogeneous nature of the medium.³⁰⁹⁻³¹² BPP is a well-documented fluorescent probe that can be employed to detect the microviscosity by measuring the excimer emission band, which is located about 450–500 nm region in its emission spectral profile.³⁰⁹ The two pyrene units of BPP easily come closer to each other to form an intramolecular excimer in low viscous medium, and the emission spectra of this compounds exhibit a usual structured monomer fluorescence band and a broad structureless excimer fluorescence band. The efficiency of the excimer formation found to be decreased and a corresponding reduction in the intensity of the excimer band is observed with the increment of microviscosity of the environment. From such a scenario, the ratio of excimer to monomer emission intensity (I_E/I_M) of BPP can be used to measure the microviscosity of a fluidic medium. Figure 3.18 shows the steady-state emission spectral behavior of BPP dissolved in the present RTILs and a conventional solvent, namely, ethanol. Figure 3.18 shows that, in comparison to ethanol, the excimer emission peak of BPP in the present RTILs is diminished. From the value of the excimer to monomer emission intensity ratio (I_E/I_M) of BPP, microviscosity of alcohol functionalized RTIL is found to be higher than that of the other. This observation also indicates that the local structures of [OH-Emim][FAP] and [Emim][FAP] are quite different.

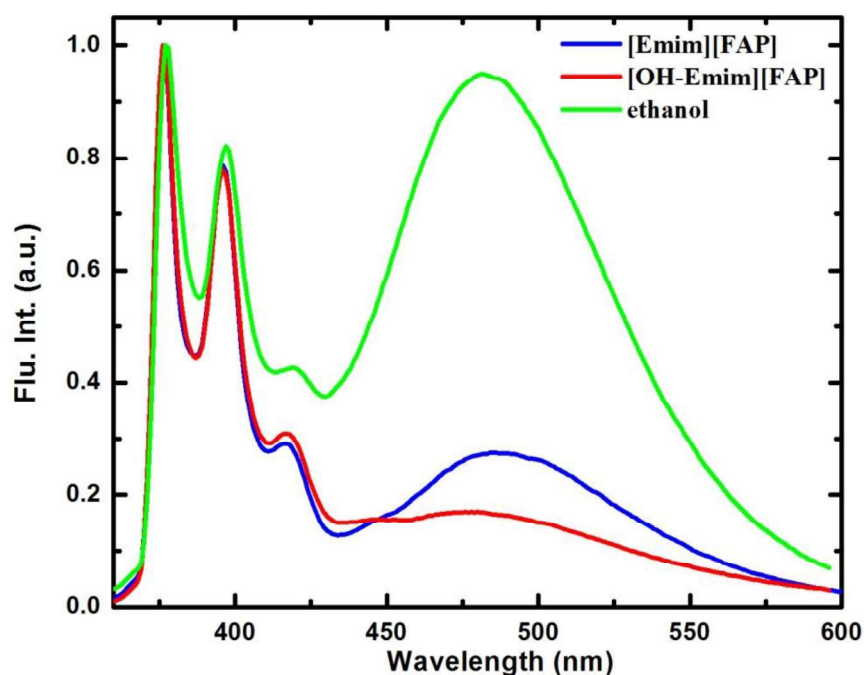


Figure 3.18. Steady state emission spectra normalized to the peak of the monomer fluorescence band [$I_M(380\text{nm}) = 1.00$] for BPP in [Emim][FAP], [OH-Emim][FAP] and ethanol; ($\lambda_{exc} = 330$ nm).

To get a closer look on whether the -OH functionalization affects the solute-solvent rotational coupling, we have further analyzed the experimentally measured rotation time with the help of Stokes-Einstein-Debye (SED) hydrodynamic theory.^{239, 247} For analysis the SED theory, we have taken the probe properties which are already available in literature.²⁰⁵ The van der Waals volume, shape factor, and calculated slip boundary condition parameter for C153 are 243 \AA^3 , 1.5, and 0.18 respectively.¹⁹⁵ The slip and stick boundary limit, which have been assigned with the help of SED hydrodynamic theory are shown in the Figure 3.19 with the experimentally measured reorientation times of C153 in the present RTILs. The experimentally rotational coupling constant ($C_{rot} = \tau_r^{exp}/\tau_r^{stk}$), which is a measure of the extent of departures from normal hydrodynamic behavior of a solute due to specific interaction is calculated and provided in Table 3.12.

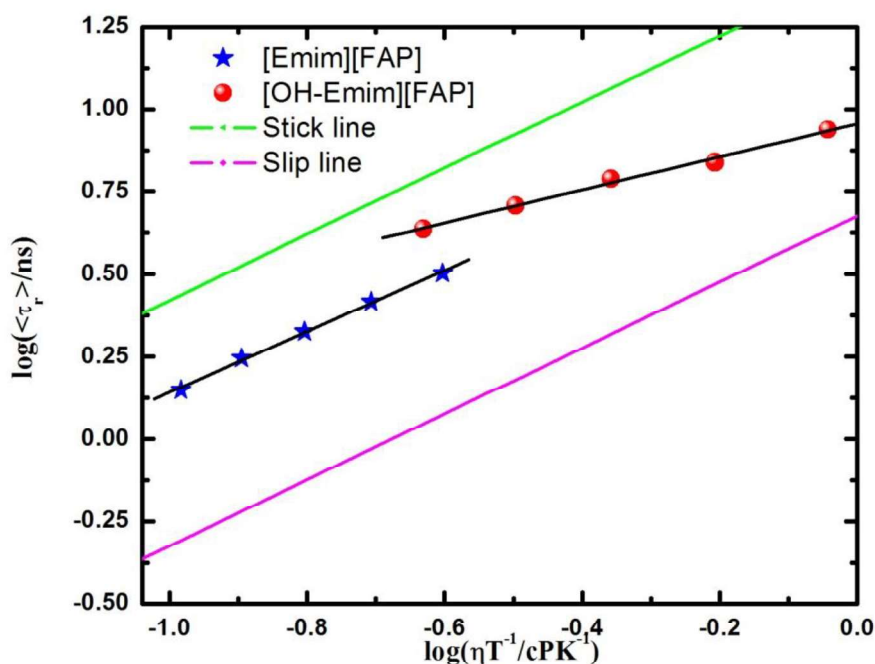


Figure 3.19. log-log plots of rotational relaxation time of C153 vs. η/T in [Emim][FAP] and [OH-Emim][FAP] with slip and stick boundary condition parameters.

It can be seen from Table 3.12 that, at 293 K, the average rotation time of C153 in [OH-Emim][FAP] is 3 times higher than that in [Emim][FAP], whereas the viscosity increases 3.6 time upon going from [Emim][FAP] to [OH-Emim][FAP]. It indicates that the rotation of C153 in the [OH-Emim][FAP] is not becoming as slow as is expected from viscosity value of the same RTIL. Interestingly Table 3.12 also reveals that when the viscosity of the [OH-Emim][FAP] is tuned (by increasing the temperature to 313 K) to the viscosity of EMIMFAP (at 293 K) the rotational motion of C153 is observed to be relatively hindered in the hydroxy-RTIL. This perhaps happens due to the solute-solvent specific hydrogen bonding interaction in case of hydroxy-RTIL.^{160, 190, 313} This observation is interesting in a sense that it indicates the decoupling of rotational motion of solute molecule with the medium viscosity. Interestingly, when we fitted the log-log plot of τ_r vs. η/T by the $\log(\langle \tau_r \rangle) = a + n \log(\eta/T)$ relation. The deviation of exponent (n)'s values from unity denotes the degree of decoupling between rotational time of solute and the viscosity of the medium.¹⁸³

For [Emim][FAP],

$$\log \langle \tau_r \rangle = (1.067 \pm 0.0196) + (0.9258 \pm 0.0242) \log(\eta/T) \quad N=5, R=0.999$$

For [OH-Emim][FAP],

$$\log \langle \tau_r \rangle = (0.955 \pm 0.0095) + (0.500 \pm 0.0236) \log(\eta/T) \quad N=5, R=0.996$$

n values are estimated to be 0.92 and 0.50 for [Emim][FAP] and [OH-Emim][FAP] respectively.

As can be seen, the degree of decoupling is significantly higher for [OH-Emim][FAP]. The observed nonlinear relationship between rotational time of solute and viscosity of the medium indicates that the hydroxyl functionalized RTIL is more heterogeneous and structurally organized than the other one. In this context, it has been recently demonstrated that decoupling of rotational motion from medium viscosity can arise due to the non-Brownian movement such as orientational jumps and the retention of inertia driven motion even much after the onset of the typical diffusion timescale.¹⁷⁸ Recent theoretical investigations by Biswas *et. al.*¹⁸⁰ have also demonstrated that the jump dynamics and H-bond fluctuations are closely related in highly viscous medium such as RTIL. In such a case, hydrodynamic description is expected to provide results which may either be inconsistent or bury the subtle effects of environmental complexity.¹⁸⁰ In light of these discussions, the present inapplicability of hydrodynamics description in describing the solute rotation in hydroxyl functionalized RTIL perhaps provide experimental evidence to the orientational jumps and the role of H-bond formation towards that event.

To understand the cation-cation interaction in the RTILs, 2D ROSEY NMR experiments has been carried out in both the RTILs in neat condition. 2D ROSEY NMR spectra of [Emim][FAP] and [OH-Emim][FAP] are provided in Figures 3.20 and 3.21, respectively. The atom numbers that are used in the molecular diagrams for these RTILs (Chart 3.2) have also

been used for assigning the ROSEY spectral signal for the respective molecules. In ROSEY spectra two types of peaks are obtained i.e. cross peak and diagonal peak. The cross peaks are more significant, as the distance between two interacting nuclei is a function of cross peak intensity.¹⁸⁶ Herein, cross peak intensity is used to understand the cation-cation interactions. Interestingly, the intermolecular interaction between two cationic moieties in the respective RTILs is found to be quite different. For [Emim][FAP], protons (H6, H7, H8) corresponding to the non polar alkyl chain of imidazolium ion interact with the protons of alkyl chain and the ring protons (H2, H4, H5) of the other imidazolium moiety (Figure 3.20). However, in [OH-Emim][FAP], protons (H6, H7, H8) of the alkyl chain of the imidazolium ion interact with only the protons (H2, H4, H5) of the polar imidazolium ring (Figure 3.21). This indicates that the microscopic structural organizations of the two RTILs are quite different.

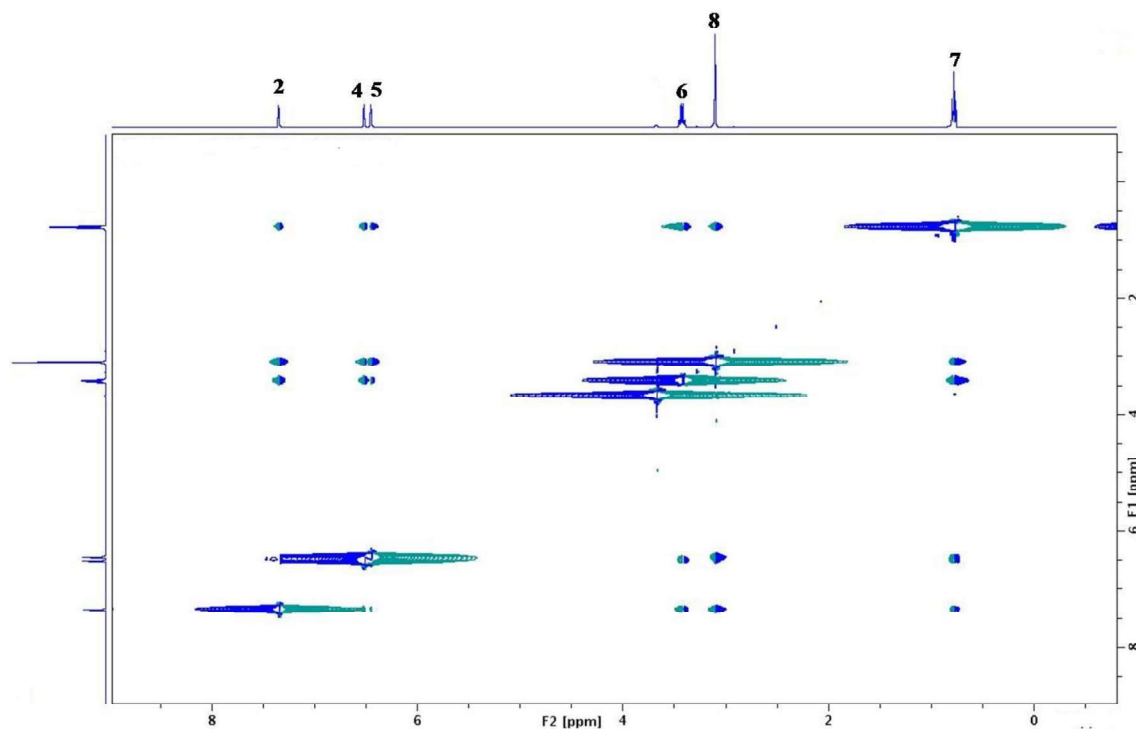


Figure 3.20. The NMR 2D ROSEY spectra of neat [Emim][FAP].

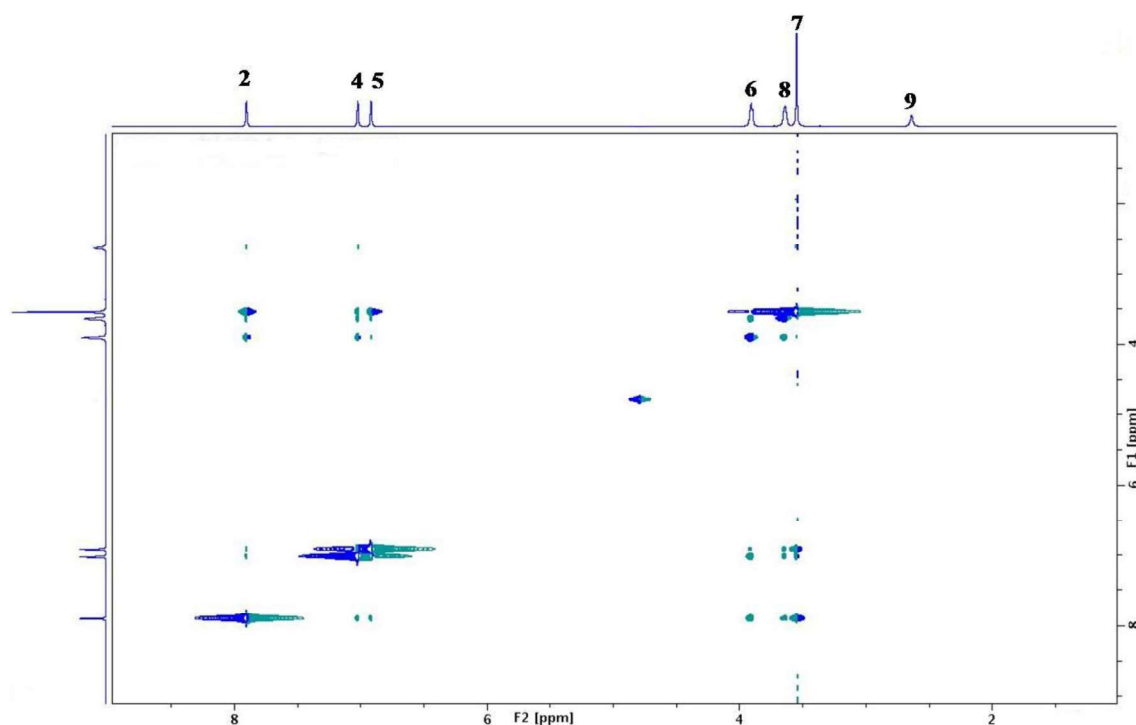


Figure 3.21. The NMR 2D ROSEY spectra of neat [OH-Emim][FAP].

The translational diffusion coefficient (D), for both neat [Emim][FAP] and [OH-Emim][FAP] are also calculated with the help of NMR experiments to get an idea about the associating nature of these two RTILs. The translational diffusion coefficients at different temperatures for both RTILs are given in Table 3.13. At any given temperature, relatively slower diffusion in case of [OH-Emim][FAP] depicts the highly associated and viscous nature of the medium. Diffusion increases with increasing temperature in both the RTILs due to the lowering of the viscosity values upon increase in the temperature.

Again, when we plot D vs. T/η by using Stokes-Einstein formula²⁷¹ it shows a linear relationships for both [Emim][FAP] and [OH-Emim][FAP] (Figure 3.22). The slope of D vs. T/η is given by $k/(6\pi R)$, Where, k is the Boltzmann constant, π = constant and R = Hydrodynamic radius of the particles. Hence, a steeper slope would indicate smaller hydrodynamic radius.²⁰⁹

Table 3.13. Calculation of translational diffusion coefficient through NMR spectroscopy

System	Temp. (K)	Vis.(cP)	Trans diff. coeff. (m ² /s.)
[Emim][FAP]	298	58.5	2.97×10 ⁻¹¹
	308	39.2	4.71×10 ⁻¹¹
	318	24.7	6.97×10 ⁻¹¹
[OH-Emim][FAP]	298	185.1	0.81×10 ⁻¹¹
	308	98.1	1.60×10 ⁻¹¹
	318	45.5	2.72×10 ⁻¹¹

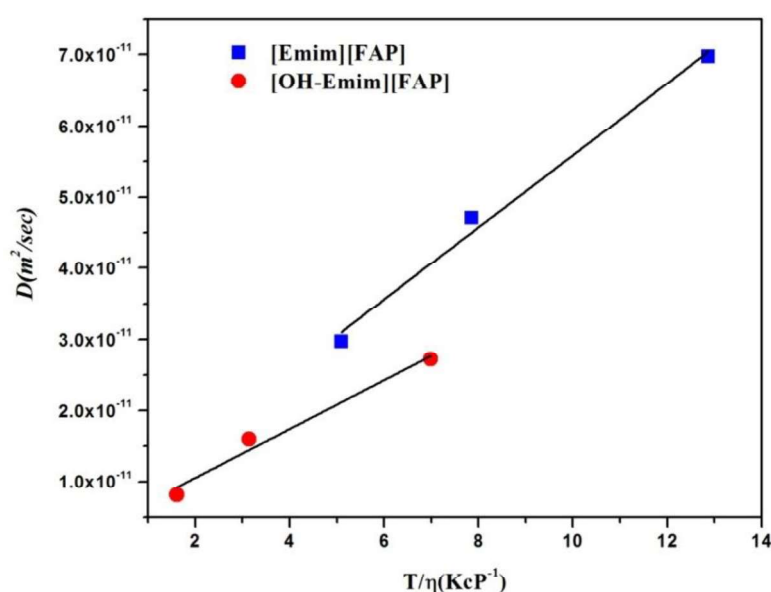


Figure 3.22. Plot of diffusion coefficient (D) against T/η for neat [Emim][FAP] and [OH-Emim][FAP].

Interestingly in the present case, the slope was found to be 0.52 JK⁻¹m⁻¹ and 0.34 JK⁻¹m⁻¹ for [Emim][FAP] and [OH-Emim][FAP] respectively. The data indicates the higher hydrodynamic radius for [OH-Emim][FAP] as compared to [Emim][FAP]. The outcome of this study also provide evidence in favor of highly associated structure for [OH-Emim][FAP] due to the intermoleculoar hydrogen bonding interaction within RTIL.

3B.4. Conclusion

In the present study has been undertaken with an aim to investigate the kinship among intermolecular interaction, structure of a task specific ionic liquid. In particular, structure-function relationship of a hydroxyl functional group ($-OH$) containing ionic liquid, ([OH-Emim][FAP]), has been investigated by employing steady state and time-resolved fluorescence and 1-D and 2-D NMR spectroscopic measurements. The experiments have also been carried out in another ionic liquid, [Emim][FAP] which is structurally similar to [OH-Emim][FAP] but does not contain the hydroxyl functional group. At ambient condition, the viscosity and the polarity of [OH-Emim][FAP] is observed to be higher than that of [Emim][FAP]. Time-resolved fluorescence measurements have shown that the solvent reorganization is significantly slow in [OH-Emim][FAP] than that in [Emim][FAP]. The slow solvent reorganization in case of hydroxyl functionalized RTIL has been explained on the basis of relatively stronger intermolecular interaction within RTIL moiety for the hydroxyl group containing RTIL. The analysis of the time-resolved fluorescence anisotropy data in light of Stokes-Einstein-Debye (SED) hydrodynamic description reveals significant decoupling of rotational motion of solute molecule with the medium viscosity in case of [OH-Emim][FAP]. The observed nonlinear relationship between rotational time of solute and viscosity of the medium indicates that the hydroxyl functionalized RTIL is more heterogeneous and organized than the other one. Since the jump dynamics and H-bond fluctuations are closely related in highly viscous medium such as RTIL, present inapplicability of hydrodynamics in describing the solute rotation in hydroxyl functionalized RTIL can be linked to the orientational jumps of viscous hydroxyl based RTIL. Experiments based on 1D and 2D NMR have also provided evidence in favor of the fact that $-OH$ functionalized RTIL is more structurally organized.

Chapter 4

Time Resolved-Fluorescence, Electron Paramagnetic Resonance (EPR), NMR, and Fluorescence Correlation Spectroscopy (FCS) Studies in Some Dicationic and Monocationic Room Temperature Ionic Liquids

This chapter demonstrates the intermolecular interactions, structure and dynamical behavior of some imidazolium-based dicationic and monocationic RTILs, two imidazolium-based dicationic ionic liquids (DILs), 1,8-bis-(3-methylimidazolium-1-yl)octane bis-(trifluoromethylsulfonyl)-amide ($[\text{C}_8(\text{mim})_2][\text{NTf}_2]_2$), 1,9-bis-(3-methylimidazolium-1-yl)nonane bis-(trifluoromethylsulfonyl)amide ($[\text{C}_9(\text{mim})_2][\text{NTf}_2]_2$) and one monocationic ionic liquid (MIL), 1-butyl-3-methylimidazolium bis(trifluoromethylsulfonyl)amide ($[\text{C}_4(\text{mim})][\text{NTf}_2]$), has been investigated through combined fluorescence, EPR, NMR and FCS. The outcome of the present investigation reveals that the behaviors of DILs are very different than usual MILs.

4. 1. Introduction

In last decade, majority of the research on RTILs have been carried out focusing on monocation-based ionic liquids (MILs).¹⁵⁰⁻¹⁹⁰ And due to the extensive research efforts, some clarity on structure-property relationship of MILs has been obtained.^{63, 85-91} Very recently, dicationic RTILs (DILs) have been developed. Some experimental and theoretical studies are also available on DILs.^{46-51, 137, 138, 140, 141, 154-156, 209, 286, 314-321} Recently, Ito et. al.⁵¹ have prepared the imidazolium-based DILs. Some ammonium-based DILs have also been synthesized by Engle and coworker.⁴⁸⁻⁵⁰ Since, DILs are consists of one dication and two monoanions,^{46, 47} greater cation and anion combinations can be possible in DILs than in MILs.^{46, 47} This in turn would be helpful to achieve

greater tunability and variability of the properties of RTILs. Moreover, some recent literature reports have suggested that DILs to be superior to MILs in terms of their physicochemical properties such as viscosity, surface tension, thermal stability etc.⁴⁶ In addition, it has also been discussed that DILs can effectively be used as high temperature lubricants,^{137, 138} dye sensitized solar cells,³¹³ and electrolyte in secondary battery^{140, 141} etc. Though several experimental and theoretical studies are available to understand the structure-property relationship of MILs,¹⁴⁶⁻²⁰² a limited number of studies on the same aspect are available for DILs.^{46, 47, 209, 286, 316-321} Anderson et. al.⁴⁷ have investigated physicochemical properties such as thermal stability, surface tension, shear viscosity of several imidazolium and pyrrolidinium cation-based DILs. They have clearly shown that thermal stability of DILs is higher than MILs.⁴⁷ Sahu et. al.^{209, 286, 316} have recently shown that dynamical behavior of 6-member alkyl linker chain containing imidazolium-based DIL is different than hexyl chain containing imidazolium-based MIL. The melting point, glass transition temperature and conductivity of some DILs have also been reported by other researchers.³¹⁹⁻³²¹ Through molecular dynamics simulation study (MD) by Cumings and coworkers¹⁵⁴ have mentioned that the structural organization of DILs are significantly different than MILs.¹⁵⁴ The aggregation behavior of imidazolium based DILs in aqueous solution have investigated by Bhargava and coworkers^{155, 156} by MD simulation study. All the above discussions point out that though some studies are done on DILs, experimental studies towards understanding the behavior of DILs in terms of intermolecular interactions, structure and dynamics is inadequate. Therefore, a deeper knowledge on structure-property correlation of DILs is extremely important, so that these systems can be used to their fullest potential.

Keeping these in mind, we have synthesized the imidazolium-based DILs, 1,8-bis-(3-methylimidazolium-1-yl)octane bis-(trifluoromethylsulfonyl)amide ($[\text{C}_8(\text{mim})_2][\text{NTf}_2]_2$) and

1,9-bis-(3-methylimidazolium-1-yl)nonane

bis-(trifluoromethylsulfonyl)amide

([C₉(mim)₂][NTf₂]₂). We report a combined time-resolved fluorescence, electron paramagnetic resonance (EPR), NMR and fluorescence correlation spectroscopy (FCS) study of [C₈(mim)₂][NTf₂]₂, [C₉(mim)₂][NTf₂]₂ along with their counterpart MIL, 1-butyl-3-methylimidazolium bis(trifluoromethylsulfonyl)amide ([C₄(mim)][NTf₂]). Here we would like to mention that we have chosen MIL in such a way that half of the size of DIL becomes close to the size of MIL having one imidazolium cation. All the spectroscopic data of DILs are compared with MIL. Steady state absorption, emission and EPR data has been used to get an idea about the polarity of DILs. The excitation wavelengths dependent emission of DILs and MIL has been used to understand the micro-heterogeneous nature of these RTILs. The rotational dynamic studies have been investigated using a neutral probe (perylene) and negatively charged probe 8-methoxypyrene-1,3,6-sulfonate (MPTS) in the above DILs and the corresponding MIL to get an idea about the solute-solvent, solvent-solvent interaction and structural organization of the media. NMR and FCS studies have also been carried out to throw more light on the micro-heterogeneous nature of the medium. The molecular structures of RTILs and probes are provided in Chart 4.1.

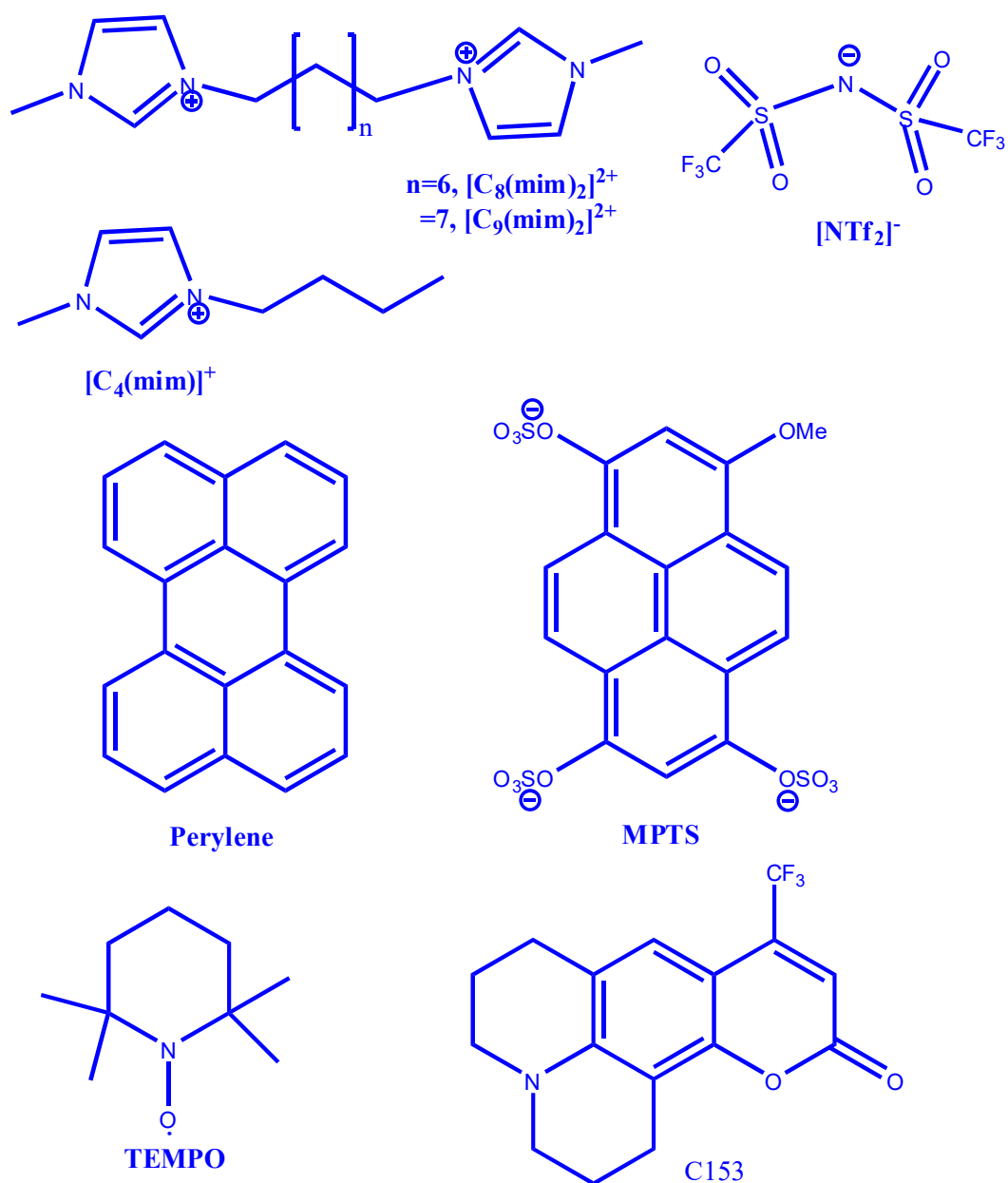


Chart 4.1. Molecular structure of RTILs, perylene, MPTS and TEMPO

4. 2. Experiments and Method

4.2.1. Materials

Coumarin 153 (C153), MPTS and perylene were purchased from Sigma-Aldrich and used as received. The RTIL $[\text{C}_4(\text{mim})][\text{NTf}_2]$ was obtained from Merck, Germany (>99% purity) with < 100 ppm water and halide. The dicationic RTILs $[\text{C}_8(\text{mim})_2][\text{NTf}_2]_2$ and $[\text{C}_9(\text{mim})_2][\text{NTf}_2]_2$

were synthesized by following a literature procedure.⁴⁶ The purity of the RTILs were checked by different conventional analytical techniques such as ¹H-NMR, ESI-MS (Electrospray ionization mass Spectrometry), and viscosity data was matched with the literature.⁴² The water content of DILs was found to be in between 176 ppm to 256 ppm.⁴² Before used the RTILs were kept in a high vacuum to avoid moisture absorption. The concentration of perylene and MPTS in these RTILs are taken $\sim 10^{-7}$ M for fluorescence studies.

4.2.2. Synthesis of DILs

4.2.2.1. Synthesis of 1,8-bis-(3-methylimidazolium-1-yl)octane bis-(trifluoromethylsulfonyl)amide ($[C_8(mim)_2][NTf_2]_2$)

1,8-bis(3-methylimidazolium-1-yl)octane bromide, $[C_8(mim)_2][Br]_2$: Synthesis of $[C_8(mim)_2][Br]_2$ was carried out by following the reported procedure proposed by Shirota and coworkers.⁴⁶ 1,8-Dibromooctane (1 mmol) was added drop wise to an acetonitrile solution of 1-methylimidazole (2.2 mmol) in reflux condition with rigorous stirring under a nitrogen atmosphere at 343 K. The reaction mixture was then condensed for 3 days in the same condition. The solution was then condensed by evaporation. The reaction product was washed by diethyl ether and a brown powder salt was precipitated. Finally, the salt was washed with diethyl ether several times. The purified product was obtained as a white solid. The product was dried under high vacuum at 308 K for several hours. The compound was characterized by ¹H-NMR and mass spectrometric studies.

$[C_8(mim)_2][Br]_2$: ¹H-NMR(DMSO-d₆): 2H(9.24 ppm, s), 2H(7.78 ppm, s), 2H(7.70 ppm, s), 4H(4.14 ppm, t), 6H(3.82 ppm, s), 4H(1.73 ppm, m), 8H(1.22 ppm, b)

$[C_8(mim)_2][NTf_2]_2$: $[C_8(mim)_2][Br]_2$ (1 mmol) was dissolved in water and aqueous lithium bis(trifluoromethylsulfonyl)amide (2.1 mmol) solution was gradually added to the solution. The mixture was stirred at room temperature for 1 day, the aqueous solution was decanted. The ionic

liquid layer was dissolved in ethyl acetate and washed with water several times. The organic layer was dried with anhydrous Na_2SO_4 , and filtered to remove the dry agent. After the solvent was evaporated, the residue was mixed with activated charcoal in acetonitrile. The activated charcoal was removed by filtration, and the solvent was evaporated. This decolorizing charcoal step was repeated 3-4 times. The ionic liquid was then dried under high vacuum at 308 K for 3 days. The product was a colorless liquid. The compound was characterized by $^1\text{H-NMR}$ and mass spectrometric studies.

$[\text{C}_8(\text{mim})_2][\text{NTf}_2]_2$: $^1\text{H-NMR}(\text{DMSO-}d_6)$: 2H(9.02 ppm, s), 2H(7.69 ppm, s), 2H(7.64 ppm, s), 4H(4.08 ppm, t), 6H(3.79 ppm, s), 4H(1.71 ppm, m), 8H(1.21 ppm, b)

ESI -MS (+ve): 556 m/z, $[\text{C}_8(\text{mim})_2\text{NTf}_2]^+$

4.2.2.2. Synthesis of 1,9-Bis(3-methylimidazolium-1-yl)nonane bis-(trifluoromethylsulfonyl)-amide ($[\text{C}_9(\text{mim})_2][\text{NTf}_2]_2$)

1,9-bis(3-methylimidazolium-1-yl)nonane bromide, $[\text{C}_9(\text{mim})_2][\text{Br}]_2$: 1,9-Dibromononane (1 mmol) was added drop wise to an acetonitrile solution of 1-methylimidazole (2.2 mmol) in reflux condition with rigorous stirring under a nitrogen atmosphere at 343 K. The reaction mixture was then condensed for 3 days in the same condition. The solution was then condensed by evaporation. The residue was yellow oil. Next, the oil was washed with diethyl ether at several times. Diethyl ether was removed by evaporation, and the oil was mixed with activated charcoal in acetonitrile. The activated charcoal was removed by filtration, and the solvent was evaporated. This decolorizing charcoal step was repeated 2-3 times. The product was dried under high vacuum at 308 K for several hours. The compound was characterized by $^1\text{H-NMR}$ and mass spectrometric studies.

[C₉(mim)₂][Br]₂: ¹H-NMR(DMSO-d₆): 2H(9.21 ppm, s), 2H(7.78 ppm, s), 2H(7.69 ppm, s), 4H(4.12 ppm, t), 6H(3.81 ppm, s), 4H(1.72 ppm, m), 10H(1.20 ppm, b)

[C₉(mim)₂][NTf₂]₂: [C₉(mim)₂][Br]₂ (1 mmol) was dissolved in water and aqueous lithium bis(trifluoromethylsulfonyl)amide (2.1 mmol) solution was gradually added to the solution. The mixture was stirred at room temperature for 1 day, the aqueous solution was decanted. The ionic liquid layer was dissolved in ethyl acetate and washed with water several times. The organic layer was dried with anhydrous Na₂SO₄, and filtered to remove the dry agent. After the solvent was evaporated, the residue was mixed with activated charcoal in acetonitrile. The activated charcoal was removed by filtration, and the solvent was evaporated. This decolorizing charcoal step was repeated 3-4 times. The ionic liquid was then dried under high vacuum at 308 K for 3 days. The product was a colorless liquid. The compound was characterized by ¹H-NMR and mass spectrometric studies.

[C₉(mim)₂][NTf₂]₂: ¹H-NMR(DMSO-d₆): 2H(9.03 ppm, s), 2H(7.69 ppm, s), 2H(7.63 ppm, s), 4H(4.08 ppm, t), 6H(3.79 ppm, s), 4H(1.71 ppm, m), 10H(1.20 ppm, b)

ESI -MS (+ve): 570 m/z, [C₉(mim)₂NTf₂]⁺

4.3. Result and Discussion

4.3.1. Steady State Absorption, Emission and EPR Studies

The steady state absorption and emission behaviour of a dipolar solute coumarin 153 (C153) has been investigated in [C₈(mim)₂][NTf₂]₂ and [C₄(mim)][NTf₂]. The absorption and emission spectra of C153 in DIL and MIL are provided in Figure 4.1. No significant change in the absorption spectra of C153 is observed in either the MIL or DIL (Figure 4.1(a)). However, a small blue shift in the absorption of C153 is observed upon changing the solvent from MIL to the DIL (Figure 4.1(a)). Similarly, in the emission spectra, the emission maximum of C153 is

observed to shift towards the blue edge as the solvent is changed from the MIL to DIL (Figure 4.1(b)). For example, the emission maxima of C153 in DIL and MIL are found to be 519 nm and 527 nm respectively. In this context, we would like to mention that Maroncelli and coworkers have observed the emission maxima values of C153 in several imidazolium-based monocationic RTILs within the range of 525 nm to 546 nm.²⁰⁶ Both absorption and emission data demonstrate that $[\text{C}_8(\text{mim})_2][\text{NTf}_2]_2$ is less polar as compared to the monocationic, $[\text{C}_4(\text{mim})][\text{NTf}_2]$. It is interesting to note here that DIL is less polar than MIL despite the fact that DIL is composed of a di-positive cations while MIL contains a mono-positive cation. No significant changes in the absorption and emission behaviour of C153 in $[\text{C}_8(\text{mim})_2][\text{NTf}_2]_2$ and $[\text{C}_9(\text{mim})_2][\text{NTf}_2]_2$ have been observed.

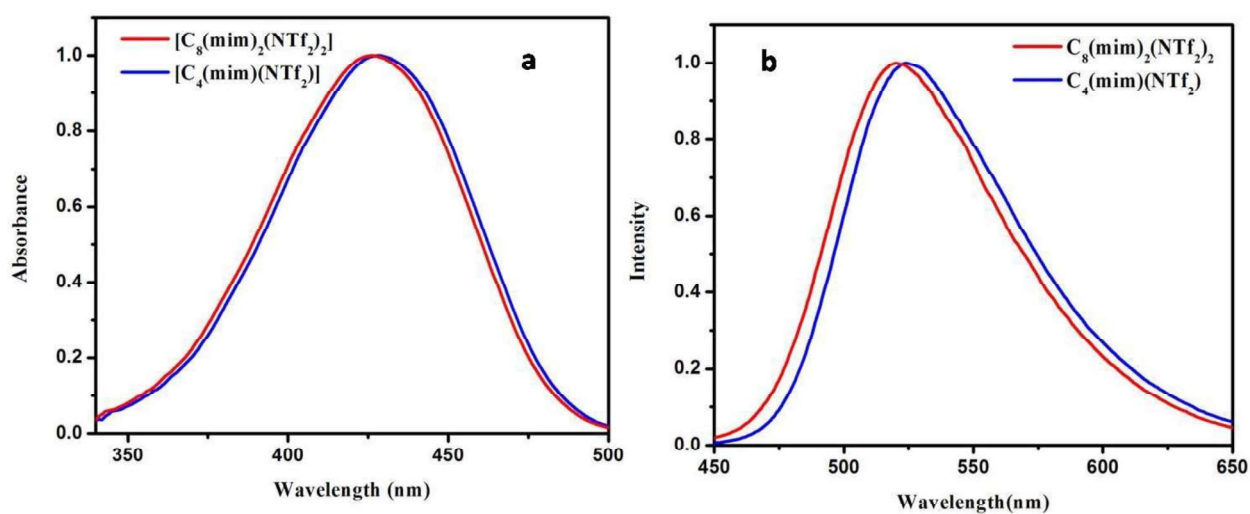


Figure 4.1. Normalized (a) absorption and (b) emission ($\lambda_{exc} = 375$ nm) spectra of C153 in $[\text{C}_8(\text{mim})_2][\text{NTf}_2]_2$ and $[\text{C}_4(\text{mim})][\text{NTf}_2]$.

Since polarity is an important physical attribute of a given solvent, we have made an attempt to get a clearer idea about the polarity of the DILs and MIL through EPR spectroscopy. Basically, we have explored the EPR spectroscopy to estimate the polarity of MIL and DILs by using an EPR active probe TEMPO (2,2,6,6-tetramethylpiperidine-1-oxyl). The free radical

probe TEMPO is a resonance hybrid of a charge transfer (CT) structure,³²² hence, the stability of the CT structure will be dependent on the polarity of the medium.³²² In fact, CT structure is known to be stabilized in polar solvent with an increase the spin density over “N” atom.³²² As a result of this, the hyperfine coupling constant (a_N) of the EPR signal can be correlated with the polarity of the medium.⁷⁸ Therefore, by analyzing the EPR spectra one can estimate the polarity value for a particular solvent. The EPR spectra of TEMPO in DILs and MILs are provided in Figure 4.2. It can be seen from Figure 4.2 that the sigmoidal nature in EPR signal is observed for the DILs (Figure 4.2 (b) and 4.2 (c)) but it is not observed for the MIL (Figure 4.2(a)). This is due to the high viscosity of DIL as compared to that of the MIL (see *vide infra*). Motion of the spin probe is restricted in highly viscous media and anisotropy in the EPR signal arises. Moreover, from Figure 4.2, the broadening of the EPR line signal of spin probe can be noticed. We would like to take a note here that RTILs are micro-heterogeneous in nature, and previously it has been demonstrated by Gramp and coworkers^{258, 259} and by us²¹⁴ independently, that EPR line signal of spin probes can be broadened due to the micro-heterogeneous nature of RTILs.

In the case of spectral broadening, calculating a_N values from the maxima of hyperfine lines could be erroneous. In view of this, in the present data, the a_N values are calculated from the distance between the centre of relevant adjacent hyperfine lines. A calibration curve is generated by plotting hyperfine splitting parameters (a_N/G) against solvent polarity parameter ($E_T(30)$) values for TEMPO in many RTILs with various other organic solvents. The $E_T(30)$ values for various solvents are collected from literature reports,^{61, 323} and from the plot (Figure 4.3), the $E_T(30)$ value for unknown samples (e.g. dicationic and monocationic RTILs) are determined. From the EPR spectral analysis, the $E_T(30)$ value for $[C_8(mim)_2][NTf_2]_2$ and $[C_4(mim)][NTf_2]$ are estimated to be 45.6 and 52.1 respectively (see Table 4.1). From EPR data we can infer that

the polarities of the DIL and MIL are close to those of acetonitrile and ethyl alcohol, respectively.⁶¹ These data also point out that the apolar linker alkyl chain of DILs plays an important role in determining the polarity of the medium.

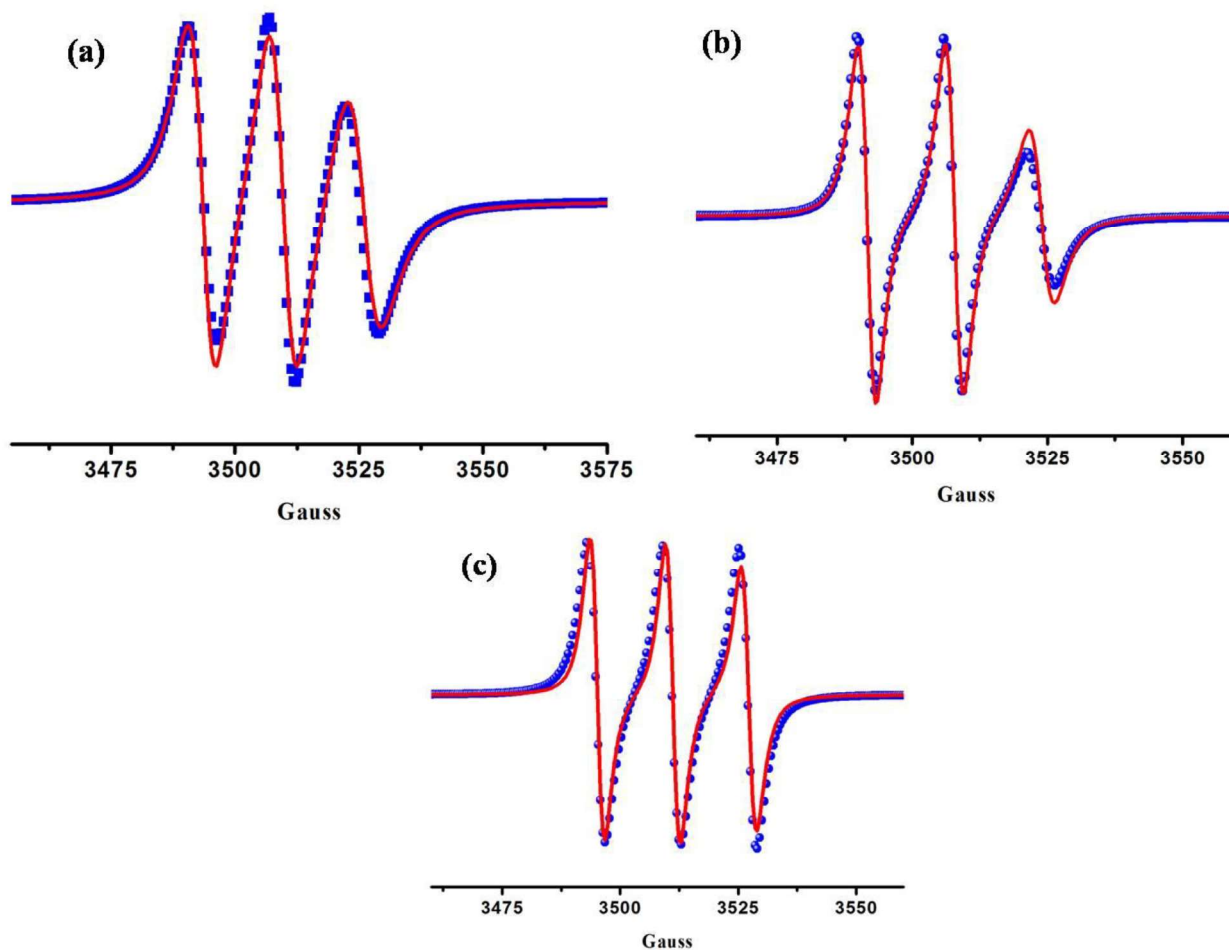


Figure 4.2. EPR spectra of TEMPO (red solid line) in (a) $[C_4(\text{mim})][\text{NTf}_2]$, (b) $[C_8(\text{mim})_2][\text{NTf}_2]_2$ and (c) $[C_9(\text{mim})_2][\text{NTf}_2]_2$. The blue dotted lines indicate the simulated spectra.

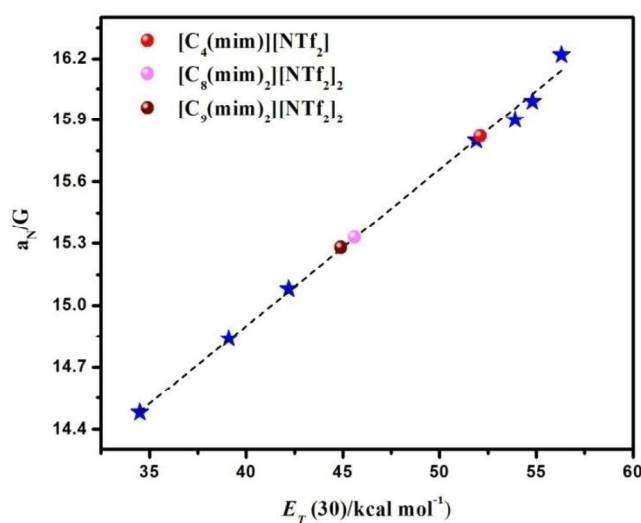


Figure 4.3. Plot of a_N/G vs. $E_T(30)$ values for TEMPO in $[C_8(mim)_2][NTf_2]_2$, $[C_9(mim)_2][NTf_2]_2$ and $[C_4(mim)][NTf_2]$. The stars indicate the values corresponding to the known solvents.

Table 4.1. The a_N/G value of TEMPO in RTILs and molecular solvents and the estimated $E_T(30)$ values

Systems	a_N/G	$E_T(30)$ (kcal mol ⁻¹)
$[C_4(mim)][NTf_2]$	15.82	52.1
$[C_8(mim)_2][NTf_2]_2$	15.33	45.6
$[C_9(mim)_2][NTf_2]_2$	15.28	44.9
$[C_4(mim)] [PF_6]$	15.99	54.8 ^a
$[C_4(mim)][BF_4]$	15.90	53.9 ^a
Benzene	14.48	34.5 ^a
Ethylene glycol	16.22	56.3 ^b
Chloroform	14.84	39.1 ^b
Acetone	15.08	42.2 ^b
Ethyl alcohol	15.80	51.9 ^{a,b}

^aReference 323, ^bReference 61

As stated earlier, the RTILs are micro-heterogeneous in nature.⁸⁵⁻⁹¹ It has also been demonstrated that many interesting physiochemical attributes of RTILs can be linked to the micro-heterogeneous nature of the medium.^{85-91, 113, 114, 160} Therefore, it is important to

understand the micro-heterogeneous behaviour of RTILs. Specifically, we have tried to understand how the micro-heterogeneous nature of DILs is different to that of their monocationic counterpart. Since structural organization of an RTIL is related to the micro-heterogeneity,^{85-91, 113, 114, 160} studies on this aspect would also provide ideas about the structural organization of RTILs. The micro-heterogeneous nature of DILs and MIL has been investigated by following the excitation wavelength dependent fluorescence behaviour of 2-amino-7-nitrofluorene (ANF). ANF is chosen as a probe for this study because of shorter excited state lifetime (~100 ps).¹⁶⁰ So the fluorescence signature of ANF in RTILs is expected to be more responsive to those short-lived domains^{177, 316} that might be created upon structural organization of RTILs. In this context, we would like to note that if there are energetically different solvated species in the ground state and the rate of energy transfer between them is slow, then instead of obeying Kasha's rule²³⁷ the emission maximum of fluorescent solute is observed to shift gradually towards the low energy (red) region with an increase in the excitation wavelength (λ_{exc}). This type of behaviour is known as the red-edge-effect (REE).^{238, 239} This study can not predict the exact length scale of heterogeneity but it can certainly provide qualitative idea about the micro-heterogeneous nature of the medium. The excitation wavelength dependent fluorescence behavior of ANF in $[C_8(mim)_2][NTf_2]_2$ and $[C_4(mim)][NTf_2]$ is displayed in Figure 4.4. In the present study, when the samples are excited from 400 nm-480 nm region, the total shift in the emission maximum of ANF are observed to be 11 nm, 12 nm and 6 nm for $[C_8(mim)_2][NTf_2]_2$, $[C_9(mim)_2][NTf_2]_2$ and $[C_4(mim)][NTf_2]$ respectively (see Figure 4.4). Therefore, the total shift of emission maxima of ANF is observed to be significantly larger in $[C_8(mim)_2][NTf_2]_2$ than that for $[C_4(mim)][NTf_2]$. The difference in the total shift of emission maxima values for the DILs and MIL indicates that the structural organization of DILs and MIL is different. In this context, we would like to

mention that in a previous study²⁸⁶ of a DIL, 1,6-bis-(3-methylimidazolium-1-yl)hexane bis-(trifluoromethylsulfonyl)amide ($[\text{C}_6(\text{mim})_2][\text{NTf}_2]_2$), which has two imidazolium rings and a 6-membered alkyl linker chain, we have shown that the total shift in the emission maxima for ANF was ~ 8 nm when the samples were excited in the 400-480 nm region. Since in the current study the shift in emission maxima for ANF in octyl linker chain-containing DIL ($[\text{C}_8(\text{mim})_2][\text{NTf}_2]_2$) is ~ 11 nm, we can say that a greater shift in the emission maxima is observed upon increase the alkyl linker chain for the DILs. As the cation ring is fixed in both of these cases only the alkyl linker chain length varies, and the present data also indicate that linker alkyl chain length plays an important role in determining the micro-heterogeneous behaviour of DILs.

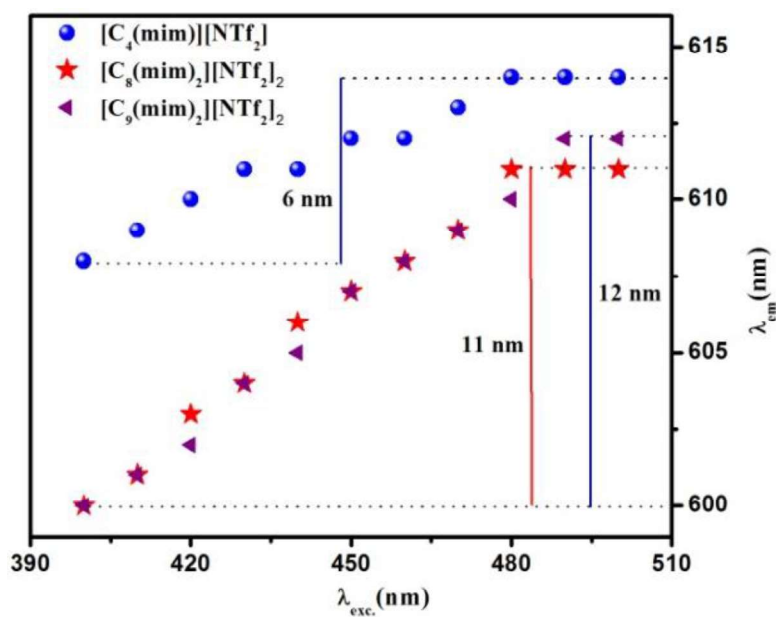


Figure 4.4. Excitation wavelength dependent emission behavior of ANF in $[\text{C}_8(\text{mim})_2][\text{NTf}_2]_2$ and $[\text{C}_4(\text{mim})][\text{NTf}_2]$.

4.3.2. Studies on Rotational Diffusion through EPR and Time-Resolved Fluorescence

Anisotropy Study: Studies on rotational diffusion can provide important information about solvent-solvent and solute-solvent interaction and thus can provide a better idea about the microenvironment of the media.²⁴⁶ Such studies with regard to understanding the media are also

important in a sense that proper understanding of the solvent-solvent and solute-solvent interactions, and the factors that affect them, is essential as these factors are also associated with chemical reactivity.²⁴⁶

4.3.2.1. EPR Studies

Since for most spin probes the line shape for EPR signal is the convolution of Lorentzian and Gaussian functions,⁷⁸ proper care must be taken during the analysis of the EPR spectrum. The EPR spectra in the present data were simulated by considering by both Lorentzian and Gaussian functions.⁷⁸ EPR studies have been investigated to understand the microenvironment of the RTILs by determining the rotational correlation time (τ_r) of the EPR active probe TEMPO in both DILs and MIL. The rotational time (τ_r) is calculated for TEMPO in DILs and MIL by analyzing the EPR spectral data of the DILs and MIL by following a reported procedure.^{324, 325} The τ_r can be calculated by using the following equation 4.1³²⁶

$$\tau_r = 1.27 \times 10^{-9} B(\text{corr}) \quad (4.1)$$

$B(\text{corr})$ is calculated by using the following equation

$$B(\text{corr}) = QSB(\text{uncorr}) \quad (4.2)$$

$B(\text{uncorr})$ is calculated by using the following equation

$$B(\text{uncorr}) = 0.5\Delta H(0) \left[\sqrt{\frac{I_0}{I_{+1}}} - \sqrt{\frac{I_0}{I_{-1}}} \right] \quad (4.3)$$

where $\Delta H(0)$ is the width of the central EPR line. I_0 , I_{+1} and I_{-1} are the intensities of the central, right, and left EPR lines, respectively. The $\Delta H(0)$, I_0 , I_{+1} and I_{-1} were obtained from the simulated EPR spectra (Figure 4.2). Q and S are obtained via the following relationships

$$Q = \left[-1 + \sqrt{(1 + 4\chi^2)} \right] / 2\chi^2 \quad (4.4)$$

$$S = (1 + 1.78\chi + 1.85\chi^2) / (1 + 2.08\chi)\chi \quad (4.5)$$

where χ is the Voigt parameter determined by the four-point line shape analysis method, following the reported procedure proposed by Bales.³²⁶ From the τ_r value one can calculate the diffusion coefficient (D) by using the following relation given below.

$$\tau_r = \frac{1}{6D} \quad (4.6)$$

The rotational time (τ_r) for TEMPO in the DILs and MIL are provided in Table 4.2. The τ_r values for TEMPO in $[C_8(\text{mim})_2][\text{NTf}_2]_2$ and $[C_4(\text{mim})][\text{NTf}_2]$ are found to be 0.26 ns and 0.11 ns respectively. This may happen due to the higher viscosity of DILs than that of MIL. Interestingly, even though the viscosity is increased ~ 14 times from MIL to DILs at a particular temperature (see Table 4.3), the rotational times increase only ~ 2.3 times from the MIL to DILs. The results have demonstrated that the increase in τ_r from the MIL to DILs is not linear with increase in the viscosity value from the MIL to DILs. This data, i.e. the non linear dependence of τ_r with medium viscosity, further suggests that the structural organization of MILs and DILs are different.

Table 4.2. Rotational correlation time (τ_r) and rotational diffusion coefficient (D) for TEMPO in $[C_8(\text{mim})_2][\text{NTf}_2]_2$, $[C_9(\text{mim})_2][\text{NTf}_2]_2$ and $[C_4(\text{mim})][\text{NTf}_2]$

Systems	τ_r (ns)	D (ns ⁻¹)
$[C_4(\text{mim})][\text{NTf}_2]$	0.11	1.51
$[C_8(\text{mim})_2][\text{NTf}_2]_2$	0.26	0.64
$[C_9(\text{mim})_2][\text{NTf}_2]_2$	0.29	0.59

4.3.2.2. Time-Resolved Fluorescence Anisotropy Study

A time-resolved fluorescence anisotropy study carried out by employing organic dye molecules often helps to get a deeper insight into the microscopic behavior of a given medium.^{183, 184, 189, 195, 196} In the present study, rotational diffusion of two organic solutes, perylene and MPTS, has been investigated in two DILs and one MIL at various temperatures. The difference in the rotational motion of two structurally similar but chemically distinguishable solutes in a particular medium can provide valuable information on solute-solvent interactions in particular and the behavior of the medium in general.^{184, 189, 195}

4.3.2.2.1. Perylene. The temperature dependent viscosities of the DILs and MIL are collected in the temperature range 293-318 K (Table 4.3). It can be seen from Table 4.3 that the viscosity increases upon going from MIL to DIL. The temperature dependence of viscosity for both of the DILs and MIL can be fitted by Vogel-Tammann-Fulcher (VTF) relation (Figure 4.5).³²⁷ The fluorescence anisotropy decay profiles of perylene in $[C_8(mim)_2][NTf_2]_2$ and $[C_4(mim)][NTf_2]$ are provided in Figure 4.6 and the rotational relaxation parameters are collected in Table 4.3. Figure 4.6 and Table 4.3 depict that at a particular temperature, the rotational time (τ_r) of perylene is higher in $[C_8(mim)_2][NTf_2]_2$ than that in $[C_4(mim)][NTf_2]$. This is due to the higher viscosity of DILs. The decrease in the rotational time (τ_r) of the solute in both the DILs and the MIL with increasing temperature can be attributed to the decrease in the viscosity of the medium. For example, the τ_r values for perylene in $[C_8(mim)_2][NTf_2]_2$ at 293 K and 318 K are found to be 4.83 ns and 2.28 ns, respectively. Interestingly, from careful inspection of the τ_r values upon going from MIL to the DILs, one can see that at a particular temperature, the increase in τ_r value is not as much as what would be expected from the increase in the viscosity values. For example, upon going from MIL to DILs the viscosity increases by ~ 14 times (see Table 4.3), whereas the

τ_r value increases only by ~ 4 times. This indicates that rotational motion of perylene has become faster in DILs as compared to that in the MIL. The relatively faster rotation of the apolar perylene in the DIL indicates that the solute-solvent interaction in the DILs is relatively less compared to that in the MIL. The rotational times for perylene in $[\text{C}_8(\text{mim})_2][\text{NTf}_2]_2$ and $[\text{C}_9(\text{mim})_2][\text{NTf}_2]_2$ are observed to be very similar.

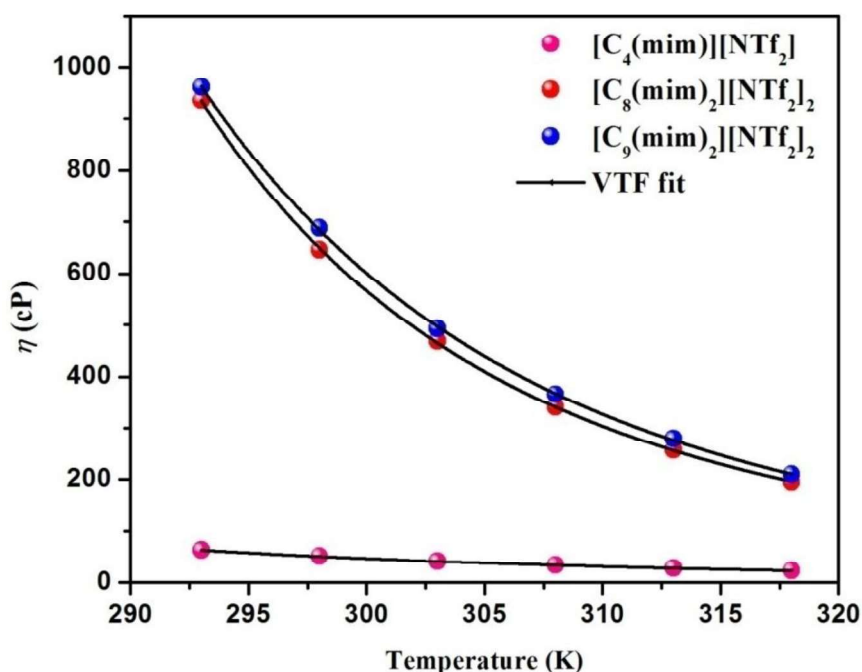


Figure 4.5. Variation of the viscosity of $[\text{C}_8(\text{mim})_2][(\text{NTf}_2)_2]$, $[\text{C}_8(\text{mim})_2][(\text{NTf}_2)_2]$ and $[\text{C}_4(\text{mim})][\text{NTf}_2]$ with temperature and fitting with the VFT equation.

To get a clearer picture of the rotational dynamics of perylene in the DILs and their corresponding MIL, the data have been analyzed through Stokes-Einstein-Debye (SED) hydrodynamic theory.^{239, 247} The van der Waals volumes (V), shape factors (f) and C_{slip} for perylene are collected from the literature data (Table 4.4).^{189, 225, 316} From the values of C_{slip} and f , the theoretical τ_r^{slip} and τ_r^{stk} for perylene in all of these RTILs are estimated.

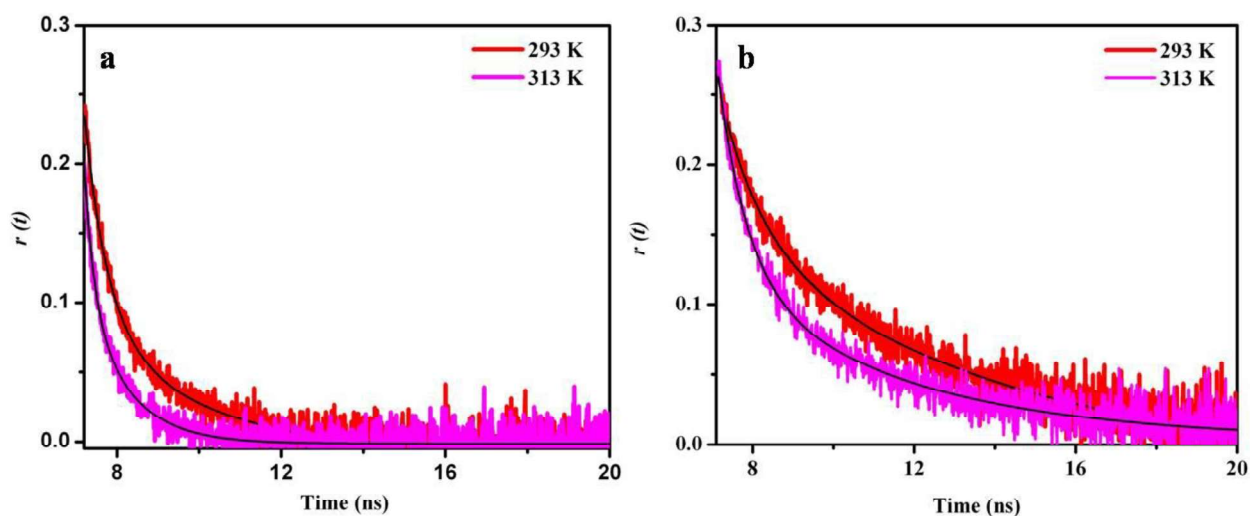


Figure 4.6. Anisotropy decay of perylene in (a) $[C_4(\text{mim})][\text{NTf}_2]$ and (b) $[C_8(\text{mim})_2][\text{NTf}_2]_2$. The time scales of both the figures are same as there is a comparison of monocationic and dicationic ILs.

Table 4.3. Reorientation time (τ_r) and viscosity (η) of perylene and MPTS in $[C_4(\text{mim})][\text{NTf}_2]$, $[C_8(\text{mim})_2][\text{NTf}_2]_2$ and $[C_9(\text{mim})_2][\text{NTf}_2]_2$

System	Temp. (K)	Viscosity (cP) ^a	Perylene		MPTS	
			τ_r (ns) ^b	C_{rot}	τ_r (ns) ^b	C_{rot}
$[C_4(\text{mim})][\text{NTf}_2]$	293	63	1.34	0.217	10.60	1.49
	298	51	1.11	0.219	8.51	1.50
	303	41	0.86	0.221	7.02	1.57
	308	34	0.67	0.242	5.80	1.59
	313	28	0.59	0.260	5.02	1.70
	318	23	0.52	0.262	4.12	1.72
$[C_8(\text{mim})_2][\text{NTf}_2]_2$	293	935	4.83	0.054	44.10	0.417
	298	646	4.12	0.069	34.08	0.474
	303	468	3.36	0.082	26.98	0.528
	308	341	3.10	0.112	20.12	0.546
	313	257	2.64	0.126	17.02	0.627
	318	195	2.28	0.138	13.06	0.643
$[C_9(\text{mim})_2][\text{NTf}_2]_2$	293	961	5.16	0.052	47.04	0.433
	298	688	4.28	0.063	37.11	0.484
	303	493	3.48	0.071	30.06	0.557
	308	366	3.12	0.091	22.97	0.586

313	279	2.78	0.106	19.00	0.648
318	210	2.32	0.122	14.32	0.650

^aExperimental error= $\pm 2\%$, ^bExperimental error= $\pm 5\%$

Table 4.4. Van der Waals volumes (V), shape factors (f) and boundary condition parameter (C_{slip}) of perylene and MPTS

Solute	$V (\text{\AA}^3)$	f	C_{slip}
perylene	225	1.76	0.085
MPTS	343	1.33	0.11

The $\log(\tau_r)$ vs. $\log(\eta/T)$ plots for perylene in DILs and MIL are provided in Figure 4.7. Figure 4.7 reveals that rotation of perylene in both the DILs is relatively faster than that in MIL, and it goes beyond the slip limit in DILs. As per hydrodynamic terminology, the faster rotation of perylene in the DILs is known as subslip behavior.^{192, 195} For example, at larger value of $\log(\eta/T)$, C_{rot} (0.05 at 293 K) for perylene is estimated ~ 2 times lower than the value ($C_{slip}=0.085$) predicted by SED theory. Since, $C_{rot}=\tau_r^{exp}/\tau_r^{stk}$, (τ_r^{exp} and τ_r^{stk} are the experimental and theoretically calculated rotational times, respectively) C_{rot} can provide an idea about solute-solvent coupling. It is evident from Figure 4.7 that the experimentally estimated reorientation times of perylene in the DILs and corresponding MIL lie between the theoretically predicted stick and slip limits. This observation indicates that no specific interaction like hydrogen bonding interaction are present between the solute and the RTILs. Nevertheless, a clear difference in the rotational behavior of perylene in the DILs and MIL has been observed.

To understand better, the rotational behavior of perylene in a monocationic RTIL, 3-methyl-1-octyl-imidazoliumbis(trifluoromethylsulfonyl)amide ([C₈(mim)][NTf₂]) is also investigated (Table 4.5 and Figure 4.8). It can be observed that the rotational behaviour of perylene in [C₈(mim)][NTf₂] is relatively hindered as compared that in DILs. The experimental rotational

time is observed to lie in between stick and slip lines (Figure 4.8). This also further suggests that the solute-solvent interactions in the MIL and DILs are quite different.

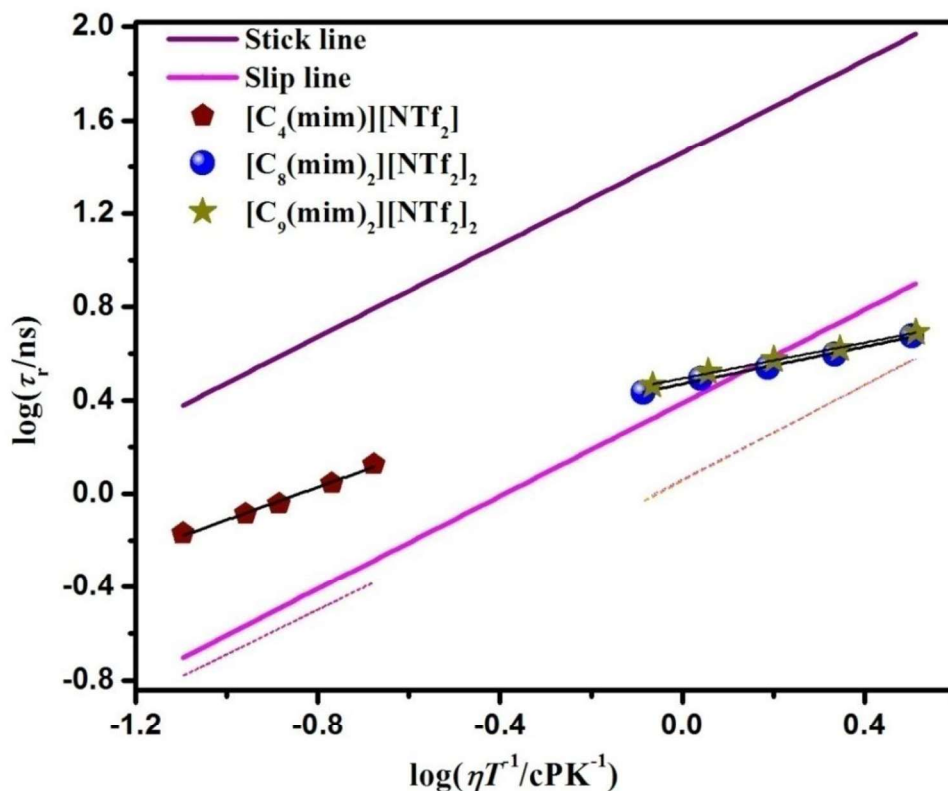


Figure 4.7. $\log(\tau_r)$ vs. $\log(\eta/T)$ plot of perylene in DILs and MIL with stick and slip boundary condition limits. Dotted pink, orange and violet line corresponds to DKS line for $[\text{C}_4(\text{mim})][\text{NTf}_2]$, $[\text{C}_8(\text{mim})_2][\text{NTf}_2]_2$ and $[\text{C}_9(\text{mim})_2][\text{NTf}_2]_2$ respectively. The solid black lines indicate fit to the data points.

Table 4.5. Reorientation time (τ_r) and viscosity (η) of perylene and MPTS in $[\text{C}_8(\text{mim})][\text{NTf}_2]$

System	Temp. (K)	Viscosity (cP) ^a	Perylene		MPTS	
			τ_r (ns) ^b	C_{rot}	τ_r (ns) ^b	C_{rot}
$[\text{C}_8(\text{mim})][\text{NTf}_2]$	293	109	1.72	0.16	18.32	1.48
	298	83	1.43	0.18	14.02	1.50
	303	65	1.24	0.20	11.10	1.54
	308	54	1.10	0.22	9.16	1.56

^aExperimental error = $\pm 2\%$, ^bExperimental error = $\pm 5\%$

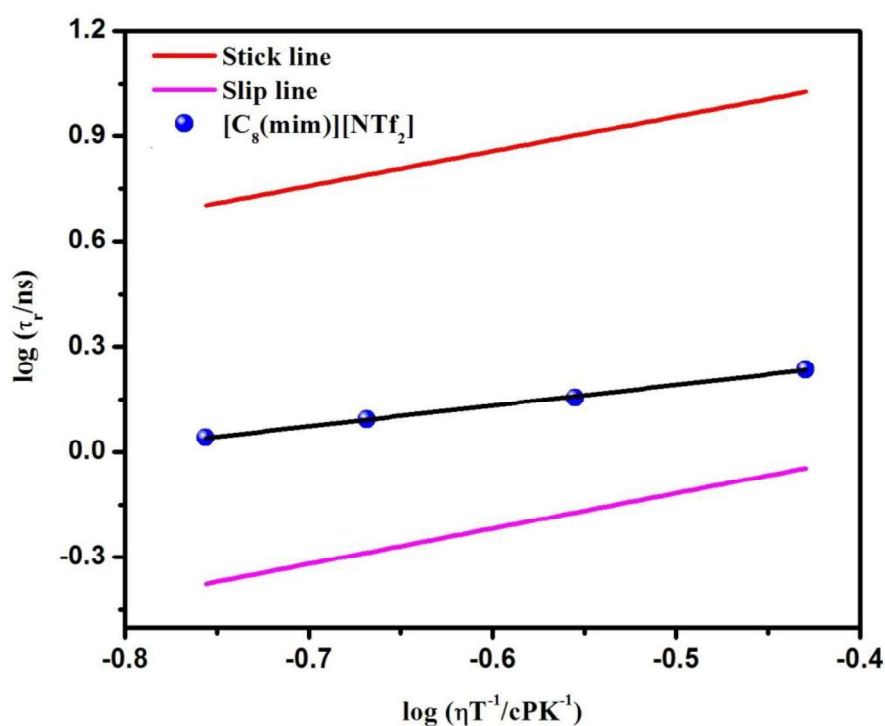


Figure 4.8. $\log(\tau_r)$ vs. $\log(\eta/T)$ plot of perylene in $[C_8(\text{mim})][\text{NTf}_2]$ with stick and slip boundary condition limits.

Again, the faster rotation of perylene can be evident, when we plot τ_r vs. η/T to an empirical relation $\tau_r = A(\eta/T)^n$, where, A and n are constant.^{183, 189, 192} The exponent, n denotes the nonlinearity of the τ_r vs. η/T plot. Thus, departure of n values from the unity can be attributed to the decoupling of diffusion motion of solute from the viscosity of the medium.^{183, 189, 192} We have earlier shown that this viscosity-diffusion coupling can be caused due to the micro-heterogeneous nature of the medium.¹⁸³

Perylene in $[C_4(\text{mim})(\text{NTf}_2)]$

$$(3.89 \pm 0.03)(\eta/T)^{0.70 \pm 0.036} \quad (\text{N}=5, \text{R}=0.98)$$

Perylene in $[C_8(\text{mim})_2][\text{NTf}_2]_2$

$$(2.95 \pm 0.01)(\eta/T)^{0.39 \pm 0.016} \quad (\text{N}=5, \text{R}=0.99)$$

Perylene in $[C_9(\text{mim})_2][\text{NTf}_2]_2$

$$(3.04 \pm 0.01)(\eta/T)^{0.38 \pm 0.016} \quad (\text{N}=5, \text{R}=0.98)$$

It can be observed from the above fitting that n deviates more from unity in $[\text{C}_8(\text{mim})_2][\text{NTf}_2]_2$ than that in $[\text{C}_4(\text{mim})][\text{NTf}_2]$. These results corroborate our previous observations from excitation wavelength dependent emission measurements that $[\text{C}_8(\text{mim})_2][\text{NTf}_2]_2$ is a more micro-heterogeneous nature than $[\text{C}_4(\text{mim})][\text{NTf}_2]$.

We have further estimated the rotational coupling constant (C_{rot}) by using equation 1.1. The C_{rot} is expressed as $C_{rot} = \tau_r^{exp} / \tau_r^{stk}$ (τ_r^{exp} and τ_r^{stk} are the experimental and theoretically calculated rotational times, respectively), and hence can be correlated to solute-solvent interactions. The average C_{rot} values for perylene in $[\text{C}_8(\text{mim})_2][\text{NTf}_2]_2$ and $[\text{C}_4(\text{mim})][\text{NTf}_2]$ are observed to be 0.10 and 0.24, respectively. The lower C_{rot} value for perylene in $[\text{C}_8(\text{mim})_2][\text{NTf}_2]_2$ also indicates the relatively faster rotation of perylene in the DILs. Here, we note that the rotational diffusion behavior of a given solute can be explained successfully by SED theory when the sizes of both the solvent and solute molecule are comparable.^{239, 247} However, it fails to describe the rotational behavior of a solute molecule for larger size solvent molecule.^{189, 195} Since in the present study the rotational diffusion behavior of perylene in relatively larger solvent (DIL) is not adequately explained by SED analysis (Figure 4.7), we resorted to quasi-hydrodynamic theories (Gierer-Wirtz (GW) and Dote-Kivelson-Schwartz (DKS) theory) to explain this behaviour.^{248, 249} At first, we analyzed our data by employing GW theory,²⁴⁸ which take into consideration both the size of the solvent and solute molecules. The boundary condition parameter (C_{GW}) is modified by using the following equation

$$C_{GW} = \sigma C_0 \quad (4.7)$$

where σ = sticking factor, denoted by the following equation

$$\sigma = \left[1 + 6 \left(\frac{V_S}{V_P} \right)^{1/3} C_0 \right]^{-1} \quad (4.8)$$

and C_0 is given by following equation 4.9

$$C_0 = \left[\frac{6\left(\frac{V_S}{V_P}\right)^{1/3}}{\left[1+2\left(\frac{V_S}{V_P}\right)^{1/3}\right]^4} + \frac{1}{\left[1+4\left(\frac{V_S}{V_P}\right)^{1/3}\right]^3} \right]^{-1} \quad (4.9)$$

where V_S and V_P is the van der Waals volume of the solvent and solute, respectively. The van der Waals volume for $[C_8(\text{mim})_2][\text{NTf}_2]_2$ and $[C_4(\text{mim})][\text{NTf}_2]$ are $356 \text{ cm}^3/\text{mol}$ and $209 \text{ cm}^3/\text{mol}$, respectively.⁴⁶ However, in the present case, the C_{GW} (calculated boundary condition parameter using GW theory) is estimated to be 0.11 for $[C_8(\text{mim})_2][\text{NTf}_2]_2$, which is higher than the value predicted by SED theory ($C_{slip}=0.085$). This means that GW theory is unable to explain the faster rotation of perylene in the DILs. In order to explain this behavior, the data has been analyzed further by using the DKS model²⁴⁹ and the boundary condition parameters are modified using equation 3.1. Please note that the DKS theory takes into consideration both the size of solvent and solute molecule as well as the free space created between solute and the solvent molecule.²⁴⁹ The $\log(\tau_r)$ vs $\log(\eta/T)$ plots of perylene with their modified boundary condition (obtained from the DKS) in DILs and MIL are also provided in Figure 4.7. It can be seen from Figure 4.7, that DKS theory is quite successful in explaining the faster rotation of perylene in DILs (larger solvent system). Hence, the present data demonstrates that the rotational behavior of perylene is significantly affected by the size of the solvent molecule and the faster rotation of perylene can be explained by considering the fact that larger size of solvent (DILs) offers lower friction to the rotating solute.

Again, please note that in the current study, the average C_{rot} for perylene in $[C_8(\text{mim})_2][\text{NTf}_2]_2$ and $[C_9(\text{mim})_2][\text{NTf}_2]_2$ are estimated to be 0.10 and 0.08, respectively. Earlier we have shown that the average C_{rot} value for perylene in $[C_6(\text{mim})_2][\text{NTf}_2]_2$ is 0.13.³¹⁶ Comparison of average coupling constant values in the DILs indicates that the average C_{rot} value for perylene is decreased as the alkyl chainlength of DILs is increased. Here, we note that previously, the slip

and subslip behavior of several nondipolar probe has been observed in alkyl chain containing imidazolium based monocationic RTILs.^{189, 191, 195} The faster rotation of a nondipolar solute 9-phenylanthracene with an increase in the alkyl chainlength of imidazolium-based monocationic RTILs has been reported by Dutt and coworker.¹⁹¹ Recently, Fayer and coworker have demonstrated the subslip behavior of perylene in monocationic RTILs.¹⁸⁹ The subslip behavior of perylene in MILs has been explained by considering the fact that perylene is located close to the longer nonpolar alkyl chain, and larger solvent molecule induces lower friction to the rotating solute molecule.¹⁸⁹ Thus, the present data also suggest that nonpolar perylene is located in the nonpolar region (i.e. alkyl linker chain) of DILs.

4.3.2.2.2. MPTS. The anisotropy decay behavior for MPTS (having sulfate anions) is also investigated in DILs and MIL, and the rotational relaxation parameters for MPTS are collected in Table 4.3. Quite interestingly, the data in Table 4.3 reveals that unlike perylene, the rotational behavior of MPTS is much hindered in both the MIL and DILs. This indicates that solute-solvent interaction is relatively stronger for MPTS than that for perylene in the concerned RTILs. This data also indicates that the locations of MPTS in RTILs are very different from those of perylene in those RTILs.

To get further insights into the MPTS-MIL and MPTS-DIL interaction, we have analyzed the rotational diffusion data of MPTS in light of SED theory. The van der Waals volumes, shape factors and C_{slip} for MPTS are collected in Table 4.4. The log-log plot of τ_r vs. η/T of MPTS along with the stick and slip lines are provided in Figure 4.9. It can be observed from the plot in Figure 4.9 that the experimental rotational times of MPTS lie above the stick line in $[C_4(mim)][NTf_2]$. However, the experimental rotational time of MPTS is observed to lie just below stick boundary line in both $[C_8(mim)_2][NTf_2]_2$ and $[C_9(mim)_2][NTf_2]_2$.

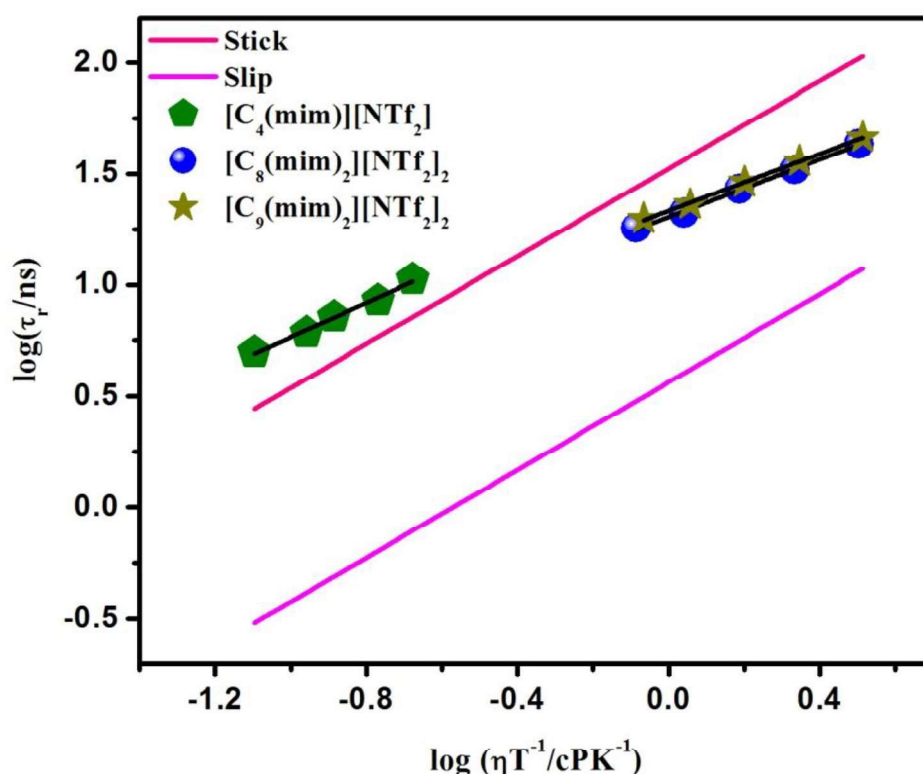


Figure 4.9. $\log(\tau_r)$ vs. $\log(\eta/T)$ plot of MPTS in DILs and MIL with stick and slip boundary condition limits. The solid black lines indicate fit to the data points.

This is an interesting observation in a sense that the rotation of MPTS is relatively hindered in MIL as compared to that in the DILs, despite the fact that viscosity of the DILs is much higher than that of the MIL at a given temperature. The relatively hindered rotation of MPTS in MIL could also be realized when we analyzed our data by estimating the rotational coupling constant (C_{rot}). Usually $C_{rot} = \tau_r^{exp} / \tau_r^{stk}$ can indicate the extent of solute-solvent coupling.^{183, 184, 192, 195} The average C_{rot} values for MPTS in $[C_8(mim)_2][NTf_2]_2$, and $[C_4(mim)][NTf_2]$ are estimated to be 0.58 and 1.62, respectively. The higher C_{rot} value for the MIL as compared to that for the DIL indicates the hindered rotation of MPTS in the MIL. The higher C_{rot} (1.62) value of MPTS in MIL also indicates that the solute is hindered due to specific solute-solvent interactions. As per the hydrodynamic description, the rotation of MPTS in MIL is known as super stick behaviour. The super stick behaviour arises due to the strong interaction between solute and solvent

molecule.^{183, 184, 189, 196, 198, 246} In this context, we would like to mention that when the rotational relaxation behavior of MPTS is also monitored in another MIL, $[C_8(\text{mim})][\text{NTf}_2]$, the MPTS also exhibited hindered rotation (superstick) in that RTIL (Figure 4.10). Here, we note that the presence of strong hydrogen bonding interaction between solute and solvent molecule is known to be the origin of superstick behaviour.^{183, 184, 189, 196, 198, 246} Very recently, we have also seen the presence of strong hydrogen bonding interaction between 7-nitrobenzo-[1,2,5]oxadiazole-4-amine (HNBD) and 1-ethyl-3-methylimidazolium alkyl sulfate RTILs.¹⁸⁴ In this context, we would like to mention that Fruchey and Fayer have seen the superstick behaviour of MPTS in monocationic RTILs.¹⁸⁹ They have demonstrated this behaviour due to strong hydrogen bonding interaction between the C(2) hydrogen of imidazole and the sulfate groups of MPTS. The C(2) hydrogen of imidazole is highly acidic ($\text{pK}_a \sim 23.8$),³⁰³ and is capable of forming hydrogen bonds with the negatively charged probe. Therefore, in the presence case, the hindered rotation of MPTS can be attributed to the presence of strong hydrogen bonding interactions between MPTS and the MIL. The lower C_{rot} value in the DILs as compared to that in the MIL indicates that MPTS-DIL interaction is relatively less as compared to that of MPTS-MIL. The lower solute solvent interaction in the DILs, despite the fact that DILs have two imidazolium rings with two acidic C(2) hydrogens, indicates that the structural organization of DILs may be very different to that of the MIL, which eventually makes rotation of MPTS in the DILs faster. In this context, we would like to mention that through molecular dynamics (MD) simulations Cummings and coworkers¹⁵⁴ have predicted that the medium-/long linker chain containing DILs may exist in folded form. They have also said that because of this structural arrangement two anions becomes available for each imidazolium cation. Very recently, Palchowdhury et. al.¹⁵⁵ has also observed the folded structure for alkyl linker chain containing DILs. A schematic model is given (Scheme

4.1) to understand the structural organization of DILs. The model is proposed based on the above theoretical studies.^{154, 155}

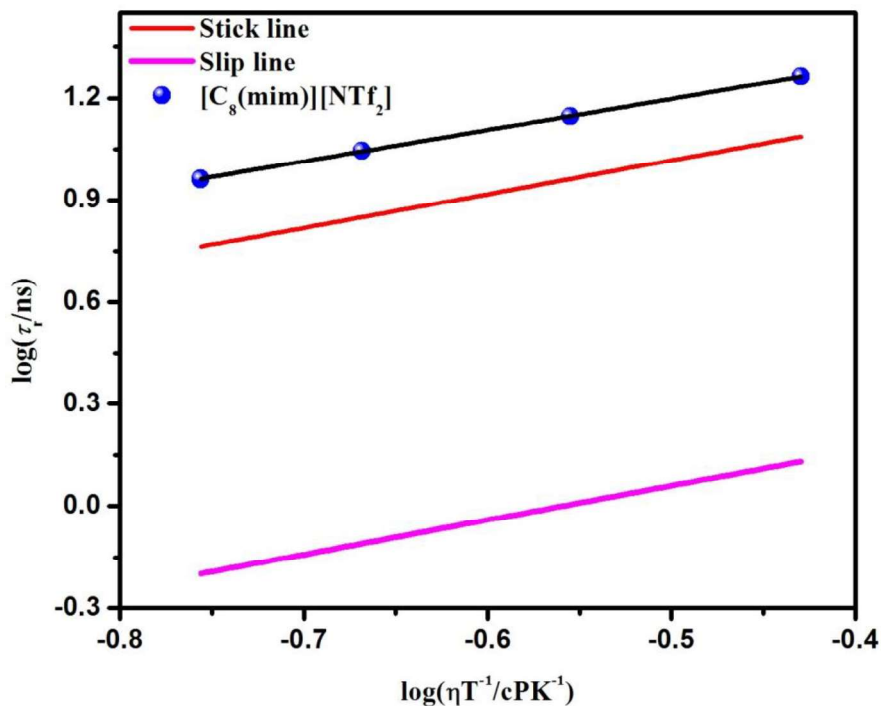
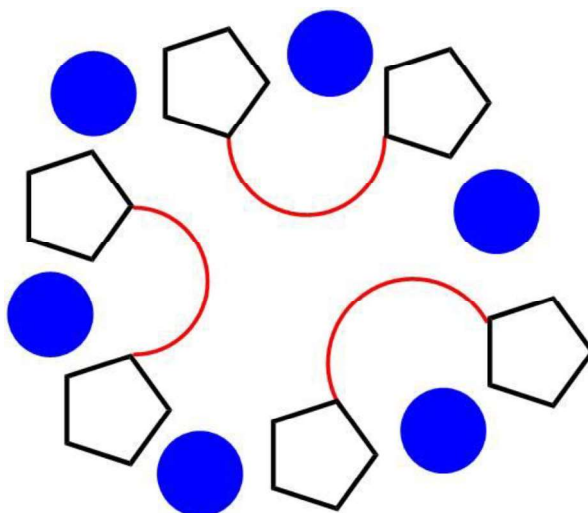


Figure 4.10. $\log(\tau_r)$ vs. $\log(\eta/T)$ plot of MPTS in $[C_8(\text{mim})][\text{NTf}_2]$ with stick and slip boundary condition limits.



Scheme 4.1. Schematic representation of long linker chain DILs in folded form.¹⁵⁴ The blue dots represent the anions, red lines are the alkyl linker chains and black rings are the cations.

In the present study we have also made an attempt to get an idea about structural organization of DIL and MIL by measuring the diffusion coefficient (D) through NMR spectroscopy. Basically, the translational diffusion coefficient (D) of imidazolium cationic moieties are estimated for neat $[\text{C}_8(\text{mim})_2][\text{NTf}_2]_2$ and $[\text{C}_4(\text{mim})][\text{NTf}_2]$. Here we would like to note that the diffusional motion of ions in RTILs is jumplike.^{180, 328-330} The factors that influence the D are mainly the mass, shape and size of cations and anions of the RTILs, apart from this the cation-anion interaction and the structural organization also influence the diffusion coefficient.³³⁰ The translational diffusion coefficient at different temperatures for $[\text{C}_8(\text{mim})_2][\text{NTf}_2]_2$ and $[\text{C}_4(\text{mim})][\text{NTf}_2]$ are provided in Table 4.6. The translational diffusion coefficients for DIL and MIL are found to be $0.201 \times 10^{-11} \text{ m}^2/\text{s}$ and $4.98 \times 10^{-11} \text{ m}^2/\text{s}$, respectively at 298 K (Table 4.6). The lower diffusion coefficient for $[\text{C}_8(\text{mim})_2][\text{NTf}_2]_2$ as compared to $[\text{C}_4(\text{mim})][\text{NTf}_2]$ is due to the higher viscosity of the former than the later. We have further analyzed our data by using SE theory.²⁷¹ As per SE theory, the slope of D versus T/η is given by $k/(6\pi R)$, where K is boltzman constant and R = hydrodynamic radius. Therefore, a steeper slope would indicate the smaller hydrodynamic radius. In this study, the slopes for $[\text{C}_8(\text{mim})_2][\text{NTf}_2]_2$ and $[\text{C}_4(\text{mim})][\text{NTf}_2]$ are estimated (from Figure 4.11) to be $0.67 \text{ JK}^{-1}\text{m}^{-1}$ and $0.45 \text{ JK}^{-1}\text{m}^{-1}$, respectively. It is fascinating to note that the slope is found to be the steepest for $[\text{C}_8(\text{mim})_2]^{2+}$ ($0.67 \text{ J K}^{-1} \text{ m}^{-1}$), though the cation is biggest in the DIL. The small hydrodynamic radius for $[\text{C}_8(\text{mim})_2]^{2+}$ perhaps also indicates that DIL in the experimental condition exists in folded form. Considering the previously mentioned recent theoretical works^{154, 155} and the outcome of the current NMR investigation, we may perhaps say that due to the structural restriction of the DIL, it becomes difficult for bulky MPTS to make stronger hydrogen bonding interaction with DILs. These results demonstrate that the structural organization of DILs and MILs are significantly different.

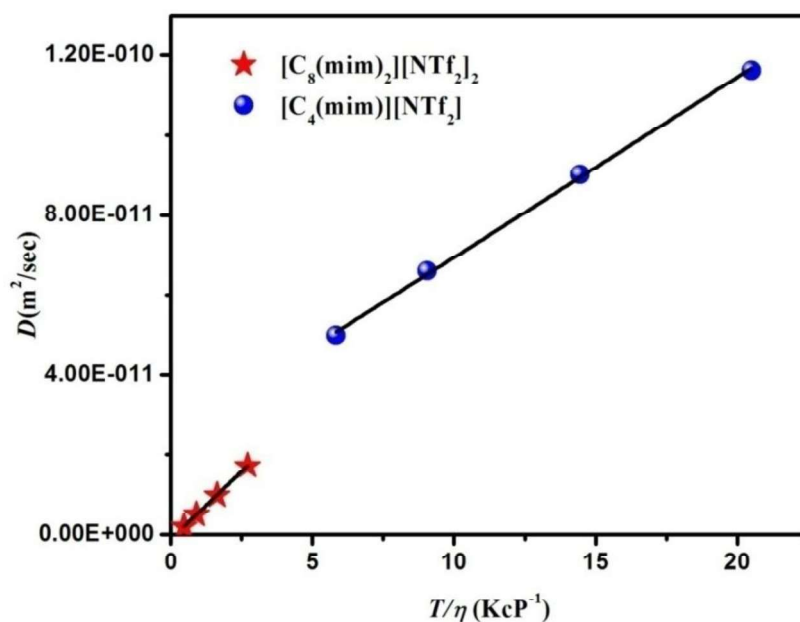


Figure 4.11. Plot of diffusion coefficient (D) vs. T/η for $[\text{C}_8(\text{mim})_2][\text{NTf}_2]_2$ and $[\text{C}_4(\text{mim})][\text{NTf}_2]$. The solid black lines indicate fit to the data points.

Table 4.6. Translational diffusion coefficient (D) for $[\text{C}_8(\text{mim})_2][\text{NTf}_2]_2$ and $[\text{C}_4(\text{mim})][\text{NTf}_2]$ through NMR spectroscopy

Systems	Temp. (K)	D (m ² /s)
[C ₄ (mim)][NTf ₂]	298	4.98×10^{-11}
	308	6.60×10^{-11}
	318	9.02×10^{-11}
	328	11.62×10^{-11}
[C ₈ (mim) ₂][NTf ₂] ₂	298	0.20×10^{-11}
	308	0.50×10^{-11}
	318	0.98×10^{-11}
	328	1.72×10^{-11}

4.3.3. FCS Studies

FCS is a valuable technique and can provide the diffusion coefficient and concentration of fluorescent molecules dissolved in a given solvent.²⁴⁵ As the diffusion coefficient depends on the molecular mass and the shape of the diffusing fluorescent species, measurement of diffusion coefficient of fluorescent species through FCS studies would be helpful to understand the various intermolecular interaction involving the fluorescent molecules.^{159, 184, 185, 202, 203} Keeping this in mind, in the present case, FCS study has been carried out in neat $[\text{C}_8(\text{mim})_2][\text{NTf}_2]_2$ and $[\text{C}_4(\text{mim})][\text{NTf}_2]$. In this study the fluorescence of neat RTILs is monitored.^{185, 202, 203} It is also expected that through this study, idea about microscopic structural organization of RTILs can be obtained. The correlation function for $[\text{C}_8(\text{mim})_2][\text{NTf}_2]_2$ and $[\text{C}_4(\text{mim})][\text{NTf}_2]$ are provided in Figure 4.12 and the data are collected in Table 4.7. The translational diffusion coefficient for $[\text{C}_8(\text{mim})_2][\text{NTf}_2]_2$ and $[\text{C}_4(\text{mim})][\text{NTf}_2]$ are found to be $0.97 \mu\text{m}^2/\text{s}$ and $10.02 \mu\text{m}^2/\text{s}$ respectively. The lower translational diffusion of $[\text{C}_8(\text{mim})_2][\text{NTf}_2]_2$ compared to that of $[\text{C}_4(\text{mim})][\text{NTf}_2]$ is due to the higher viscosity of the medium. The number density of the fluorescent species of $[\text{C}_8(\text{mim})_2][\text{NTf}_2]_2$ and $[\text{C}_4(\text{mim})][\text{NTf}_2]$ in diffusing volume is compared in Table 4.7. Interestingly, the data reveals that the number density of the MIL is higher than that of the DIL. The presence of fewer fluorescing species for DIL than that for the MIL perhaps indicates that the size of fluorescing species in dicationic RTIL is smaller as compared to that in MIL. To understand it better, we have further calculated the particle size by using Stokes-Einstein equation.²⁷¹ The hydrodynamic radius for DIL and MIL are provided in Table 4.7. The hydrodynamic radius for DIL and MIL are found to be 3.38 \AA and 4.36 \AA respectively (Table 4.7). Here, we would like to mention that Kim and coworkers²⁰² have reported

the hydrodynamic radius for several imidazolium based mono cationic RTILs through FCS mesurment in the range of 3.0 Å – 6.6 Å.

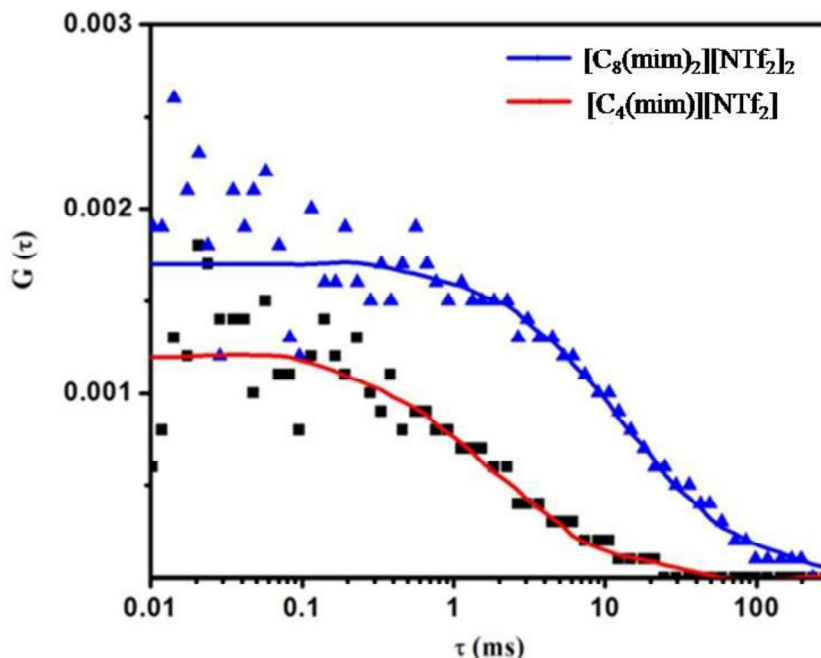


Figure 4.12. FCS plot for $[C_8(\text{mim})_2][\text{NTf}_2]_2$ and $[C_4(\text{mim})][\text{NTf}_2]$.

Table 4.7. The obtained physical parameters through FCS for $[C_8(\text{mim})_2][\text{NTf}_2]_2$ and $[C_4(\text{mim})][\text{NTf}_2]$ at 298 K

Systems	Concentration (nM)	D ($\mu\text{m}^2/\text{s}$)	Viscosity (cP)	R (\AA)
$[C_4(\text{mim})][\text{NTf}_2]$	2840 ± 160	10.02 ± 0.8	51	4.36
$[C_8(\text{mim})_2][\text{NTf}_2]_2$	2261 ± 140	0.97 ± 0.07	646	3.38

The observations of a relatively smaller hydrodynamic radius for DIL through present FCS study also provide evidence in favor of a folded structure of the present DILs. The outcome of the present study also establishes that the FCS studies in RTILs can be very useful in understanding the microscopic structural organization of RTILs.

4.4. Conclusion

In the present study, a combined fluorescence, EPR, NMR and FCS studies have been carried out on imidazolium-based dicationic and monocationic RTILs basically to understand if the behavior of dicationic ionic liquids (DILs) is different from that of the usual monocationic RTILs. The steady state absorption, emission and EPR data reveal that DILs are less polar than MIL. The excitation wavelength dependent fluorescence studies have suggested that DILs are more micro-heterogeneous in nature than the corresponding MIL. The rotational diffusion of two organic solutes, perylene and MPTS in DILs and MIL at various temperatures have revealed the solute-solvent, solvent-solvent interactions and structural organization of the respective media. The rotational relaxation data has been analyzed by SED theory. The experimental rotational time for perylene in MIL is observed to lie between the limits predicted by SED, whereas it deviates considerably in case of the DILs. The faster rotation of perylene in DILs is explained by considering quasi-hydrodynamic theory, where both solute and solvent size and the free space between solute and solvent is considered. Unlike perylene, the rotation of MPTS is observed to be much hindered in both the DILs and MIL. The relatively hindered rotation for MPTS in the RTILs has been explained on the basis of stronger solute-solvent hydrogen bonding interactions. Interestingly, upon careful observation, it has been found that experimental rotational times for MPTS lie above the stick line in MILs, but is observed to lie just below the stick line in DILs. This observation essentially signifies that MPTS-MIL interactions are relatively stronger than MPTS-DIL interactions. The NMR and FCS studies have indicated that DILs in the experimental condition can exist in folded form, and perhaps because of this structural restriction of DIL, it becomes difficult for bulky MPTS to make stronger hydrogen bonding interactions with DILs, which ultimately causes the faster rotation of MPTS in that medium. The present data demonstrates that the structural organization of $[C_8(\text{mim})_2][\text{NTf}_2]_2$ and $[C_9(\text{mim})_2][\text{NTf}_2]_2$

(DILs) are significantly different than their counter MIL, ([C₄(mim)][NTf₂]). The outcome of the present study is expected to entail a significant step forward in understanding the structure-property relationship in dicationic ionic liquids.

Chapter 5

Effect of Anion Chain Length on the Aggregation Behavior of Neat Imidazolium-Based Alkyl Sulfate Room Temperature Ionic Liquids: A Combined Time Resolved Fluorescence Anisotropy, NMR and Fluorescence Correlation Spectroscopy (FCS) Study

This chapter describes the aggregation behavior of a series of neat 1-ethyl 3-methylimidazolium alkyl sulfate (alkyl = ethyl, butyl, hexyl, and octyl) RTILs through combined time-resolved fluorescence spectroscopy, 1-D, 2-D-NMR spectroscopy, and fluorescence correlation spectroscopy (FCS). The outcome of the present studies suggest that the fluorescence of neat RTILs originate from the associated/aggregated species and the alkyl chainlength on the anions play an important role in governing the aggregation behavior of these RTILs.

5.1. Introduction

The past decade has witnessed tremendous emphasis on research activities on ionic liquids.^{1-35, 142-205} The research activities in terms of both experimental¹⁵⁸⁻²⁰⁵ and theoretical¹⁴²⁻¹⁵⁷ work on ionic liquids are aimed at understanding the structure-property-dynamics relationships in these media.^{83, 85-91} Among the experimental works, time-resolved fluorescence studies have been found to be very popular, where studies have been carried out to get an idea about the underlying dynamics in ionic liquid medium, by employing an external probe.^{183-185, 187-201} However, studies on ionic liquids in neat condition are rather limited.²⁰¹⁻²⁰⁴

Samanta and co-workers^{160, 161} have earlier shown that neat ionic liquids are not optically transparent. They have demonstrated that imidazolium based ionic liquids have significant absorption in the ultraviolet region, and the absorption tail can extend upto visible region.¹⁶¹

More interestingly, they have observed that these liquids are fluorescent and their fluorescence depends on the excitation wavelength.¹⁶¹ Essentially these studies have demonstrated that optical absorption and emission behavior of ionic liquid originates from their associated structures. However, there are some reports available where it has been claimed that the absorption and emission from ionic liquids come from the chemical impurities.^{330, 332} In recent times some more interesting studies mainly dealing with the fluorescence behavior of neat ionic liquids have emerged.²⁰¹⁻²⁰⁴ The outcomes of these work supports the conclusions obtained earlier by Samanta and co-workers¹⁶¹ where it has been shown that associated species within ionic liquids are primarily responsible for the inherent fluorescence behavior of neat ionic liquids. Among the recent work on fluorescence behavior of neat ionic liquids, the independent work by Kim^{202, 203} and Dutt²⁰¹ are noteworthy. Kim and coworkers, through 2D scan fluorescence spectroscopy have demonstrated that long-wavelength fluorescence component of ionic liquids arise from molecular aggregates in the bulk ionic liquids. By exploiting fluorescence correlation spectroscopy they have also demonstrated that fluorescence originates from the aggregated structure of molecules in the neat ionic liquids. They have even measured the number density of the fluorescing species.²⁰² To get a better understanding on the characteristic of the emitting species of ionic liquids Dutt and coworkers²⁰¹ have investigated the rotational dynamic of several 1-alkyl-3-methyl imidazolium based ionic liquids in their neat condition. They have obtained experimentally measured rotational relaxation time (τ_r) 3 times longer than the estimated ones (using Stokes-Einstein-Debye (SED) theory) for 1-alkyl-3-methyl imidazolium cation, suggesting that the emission originates from associated species rather than monomeric imidazolium moiety. It is pertinent to mention in this context that few recent studies while investigating the time resolved fluorescence behavior of neat RTILs have commented through

electronic energy transfer studies that aggregated structures in neat RTILs could be limited in presence of longer alkyl chain.²²⁷ However, this data contradicts other recent observation in neat RTILs where it has been demonstrated that longer alkyl chains facilitates domain aggregation.^{188, 195, 226} Moreover, we have also shown in a recent study that there is no one-to-one correlation between emission wavelength dependent fluorescence lifetime data with structural organization of neat RTILs.²⁰⁴ All these facts indicate that several fundamental aspects associated with the ionic liquid aggregates is not yet known, and hence more studies are required to get proper understanding on the ionic liquid aggregates. It is, therefore, important to study the fluorescence behavior of neat ionic liquids with a systematic variation in their structures. Additionally, studies such as fluorescence correlation spectroscopy, time-resolved fluorescence anisotropy and NMR spectroscopy should also be exploited together so that a comprehensive and quantitative idea about the aggregation behavior of neat RTILs is obtained.

In the light of the above discussion, the aggregation behavior of a series of 1-ethyl-3-methylimidazolium alkyl sulfate ionic liquids (Chart 5.1) in their neat condition has been investigated through a combined time resolved fluorescence anisotropy, NMR spectroscopy and fluorescence correlation spectroscopy (FCS) study. These RTILs are purposefully chosen so that a systematic variation of alkyl group in their anionic moiety is maintained. While choosing the ionic liquid systems we have also kept in mind the fact that variation in alkyl chain length will induce variation in their physicochemical properties in a systematic manner.¹⁹¹⁻¹⁹⁹ In the present study, we have resorted to fluorescence anisotropy measurements as it has been used to calculate the hydrodynamic radius of the rotating fluorescent species, through the time constant of anisotropy decay,^{256, 239, 247} NMR spectroscopy is employed in the present case keeping in mind the fact that by monitoring a change in the chemical shift values and width of the concerned proton signal one

would be able to comment on the molecular association.³³³ Further, homonuclear 2D NMR Rotating frame Nuclear Overhauser Effect Spectroscopy (ROESY) has been used to probe the interaction among anion and cation,²¹⁹ in neat RTILs, and hence an idea about self aggregation behavior of RTILs is expected to be obtained. Since FCS is another powerful technique as it is extremely sensitive to the concentration and the diffusion coefficient of solute molecules,^{202, 245} in the present study this technique is also exploited. It is expected that by measuring the number density and diffusion coefficients of the fluorescing species an idea about RTIL aggregates can be obtained.²⁰²

In the present work, time-resolved fluorescence anisotropy data on neat RTILs reveal that the rotating fluorescing species are the associated species and not the monomeric ones. Further, peak positions of ¹H NMR spectra of neat RTILs are observed to be shifted on dilution. This observation points out that the neat RTILs exist in aggregated form and aggregation breaks upon dilution. The particles size obtained from translational diffusion coefficient (*D*) of the aggregated species through NMR spectroscopy is observed to decrease with increasing the anion chain length. The 2D NMR (ROSEY) experiment provides the information about anion-cation interactions. The outcome of the combined fluorescence, NMR and FCS studies will entail a significant step forward in our understanding of the aggregation behavior of neat ionic liquids.

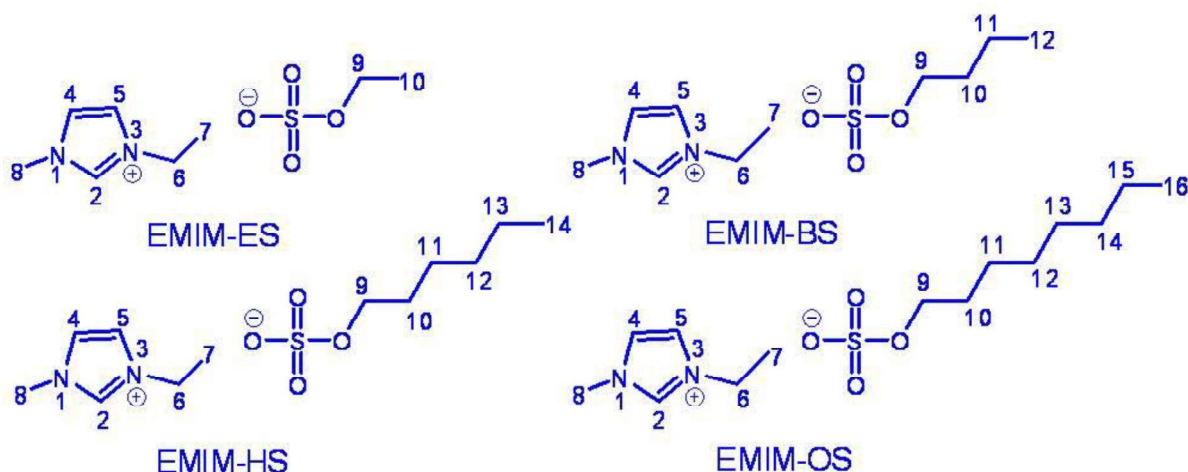


Chart 5.1. Molecular structures of 1-ethyl 3-methyl imidazolium ethyl sulfate (EMIM-ES), 1-ethyl 3-methyl imidazolium butyl sulfate (EMIM-BS), 1-ethyl 3-methyl imidazolium hexyl sulfate (EMIM-HS) and 1-ethyl 3-methyl imidazolium octyl sulfate (EMIM-OS).

5.2. Experiments and Method

The ionic liquids, EMIM-ES, EMIM-BS, EMIM-HS and EMIM-OS are obtained from Merck Germany (>99% purity). The halide and water content of these RTILs are < 100 ppm. The ionic liquids are rigorously purified. The purity of these RTILs are confirmed by different conventional analytical methods e.g. NMR and ESI-MS (Electrospray ionization mass Spectrometry) techniques. Prior to photophysical studies, ionic liquids were kept in high vacuum to avoid moisture. Then, the RTILs was transferred into long-necked quartz cuvette for fluorescence spectroscopy. Septum and parafilm were also used to avoid moisture absorption. Dimethyl sulfoxide (DMSO) and Dimethyl sulfoxide-deuterated (DMSO-d₆) (99.9%) were obtained from across chemical. Rhodamine 6G (Rh6G) was used for calibration of FCS instrument and obtained from sigma Aldrich.

5.3. Result and Discussion

5.3.1. *Steady State Absorption and Emission of Neat RTILs*

Representative absorption and emission spectra of neat EMIM-ES and EMIM-OS RTILs are provided in Figure 5.1. As can be seen, from the figure that all the neat RTILs have significant absorption in the UV region. A long absorption tail which extends beyond 375 nm is also observed. The intense band (~ 250 nm) is believed to be due to the π - π^* transition of monomeric imidazolium moiety and long absorption tail is due to the existence of energetically different associated species.^{161, 227} No systematic change in the absorption profile of RTILs is observed with the increase in the alkyl side chain length.²⁰⁴ The emission spectral profiles for both EMIM-ES and EMIM-OS are observed to be similar (Figure 5.1). In both the cases a broad emission with a maximum at ~ 450 nm is observed. Thus it would be difficult to obtain idea about structural organization of these RTILs based on the steady state absorption and emission data. In a recent study we have studied the emission wavelength dependent lifetime measurements for alkylsulfate RTILs.²⁰⁴ There, we have shown that it is not possible to obtain meaningful information from these data about the structural organization of the RTILs.²⁰⁴ Excitation wavelength dependent emission behavior (Figures 5.2) is also observed in the present RTILs. This observation supports that neat ionic liquids exist in aggregated forms having energetically different species in the ground state.^{160, 161} The fact that RTILs are heterogeneous is also nicely demonstrated by Hunger and his coworkers recently.³³⁴ In the present case we have also studied the fluorescence behavior of the RTILs by taking the shortest and the largest member of the series by gradually adding water to neat RTILs (Figure 5.3). It has been observed that with increase in the water mole fraction, the emission maxima remain same but the emission intensity decreases. Interestingly, with addition of same mole fraction of water, the decrease in emission

intensity observed to be more for EMIM-OS than that of EMIM-ES (Figure 5.3). This observation indicates that the association in neat RTILs breaks down on addition of water in both the cases, and presumably the said associations are relatively stronger in EMIM-ES than that in EMIM-OS. Similar trend is observed upon gradually addition of DMSO to neat RTILs.

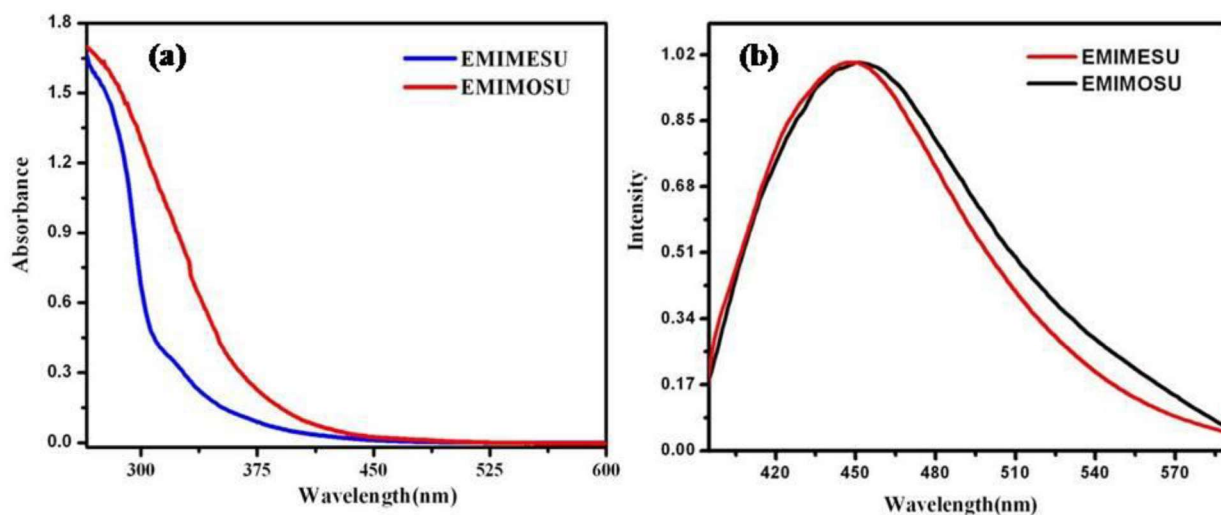


Figure 5.1. (a) Absorption and (b) normalized emission spectra ($\lambda_{exc} = 375$ nm) of neat EMIM-ES and EMIM-OS.

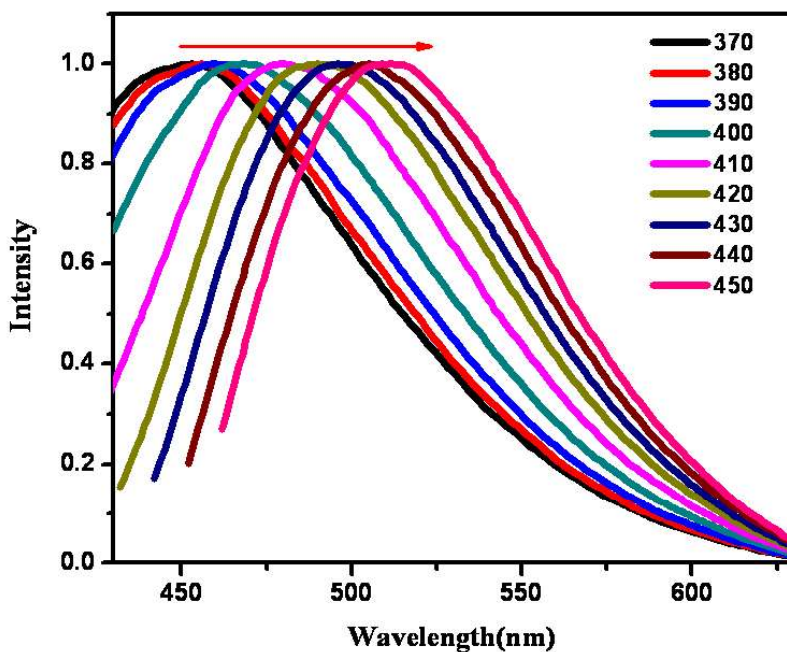


Figure 5.2. Normalized emission spectra of neat EMIM-ES at different excitation wavelengths.

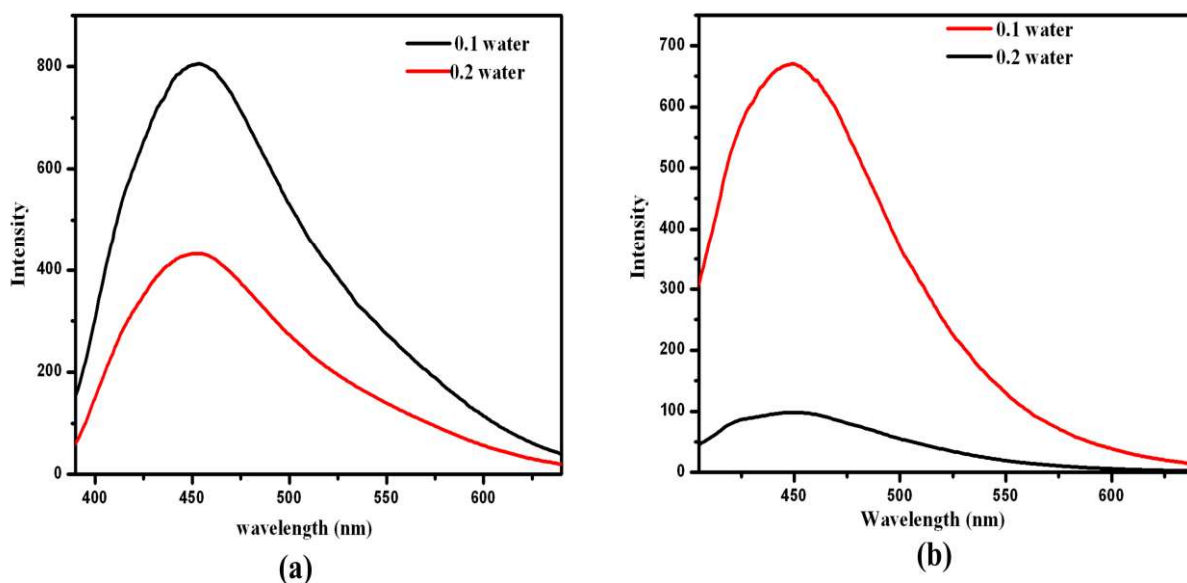


Figure 5.3. Emission spectra of neat (a) EMIM-ES and (b) EMIM-OS with addition of different mole fraction of water. $\lambda_{exc} = 375$.

5.3.2. Rotational Dynamic Study of Neat RTILs

We have resorted to study rotational relaxation dynamics of neat RTILs through fluorescence anisotropy measurements keeping in mind the fact that the molecular rotation can serve as the tool for extracting information about intermolecular interactions and eventually molecular aggregation behavior.²⁰¹ Compared to fluorescence lifetime (τ) rotational relaxation time is believed to be more effective (τ_r) in describing local environment.²⁰¹ In the present study, we have systematically analyzed the fluorescence anisotropy decays of all the four neat alkyl sulfate ionic liquids. Anisotropy decays plots for them are provided in Figure 5.4. Viscosity (η) and reorientation time (τ_r) of all the RTILs at different temperatures are collected in Table 5.1. The viscosity of all these RTILs is matched with literature values.¹⁹⁵ All the anisotropy decay profiles are fitted to a single-exponential decay function.

Table 5.1. Reorientation time (τ_r) and viscosity (η) of all four neat RTILs at different temperatures

Systems	Temp. (K)	η (cP) ^a	τ_r (ns) ^b
EMIM-ES	293	105	8.33
	298	75	6.90
	303	58	5.77
	308	46	4.66
	313	34	3.83
EMIM-BS	293	191	12.14
	298	141	9.19
	303	106	7.54
	308	82	6.15
	313	63	4.90
EMIM-HS	293	389	18.87
	298	284	15.03
	303	211	12.43
	308	160	10.21
	313	122	8.54
EMIM-OS	293	646	31.06
	298	453	24.00
	303	329	18.60
	308	245	15.04
	313	183	11.29

^aExperimental error= $\pm 2\%$, ^bExperimental error= $\pm 5\%$,

One can see both from the anisotropy decay profiles (Figure 5.4) and the data from Table 5.1 that with increase in the temperature, faster rotation is observed for all the systems due to the fact that viscosity of RTILs decreases with increase in the temperature. It may be noted here that study of molecular reorientation in liquids is proven to be very popular because of the fact that well developed theoretical frameworks^{334-336, 239, 247} are available to analyze the experimental data. To get a better idea about rotational dynamic of these ionic liquids, we have analyzed the data by using Stokes-Einstein-Debye (SED) hydrodynamic theory.^{239, 247}

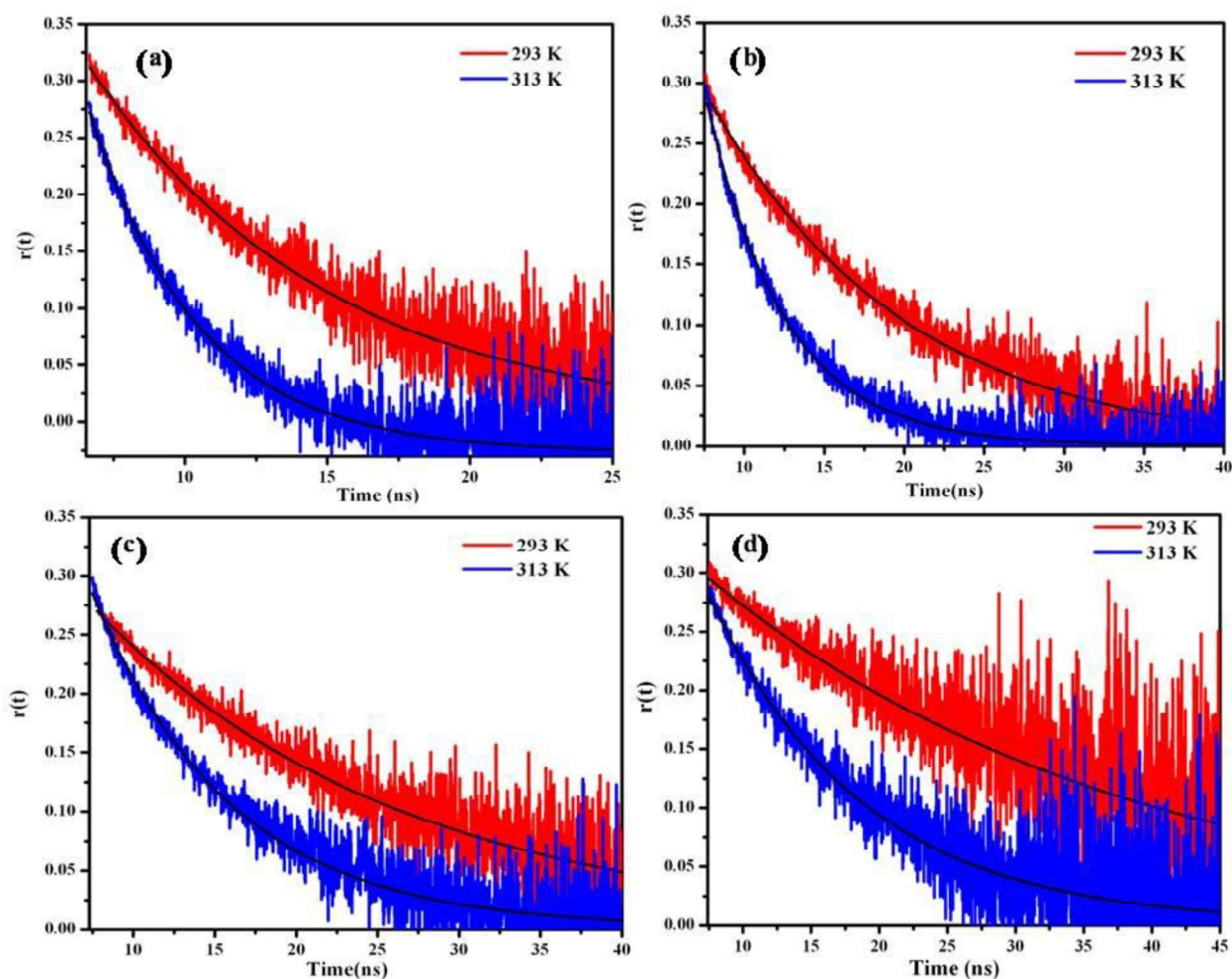


Figure 5.4. Anisotropy decay of (a) EMIM-ES, (b) EMIM-BS, (c) EMIM-HS and (d) EMIM-OS, respectively, at 293 and 313 K where $\lambda_{exc} = 375$ nm and $\lambda_{em} = 450$ nm. The solid black lines indicate fit to the data points.

In the present study the SED theory has been applied by considering EMIM as a rotating species in the case of all four neat RTILs, as in all the cases, cation is fixed and only the anion chain length is varied. Similar consideration has been made by Dutt and his coworkers²⁰¹ while studying the fluorescence anisotropy of some neat RTILs. The axial radii, van der Waals volumes (V), shape factors (f) and C_{slip} of EMIM are estimated from the literature available numerical values.²⁰¹ From the values of C_{slip} and f , we have estimated the theoretical τ_r^{slip} and τ_r^{stk} at different temperatures for all the neat RTILs. The experimental rotational time (τ_r) is compared

with the ones that is estimated theoretically through SED equation. Figure 5.5. demonstrates the log-log plot of τ_r vs. η/T along with their τ_r^{stk} and τ_r^{slip} line at different temperatures. Interestingly, the experimentally measured τ_r values for all neat RTILs are found to lie above their respective stick prediction (Figure 5.5). This phenomenon of hindered rotation in hydrodynamics is known as superstick behavior.^{239, 247} More interestingly, upon increasing the chainlength i.e. for EMIM-ES, EMIM-BS, EMIM-HS and EMIM-OS the experimentally measured τ_r values are observed to be 2.25, 1.64, 1.36 and 1.32 times higher than their theoretically calculated τ_r^{stk} values, respectively. We have also calculated the hydrodynamic volume, V_h (where $V_h=fCV$) of the rotating species for the neat ionic liquids using SED theory.^{239, 247} Hydrodynamic volumes for the RTILs are provided in Table 5.2. As can be seen from the data that are collected in Table 5.2 that even though the size of the anion increases from EMIM-ES to EMIM-OS but the hydrodynamic volume decreases. The hydrodynamic volume of the rotator of EMIM-ES is higher than that of EMIM-OS, which suggest that the EMIM-ES is more associated in nature.

This observation indicates two points, first that the rotating fluorescing species are not only the monomer, rather aggregates. It is pertinent to mention in this context that Weingärtner¹¹ has depicted that imidazolium-based ionic liquids can exist as ion pairs and larger ion clusters. Second the size of the aggregates decreases with an increase in the alkyl side chainlength on the anionic moiety. This result is quite interesting. Please note that it has been recently reported that the increase in the alkyl chain length on the cationic moiety of RTILs facilitates aggregation.^{195, 188, 226} It may be mentioned here that Stricoli and coworkers²²⁷ through resonance energy transfer studies have demonstrated that increase in alkyl chainlength actually limits aggregation. The decrease in the hydrodynamic volume with an increase in the alkyl side chain of the constituent

of the RTIL can also be observed from a recently published report by Dutt and coworkers.²⁰¹ There it can be seen that the rotational relaxation time of neat 1-alkyl 3-methyl imidazolium tetrafluoroborate and 1-alkyl 3-methyl imidazolium hexafluorophosphate RTILs (alkyl= ethyl and hexyl) decreases with increasing the cation chainlength.²⁰¹ This data indicates that for relatively smaller systems, the rotating species rotate along with the anion, but as the alkyl chainlength on the anion increases the association between imidazolium and sulfate anion gradually decreases and consequently the influence of relatively larger anions on the rotating species is also reduced. The fact that there is a decrease in the interaction between the imidazolium and the alkyl sulfate moiety of RTILs with an increase in the length of alkyl group is established through NMR 2D-ROESY experiments (*vide infra*). NMR 2D-ROESY experiment reveals that the anion-cation interaction in shorter alkyl chain (EMIM-ES) RTIL is approximately 3.3 times higher than that of longer alkyl chain (EMIM-OS) RTIL (*vide* Table 5.4). Here we note that Cabeza and co-workers^{174, 337, 338} investigated the physical properties e.g. density, conductance etc. of these RTILs with water or ethanol mixtures. They have also demonstrated^{174, 339} that the ion-ion interactions prevailing in RTILs are the main cause behind the deviation of electrical conductivities of pure RTILs from pseudo-lattice based Bahe-Varela model.^{340, 341} The authors have shown that with increase in mole fraction of RTIL in the aqueous solution of RTIL, the normalized electrical conductivity deviates more from the Bahe-Varela universal representation of electrical conductivity.¹⁷⁴ This deviation is shown to be more in case of EMIM-ES than EMIM-BS and EMIM-OS.¹⁷⁴ This indicates that the ion-ion interaction is more in EMIM-ES than EMIM-BS and EMIM-OS. Therefore, above results support our present observation where relatively stronger ion-ion interaction is observed for EMIM-ES as compared to other RTILs.

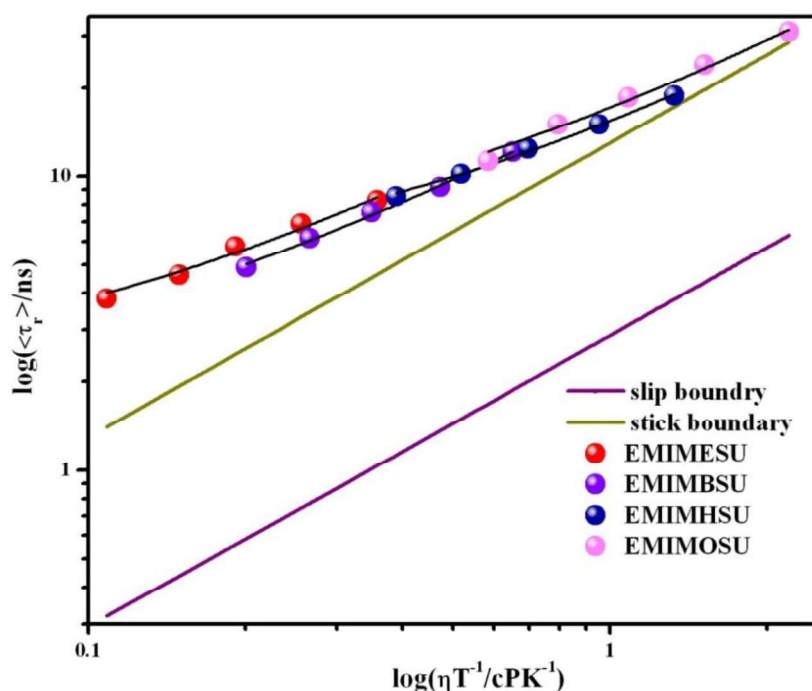


Figure 5.5. $\log(\tau_r)$ vs. $\log(\eta/T)$ plot with stick and slip boundary condition limits. The solid black lines indicate fit to the data points.

Table 5.2. Calculation of volume of rotating species at different systems using Stokes-Einstein equation

Systems	Volume (\AA^3)	Particle size (\AA)
EMIM-ES	378	4.40
EMIM-BS	268	4.00
EMIM-HS	217	3.72
EMIM-OS	202	3.64

Again, we would like to take a note here that recently Prabhu et al ²⁰¹ have shown that for a particular $\log \eta/T$, the reorientation time of 1-ethyl 3-methyl imidazolium cation RTIL is independent on the nature of the anion.²⁰¹ In this context, the present observation is also interesting in a sense that the reorientation time obtained in the present work, is found to depend on the length of alkyl groups on the anion.

5.3.3. NMR Spectroscopic Study

To obtain further idea about aggregation behavior of these RTILs, NMR spectroscopic studies have been carried out by employing the smallest (EMIM-ES) and largest (EMIM-OS) member of the series. The representative ^1H -NMR spectrum of neat EMIM-ES and EMIM-OS is displayed in Figures 5.6 and 5.7 (upper panel) respectively. We would like to take a note here that recently, LaPlante and co-workers³³³ have demonstrated a strategy that can be used to detect the aggregate formation by using the simple NMR technique. It has been demonstrated that since shift in resonance (δ ppm) arises due to the local environment changes in the magnetic field around the molecule, this feature of NMR signal can serve as an indicator of aggregation process. They have also demonstrated that the shape (broad or sharp) of NMR signal also relates to the size and tumbling rate of a species. A larger species is expected to exhibit a broad NMR signal due to its slower tumbling rate.³³³ In solution, where molecule exists in molecular form, they are separated from each other and they tumble freely, and peak position is also not shifted upon further dilution; but, for aggregates, molecules exist in self associated structures, and they tumble relatively slowly as compared to the monomeric forms which ultimately causes the broadening of the NMR signal.³³³ Moreover, a shift in peak position is also observed upon dilution due to change in the intermolecular interactions.³³³ Interestingly, in the present case, fairly broad ^1H NMR peaks are observed when the experiments are done by employing only RTILs in their neat condition. Upon dilution of the neat ionic liquids, with DMSO- d_6 , the broad ^1H NMR peak gradually shifts towards the higher chemical shift region, and also the sharper NMR signal, as compared to the same signal for neat RTILs, is obtained (Figures 5.6 and 5.7). The broad peak is obtained due to the fact that the neat RTILs exist in the aggregated form, and due to their larger size a slower tumbling rate of the molecules are expected.³³³

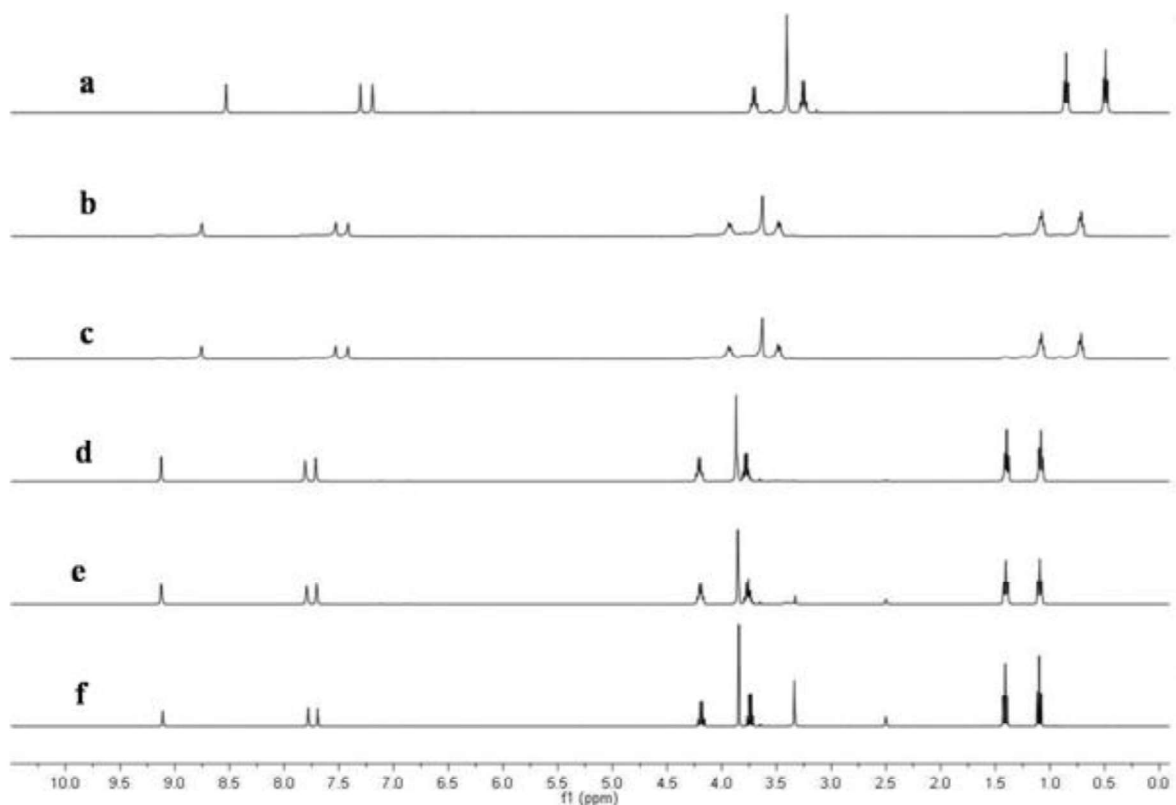


Figure 5.6. ^1H NMR spectra of (a) neat EMIM-ES, (b) EMIM-ES+DMSO- d_6 (1:1) mixture, (c) EMIM-ES+DMSO- d_6 (1:2), (d) EMIM-ES+DMSO- d_6 (1:4), (e) EMIM-ES+DMSO- d_6 (1:8), (f) EMIM-ES+DMSO- d_6 (1:16).

The full width half maximum (FWHM) is also calculated (Table 5.3) for both EMIM-ES and EMIM-OS ionic liquid in their neat condition and in very dilute condition, EMIM-ES:DMSO- d_6 (1:16). Interestingly, with dilution of neat EMIM-ES and EMIM-OS to the same extent for both RTIL, the more changes in the FWHM values are observed for EMIM-OS than that for EMIM-ES (Table 5.3). This result also indicates the relatively stronger self-association in EMIM-ES than that in EMIM-OS.

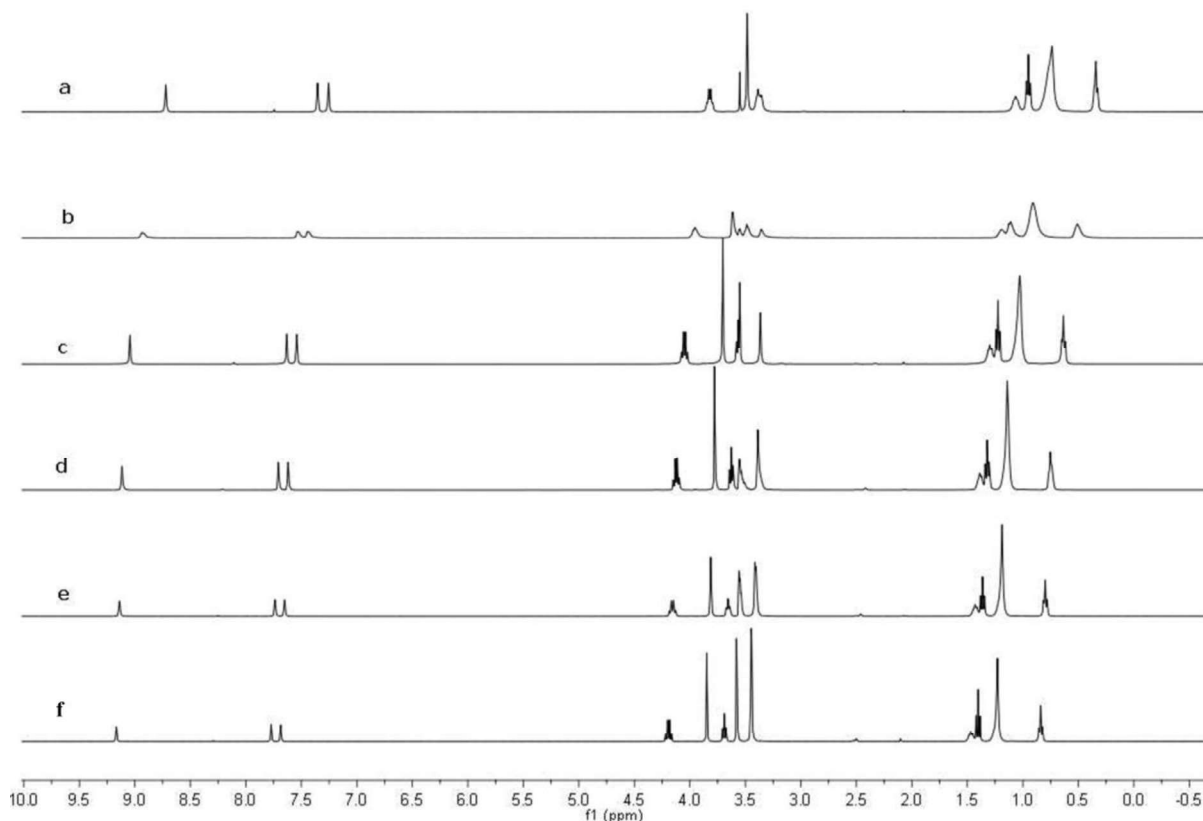


Figure 5.7. ^1H NMR spectra of (a) neat EMIM-OS, (b) EMIM-OS+ DMSO- d_6 (1:1) mixture, (c) EMIM-OS+ DMSO- d_6 (1:2) mixture, (d) EMIM-OS+DMSO- d_6 (1:4) mixture, (e) EMIM-OS+DMSO- d_6 (1:8) mixture, (f) EMIM-OS+ DMSO- d_6 (1:16) mixture.

Table 5.3. FWHM values corresponding to relevant proton NMR signals of neat EMIM-ES and EMIM-OS and their mixtures with co-solvent (RTIL+ DMSO- d_6 (1:16) mixture)

System	Protons	FWHM, Neat RTIL (Hz)	FWHM, very diluted RTIL (Hz)
EMIM-ES	H(10)	16	12
	H(7)	16	8
	H(9)	12	8
	H(8)	4	4
	H(6)	12	8
	H(5)	8	4
	H(4)	4	4
	H(2)	4	4
EMIM-OS	H(16)	16	4
	H(11-15)	24	8
	H(10)	16	12
	H(7)	20	16
	H(9)	24	12

H(8)	4	4
H(6)	16	8
H(5)	4	4
H(4)	4	4
H(2)	4	4

Note that idea about the structure of neat RTILs are generally obtained from X-ray and neutron diffraction,³⁴² molecular dynamics simulations,¹⁴⁴⁻¹⁴⁶ and Raman and optical Kerr spectroscopy.³⁴³ Very recently Castner's group has demonstrated that NMR technique can be exploited to obtain information on the structure and interactions between ions in RTILs.²¹⁹ It is possible to know the interaction of anion and cation in solution through Nuclear Overhauser effect (NOE).²¹⁵⁻²¹⁹ The homonuclear 2D NOE such as $\{^1\text{H}-^1\text{H}\}$ ROESY spectroscopy has been successfully used to probe inter-ionic interaction in RTILs.²¹⁹ In ROSEY spectra two types of peaks are obtained i.e. cross peak and diagonal peak. The cross peak is more significant, as the distance between two interacting nuclei is a function of cross peak intensity.²¹⁹ In the present study, interactions between cation and the anion of neat RTILs have been studied by taking the smallest, EMIM-ES and the largest EMIM-OS member of the series through ROESY spectra. The atom numbers that are used in the molecular diagrams for these RTILs (Chart 5.1) have also been used for assigning the ROSEY spectral signal for the respective molecules. The $\{^1\text{H}-^1\text{H}\}$ -ROESY spectra of neat EMIM-ES and EMIM-OS are given in Figures 5.8 and 5.9, respectively. Integrated peak volume of all observed $\{^1\text{H}-^1\text{H}\}$ ROSEY cross peak of neat EMIM-ES and EMIM-OS are provided in Table 5.4. The particular cross peak intensity in the $\{^1\text{H}-^1\text{H}\}$ ROESY spectra signifies the strength of the interaction between cation and the anion.²¹⁹ While considering EMIM-ES and EMIM-OS one should remember that in both the cases the cation, EMIM, is common, only the anion is varied. As can be seen from Figures 5.8 and 5.9, for both RTILs, a common cation-cation interaction between the proton at the 2 position of one

imidazolium cation and the proton at the 4 of other imidazolium cation is observed. As in both cases where the cation is fixed, we have considered a common cation-cation interaction, 2 position of hydrogen with 4 position of hydrogen of imidazolium (Figures 5.8 and 5.9), and it is considered that this interaction is approximately equal. Quite interestingly, it has been observed that the proton at the 2 position of imidazolium cation is strongly interacting with the proton at the 9 position of the alkyl sulfate anion for both RTILs (Figures 5.8 and 5.9, respectively). However, the cross peak intensity that has been observed due to the interaction between the said protons is observed to be 3.3 times higher in EMIM-ES than that in EMIM-OS shown in Table 5.4. The strong cross peak intensity of EMIM-ES indicates the stronger cation-anion interaction for EMIM-ES than that for EMIM-OS. This indicates that the cation-anion interaction decreases with increase in the anion chainlength.

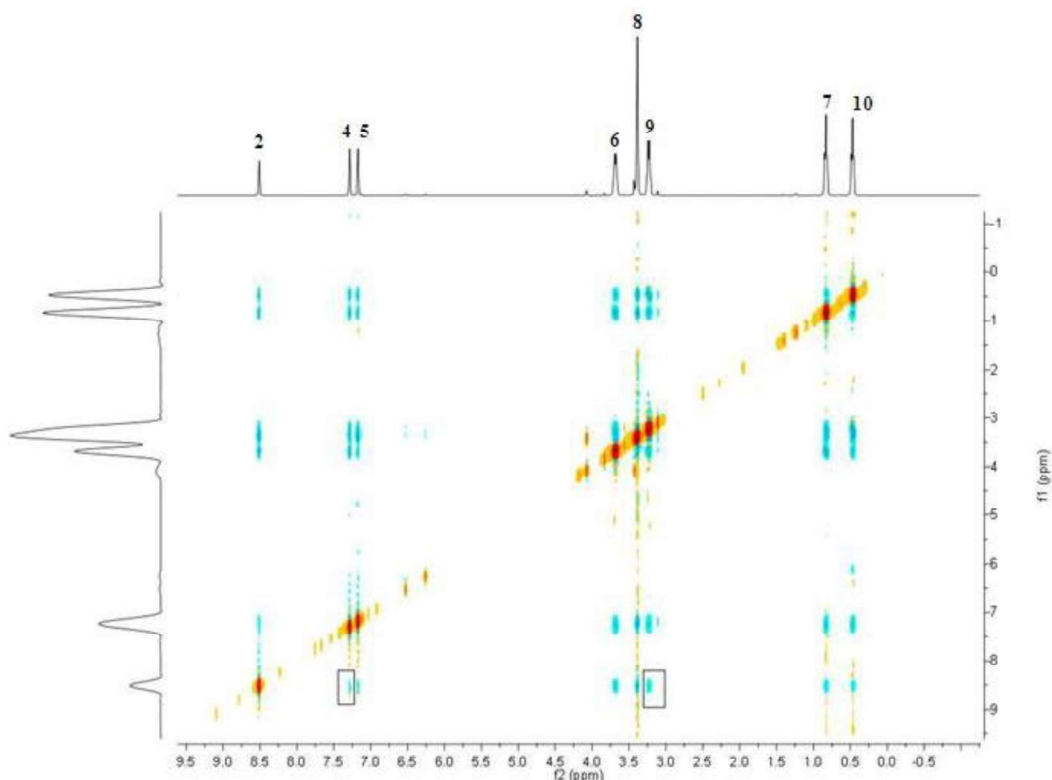


Figure 5.8. NMR 2D ROSEY spectra of neat EMIM-ES at 298 K. The box inside the figure indicates the common interaction with EMIM-OS RTIL in same condition.

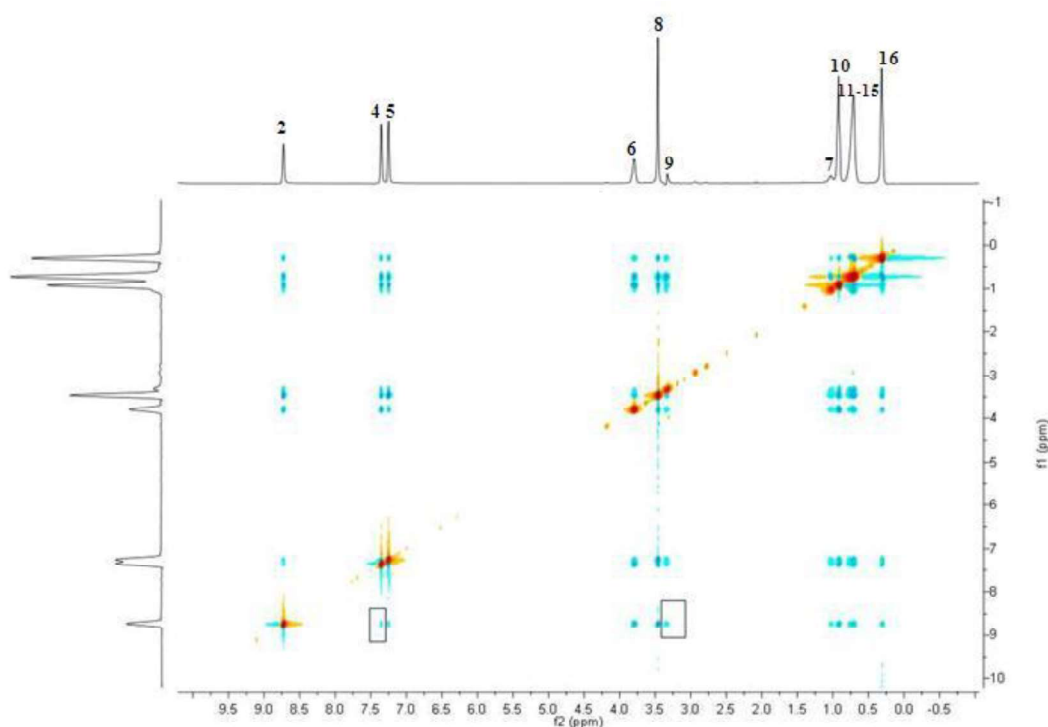


Figure 5.9. NMR 2D ROSEY spectra of neat EMIM-OS at 298 K. The box inside the figure indicates the common interaction with EMIM-ES RTIL in same condition.

Table 5.4. Integrated peak volume of all observed $\{^1\text{H}-^1\text{H}\}$ ROSEY cross peak of neat EMIM-ES and EMIM-OS. $n_{\text{H}1}$ and $n_{\text{H}2}$ are the number of proton in solution and $N = n_{\text{H}1} + n_{\text{H}2}$. Integrated volume is the analyzed integral value by top spin NMR software. The corrected volume is the integrated volume divided by the normalization factor $(n_{\text{H}1}n_{\text{H}2}/N)$ for EMIM-ES and $(n_{\text{H}1}n_{\text{H}2}/N)(0.08/0.14)$ for EMIM-OS {the factor $(0.08/0.14)$ is multiplied with corrected volume in EMIMOSU due to normalized the volume with respect to EMIM-ES}

System	Interaction of atom	$n_{\text{H}1}$	$n_{\text{H}2}$	$n_{\text{H}1}n_{\text{H}2}/N$	Integrated volume	Corrected volume
EMIM-ES	H(2,4)	1	1	0.50	0.04	0.08
	H(2,9)	1	2	0.66	0.19	0.28
EMIM-OS	H(2,4)	1	1	0.50	0.07	0.08
	H(2,9)	1	2	0.66	0.10	0.085

Further, the translational diffusion coefficients (D), for both neat EMIM-ES and EMIM-OS are estimated with the help of NMR experiments. The translational diffusion coefficients (D), of cation and the anion has been measured simultaneously by monitoring the protons of the

respective entity. Diffusion coefficient data at several temperatures are provided in Table 5.5. The translational diffusion coefficients of cation in EMIM-ES and EMIM-OS are found to be $1.2 \times 10^{-11} \text{ m}^2/\text{s}$ and $0.28 \times 10^{-11} \text{ m}^2/\text{s}$, respectively, at 298 K (Table 5.5). It has also been observed that the diffusion coefficient of anion is lower than that of cation at a particular temperature. The less diffusion coefficient for anion as compared to the cation for the same RTIL is due to the larger molecular mass of the diffusing species.

Table 5.5. Calculation of translational diffusion coefficient through NMR spectroscopy

Systems	Temp. (K)	Trans diff.(cation) m^2/sec	Trans diff. (anion) m^2/sec
EMIM-ES	298	1.9×10^{-11}	1.2×10^{-11}
	308	2.9×10^{-11}	1.9×10^{-11}
	313	4.52×10^{-11}	3.08×10^{-11}
EMIM-OS	298	0.35×10^{-11}	0.28×10^{-11}
	308	0.64×10^{-11}	0.48×10^{-11}
	313	1.1×10^{-11}	0.82×10^{-11}

We have further explored the diffusion coefficient data to calculate the hydrodynamic radius of the diffusing species through Stoke-Einstein relation (equation 2.17).²⁷¹ The estimated hydrodynamic radii of both neat RTILs at 298 K are provided in Table 5.6. The radii of the cation of EMIM-ES and EMIM-OS are found to be 1.53 \AA and 1.37 \AA , respectively and the radius of anion is found to be 2.4 \AA and 1.77 \AA , respectively. Note that the present hydrodynamics radius data of the RTILs are very similar to the hydrodynamic radii data of the same RTILs that are estimated through rotational anisotropy (Table 5.2). This indicates that in both measurements the similar types of species have been probed. The present data also

corroborate our earlier observation where hydrodynamic radius of RTILs is observed to decrease from EMIM-ES to EMIM-OS.

Table 5.6. Hydrodynamic radius of molecule in different RTILs

Systems	Radius (cation) (Å)	Radius (anion) (Å)
EMIM-ES	1.53	2.4
EMIM-OS	1.37	1.77

5.3.4. FCS Studies

To get better idea about aggregation behavior of these RTILs, FCS has been exploited by employing the smallest (EMIM-ES) and the largest (EMIM-OS) members of the neat RTILs so that a trend on their aggregation behavior is obtained. In this study, the visible fluorescence of concerned RTILs is investigated by exciting the samples at 405 nm. The observed correlation function of EMIM-ES and EMIM-OS are provided in Figures 10 (a) and (b), respectively. The relevant parameters obtained in FCS measurements are provided in Table 5.7. The number density of the fluorescing species in both neat RTILs in diffusing volume is compared. Interestingly, the data that are collected in Table 5.7 reveals that though the length of the alkyl side chains in the sulfate anion is increased from ethyl to octyl, the number density of fluorescent species in the diffusing volume has decreased from EMIM-ES to EMIM-OS. The presence of less number of fluorescing species in EMIM-OS as compared to that in EMIM-ES perhaps also suggests that as the alkyl chainlength increases the association between imidazolium and sulfate anion gradually decreases, and thus a decrease in influence from anions on the defusing species is observed.

We have also measured the translational diffusion coefficient (D) for EMIM-ES and EMIM-OS from FCS measurements. In the present case, it has been observed that translational diffusion

coefficient decreases from EMIM-ES to EMIM-OS due to the increase in the viscosity from ethyl to octyl analogue. The translational diffusion coefficient of EMIM-ES and EMIM-OS are estimated to be 2.0×10^{-11} m²/s and 4.8×10^{-12} m²/s, respectively at 298 K. The translational diffusion coefficient obtained through FCS experiment is of the same order as obtained with the NMR experiment for both RTILs.

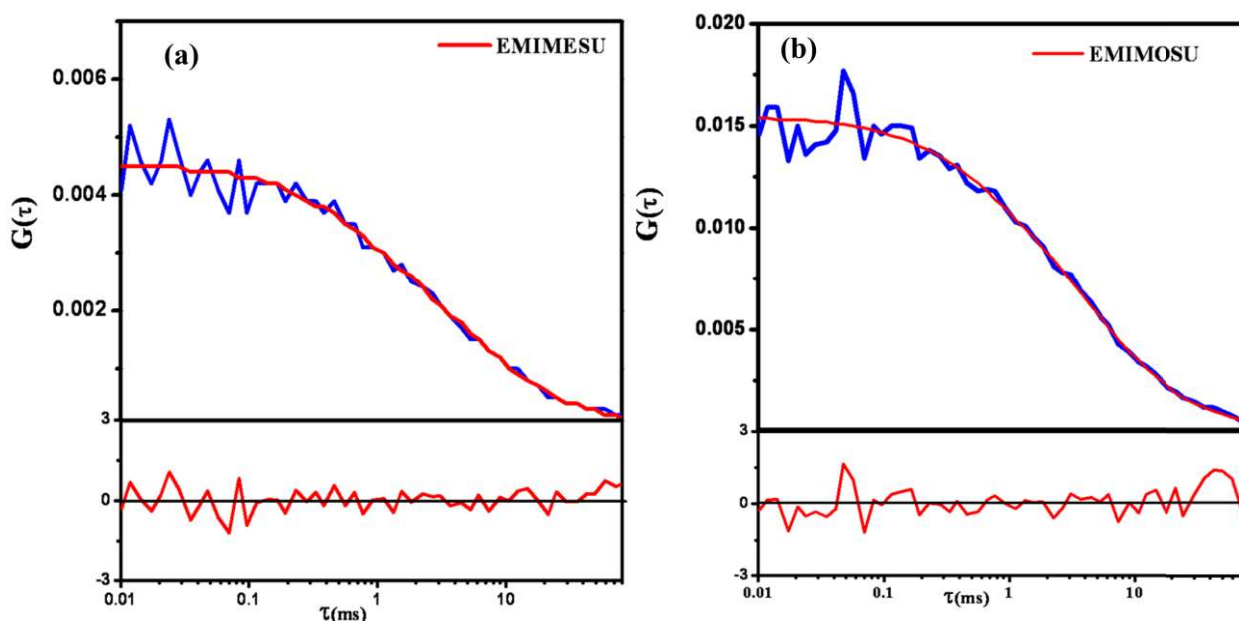


Figure 5.10. FCS results for neat (a) EMIM-ES, and (b) EMIM-OS RTILs. Solid red lines indicate fit to the data points.

Table 5.7. The physical parameters obtained from FCS measurement

System	$D(\mu\text{m}^2\text{s}^{-1})$	Concentration (nM)	Viscosity (cP)	Hydrodynamic radius (\AA)
EMIM-ES	20 ± 4	250 ± 30	75	1.45
EMIM-OS	4.8 ± 0.3	180 ± 10	453	1.0

We have further calculated the particles size by applying Stoke-Einstein equation (equation 2.17).²⁷¹ The calculation reveals that the particle size is decreased from EMIM-ES to EMIM-OS (Table 5.7). The particles size has decreased ~ 30 % as we go from EMIM-ES to EMIM-OS. The trend of decrease in the particle size on going from EMIM-ES to EMIM-OS is consistent with

the results that have been obtained by other measurements such as fluorescence anisotropy and NMR spectroscopy. These results also seem to indicate that upon going from EMIM-ES to EMIM-OS the association between imidazolium and sulfate anion is decreased and consequently the influence of relatively large sized anions on the defusing species is also reduced.

These results indicate that for relatively smaller systems, the diffusing species diffuses along with the anion, but as the alkyl chain length on the anion increases the influence of anions gradually decreases. The results of the fluorescence anisotropy measurements are consistent with the findings of NMR and FCS measurements. The present results are interesting in a sense that for RTILs containing the aliphatic cations, it has been observed that longer chains facilitate domain aggregation.^{188, 201, 226, 344} Note that recently Stricoli and co-workers²²⁷ have demonstrated that extent of aggregated structures in RTILs could be limited in presence of longer alkyl chain and large anions.²²⁷ It may be also noted here that self-organization within RTILs is mainly governed by electrostatic interactions, van der Waals forces and hydrogen bonding interactions. Moreover, their self-organisation behaviour also depends on ionic affinity, alkyl chain segregation and cation-anion interaction.^{340, 345} With an increase in the alkyl group the hydrophobic interactions within anions might become relatively stronger which perhaps reduces the imidazolium and sulphate anion interaction. The outcome of the present study indicate that subtle changes in the intermolecular forces that are responsible for ionic liquid aggregation can lead to different aggregation behaviour within different type of ionic liquids. We would like to take a serious note that further studies by exploiting molecular dynamics simulation calculation are expected to be helpful to find out the exact reason for this chainlength dependent aggregation behaviour of neat alkyl sulfate RTILs.

5.4. Conclusion

In this work, we have reported the aggregation behavior of a series of neat 1-ethyl 3-methylimidazolium alkyl sulfate ionic liquids with a systematic variation of anionic chainlength through a combined time resolved fluorescence anisotropy, NMR spectroscopy and FCS spectroscopy. A systematic variation in the length of alkyl side chains (alkyl=ethyl, butyl, hexyl and octyl) of the anionic moiety has been maintained so as to obtain a clear picture about their aggregation behavior. Interestingly, experimentally measured rotational relaxation times (τ_r) of ethyl, butyl, hexyl and octyl systems are estimated to be 2.25, 1.64, 1.36 and 1.32 times higher than the estimated (from Stokes-Einstein-Debye theory) values for the same for the respective systems. This indicates that the volume of the rotating fluorescing species decreases even though the length of the alkyl moiety on the anions is increased. The shift in the ^1H proton signal as well as a change in the width of the same signal upon dilution of the neat ionic liquids indicates that ionic liquids exists in the aggregated form. Further investigation through 2D-ROSEY experiment shows that interaction between imidazolium and sulfate is relatively stronger in ethyl system than that in longer octyl system. The translational diffusion coefficient and hydrodynamic volume calculated through NMR spectroscopy and fluorescence correlation spectroscopy (FCS) measurements independently show that the hydrodynamic volume decreases with an increase of the anion chain length. The NMR and FCS results are consistent with the findings of the fluorescence anisotropy study. The present results are interesting in a sense that for RTILs containing the aliphatic cations, it has been observed that longer chains facilitate domain aggregation. The present results are also expected to provide a testing ground for the theoreticians in terms of finding kinship among intermolecular interactions, structure, and dynamics in neat RTILs.

Chapter 6

Effect of Anion Chain Length and Nature of Cation on the Microscopic Structural Organization of Neat 1-Ethyl-3-Methyl Imidazolium Alkyl Sulfate, Ammonium and Pyrrolidinium Based Ionic Liquids: A Resonance Energy Transfer (RET) Study

In this chapter, the resonance energy transfer (RET) studies have been investigated from neat ionic liquids (donor) to rhodamine 6G (R6G) (acceptor) molecules to understand the microscopic structural organization of neat RTILs. Basically, three different sets of RTILs are taken for this studies, where in first set (1-ethyl-3-methyl imidazolium alkyl sulfate) the alkyl side chainlength on the anionic moiety is systematically varied, in second set variation is done on the cation (aromatic and nonaromatic) and in another set, the branched chainlength on the cationic moiety of RTILs is varied. The outcome of this work demonstrates that the rate of energy transfer, donor acceptor distance etc. depend upon the alkyl chainlength on the anionic moiety, nature of cation and branching of the cation of RTILs.

6.1. Introduction

Even though several photophysical studies have been carried out to understand the structural organization of RTILs, experiments based on resonance energy transfer (RET) in RTILs have not been widely explored.^{168-173, 212, 213} Among these the studies by Mandal and coworkers^{212, 213} are noteworthy where investigation has been carried out by employing RTILs having different alkyl group on cations, and different types of anions.^{212, 213} Please note that RET is a phenomenon in which the excitation energy of the donor is non- radiatively transferred to the acceptor.²⁴⁵ More importantly, efficiency of RET process strongly depends on the distance between donor and the

acceptor (10 to 100 Å),²⁴⁵ and by virtue of this, it has been used as a “spectroscopic ruler” in molecular biology.^{245, 250, 251} Perhaps one of the greatest advantage of RET process is to monitor events in heterogeneous environments such as cells, protein assemblies, polymer matrices etc., in noninvasive manner.^{245, 250, 251} RET being a distance dependent phenomenon, a small change in the donor-acceptor distance of the concerned system can affect the RET efficiency.²⁴⁵ In the present study the neat RTILs are used as the donor. Moreover, it is also known that RTILs are fluorescent because of its aggregated/associated structures.^{186, 201-203} Therefore, in the present RET study between RTILs and rhodamine 6G (R6G), the relevant FRET parameters, such as RET efficiency, donor-acceptor distance etc. are expected to depend on the local structure of ionic liquids. Hence the study of RET with a systematic variation of ionic liquids (e.g. anion chain length, or cation chain length or nature of cation or nature of anion) would help to understand the structural organization of this medium. In fact, some recent studies have demonstrated the usefulness of RET studies towards understanding the behavior of RTILs.^{168-173, 212, 213} Moreover, recent work by Bhattacharya and coworkers¹⁷¹ has demonstrated that the λ_{ex} dependent FRET study can provide information about the spatially resolving FRET in different regions of the ionic liquid based micellar system. Therefore, it would be interesting to study microenvironment of RTILs by varying the alkyl chainlengths on the anionic moiety of RTILs through RET studies. Since recent computer simulation studies^{151-153, 346} have depicted that structural organization will also depend on planar and nonplanar nature of the cations it would also be an worthwhile objective to obtain an idea about the microscopic structural arrangements of such RTILs through RET studies. As branching on the cationic moiety of RTILs is expected to play an important role towards their structure organization and physicochemical properties, it

would be very interesting to examine the microscopic structural organization of these RTILs by varying the branching on the ionic constituent of RTILs through RET studies.

Keeping this in mind, we have studied the RET phenomenon between several neat ionic liquids (donor) and rhodamine (acceptor) in a systematic fashion. Since it has been demonstrated that the RTILs have significant fluorescence in their neat conditions, the RTILs are used as donor for the current study. Among the RTILs, several 1-ethyl-3-methyl imidazolium alkyl sulfate (alkyl=ethyl, hexyl and octyl), has been used so that a systematic variation on the anion moiety is maintained while keeping the cation constant. This structural variation on anion is expected to be helpful in understanding the influence of alkyl chainlength of the anions on the overall structural organization of RTILs. Rhodamine 6G dye (R6G) is chosen as the acceptor molecule as it satisfies the spectral overlap criterion for RET process that is absorption spectrum of R6G has significant overlap with the emission spectrum of individual RTIL that is used in this study. Moreover, since rhodamine is a charged species, and so is RTIL, it is expected that ensuing electrostatic interaction between rhodamine and RTILs would also be helpful for them to come close to each other which would eventually facilitate the RET process between them. Further, to investigate whether the nature of cations play any role in the structural organizations of RTILs, we have also studied the RET phenomena on by introducing the planar and nonplanar cation based RTILs namely 1-methyl-3-butylimidazoliumbis(trifluoromethane)sulfonimide (BMIM-NTf₂), and 1-Butyl-1-methylpyrrolidiniumbis(trifluoromethane)sulfonamide (BMPyr-NTf₂) respectively. Again, the role of branching on the cationic moiety of RTILs on the RET process has also been exploited by taking two branched RTILs, namely, tributylmethylammoniumbis(trifluoromethane)sulfonamide (TBMA-NTf₂) and trioctylmethylammoniumbis(trifluoromethane)sulfonamide (TOMA-NTf₂). Additionally, to explore the potential of RTILs as

functional fluorescent materials for future applications, the RET studies have been carried out by synthesizing a RTIL-based gel comprising an alkyl chain containing RTIL (EMIM-OS) and guar gum (natural polysaccharide). The chemical structures of all these RTILs, R6G and guar gum have been provided in Chart 6.1.

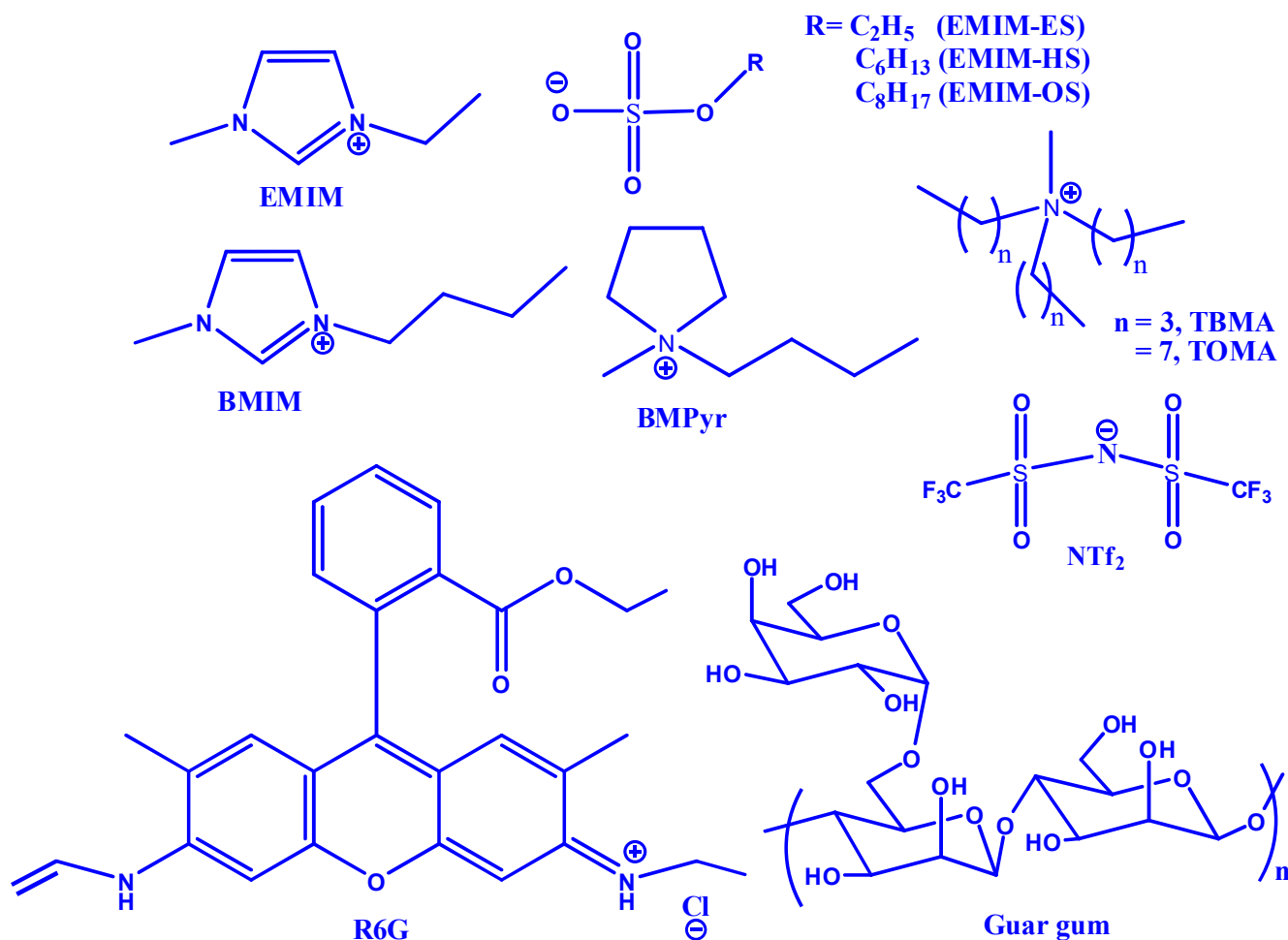


Chart 6.1. Molecular structure of RTILs, rhodamine 6G (R6G) and guar gum.

6.2. Experimental Section

The ionic liquids EMIM-ES, EMIM-HS and EMIM-OS, were obtained from Merck Germany (>99% purity). BMIM-NTf₂ and BMPyr-NTf₂, TBMA-NTf₂ and TOMA-NTf₂ were obtained from Io-il-tech. The water and halide content of these RTILs were found to be <100 ppm. R6G and guar gum were purchased from Sigma Aldrich chemical.

6.3. Result and Discussion

6.3.1. Fluorescence Behavior of Neat RTILs

Before RET studies, the absorption and the fluorescence behavior of all the neat RTILs are thoroughly examined. The representative absorption and emission spectra of neat EMIM-ES are provided in Figure 6.1. All the RTILs used in this study exhibit significant absorption in the UV region. Additionally, for all the systems, a long absorption tail has also been observed beyond 400 nm (Figure 6.1(a)). The long absorption tail indicates the presence of energetically different associated species in the ground state.^{161, 227} Essentially, absorption behavior of these RTILs are observed to be quite similar to other imidazolium-based RTILs. In the emission, all the neat RTILs show a broad emission band with a maximum at ~450 nm (Figure 6.1(b)). Interestingly, emission of all the neat RTILs is observed to depend on excitation wavelength (Figure 6.2). This effect is usually known as REE.^{238, 239} We would also like to mention that in the present RTILs, with increase in the alkyl chainlength (both in linear systems and branched systems), hydrophobic character of the RTILs will also increase. Moreover, a change in the anionic moiety (keeping the cation constant) will also lead to change in the electrostatic interactions (among constituents of RTILs). These intermolecular interactions are expected to play an important role in the formation of different associated structures for the concerned RTILs.

The efficiency of RET process is intricately related to the distance (10 to 100 Å) between donor and acceptor due to the fact that the interaction among them is of a dipole-dipole in nature.²⁴⁵ In the present study, we chose RTILs as the donor and another ionic molecule (R6G) as the acceptor. As stated earlier, an ionic probe has been chosen so that ion (RTIL, Donor)-ion (R6G, acceptor) interaction would allow them to stay in close to proximity, consequently an efficient RET process between them can take place.

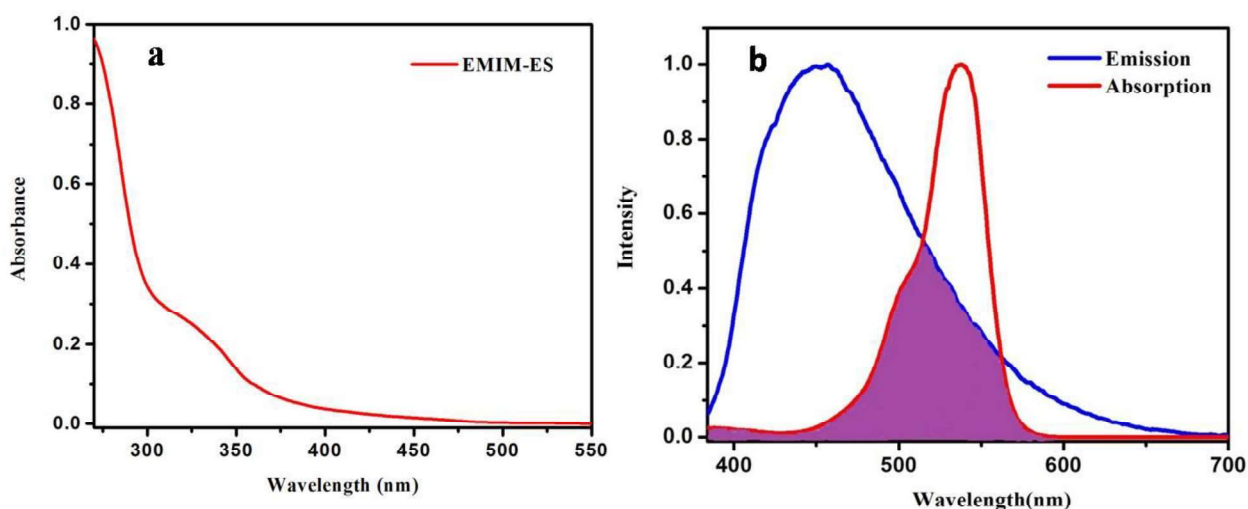


Figure 6.1. (a) Absorption spectrum of neat EMIM-ES and (b) normalized absorption and emission spectra of R6G and EMIM-ES. The highlighted region in figure 1(b) is the overlap region.

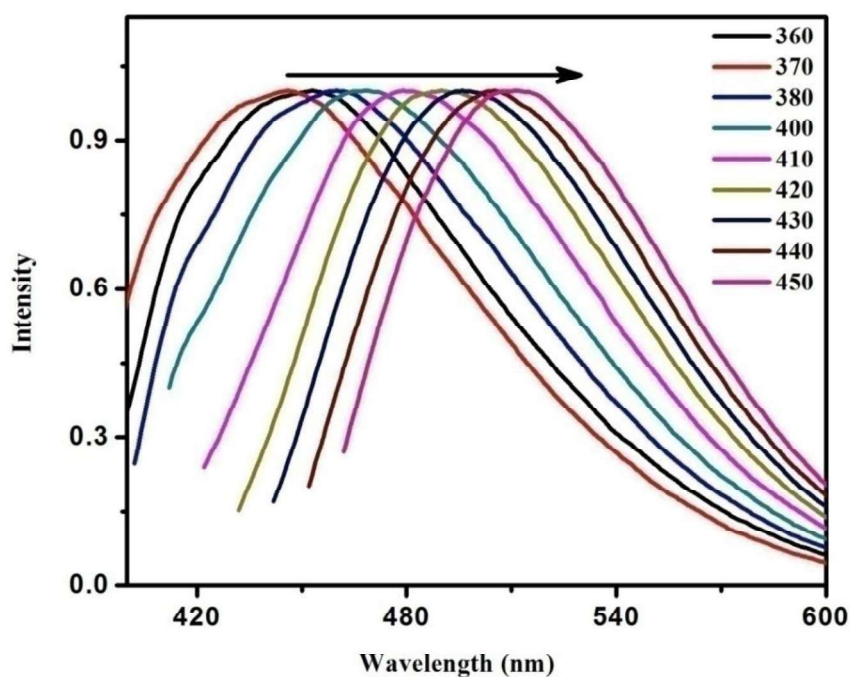


Figure 6.2. Normalized emission spectra of EMIM-ES at different excited wavelength ($\lambda_{exc} = 360-450$ nm).

The present RTILs are used as the donor due to their considerable fluorescence intensity (see Figure 6.1(b)) in neat condition. Moreover, the RTILs as donor and R6G as the acceptor have also satisfied the overlap (emission of the donor and absorption of the acceptor) criteria,

which is essential for any RET process. The representative emission and absorption spectra of donor (EMIM-ES) and acceptor (R6G) are given in Figure 6.1(b). Figure 6.1(b) reveals that there is a significant spectral overlap between the emission spectra of donor (RTILs) and the absorption spectra of acceptor (R6G). This also indicates that there is sufficient energetic coupling between them for an efficient RET process to occur.

6.3.2. Investigation of RET Process through Steady State Measurements

Initially, the RET interaction between the donor (RTIL) and acceptor (R6G) has been investigated by steady state fluorescence measurements. For the fluorescence intensity-based measurements, the samples have been excited at 375 nm, where the absorption of the donor (RTILs) is maximum but the absorption of the acceptor (R6G) is minimum. The excitation wavelength is chosen carefully so as to avoid direct excitation of the acceptor. The emission spectrum of donor (EMIM-ES) without and with gradual addition of acceptor (R6G) is provided in Figure 6.3. As can be seen from Figure 6.3, upon increasing the concentration of the acceptor, the emission of the donor (RTIL) gradually decreases and the emission of acceptor (R6G) gradually increases. The quenching of donor emission intensity with the addition of acceptor molecules indicates that RTIL and R6G are in RET communication. Again, the change of emission maximum to blue end for donor is also observed (Figure 6.3). This is not surprising because upon addition of acceptor to the donor solution, the electrostatic interaction takes place between the donor ionic liquids and the acceptor R6G molecule. Perhaps because of this reason, upon addition of acceptor molecules the red shift of donor emission is observed. The quenching of donor fluorescence by acceptor molecules is further analyzed by Stern-Volmer plot.^{245, 250} The plot of F_0/F against acceptor concentration is shown in Figure 6.4. A linear fit of the Stern-

Volmer plot ^{245, 250} indicates either a pure static or a pure dynamic quenching process during the event. ^{245, 250}

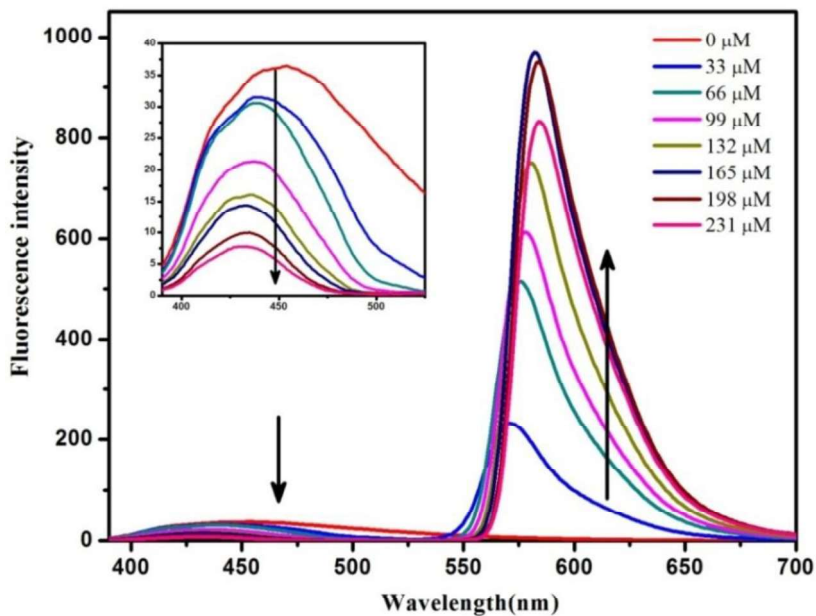


Figure 6.3. Variation of emission intensity of EMIM-ES ($\lambda_{ex}= 375$ nm) upon gradual increase in the concentration of R6G. The inset indicates that the emission intensity of EMIM-ES decreases with increase in the acceptor concentration (from 0 μ m to 231 μ m).

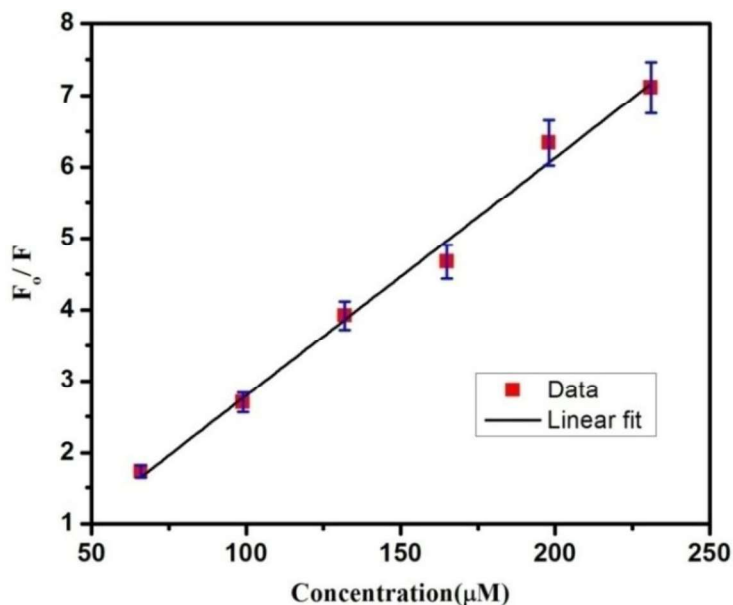


Figure 6.4. Stern-Volmer plot showing the concentration variation change in the fluorescence of the donor (EMIM-ES). The blue lines denote the error bars from the data points. The error bar for the data points is $\pm 5\%$.

6.3.3. Investigation of RET Process through Time-Resolved Measurements

In order to verify whether static or dynamic quenching process is responsible for the present quenching behavior, the fluorescence decay measurements of the donor has been performed using time-correlated single photon counting (TCSPC) technique. The representative decay profile of EMIM-ES in absence and in presence of R6G is given in Figure 6.5 and the relevant decay parameters are collected in Table 6.1.

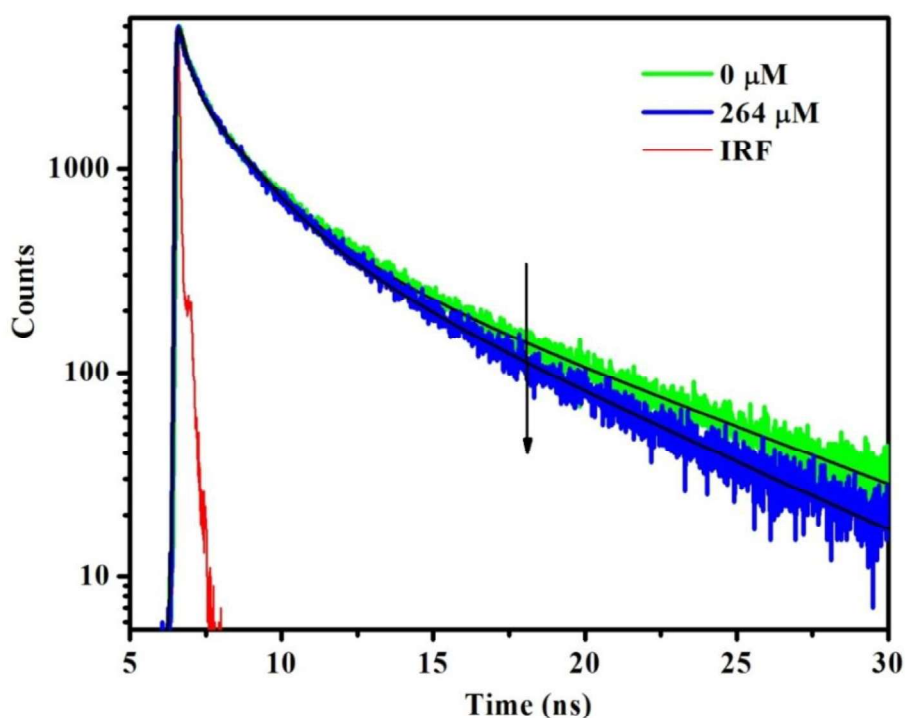


Figure 6.5. Fluorescence decay curves of EMIM-ES without and in the presence of acceptor ($\lambda_{ex} = 375$ nm and $\lambda_{em} = 450$ nm). The solid black lines denote fit to the data points.

It can be seen both from Figure 6.5 and Table 6.1 that as the concentration of the acceptor is increased the lifetime of the donor (RTILs) is decreased. The average lifetime has been found to decrease from 25 % to 20 % when the concentration of acceptor is varied from 0 μ M to 264 μ M (Table 6.1). The decrease of lifetime of the donor upon increase in the concentration of the acceptor indicates that the fluorescence quenching in the present case takes place through

dynamic quenching process. Again, a linear plot as shown in Figure 6.6 is obtained when we plotted τ^0/τ vs. concentration. This data demonstrated that the process is dynamic in nature for the said system.

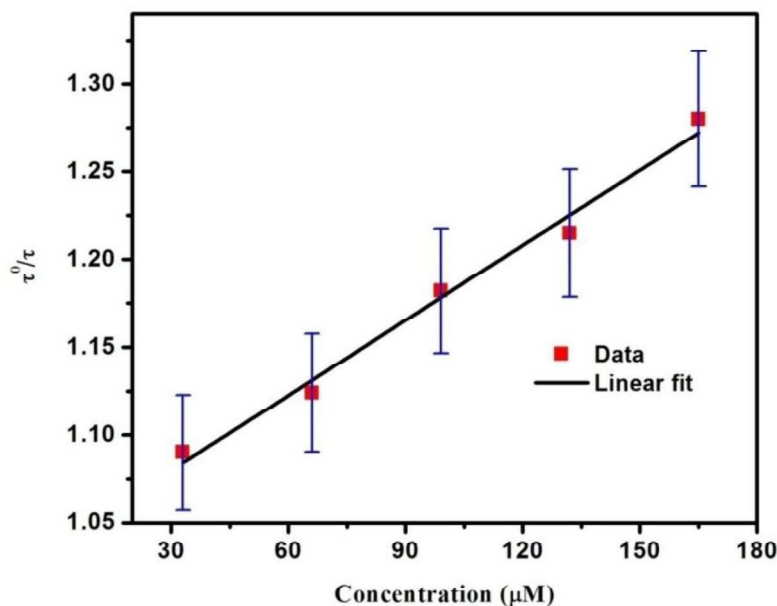


Figure 6.6. Stern–Volmer plot of τ^0/τ vs. concentration for EMIM-ES and R6G system. The blue lines denote the error bars from the data points. The error bar for the data points is $\pm 5\%$.

Even though the decrease of fluorescence lifetime of the donor with increase in the concentration of the acceptor demonstrates dynamic quenching process, it does not exclusively prove that RET between donor (RTILs) and acceptor (R6G) is primarily responsible for the quenching process.^{245, 250} In this context it may also be noted that dynamic quenching can take place due to variety of reasons other than RET.^{245, 250} Therefore, it is necessary to study the RET process more carefully.

Table 6.1. Time constants of fluorescence decay of the donor (RTILs) in the presence of acceptor (R6G) at different concentration (where $\lambda_{ex} = 375$ nm and $\lambda_{em} = 450$ nm)

System	Concentration(μ M)	B ₁	τ_1 (ns)	B ₂	τ_2 (ns)	B ₃	τ_3 (ns)	$\langle\tau\rangle^a$ (ns)
EMIM-ES	0	0.63	0.30	0.29	1.96	0.08	7.53	1.36
	33	0.60	0.21	0.29	1.59	0.11	5.96	1.24
	66	0.59	0.20	0.29	1.50	0.12	5.51	1.21
	99	0.59	0.17	0.29	1.39	0.12	5.39	1.15
	132	0.60	0.17	0.28	1.41	0.12	5.28	1.12
	165	0.60	0.15	0.29	1.36	0.11	5.26	1.06
	198	0.60	0.15	0.29	1.32	0.11	5.22	1.04
EMIM-HS	0	0.48	0.34	0.33	2.14	0.19	6.64	2.13
	33	0.47	0.26	0.33	2.01	0.20	6.24	2.03
	66	0.46	0.18	0.34	1.84	0.20	6.04	1.92
	99	0.46	0.16	0.34	1.74	0.20	5.94	1.85
	132	0.45	0.15	0.35	1.62	0.21	5.66	1.82
	165	0.44	0.14	0.35	1.52	0.21	5.60	1.76
	198	0.44	0.12	0.35	1.48	0.21	5.48	1.72
EMIM-OS	0	0.46	0.36	0.36	2.39	0.18	6.98	2.31
	33	0.45	0.29	0.36	1.90	0.19	6.43	2.03
	66	0.44	0.27	0.36	1.73	0.20	6.04	1.94
	99	0.44	0.24	0.36	1.59	0.20	5.84	1.84
	132	0.43	0.28	0.39	1.48	0.18	5.73	1.72
	165	0.45	0.21	0.36	1.44	0.19	5.57	1.67
	198	0.45	0.21	0.36	1.44	0.19	5.57	1.67
BMIM-NTf ₂	0	0.54	0.31	0.36	3.18	0.10	9.48	2.26
	33	0.56	0.23	0.28	2.42	0.16	7.28	1.97
	66	0.59	0.17	0.25	2.20	0.16	6.92	1.76
	99	0.60	0.16	0.24	2.06	0.16	6.68	1.65
	132	0.61	0.15	0.24	2.12	0.15	6.64	1.59
	165	0.61	0.15	0.25	2.10	0.14	6.67	1.55
	198	0.61	0.15	0.25	2.10	0.14	6.67	1.55
BMPyr-NTf ₂	0	0.57	0.24	0.32	1.78	0.11	6.46	1.42
	33	0.58	0.22	0.30	1.54	0.12	5.93	1.30
	66	0.57	0.18	0.30	1.42	0.13	5.50	1.24
	99	0.59	0.16	0.29	1.46	0.12	5.63	1.19
	132	0.60	0.19	0.29	1.48	0.11	5.76	1.17
	165	0.61	0.17	0.28	1.42	0.11	5.74	1.13
	198	0.61	0.17	0.28	1.42	0.11	5.74	1.13
TBMA-NTf ₂	0	0.58	0.27	0.34	1.68	0.08	7.99	1.58
	33	0.57	0.26	0.32	1.62	0.10	7.30	1.42
	66	0.57	0.25	0.31	1.68	0.11	7.11	1.36
	99	0.60	0.32	0.28	1.72	0.12	6.86	1.28
	132	0.61	0.31	0.25	1.74	0.14	6.76	1.22
	165	0.62	0.34	0.23	1.76	0.15	6.68	1.18
	198	0.62	0.34	0.23	1.76	0.15	6.68	1.18
TOMA-NTf ₂	0	0.48	0.38	0.33	1.98	0.19	6.78	2.46

33	0.51	0.37	0.32	2.08	0.21	6.68	2.32
66	0.53	0.35	0.28	2.11	0.20	6.62	2.22
132	0.54	0.32	0.26	2.21	0.21	6.56	2.12
165	0.56	0.29	0.22	2.28	0.22	6.51	1.92

^aExperimental error = $\pm 5\%$

In order to check whether RET is happening or not, the fluorescence decay behavior of the acceptor moiety has also been carefully monitored. If RET is operational between RTILs and R6G then a clear rise in the fluorescence intensity decay profile of the acceptor on a shorter time scale followed by a decay on a longer time scale is expected to be seen.^{245, 250, 251} Decay profile of the acceptor (R6G) in presence of donor (EMIM-ES) are shown in Figure 6.7 and data are collected in Table 6.2. A clear rise (see inset of Figure 6.7) followed by decay of the acceptor (Figure 6.7) unambiguously proves that the donor (RTILs) and acceptor (R6G) are in RET communication. In order to understand whether RET depends on the alkyl chainlength of anions, the energy transfer studies has also been carried out by employing anions having different anions chain length (ethyl, hexyl and octyl) with a fixed cation (1-ethyl-3-methyl imidazolium). The relevant parameters corresponding to the RET process for different donor (RTIL)-acceptor (R6G) pair are provided in Table 6.2. As can be seen from Table 6.2, the rise time has also been observed for other RTIL-R6G pairs. However, the rise time, which indicates the time constant of RET process, is observed to depend on the alkyl chain length (Table 6.2). For example, the time constant for RET is found to increase from 0.58 ns to 1.66 ns upon going from smaller (EMIM-ES) ethyl derivative to larger octyl (EMIM-OS) system (Table 6.2). Recently literature reports^{168, 212} based on the outcomes of FRET studies in constrained media (ionic liquid based micellar system etc.) have demonstrated that the time scale of FRET (rise time) increases upon increase in the size of the micelles. Essentially a change in the rise time is expected to arise because of the change in the donor-acceptor distance caused due to change in the structural organization of the

concerned media. In light of this argument we can also say that in the present case the increase of rise time upon increasing the alkyl chainlength (ethyl to octyl) is caused due to a change in the structural organization from EMIM-ES to EMIM-OS. We would also like to note here that recent studies^{186, 347} have shown that smaller alkyl chain containing sulfate RTIL shows stronger anion-cation interaction and efficient packing as compared to the larger alkyl chain containing system. Interestingly, a decrease in electrical conductivity with increasing alkyl chainlength of sulfate RTILs has also been observed.³⁴⁷ The outcomes of these studies have also indicated that the length of alkyl side chains play important role in governing the nanostructural organization of sulfate RTILs.

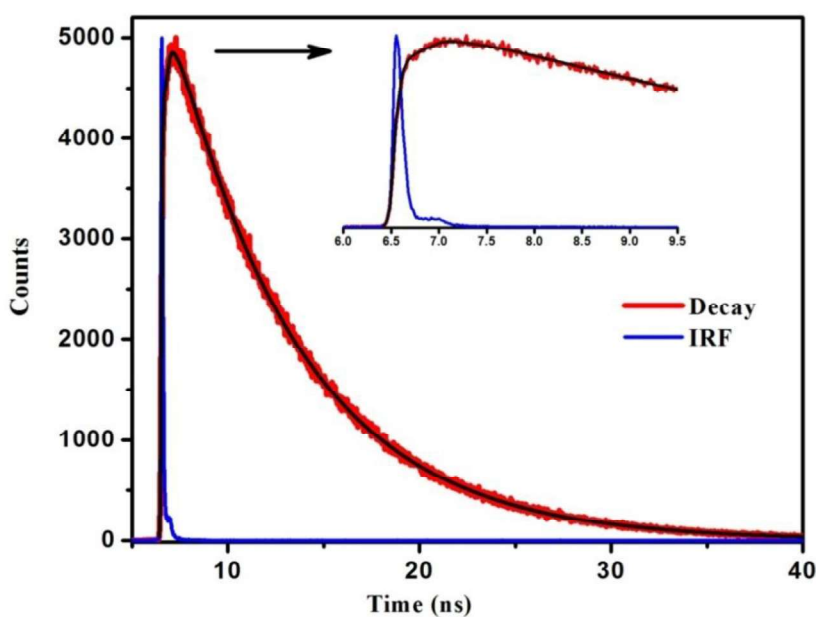


Figure 6.7. Fluorescence decay curve of the acceptor (R6G) ($\lambda_{\text{ex}} = 375 \text{ nm}$ and $\lambda_{\text{em}} = 580 \text{ nm}$; concentration of acceptor = $231 \mu\text{M}$) in presence of donor (EMIM-ES). A clear rise has been shown in the inset. The solid black line indicates fit to the data points.

Table 6.2. Time constants of fluorescence decay of the acceptor (R6G) in difference concentration

System	Concentration (μM)	Life time $\langle \tau \rangle^a$ (ns)	Rise time ^a (ns)
EMIM-ES	132	6.82	0.58
	165	6.97	0.59
EMIM-HS	132	6.73	1.22
	165	6.84	1.20
EMIM-OS	132	6.58	1.66
	165	6.72	1.69
BMIM-NTf ₂	198	5.78	1.94
	231	5.92	1.97
BMPyr-NTf ₂	132	6.92	1.12
	165	7.12	1.14
TBMA-NTf ₂	132	1.04	6.73
	165	1.06	6.84
TOMA-NTf ₂	132	1.86	6.54
	165	184	6.68

^aExperimental error = $\pm 5\%$

To get further insights into the microscopic structural organization of RTILs, the data obtained from RET experiments have been analyzed further in light of Förster theory.^{245, 250, 251} According to this theory, the degree of the spectral overlap ($J(\lambda)$) can be calculated by using equation 6.1

$$J(\lambda) = \int d\lambda F_D(\lambda) \varepsilon(\lambda) \lambda^4 \quad (6.1)$$

where $F_D(\lambda)$ is the donor emission spectrum, normalized to an area of 1, $\varepsilon(\lambda)$ is the molar absorption coefficient of the acceptor. The Förster radius = R_0 . The Förster radius (R_0) is obtained by using equation 6.2

$$R_0 = 0.211 [\kappa^2 \Phi_D n^{-4} J(\lambda)]^{1/6} \quad (6.2)$$

where κ^2 = orientation factor and $\kappa^2 = 2/3$ for fast and random donor-acceptor orientations. We would like to take a note here that $\kappa^2 = 2/3$ has also been used previously by other researchers while calculating FRET for different RTIL-based systems.^{168-172, 212, 213} Please note that the values of κ^2 lie in the range of 0 to 4.¹⁶⁸⁻¹⁷² The zero value of κ^2 indicates no RET process. Since

in the present donor-acceptor system the donor (RTILs) and acceptor (R6G) are in RET communication, the value of κ^2 is expected to be greater than 0. In general, the value of κ^2 is used as 2/3 for the random orientation of transition dipoles. Moreover, literatures shows that the calculated Förster distance is found to vary slightly in the entire range of κ^2 values.¹⁶⁹⁻¹⁷¹ Because of this reason in the present study we have used $\kappa^2 = 2/3$ (random orientation) for the calculation of Förster distance. Φ_D = quantum yield of donor in absence of acceptor and n = refractive index of the medium. Again, the rate of energy transfer (K_{RET}) and the donor-acceptor distance (R_{DA}) can be calculated by using equation 6.3

$$K_{RET} = \frac{1}{\tau_{rise}} = \frac{1}{\tau_D^0} \left(\frac{R_0}{R_{DA}} \right)^6 \quad (6.3)$$

where τ_{rise} = rise time of the acceptor, τ_D^0 = life time of the donor in absence of the acceptor, R_0 = Förster radius and R_{DA} = donor-acceptor distance. Energy transfer efficiency is the fraction of donor deactivation events caused by FRET.²⁴⁵ Thus, it is also the ratio of FRET rate over the sum of all rates of donor deactivation. The energy transfer efficiency (E) is calculated by using equation 6.4

$$E = R_0^6 / (R_0^6 + R_{DA}^6) \quad (6.4)$$

The rise time has been used to calculate E and R_{DA} so that a better accuracy in the calculation is obtained. The relevant FRET parameters that are estimated by using Förster theory are summarized in Table 6.3. As can be observed from the Table 6.3, upon increasing the length of alkyl side chain on the anionic moiety (EMIM-ES to EMIM-OS), the magnitude of spectral overlap ($J(\lambda)$), rate of energy transfer (K_{RET}) and energy transfer efficiency (E) decreases. Importantly, the donor-acceptor distance (R_{DA}) is found to increase with increasing the anion chainlength i.e. from ethyl to octyl.

Table 6.3. The magnitude of relevant RET parameters

System	Φ_D	$J(\lambda) (10^{16})$ $(M^{-1}cm^{-1}nm^4)$	τ_D^0 (ns)	τ_{rise} (ns)	R_0 (Å)	R_{DA} (Å)	E	K_{RET} ($10^8 s^{-1}$)
EMIM-ES	0.01	3.56	1.36	0.58	40.35	35.0	70	17.24
EMIM-HS	0.03	3.38	2.13	1.22	48.13	43.9	65	7.57
EMIM-OS	0.04	3.18	2.31	1.66	50.21	47.5	58	6.02
BMIM-NTf ₂	0.02	1.82	2.26	1.94	41.55	40.5	54	5.10
BMPyr-NTf ₂	0.01	1.58	1.42	1.12	36.27	34.9	56	8.92
TBMA-NTf ₂	0.07	2.17	1.58	1.06	52.77	49.0	60	9.43
TOMA-NTf ₂	0.13	1.89	2.46	1.86	57.88	54.8	57	5.37

An increase in the donor-acceptor distance (R_{DA}) from 35.0 Å to 47.5 Å has been observed upon going from EMIM-ES to EMIM-OS (Table 6.3). Here we note that the neat RTILs exist in associated structures, and form polar and nonpolar domains.^{186, 201, 346} In this context, the work by Leal and coworkers³⁴⁶ on alkylsulfate ionic liquids is noteworthy. With the help of both theory and experiments they have demonstrated that while the fluid structure of RTIL like [BMIM][PF₆], having smaller/spherical anions (PF₆⁻), is dominated by polar domains, fluid structure of neat 1-butyl-3-methylimidazolium octyl sulfate RTIL is dominated by apolar domains formed by alkyl chains.³⁴⁶ Simulation studies reveal that in the octylsulfate RTIL, nonpolar domains disrupt the polar domain and spread through the polar domains of the RTIL.³⁴⁶ With the outcome of this study one can say that the dominance of apolar domain, created by alkyl chains, over the polar domain will be relatively less in the fluid structure of smaller alkyl group containing system EMIM-ES than the larger EMIM-OS. And because of these structural

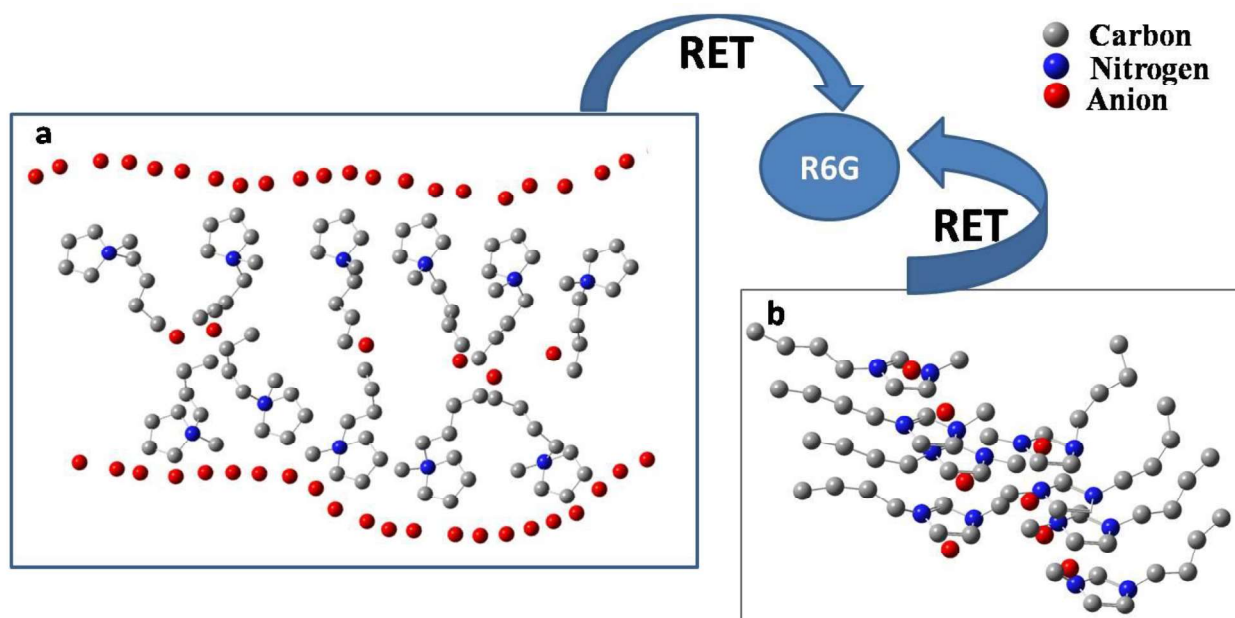
arrangements, it is expected that electrostatic (charge-charge) interaction between a charged probe like R6G (acceptor in the present study) and RTIL will be more favorable in case of EMIM-ES than that in EMIM-OS. As a result of this, the significant variation of the energy transfer efficiency (E) and the donor-acceptor distance (R_{DA}) upon changing the alkyl chain length of the concerned RTILs are observed in the present study. Therefore, essentially these data demonstrates the influence of alkyl side chain length on the anionic moiety towards the structural organization of alkylsulfate RTILs. Here, we would like to note that Cabeza and coworkers³³⁷ have demonstrated that neat 1-ethyl-3-methylimidazolium octyl sulfate RTIL forms gel type materials when mixed with water. However, other smaller members (e.g. ethyl or hexyl) cannot form such a gel when mixed with water.³³⁷

Again, in order to understand whether the nature of cations has any influence on the RET process due to the difference that may have in their microscopic structural organization, the RET investigation has also been carried out by introducing one imidazolium (BMIM-NTf₂) and one pyrrolidinium (BMPyr-NTf₂) cation based RTIL, where in both the cases anion is fixed (NTf₂). The length of the alkyl side chain length on the cation has also been purposefully kept constant in both the RTILs so that the effect of chain length remains same in both cases, but the influence of the nature of the cation on the RET process, if any, should become apparent during the study. In this context it may be mentioned again that recent studies based on theoretical calculations have indicated that imidazolium and pyrrolidinium cation can induce different structural organization/ordering to microstructure of RTILs.^{151, 152}

Interestingly, during the FRET experiments, different rise time (consequently K_{RET}) has been observed for BMIM-NTf₂ and BMPyr-NTf₂ (Table 6.2). Moreover, energy transfer efficiency (E) and donor-acceptor distance (R_{DA}) are also observed to be quite different in case of

BMIM-NTf₂ and BMPyr-NTf₂ RTILs (Table 6.3). It should also be noted that even though the nonpolar alkyl chainlength is same in both the RTILs, the donor-acceptor distance (R_{DA}) is found to be 40.5 and 34.9 Å for BMIM-NTf₂ and BMPyr-NTf₂, respectively (Table 6.3). These results demonstrate that the RET is not only dependent on the chainlength, but also depends on the nature of the cationic moiety of RTIL. However, it may also be noted here that the difference in the FRET parameters (donor-acceptor distance) for BMIM-NTf₂ and BMPyr-NTf₂ may also arise other than the planarity effects. The conjugated/non-conjugated ring, the di-nitrogen imidazolium ring vs. single-nitrogen pyrrolidinium, and the placement of the methyl and butyl substituents on the ring, may also impact the RET parameters. The present data for BMIM-NTf₂ and BMPyr-NTf₂ RTIL systems are interesting as this may help to understand the structural organization of imidazoleum and pyrrolidinium-based RTILs. The experimental observations of the RET experiments for BMIM-NTf₂ and BMPyr-NTf₂ systems can be explained with the help of a schematic model (Scheme 6.1). The model has been proposed based on the outcomes of the theoretical studies on the imidazolima and pyrrolidinium-based ionic liquid systems.^{151, 152} Since in BMPyr-NTf₂, the cation is ammonium type, it may exists in lamellar¹⁵¹ type structures. As is shown in Scheme 6.1(a), in lamellar type structure the alkyl group and the cationic moiety are segregated together and the cation are placed up or down and half of the anion are situated between the cation and alkyl group.¹⁵¹ Therefore, in case of ammonium type RTIL system, the alkyl (here, butyl) groups of cations can locate themselves inside and the polar groups (anions and cations) on the outside (Scheme 6.1(a)). Because of this geometrical arrangement in the ammonium RTIL, bulkier alkyl group do not pose any restrictions on the acceptor (R6G) molecule to come close to the RTIL core and have efficient FRET interaction with donor RTIL. However, in BMIM-NTf₂, the cation is planar imidazolim, and can exists in bilayer type

structure where the alkyl chain of the cation can reside outside and the polar groups inside (Scheme 6.1(b)).¹⁵² As a result of this arrangement, the bulkier alkyl group, which is exposed outside, creates hindrance to the incoming acceptor molecule for an efficient donor (RTIL) acceptor (R6G) interaction (Scheme 6.1(b)). Therefore, because of the difference in the structural organization of BMIM-NTf₂ and BMPyr-NTf₂ more efficient RET is observed in BMPyr-NTf₂ than that in BMIM-NTf₂. The present data is interesting in a sense that the outcome of this experimental work would be helpful in understanding the structural organization and microstructure of imidazolium and pyrrolidinium RTILs.



Scheme 6.1. Schematic representation of RET between donor (RTIL) and acceptor (R6G) (a) Lemellar type structure of BMPyr-NTf₂.¹⁵¹ (b) Bilayer structure of BMIM-NTf₂.¹⁵²

Again, to investigate the effect of branching on the cationic moiety of RTILs, we have exploited the RET studies by employing two branched RTILs, such as tributylmethylammonium (TBMA) and trioctylmethylammonium (TOMA), where in both the cases anion is fixed (NTf₂), but the alkyl chainlength are varied in the branch. Interestingly, during the FRET experiments, the different rise time (τ_{rise}) has been observed for TBMA-NTf₂ and TOMA-NTf₂ (Table 6.2).

Moreover, energy transfer efficiency (E) and donor-acceptor distance (R_{DA}) are also observed to be quite different in case of TBMA-NTf₂ and TOMA-NTf₂ (Table 6.3). For example, the donor-acceptor distance (R_{DA}) is found to be 49.0 and 54.8 Å for TBMA-NTf₂ and TOMA-NTf₂, respectively (Table 6.3). This results indicate that the RET is dependent on the overall size of the branch. We would like to note here that Leal and co-workers³⁴⁶ through both theory and experiments have shown that apolar alkyl chain can permeate to polar domain and fluid structure of an apolar alkyl chain containing IL can be dominated by the apolar chain. Naturally, the dominance of apolar chain on the fluid structure of RTILs would be more for larger alkyl chain containing system. Keeping in mind the outcome of the Leal and co-workers³⁴⁶ on the influence of apolar alkyl chainlength on the polar domain, perhaps we can also say here that fluid structure of branched RTILs would also be dominated by alkyl chainlength in the branch and because of this the non-polar group would screen the charge density of polar domain. This factor would restrict the approach of the charged acceptor molecules to donor molecule. Due to this reason the donor-acceptor distance would be relatively more for larger alkyl chain containing RTILs than the same for smaller one. Therefore, upon increasing the alkyl chainlength on the cationic branch i.e upon going from TBMA-NTf₂ and TOMA-NTf₂, the donor-acceptor distance between RTILs and the R6G increases. Intuitively, we can also say that steric crowding due to branched chains would also restrict the acceptor molecule to come close to the donor molecule. As a result, the RET efficiency (E) decreases upon going from smaller branched IL to relatively higher branched IL (see Table 6.3). In this context we would like to mention that while working on the influence of alkyl chainlength on the cationic moiety of imidazolium based RTILs, Mandal and coworkers²¹² have not observed any change in the donor-acceptor distance with increasing the linear alkyl chainlength on the cation. However, in the present case, we have seen a significant

change in the donor-acceptor distance with increasing the overall size of the branch on the cationic moiety (Table 6.3). Therefore, these data indicate that the structural organization of branched and linear chain RTILs is quite different. We also note here that excitation wavelength dependent RET studies have also been carried out by exciting the samples at two different wavelengths (375 nm and 405 nm). However, no significant changes of RET parameters have been observed at these wavelengths.

In recent times, it has been shown that organogel-based materials have the potential to be used in many energy related applications.³⁴⁸ Recently, RTIL-based gel materials have also been developed.^{337, 349} We have also prepared a novel RTIL-based gel material in view of its potential use in materials science. In the present study, the RTIL-based gel is prepared by heating the mixture of guar gum (natural polysaccharide) with neat RTIL (EMIM-OS) for several hours at 373 K, followed by cooling at room temperature which results in the EMIM-OS/guar gum gel.³⁴⁹ The gel is characterized by visual appearance and by thermogravimetric analysis (TGA) (Figure 6.8). The EMIM-OS/guar gum gel exhibits broad emission band (Figure 6.9). Again the EMIM-OS/guar gum/R6G gel has also been prepared by using the mixtures of EMIM-OS, guar gum and R6G (198 μ M). The fluorescence spectra of EMIM-OS/guar gum/R6G gel are provided in Figure 6.9. Interestingly, it can be observed from Figure 6.9 that upon introduction of the R6G, the fluorescence intensity of the RTIL (EMIM-OS) peak decrease significantly in the EMIM-OS/guar gum/R6G gel as compared to that of the EMIM-OS/guar gum gel.

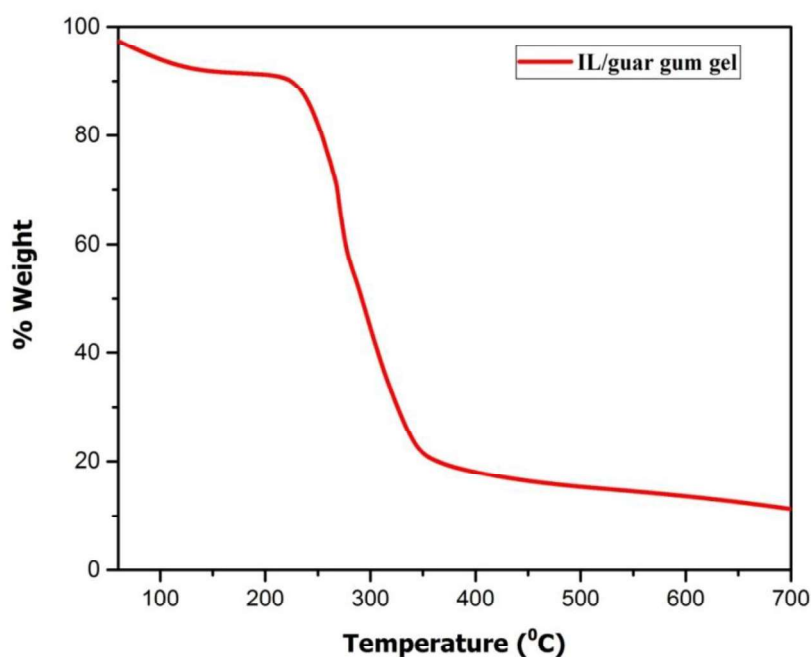


Figure 6.8. Thermogravimetric analysis (TGA) spectrum of RTIL (EMIM-OS) /guar gum gel.

Moreover, a clear rise time (0.24 ns) of the acceptor (R6G) has also been observed (Figure 6.10). These observations indicate the occurrence of RET process between RTIL and R6G also in gel medium (EMIM-OS/guar gum/R6G). The rate (K_{RET}) of RET process and energy transfer efficiency (E) for gel medium are found to be $4.16 \times 10^9 \text{ s}^{-1}$ and 77 respectively. Interestingly, it can be observed both from the fluorescence spectrum and fluorescence microscopic image (Figure 6.11) that in the gel (EMIM-OS/guar gum/R6G) fluorescence originates due to R6G rather than RTIL. The present RTIL-based gel has the potential to be used as a fluorescent gel material for various applications. Further studies in this direction are in progress in our laboratory.

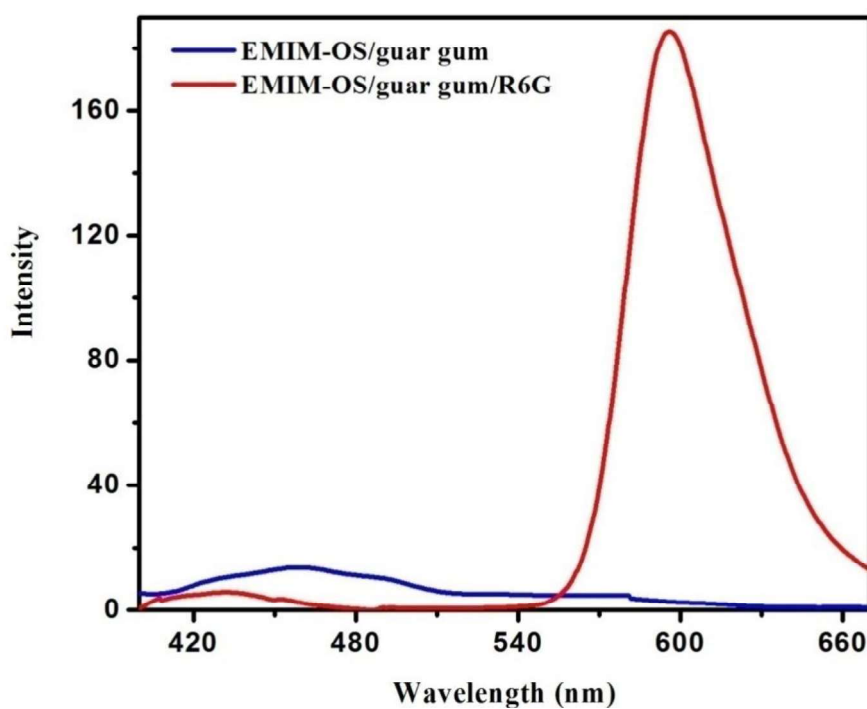


Figure 6.9. Emission spectra of EMIM-OS/guar gum and EMIM-OS/guar gum/R6G gel ($\lambda_{ex} = 375$ nm).

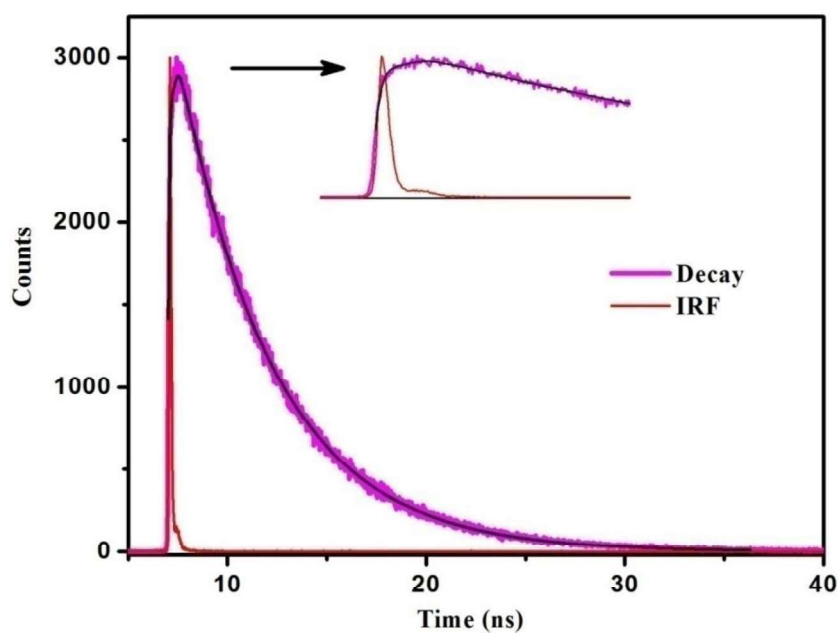


Figure 6.10. Fluorescence decay curve of the acceptor (R6G) ($\lambda_{ex} = 375$ nm and $\lambda_{em} = 580$ nm) in EMIM-OS/guar gum/R6G gel system. The solid black line denotes fit to the data points.

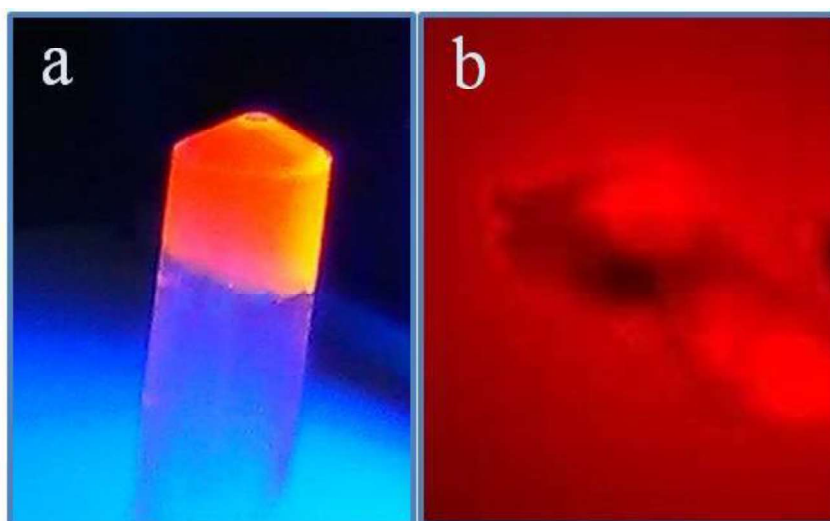


Figure 6.11. Image of (a) EMIM-OS/guar gum/R6G gel in presence of UV- irradiation and (b) Fluorescence microscopic images of EMIM-OS/guar gum/R6G gel when excited at 488 nm.

6.4. Conclusion

In the present report, studies on RET process between the RTILs (donor) and R6G dye (acceptor) have been investigated with an aim to understand the role of ionic constituents of RTILs on their structural organization. It has been observed that the anion chainlength, nature of cations and branching on cationic moiety of RTILs strongly influence the RET process. With increasing the anions chainlength of alkyl sulfate RTILs i.e. from EMIM-ES to EMIM-OS, the donor-acceptor distance (R_{DA}) is found to increase and FRET efficiency is found to decrease. This has been explained on the basis of the fact that fluid structure of smaller alkyl group containing system EMIM-ES and larger EMIM-OS are quite different. It has also been observed that the nature of cations of RTILs also affects the RET process significantly. The shortest R_{DA} and consequently higher energy transfer efficiency is found between the BMPyr-NTf₂ and R6G pair as compared to the BMIM-NTf₂ and R6G. These experimental observations have been attributed to the difference in the nanostructural organization of BMIM-NTf₂ and BMPyr-NTf₂ systems. This fact is explained by considering the outcome of the theoretical studies on imidazolium and

pyrrolidinium ionic liquid based system, according to which the BMPyr-NTf₂ exists in lamellar type of structure whereas BMIM-NTf₂ remains in bilayer type structure. Again the R_{DA} between RTILs and the R6G increases upon increasing the alkyl chainlength on the cationic branch i.e upon going from TBMA-NTf₂ to TOMA-NTf₂. This is because of the non-polar branched group restricts the acceptor (R6G) to come to close to donor (RTILs) molecule. Additionally, observation of RET process also in a RTIL-based gel system indicate the potential use of this fluorescent gel materials for future applications. The outcomes of the present study are expected to be helpful to provide comprehensive and quantitative picture which will entail a significant step forward in our understanding of the subtleties of the nano structural organization of various type of RTILs.

Chapter 7

Influence of Ionic Liquids on the Aggregation Behavior of 4-Aminophthalimide (AP) and 4-(N,N-Dimethyl) Amino-N-Methylphthalimide (DMP)

This chapter describes the aggregation behavior of two fluorescent molecules, 4-aminophthalimide (AP) and 4-(N,N-dimethyl)amino-N-methylphthalimide (DMP). The present work has been investigated to get an idea about the effect of intermolecular hydrogen bonding interactions on the aggregation behavior of these molecules. Additionally, the influence of ionic liquids (ILs) on the aggregates of both AP and DMP has also been demonstrated. The outcome of the present study demonstrates that intermolecular interactions play an important role for the formation of aggregated states through self assembly of molecules and fine tuning of intermolecular interactions may lead to different mode of aggregations. Longer alkyl chain containing IL is found to be helpful in dissociating the colloidal aggregates.

7.1. Introduction

Design and development of molecular materials form an important area of contemporary research owing to their wide range applications. This is mainly because of the fact that their physicochemical properties are found to lie between the properties of molecular and bulk forms.³⁵⁰ In this context, development of organic nano/microparticles appears to be quite attractive as they offer much more variability and flexibility in material design and synthesis as compared to inorganic ones that are based on atomic or ionic lattice.³⁵¹⁻³⁵⁵ Nevertheless, organic nano/microparticles are promising molecular materials for optoelectronic devices,^{356, 357} sensor applications³⁵⁸ etc. Several studies have been carried out in recent years demonstrating mainly

fabrication³⁵⁹⁻³⁶² of organic nanomaterials and much less emphasis has been given to understand how different modes of aggregation lead to changes in the optical properties of these molecules.³⁶³⁻³⁷⁴

Organic nanocrystals are generally formed by the self-assembly of the individual monomer, which acts as driving force for synthesis of nanoparticles. Driving forces for self-assembly are based on different intermolecular forces like van der Waals interaction, hydrogen bonding, co-ordination bonding, and π - π stacking etc.³⁷⁵⁻³⁷⁷ The impact of various intermolecular interactions can be realized as the crystal evolves from the nanoscopic size domain to a microcrystalline and bulk solid.^{355, 378} Moreover, intermolecular interactions also play an important role in influencing the electronic properties of organic nano/micro particles.³⁵³ For example, aggregation-induced emission from organic nano/microcrystal are believed to be caused by changes in the intermolecular vibronic interactions from molecular to aggregated states.³⁷⁹ Hence, it is extremely important to understand the correlation among intermolecular interactions, structure and optical properties of organic nano/micro crystals so that organic molecular materials having desired electronic properties are designed and developed for future applications.

In recent times, it has been observed that micelles can act as an excellent media for encapsulation of small drug molecules, which can eventually help to increase the solubility of drug molecules in solution.³⁸⁰⁻³⁸² Surfactants like sodium dodecyl sulfate (SDS), TRITON-X, cetyltrimethylammonium bromide (CTAB) are usually used for the preparation of micelles.^{383, 384} Recently long alkyl chain ionic liquids (ILs) or surface active ionic liquids (SAILs) have also been used for the preparation of micelles. Some studies have revealed that SAILs can act as better systems for the formation of micelles over conventional surfactants.³⁸⁵⁻³⁸⁷ Moreover,

SAILs possess some interesting properties such as low toxicity, high thermal stability, negligible vapour pressure etc.³⁸⁸ Since micelles can influence the structure of aggregates, it would be very interesting to understand the effect of ILs, particularly SAILs, towards the AP and DMP aggregates.

Considering the above-mentioned facts, in the present study, we have investigated the photophysical behaviors of the two fluorescent molecules 4-aminophthalimide (AP) and 4-(N,N-dimethyl)amino-N-methylphthalimide (DMP), in molecular as well as aggregated forms. As can be seen, in DMP, all hydrogen atoms of AP have been replaced by methyl groups so that the effect of hydrogen bonding interactions (N-H \cdots) towards aggregation behavior is exclusively monitored. Among the two probes, 4-aminophthalimide (AP) is a highly fluorescent probe that has been extensively applied in biopolymers.³⁸⁹⁻³⁹² It has also been used for studies on the solvation and rotational dynamics in different solvents including ionic liquids.³⁹³⁻³⁹⁵ Absorption, fluorescence emission, fluorescence lifetime and quantum yield of AP undergo significant changes with changing polarity of the solvent.³⁹⁶⁻³⁹⁹ The influence of ILs on the aggregates of both AP and DMP have also been investigated by employing one short alkyl chain containing IL, namely, 1-butyl-3-methylimidazolium bromide ([C₄(mim)]Br) and another long alkyl chain containing IL, 1-Dodecyl-3-methylimidazolium bromide ([C₁₂(mim)]Br). The molecular structure of AP, DMP and ILs are provided in Chart 7.1.

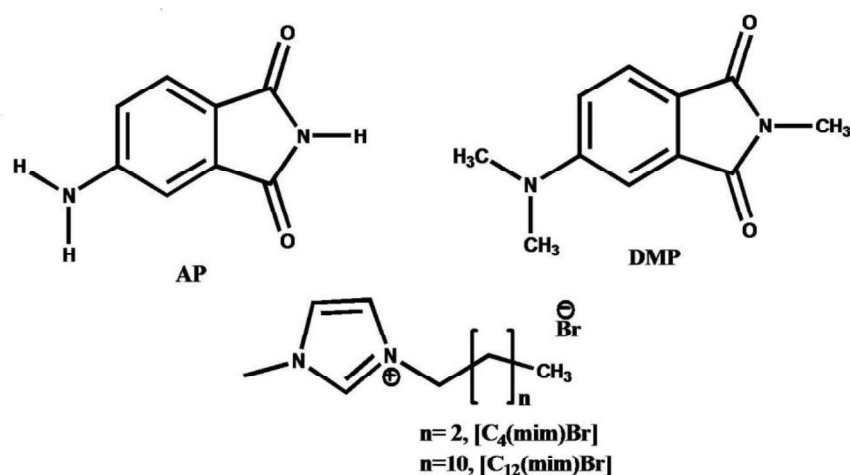


Chart 7.1. Molecular structures of AP, DMP and ILs.

All the aggregates are characterized via field emission scanning electron microscope (FESEM) imaging techniques. Crystallographic analysis has been done to get further insight into the various forces of interaction that may be responsible for the aggregation behavior of these two EDA systems. Photophysical investigations on these well characterized systems have been carried out. A red and blue shift in absorption spectrum of the aggregates indicates the formation of H and J aggregates for AP and DMP respectively. Theoretical studies (DFT and TD-DFT) have been carried out to investigate how different modes of aggregation lead to changes in the UV-VIS spectra of these molecules. Influence of ILs on their aggregation behavior has also been demonstrated.

7.2. Experimental Sections

7.2.1. Materials

4-aminophthalimide and other starting materials for synthesis of DMP such as 5-amino-2-methylisoindoline-1, 3-dione, paraformaldehyde, Sodium cyanoborohydride ($NaBH_3CN$), and ethyl acetate were obtained from Sigma-Aldrich and used as received without further purification. For photophysical studies, HPLC grade dimethyl sulfoxide (DMSO) and for NMR

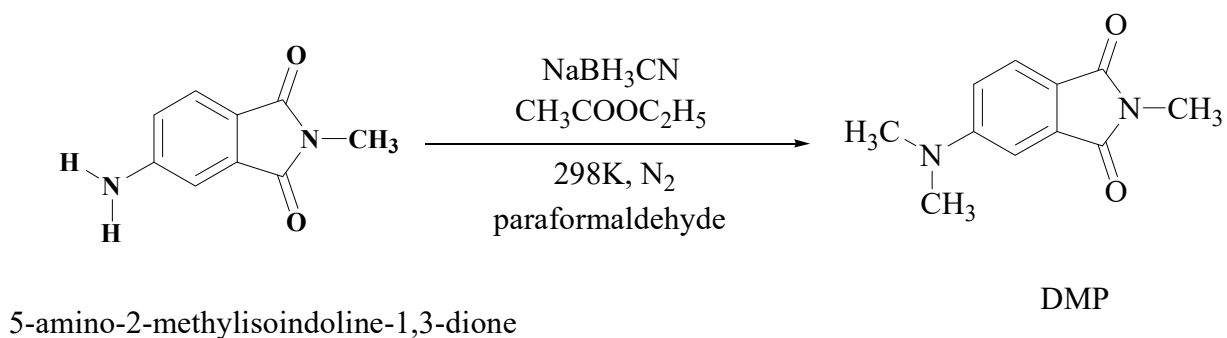
studies DMSO-d₆ were procured from Sigma-Aldrich and used without further purification. [C₄(mim)]Br was obtained from Io-il-tech. [C₁₂(mim)]Br was synthesized by following the literature procedure.⁴⁰⁰ The product was characterized by ¹H-NMR and mass spectrometry analysis.

[C₁₂(mim)]Br: ¹H-NMR: (DMSO-d₆): 9.12 (s, 1H), 7.77 (s, 1H), 7.70 (s, 1H), 4.14 (t, 2H), 3.84 (s, 3H), 1.76 (m, 2H), 1.23 (m, 18H), 0.85 (t, 3H).

ESI-MS: 252 (M + H)⁺.

7.2.2. Synthesis and Characterization of DMP

DMP has been synthesized by the reaction of 5-amino-2-methylisindoline-1, 3-dione and paraformaldehyde in presence of sodium cyanoborohydride (NaBH₃CN), ethyl acetate (25ml) was used as solvent in reflux condition in N₂ atmosphere (Scheme 7.1). After synthesis, DMP was characterized by ¹H NMR spectroscopic and Mass spectrometric analysis.



Scheme 7.1. Synthetic route of DMP molecule

¹H-NMR; (DMSO-d₆): 3H(s, 2.98), 6H(s, 3.08), 1H (d, 6.90), 1H(s, 7.00) 1H (d, 7.59)

ESI-MS: 205(M+H⁺). Yield 85%

7.2.3. Preparation of AP and DMP Solution

A dilute $\sim 10^{-6}$ (M) solution of AP and DMP in DMSO were used for the photophysical investigation of molecular form.

7.2.4. Preparation and Characterization of AP and DMP Aggregate

The AP and DMP aggregate were prepared by the reprecipitation method. Typically 30 μ L of a DMSO solution of AP (0.01 M) was rapidly injected into 3mL of Milli-Q-water with vigorous stirring. After addition, the stirring was continued for 15 minutes. To confirm aggregation, FESEM images of AP and DMP aggregates were taken. To prepare the FESEM sample, freshly prepared aggregate solution was coated on cleaned alumina-foil and kept for drying.

7.3. Results and Discussion

7.3.1. Optical Studies of AP and DMP in Molecular Form

The absorption spectra of AP and DMP have been recorded in DMSO medium. The absorption spectra of both AP and DMP are provided in Figure 7.1. While the absorption maximum of AP appears at 374 nm, DMP shows a peak maximum at 397 nm. The 23 nm red shift of absorption maximum for DMP can be attributed to the greater inductive effect of the electron donating methyl group in DMP derivative. The red-shift of absorption is also supported by the estimated ground state dipole moment values of AP (5.29 D)³⁹⁹ and dimethyl analogue (N, N dimethyl 4 aminophthalimide) of AP (5.65 D). The molar extinction coefficient for AP and DMP are estimated to be $5 \times 10^3 \text{ M}^{-1}\text{cm}^{-1}$ and $6 \times 10^3 \text{ M}^{-1}\text{cm}^{-1}$ at their respective absorption maxima. These spectroscopic data indicates that absorption band for AP and DMP are of intramolecular charge transfer (ICT) in nature.

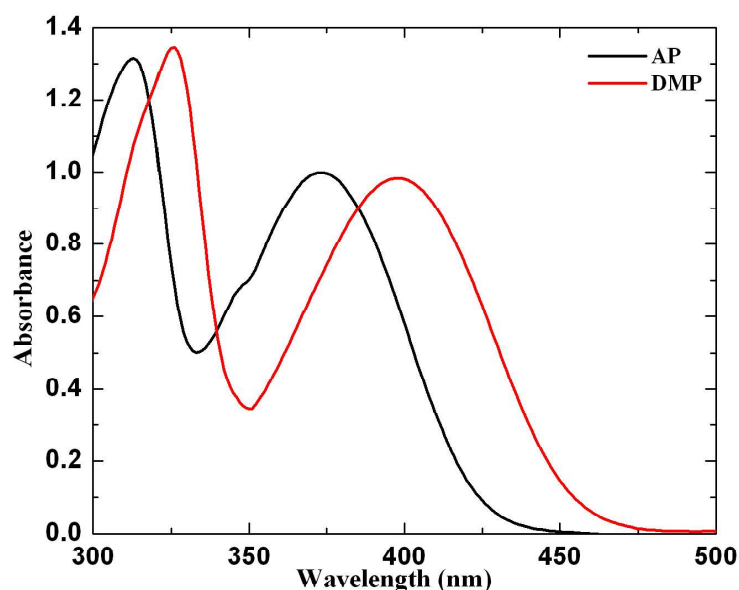


Figure 7.1. Absorption spectra of AP and DMP in molecular form in DMSO (5×10^{-6} M) solution at room temperature. Spectra are normalized at respective lowest energy peak maxima.

The steady state emission spectra of AP and DMP in DMSO are shown in Figure 7.2. The emission maxima for AP and DMP are found to be at 474 nm and 519 nm, respectively. The bathochromic shift in emission maxima on going from AP to DMP is found to be more (45 nm) as compared to the shift in absorption spectra (Figure 7.1). This observation indicates that the change in dipole moment from AP to DMP in the excited state is more as compared to the same for them in the ground state. Interestingly, the emission intensity is observed to be significantly less for DMP as compared to the same for AP. In fact, quantum yield of DMP is found to be ~ 10 fold lower than that of AP. This observation can be rationalized by considering the presence of non-fluorescent TICT state below the ICT state of DMP in polar medium.³⁹⁹

Fluorescence decay times are also measured for AP and DMP in DMSO. A representative fluorescence decay profile of AP and DMP are shown in Figure 7.3. The lifetime of AP molecule ($\tau = 18.5$ ns) is observed to be significantly higher than that of DMP molecule ($\tau = 0.280$ ns).

The lower lifetime value in case of DMP also indicates the presence of non-radiative decay pathway occurring from ICT→TICT energy level.³⁹⁹

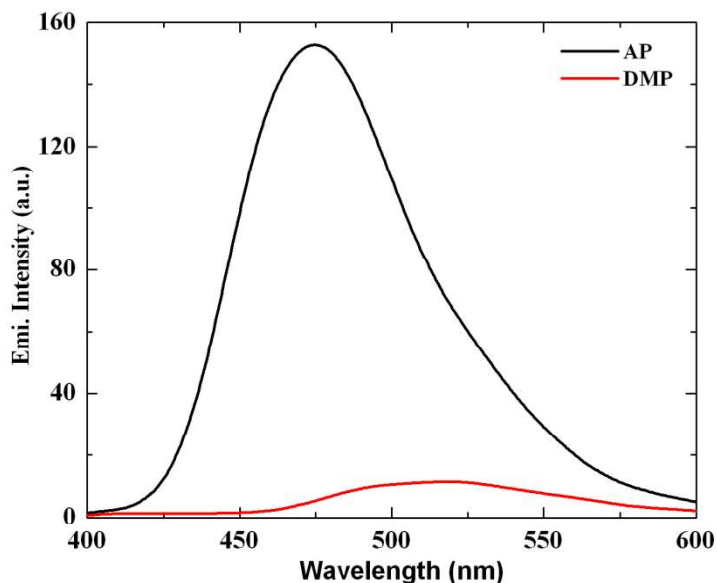


Figure 7.2. Emission spectra of AP and DMP in molecular form in DMSO (5×10^{-6} M) solution at room temperature. $\lambda_{exc.} = 375$ nm.

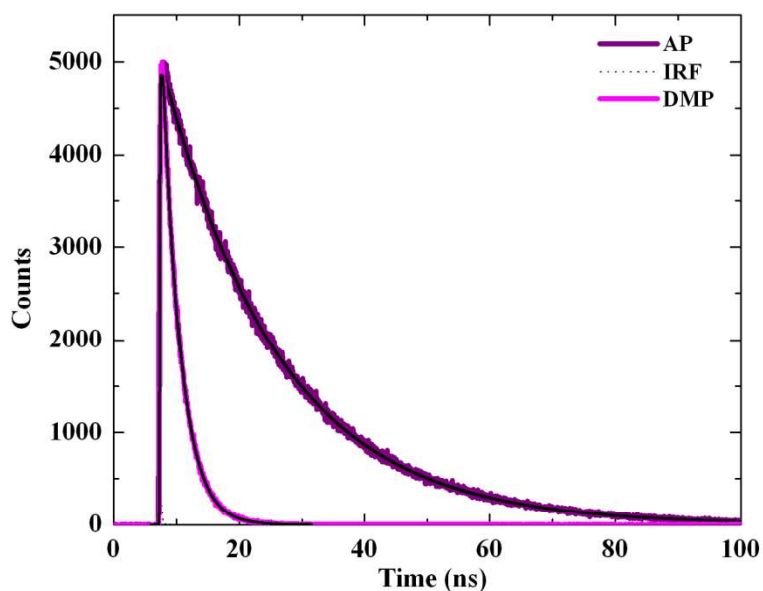


Figure 7.3. Fluorescence decay profiles of AP and DMP in molecular form at room temperature. $\lambda_{exc.} = 375$ nm. Solid black lines indicate the single exponential fit to the experimental data points. Chi-square (χ^2) values for AP and DMP are 1.19 and 1.07 respectively.

7.3.2. Microscopic Analysis of AP and DMP Aggregates

To investigate the particle size of the aggregates of AP and DMP, the FESEM images have been captured at room temperature (Figure 7.4). AP particles are found to be nearly spherical in shape, whereas DMP are nearly square. At room temperature, the most probable size of the aggregates from AP and DMP system are measured to be ~ 250 nm and ~ 220 nm respectively. The effect of both concentrations and temperatures on the aggregation behavior of AP and DMP are also investigated. For both AP and DMP, sizes of the particles are observed to increase with increase in the monomer concentration. For example, when monomer concentration is doubled, sizes of AP and DMP particles are found to be ~ 500 nm and ~ 400 nm respectively. With increase in temperature particle sizes of both aggregates are also increased (~ 400 nm) (Figure 7.5).

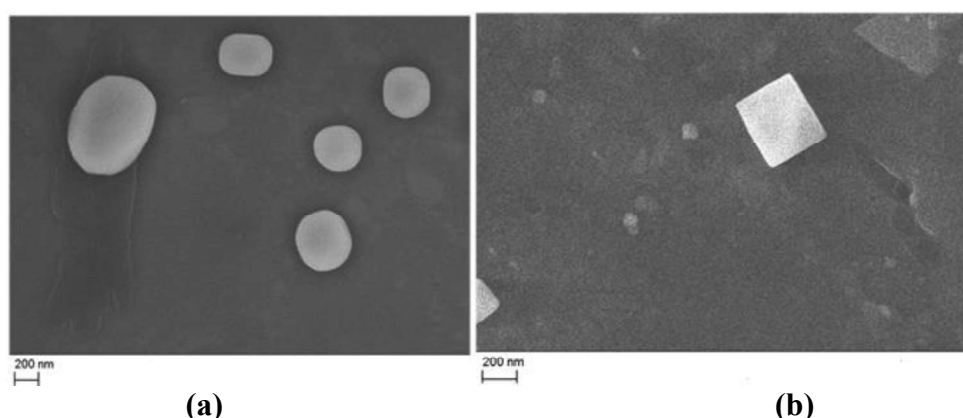


Figure 7.4. FESEM images of (a) AP and (b) DMP aggregates at room temperature.

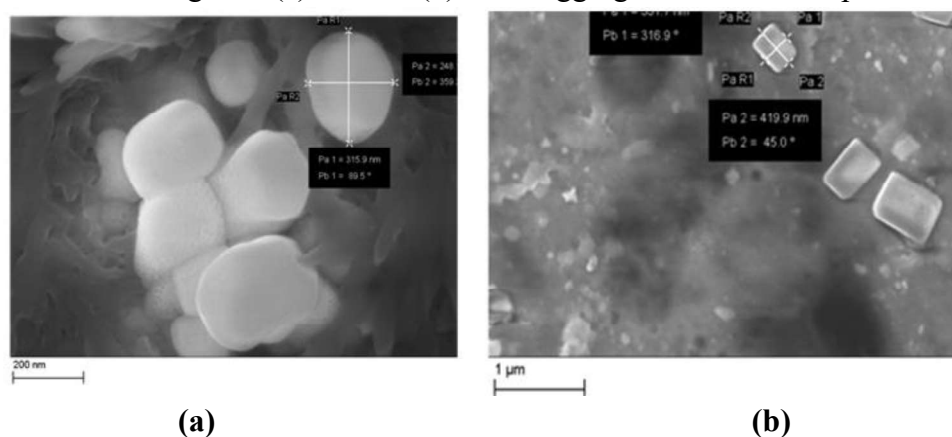


Figure 7.5. FESEM images of (a) AP and (b) DMP aggregates at higher temperature ($T= 65^{\circ}$ C).

7.3.3. Spectroscopic Studies on AP and DMP Aggregates

Photophysical properties of well-characterized aggregates have been studied and compared with those in molecular form. Figures 7.6 and 7.7 compare the absorption spectra of AP and DMP in their molecular and aggregated (colloidal) form respectively. Table 7.1 collects the absorption spectral data for AP and DMP in their molecular and aggregated states. As can be seen from Figure 7.6, the absorption spectral profile of AP-aggregates is blue shifted as compared to AP molecular form. However, interestingly, absorption spectra for DMP-aggregates are found to be red shifted as compared to DMP (Figure 7.7). This blue shift in the absorption for AP aggregates and red shift in the absorption for DMP aggregates as compared to their respective molecular forms indicates the formation of H and J aggregates for AP and DMP respectively. H and J aggregates formation of the derivatives AP and DMP, respectively, in water-DMSO mixed solvent system is also true for other solvent systems, such as water-acetonitrile, water-dioxane medium (Figure 7.8). For electron donor acceptor (EDA) systems like AP or DMP, a bathochromic shift of the absorption band is expected to be observed upon increasing the polarity of the medium for the charge transfer transition. Thus, the present blue shift in the absorption spectrum of AP aggregates clearly demonstrates that this shift is due to the formation of H-type aggregates of AP. Further, in order to confirm that the red shift in the aggregated state of DMP is not exclusively due to the change in the solvent polarity, the absorption spectrum of DMP has been recorded in polar (methanol + water) system. The polarity of (methanol + water) system is maintained close to that of (DMSO + water) system. The absorption maxima of DMP in polar (methanol + water) is found to be 404 nm, which is much lower than that observed for DMP aggregates (417 nm). The relatively larger red shift of the absorption maximum of DMP aggregates confirms that this shift is due to the aggregation of the particles and not due to the

change in solvent polarity. These shifts in spectra behavior of aggregated form of AP and DMP can be explained with the help of molecular exciton theory.³⁹⁷ According to this theory, a molecule is considered as a point dipole, and the energy level corresponding to the excitonic state of the aggregate splits into two levels through the interaction of transition dipoles.⁴⁰¹ The splitting of the excitonic states leads to electronic transition to occur either at lower or higher energy from the corresponding monomeric form. These higher and lower energy transitions represent H and J aggregates, respectively. The varying nature of dipole-dipole interaction between two molecules in the aggregates are believed to be primarily responsible for splitting of energy states in the aggregates.^{401, 402} A schematic diagram form excitonic splitting for AP and DMP dimer are shown in Figure 7.9. Because it is also known from molecular exciton theory^{401, 402} that a face-to-face (parallel arrangements) of transition dipoles in case of H-aggregates shifts absorption maximum to the blue and head-to-tail (anti parallel) arrangement for J-aggregation shifts absorption maximum to the red, H-type aggregates for AP and J-type aggregates for DMP in the present case indicates that the arrangements of molecules and consequently the electronic coupling between two molecules in the respective aggregates are different. Crystal structure analysis and theoretical calculation based on different modes of aggregates throws more light on this aspects (*vide infra*).

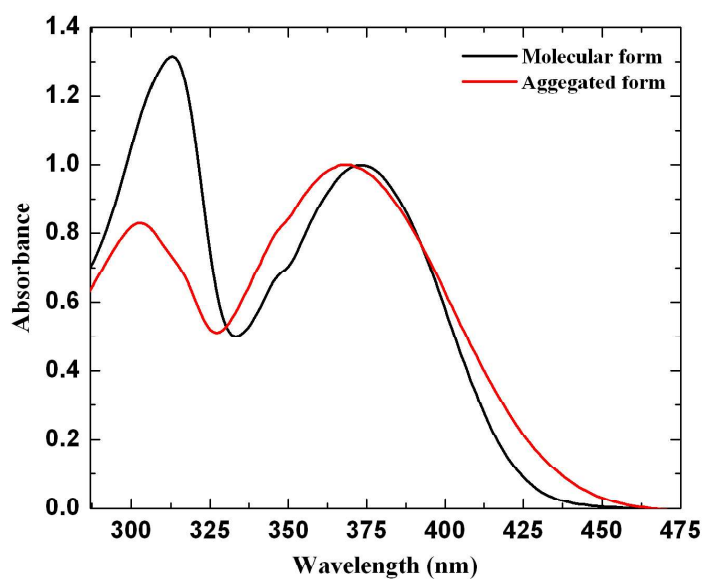


Figure 7.6. Normalized absorption spectra of AP in molecular form in DMSO (5×10^{-6} M) solution and in aggregated form in 99% water-DMSO medium at room temperature. Spectra are normalized corresponding to second peak maxima.

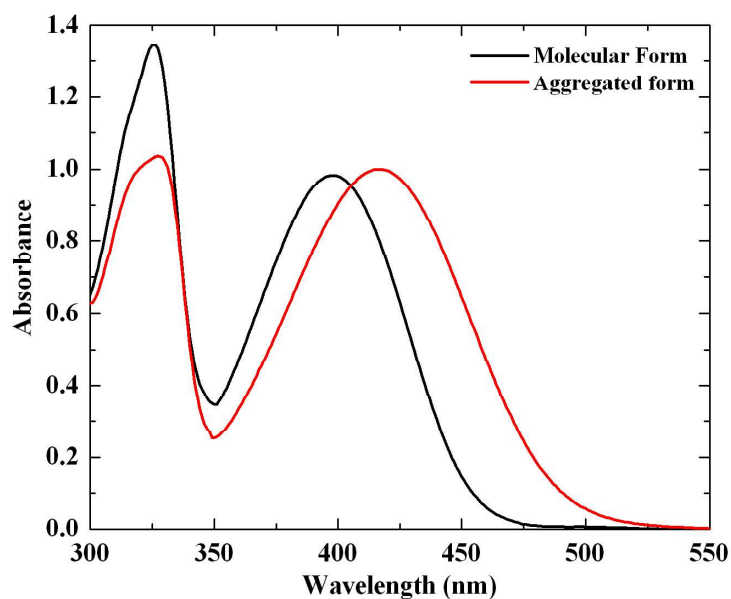


Figure 7.7. Normalized absorption spectra of DMP in molecular form in DMSO (5×10^{-6} M) solution and in aggregated form in 99% water-DMSO medium at room temperature. Spectra are normalized corresponding to second peak maxima.

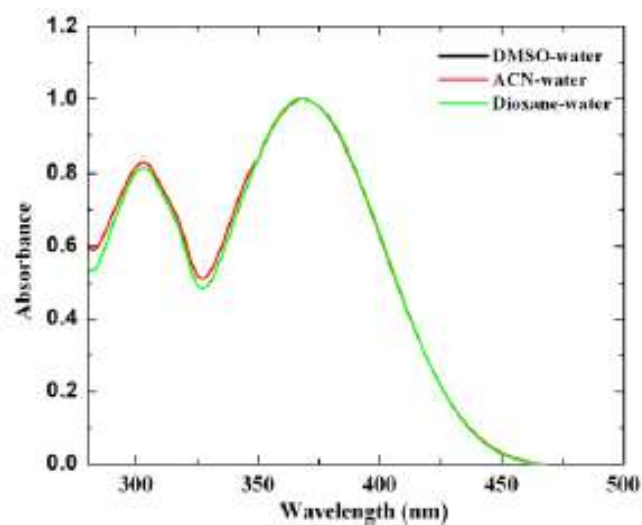


Figure 7.8. Absorption spectra in aggregated form of AP in different 99% water-solvent medium at room temperature. Spectra are normalized corresponding to second peak maxima.

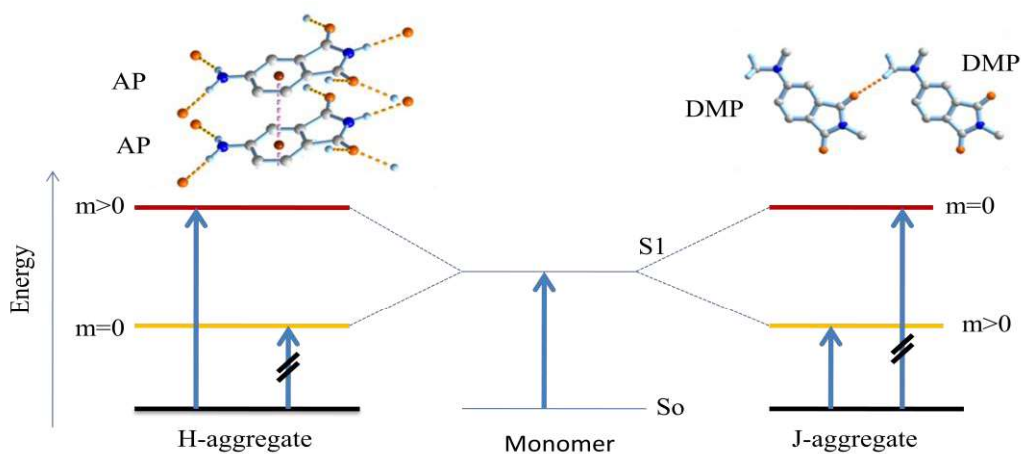


Figure 7.9. Schematic diagram illustrating allowed transition for H- and J- aggregates. Here ‘m’ represents transition moment integral, which must be greater than zero for allowed transitions.

Table 7.1. Absorption $\lambda_{max}^{abs.}$ (nm) and emission maxima $\lambda_{max}^{em.}$ (nm) of AP and DMP in molecular form in DMSO (5×10^{-6} M) solution and in aggregated form in 99% water-DMSO (5×10^{-5} M) solution

Systems	$\lambda_{max}^{abs.}$ (nm) ^a	$\lambda_{max}^{em.}$ (nm) ^b
AP Molecule	374	474
AP aggregate	368	551
DMP molecule	397	518
DMP aggregate	417	595

^{a,b}Experimental error= $\pm 2\%$

The excited states of these aggregates are investigated through steady state and time-resolved fluorescence studies. Figure 7.10 shows the emission spectra of AP and DMP in their aggregated forms. Data for emission maxima of AP and DMP in molecular as well as aggregated forms are provided in Table 7.1. As can be seen from figure 7.10, the emission maxima for both aggregates are red shifted than the respective molecular forms (homogeneous solution). Figure 7.10 also shows that the emission intensity of DMP aggregate is significantly less than that of AP aggregate. Moreover, data that are collected in Table 7.1 also demonstrate large Stokes-shifted emission for both AP and DMP aggregates. This large Stokes shift perhaps indicate that emission in these systems do not originate from the same state to which they were excited vertically.³⁷⁸ Interestingly, the emission intensity of both AP and DMP aggregates are significantly less as compared to their monomer (Figure 7.11), this is due to the aggregation caused quenching of the excited states.^{403, 404} Fluorescence decay profiles of AP and DMP in aggregated forms at room temperature are shown in Figure 7.12. The average lifetime values corresponding to the aggregates of AP and DMP are estimated to be $\tau = 1.19$ ns and 0.213 ns respectively. This lifetime data when compared with the respective monomers of AP and DMP clearly indicates that the average lifetime of the aggregated system has decreased. This data also supports the aggregation caused quenching of the excited states.^{403, 404}

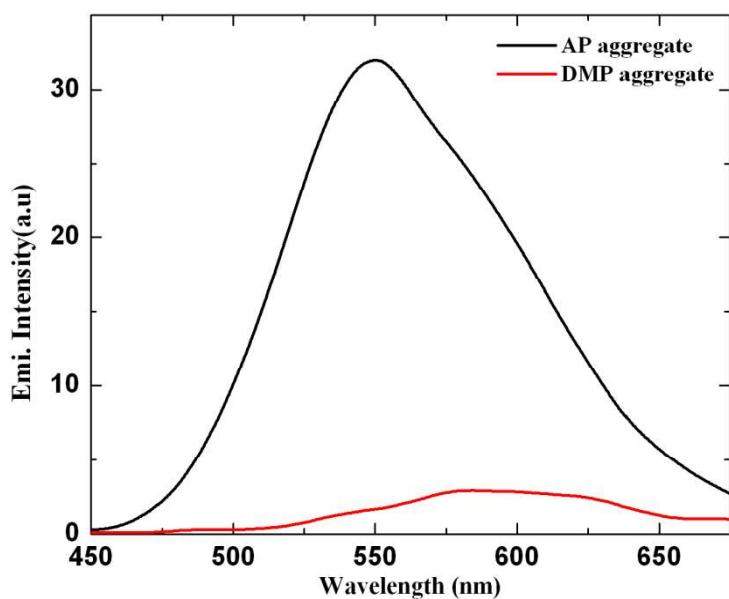


Figure 7.10. Emission spectra of AP and DMP in aggregated form in 99% water-DMSO medium at room temperature. $\lambda_{exc} = 375$ nm.

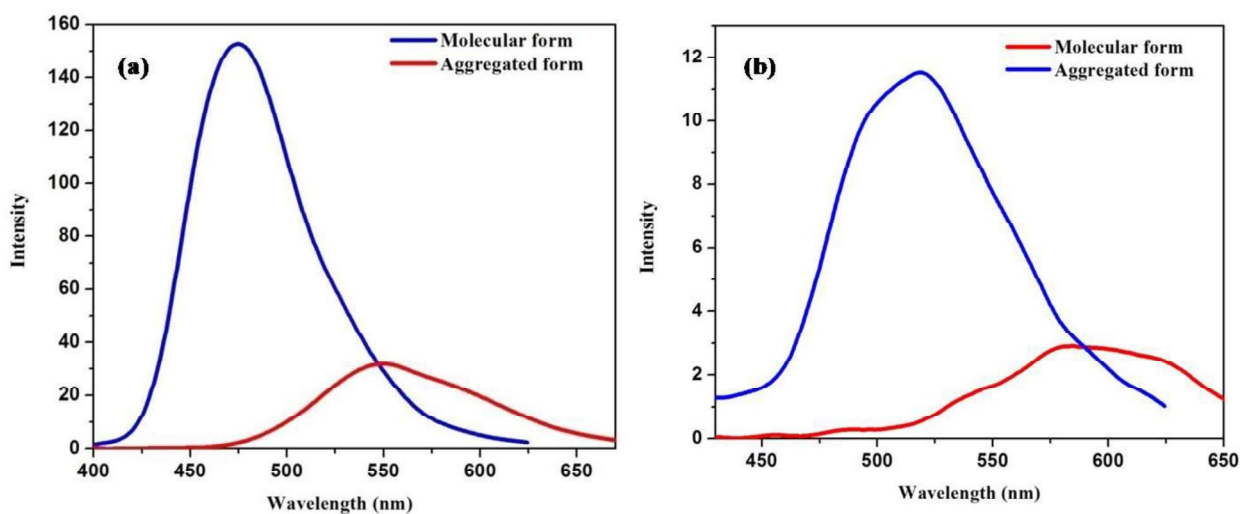


Figure 7.11. Emission spectra of (a) AP and (b) DMP in molecular form in DMSO (5×10^{-6} M) solution and in aggregated form in 99% water-DMSO medium at room temperature. $\lambda_{exc} = 375$ nm.

We would also like to note here that lifetime values are independent on different emission wavelength (Figure 7.13). It may be mentioned in this context that very recently Durantini et al.⁴⁰⁵ demonstrated that when AP was excited around 300 nm in water, the emission maximum

was found to be at 562 nm, whereas the emission maximum was found to be at 546 nm on excitation at 370 nm. Moreover, the fluorescence decays of AP in water showed no emission wavelength dependence at $\lambda_{exc} = 300$ nm, whereas it was found to be different when $\lambda_{exc} = 370$ nm was used. The excitation wavelength dependent emission behavior has been explained by considering the keto-enol tautomerism of the derivative AP in pure water.⁴⁰⁵ However, in the present study (99% water–DMSO) the excitation wavelength-dependent emission behavior of AP has not been observed (Figure 7.14) This behavior is not surprising in a sense that in 99% water–DMSO binary mixture, AP forms aggregate (supramolecular assembly) through the involvement of all of its hydrogen atoms (vide crystal structures of AP). In this context, we would also like to mention that keto-enol tautomerism was observed by Durantini et al.⁴⁰⁵ at much lower solute concentration. In the present case, equilibrium shifts to keto form, which aggregates to the supramolecular assembly, and hence, behavior observed by Durantini et al.⁴⁰⁵ is not observed. Further, we have studied the aggregation behavior of 5-amino-2-methylisindoline-1,3-dione (starting material of DMP) in 99% water–DMSO binary mixture Figure 7.15. As can be seen from Figure 7.15, the absorption spectral profile of the aggregated form of this molecule is blue shifted as compared to its molecular form. While the absorption maximum of this system in its molecular form appears at 382 nm, its aggregated form shows a peak maximum at 376 nm. This blue shift (6 nm) of the absorption maximum for methylisindoline-1,3-dione aggregates indicates the formation of H aggregates. The emission maximum of this molecule in its molecular and aggregated forms appears at 486 nm and 560 nm, respectively (Figure 7.16). These data corresponding to the molecular and aggregated forms of the three systems, AP, methylisindoline-1,3-dione and DMP, clearly indicate that hydrogen

bonding interaction can play an important role towards the aggregation behavior of organic molecules.

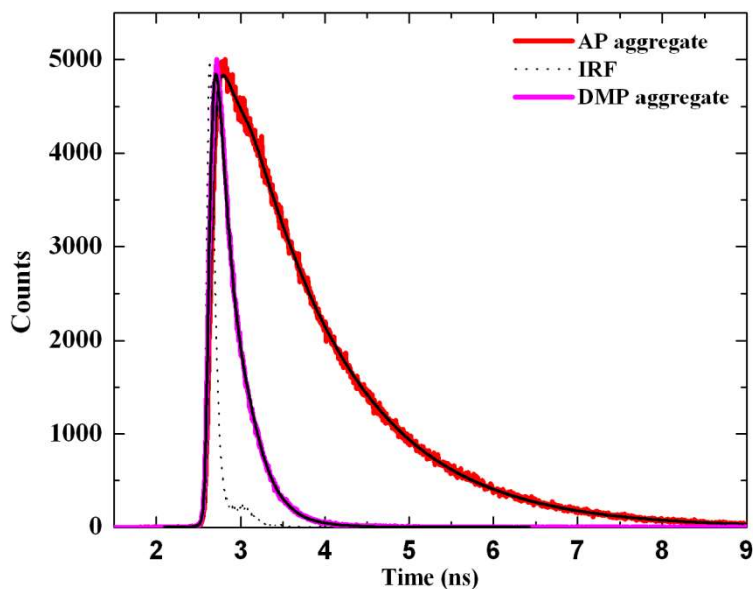


Figure 7.12. Fluorescence decay profiles of AP and DMP in aggregated forms at room temperature. $\lambda_{exc.} = 375$ nm. Solid black lines indicate the single exponential fit to the experimental data points. Chi-square (χ^2) values for AP and DMP aggregates are 1.23 and 1.12 respectively.

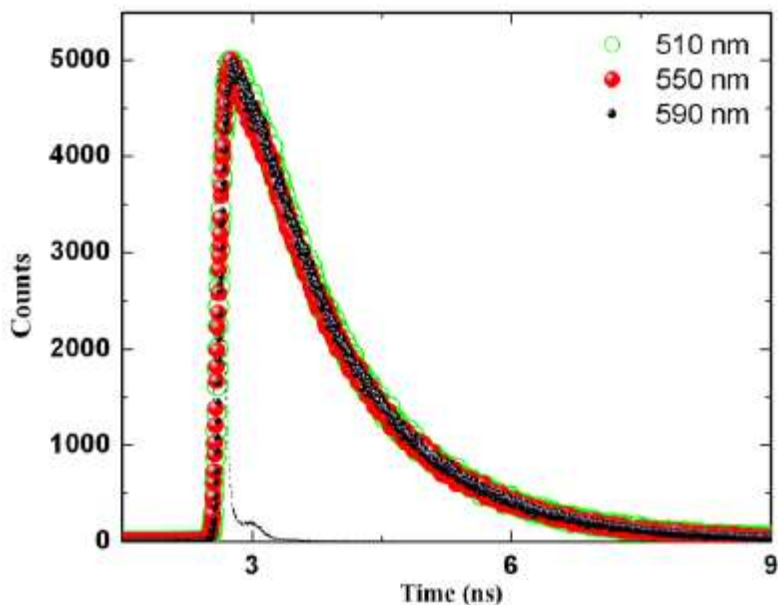


Figure 7.13. Wavelength dependent fluorescence decay profiles of AP in aggregated forms at room temperature. $\lambda_{exc.} = 375$ nm.

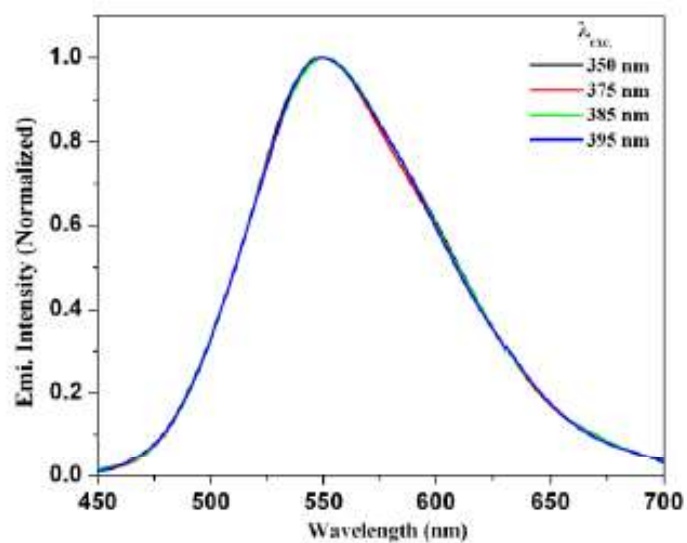


Figure 7.14. Emission spectra of AP aggregates at different excitation wavelength (λ_{exc}).

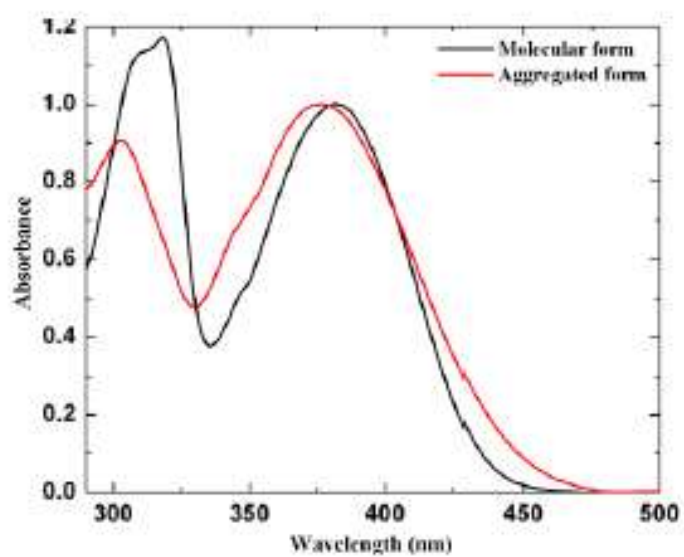


Figure 7.15. Absorption spectra of 5-amino-2-methylisindolne-1, 3-dione in molecular form in DMSO (5×10^{-6} M) solution and in aggregated form in 99% water-DMSO medium at room temperature. Spectra are normalized corresponding to second peak maxima.

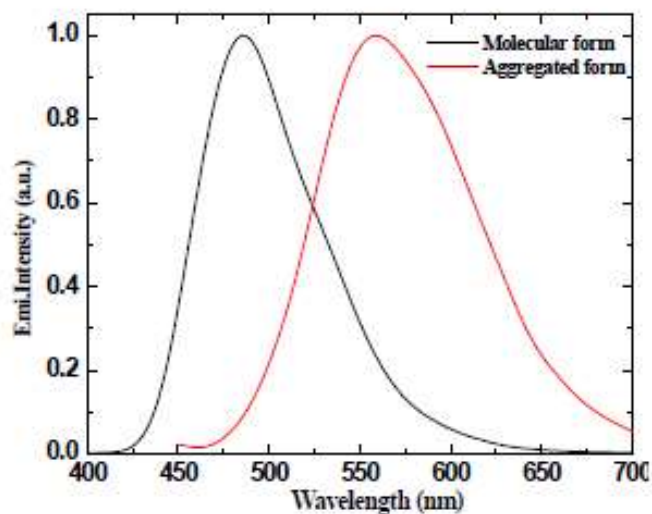


Figure 7.16. Emission spectra of 5-amino-2-methylisoindolne-1, 3-dione in molecular form in DMSO (5×10^{-6} M) solution and in aggregated form in 99% water-DMSO medium at room temperature. Spectra are normalized corresponding to second peak maxima.

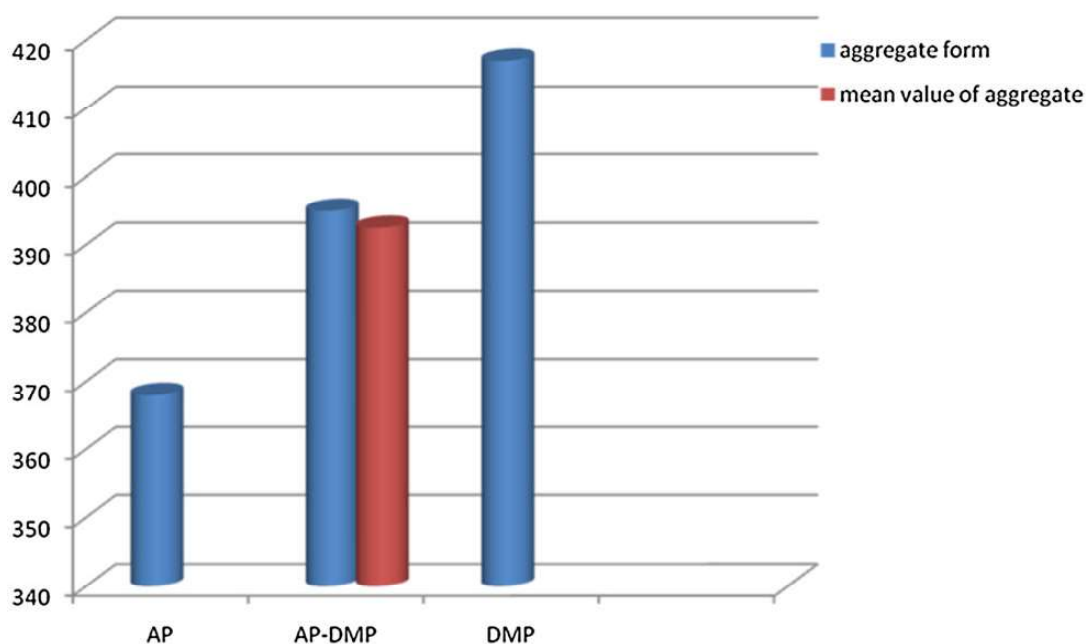


Figure 7.17. The absorption maxima of 1:1 AP-DMP aggregate, along with AP and DMP aggregate

We have also studied the absorption behavior of AP-DMP hetero-aggregates. The hetero aggregates are formed by taking AP and DMP in 1:1 mole ratio. Interestingly the observed

hetero- aggregates exhibits the absorption maxima at 395 nm which is very close to mean value of absorption maxima ($\frac{368+417}{2} = 392.5 \text{ nm}$) obtained for individual aggregates from AP and DMP respectively. Figure 7.17 represents the absorption maximum for hetero-aggregates along with absorption maxima for individual AP and DMP aggregates.

7.3.4. Crystal Structures of AP and DMP

To understand the role of intermolecular interactions during self-assembly of molecules the crystal structures of both AP and DMP has been analyzed. It may be mentioned that intermolecular effects arising from interactions between molecules depends on the geometry of the packing structure.⁴⁰⁶ Moreover, the various intermolecular interactions also play crucial role in governing the photophysical properties of aggregates.³⁷¹ Hence, the study of intermolecular interaction through the analysis of the packing geometry of molecules will not only be helpful to understand the molecular aggregation pattern but also their influence in controlling photophysical properties.

Crystals of DMP, suitable for X-ray diffraction, were obtained by recrystallization of the crude product from methanol. The compound crystallizes in orthorhombic crystal fashion with space group $P2_1/n$ bearing four molecules per unit cell whereas AP crystallizes in same manner with space group $Pna2_1$.⁴⁰⁷ The molecular structure of DMP and AP are illustrated in Figure 7.18 The crystal structure refinement data and selected structural parameters are collected in Tables APPX1 and APPX2 (appendix), respectively.

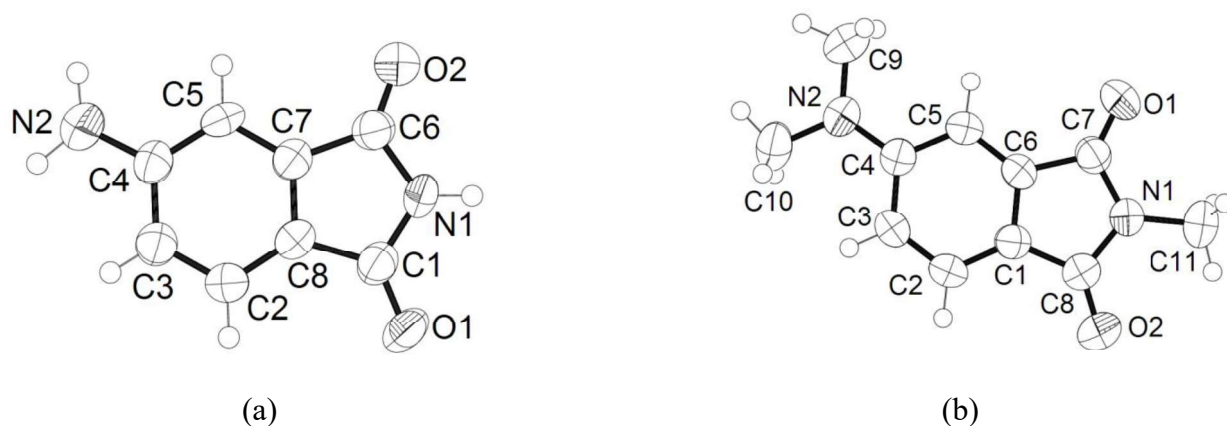


Figure 7.18. ORTEP diagram (50% displacement thermal ellipsoids) with atomic numbering scheme of (a) AP and (b) DMP.

Both the molecules exhibit nearly planar geometry. The displacement of atoms from the mean plane through non-hydrogen atoms are given in Table APPX3. The fact that amine groups (NH_2 for AP and NMe_2 for DMP) is planarized is evident from sum of their bond angles AP (HNH), 358.85° ; DMP (CNC), 359.72° ; and torsion angles (each being close to 0° or 180°). Furthermore, the dihedral angle of amine group and the mean planes of the adjacent phenylene ring AP, $5.20(8)^\circ$; DMP, $3.35(71)^\circ$ (Tables APPX4 and APPX5) also supports the planarization of the NH_2 and NMe_2 groups attached to aryl ring.⁴⁰⁸

We have also carefully looked at the packing structures of both systems. As can be seen from Figure 7.19, for AP, all three hydrogens from amido and amine N atoms forms N-H---O hydrogen bonding interactions, where H atom of one AP molecule is found to be associated with the O acceptor from the neighboring molecules. Interestingly, packing diagram reveals that alternate molecules are parallel to each other. The molecules in the lattice are interlinking by head to head fashion (Figure 7.19). The parallel aryl rings of the molecules are close enough (centroid to centroid $3.7216(5) \text{ \AA}$) to form channelized π --- π stacking (Figure 7.20). The parallel geometry of two adjacent molecules in the packing diagram of AP supports the formation of H-

type aggregates for AP as parallel alignment of transition dipole moments is required to form H aggregates.

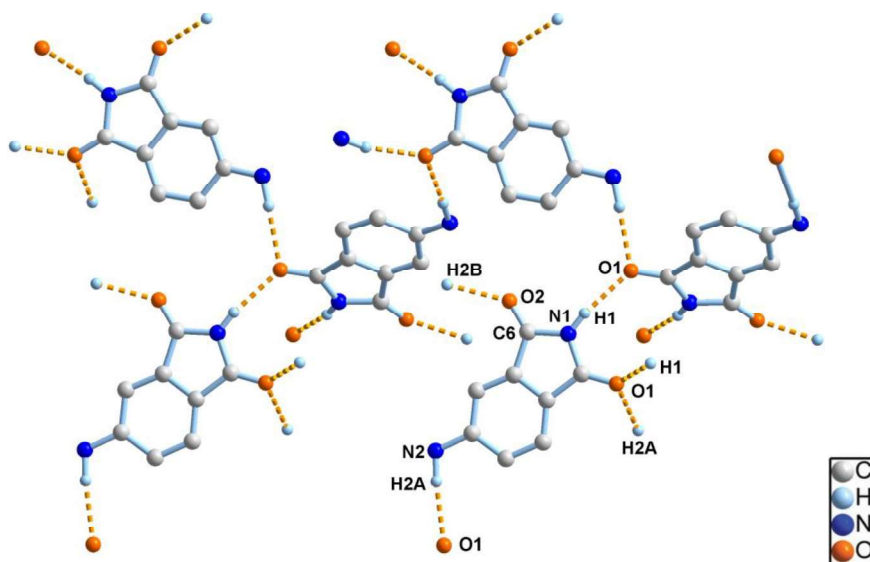


Figure 7.19. Interplay of N-H---O hydrogen bonding interactions involving the bifurcated oxygen acceptor O1 in building 3D crystal lattice of AP.

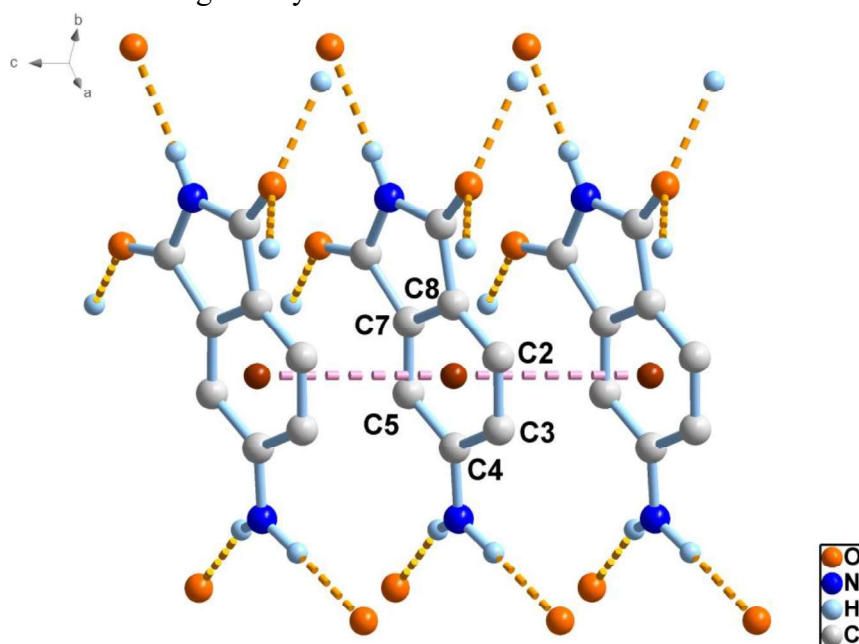


Figure 7.20. The parallel aryl rings of AP molecules form channelized π --- π stacking.

Quite interestingly, DMP, where all the hydrogen atoms are replaced by methyl group, exhibits very different crystal packing as compared to AP. DMP molecules are found to be packed

through two kinds of C-H...O and a weak C-H... π interactions (Table 7.2). The CH₃ protons adjacent to N atom in the amine fragment are sufficiently acidic to form hydrogen bonds with the oxygen acceptor from the neighboring molecules. In DMP the C-H...O interactions appears to be crystal director force, which build 2D supramolecular array of anti-parallel chains by head to tail interlinking of molecules in the lattice (Figure 7.21). The weak C-H... π interaction organizes the 2D sheets into 3D supramolecular assembly. The topological properties of weak C-H... π (C7) interactions 2.806 Å (ring to ring distance is 3.846 Å with an angle 66.2°) is apparent as its reciprocal nature results in the formation of a zero dimensional centrosymmetric dimeric units (Figure 7.21), which consequence 3D weaving of sheet array in the crystal packing of DMP.

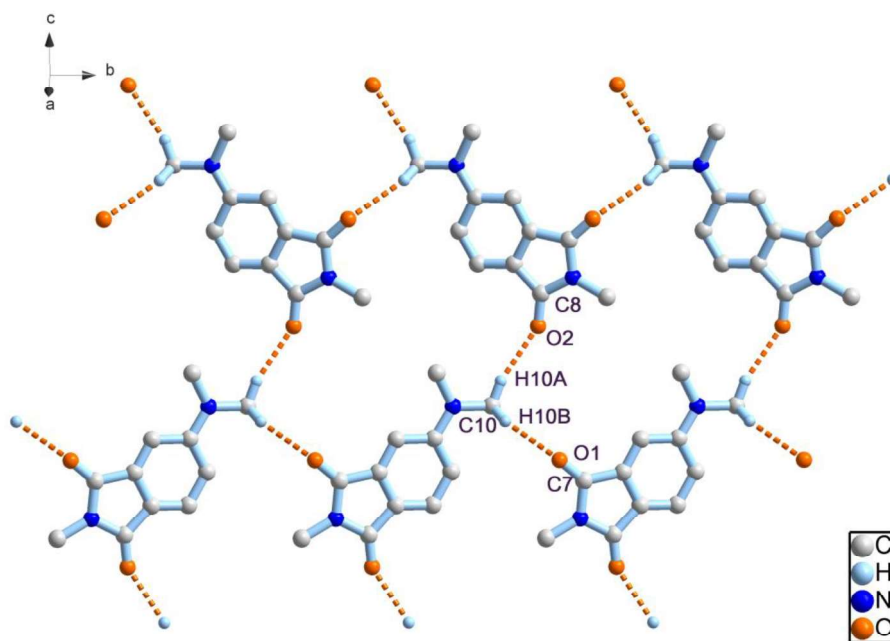


Figure 7.21. Role of C-H...O interactions in head to tail interlinking of molecules in repeating *anti*-parallel chains and 2D supramolecular array of DMP.

Table 7.2. Hydrogen bond parameters obtained from crystal structures of AP and DMP

Systems	D-H...A	D-H (Å)	H/ π ...A (Å)	D-A (Å)	D-H...A (°)
DMP molecule	C10-H10B...O1 ⁱ	0.96	2.618 (14)	3.529 (25)	158.710 (124)
	C10-H10A...O2 ⁱⁱ	0.96	2.418 (14)	3.400 (26)	160.251(126)
	C10-H10C--- π (C7)	0.96	2.8854(15)	3.6153(26)	133.622(133)
AP molecule	N1-H1...O1 ⁱⁱⁱ	0.88	2.059 (420)	2.922 (41)	168.255 (3853)
	N2-H2A...O1 ^{iv}	0.99	2.128 (602)	3.119 (54)	172.596 (5048)
	N2-H2B...O2 ^v	0.91	2.106 (536)	2.992 (48)	162.945 (4816)
	π --- π (centroid defined by C2- C8)		3.7216(5)		

Symmetry codes: (i) $\frac{1}{2}+x, \frac{3}{2}-y, \frac{1}{2}+z$; (ii) $-1+x, y, 1+z$; (iii) $-1+x, y, 1+z$; (iv) $1-x, -y, \frac{3}{2}+z$; (v) $\frac{3}{2}-x, -\frac{1}{2}+y, \frac{1}{2}+z$; (vi) $1-x, 1-y, \frac{1}{2}+z$.

7.3.5. Theoretical Calculation of the Experimental Results

Theoretically we have studied the nature of aggregation of AP and DMP molecules and investigated how different modes of aggregation lead to changes in the UV-VIS spectra of these molecules. The ground states of monomers AP, DMP, and the hetero dimers (AP-DMP) were fully optimized while only H-atoms were optimized in the case of self-assembled aggregated dimers AP-AP and DMP-DMP using the hybrid DFT functional M06-2X^{409, 410} with 6-31+g(d, p) basis set as implemented in Gaussian 09.^{397, 398} The hybrid meta exchange-correlation functional, M06-2X from Truhlar's group has been successful in accounting for medium-range electron correlation in charge-transfer systems and correctly incorporates dispersion forces.⁴¹¹⁻⁴¹³ Additional frequency calculations were also performed for the fully optimized monomers and hetero dimers for ensuring real vibrational modes for the minimum ground state structures. The computed absorption spectra were obtained through time-dependent DFT (TD-DFT) formalism.⁴¹⁴⁻⁴¹⁸ All the calculations are performed in gas phase. In our simplified models we have considered both linear and π -stack arrangements independently, for the self-assembled

homo-dimers of AP and DMP taken from the respective crystal structures (Figure 7.22). The center to center distance between two phenyl rings in AP and DMP are 6.63 Å and 8.49 Å respectively, while the π -stacking interaction between the two molecules in AP and DMP self-assembled aggregated dimmers are 3.72 Å and 3.84 Å respectively. The value is quite similar to their single crystal X ray structure analysis. This indicates moderately strong π -stacking interactions between two chromophoric units of AP and DMP.^{416, 417} Since the molecules are closer in the π -stacked configuration of the monomers exciton splitting and hence shift in λ_{\max} should arise due to π -stacking rather than linear arrangements. We have also considered two hetero type π -stacked dimers formed between AP and DMP with the parallel and anti parallel interaction where the two chromophores slipped parallel to each other with the stabilization energies of -12.0 kcal/mol and -15.8 kcal/mol respectively (Figure 7.22).

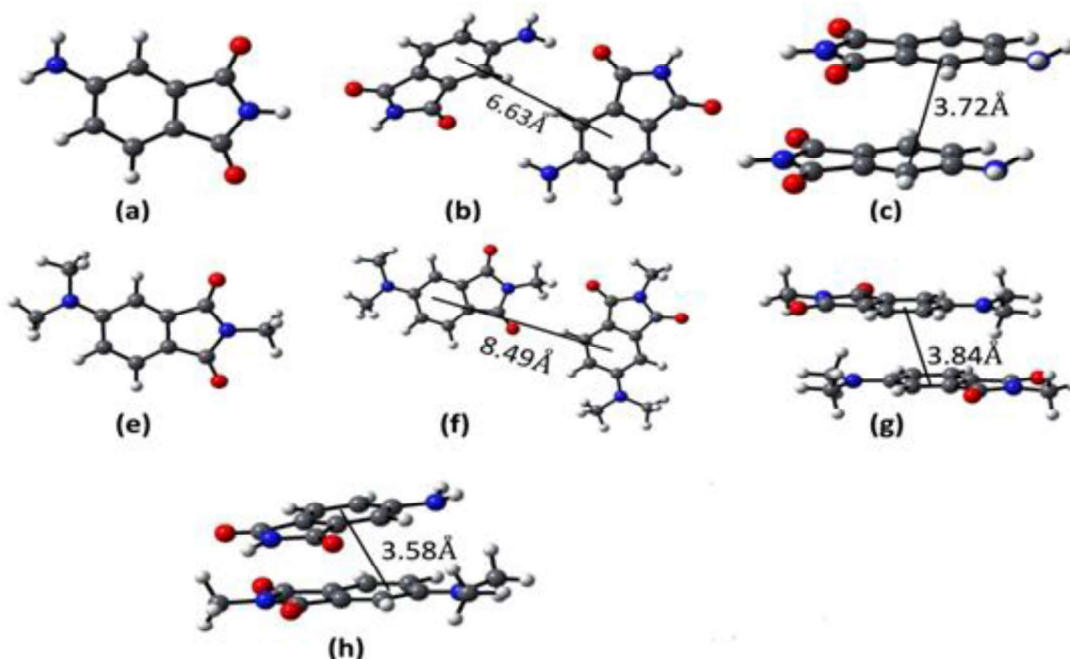


Figure 7.22. Ground State optimized structures (at M06-2X/6-31+G(d,p) level in gas phase) for (a) AP monomer, (b) AP linear dimer, (c) AP π -stacked dimer, (e) DMP monomer, (f) DMP linear dimer, (g) DMP π -stacked dimer and (h) AP-DMP parallel.

Table 7.3. The computed λ_{max} for AP and DMP, in monomer, homo and hetero dimmers form

Systems	λ_{max} (nm)	f (oscillator strength)	Transitions
AP monomer	339.2	0.07	H- L; 100%
AP linear dimer	368.7	0.09	H-L+1; 100%
AP stacked dimer	331.8	0.06	H-1-L; 94.9% H-L+1; 5.1%
DMP monomer	371.6	0.08	H-L; 100%
DMP-linear	375.3	0.12	H-L+1; 100%
DMP-stacked	381.3	0.15	H-1-L; 54.6% H-L+1; 45.4%
AP-DMP (parallel)	375.5	0.06	H-L+1; 100%

The computed λ_{max} (Figure 7.23) for AP, DMP, and their homo and hetero aggregation at TD-B3LYP/6-31 + G (d, p) levels of theory are summarized (Table 7.3). Here optical transitions refer to the $S_0 \rightarrow S_1$ transition. Hence, the spectroscopic studies indicate that the AP dimer shows a blue shift of 7.4 nm as a consequence of parallel π -stacked arrangement, while for the anti parallel arrangement of the DMP molecules leads to a red shift 9.7 nm on forming dimer which is expected for a J-aggregate like state of association based on a simple dipole-dipole interaction induced exciton splitting.^{420, 421} Linear arrangement of AP indicates red shift which is opposed by the experimental observation. Hence, the blue shifted spectra of AP self-assembled dimer arise due to the π -stacked arrangement. The UV-visible spectrum of linearly arranged DMP dimer shows a small change from its monomer (3.7 nm red shifted). So, our calculation suggests that for both AP and DMP the blue and red shift in the spectra observed in our experiment could be due to the results of π -stacking rather than a linear arrangement. Our calculation shows that for the anti parallel π -stacked arrangement, the computed λ_{max} is 30.7 nm blue shifted with respect to AP monomer and 1.7 nm red shifted with respect to DMP monomer. This is in agreement with

the experimental results (Table 7.1). Since from the consideration of binding energy, the anti parallel π -stacked AP-DMP hetero dimer is more stable than parallel π -stacking arrangement by an amount of -3.8 kcal/mol, we believe that the experimentally observed spectra is arising due to the anti parallel π -stacking of the AP-DMP hetero dimer.

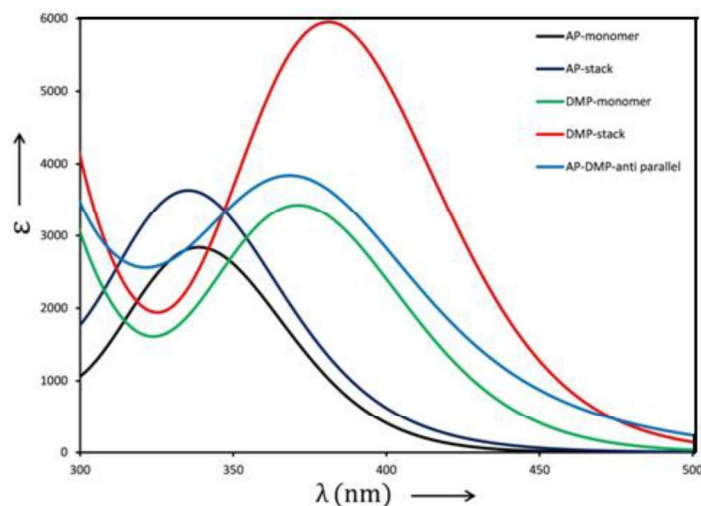


Figure 7.23. The computed λ_{max} for AP and DMP and their homo and hetero aggregation at TD-B3LYP/6-31+G (d, p) level of theory.

7.3.6. Effect of Ionic Liquids on Aggregates

The effect of ILs on the colloidal aggregates of both AP and DMP have also been investigated by employing one short alkyl chain containing IL ($[C_4(mim)]Br$), and one long alkyl chain containing IL ($[C_{12}(mim)]Br$). Initially, spectroscopic measurements have been carried out with gradual addition of short chain IL ($[C_4(mim)]Br$) to both AP and DMP aggregates. The absorption and emission spectra of AP in presence and absence of ($[C_4(mim)]Br$) are provided in Figure 7.24(a) and 7.24(b), respectively. No significant change in the absorption and emission profile of AP aggregates is observed with addition of $[C_4(mim)]Br$ (Figure 7.24). Like AP aggregates, DMP aggregates also show similar behavior in presence of $[C_4(mim)]Br$.

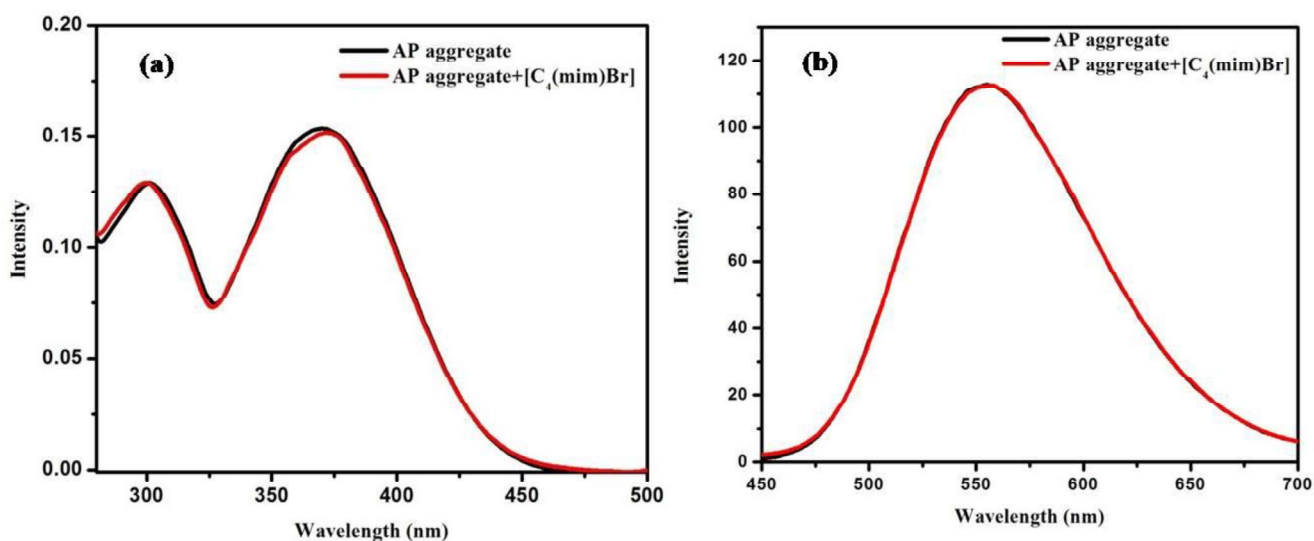


Figure 7.24. (a) Absorption and (b) emission spectra of AP aggregates in presence and absence of $[C_4(\text{mim})]\text{Br}$.

However, a significant change in the absorption spectra of AP aggregates has been observed with addition of $[C_{12}(\text{mim})]\text{Br}$ (Figure 7.25(a) and Table 7.4). More interestingly, with addition of $[C_{12}(\text{mim})]\text{Br}$ in the colloidal solution of AP, the absorption maxima of AP aggregates is observed to shift 5 nm to the red end (Table 7.4). This indicates that upon addition of relatively longer IL, the AP aggregates dissociates and convert to monomeric form. Again, for DMP, the absorption maxima shift ~ 11 nm to the blue end upon addition of $[C_{12}(\text{mim})]\text{Br}$ (Figure 7.26 (a) and Table 7.4). This also suggests that upon addition of longer alkyl chain IL, the DMP aggregates also dissociates and form monomers. These data demonstrates that dissociation of colloidal aggregates takes place in the presence of longer chain IL. Interestingly, in the emission, the emission maxima of AP aggregates shifts ~ 20 nm towards the blue side and emission intensity also increases with addition of longer alkyl chain IL (Figure 7.25 (b)). Like AP aggregates, DMP aggregates show ~ 45 nm blue shift of emission band (Figure 7.26 (b)). All these observation suggests that the dissociation of colloidal aggregates takes place upon addition of longer alkyl chain IL. Please note that similar results have also been observed during

encapsulation of curcumin (a drug molecule) into the micelles of [Bmim][C₈SO₄].⁴²² Moreover, upon carefully look, a sudden change in the emission spectra with addition of IL can be observed in both AP and DMP aggregates. The sudden change in the emission spectra appears at 11.6 mM and 11.2 mM concentration of IL for AP and DMP, respectively (Figures 7.25 (b) and 7.26 (b)). In this context, we would like to mention that [C₁₂(mim)]Br belongs to the class of surface active ILs, and form micelles in aqueous solution above a critical micelle concentration (CMC) of 10.9 mM at 298 K.³⁸⁷ Therefore, in the present scenario, the sudden change in the emission profiles can be attributed to the formation of micelles of this IL in aqueous solution. This observation indicates that micelle formation is responsible for dissociation of both AP and DMP colloidal aggregates.

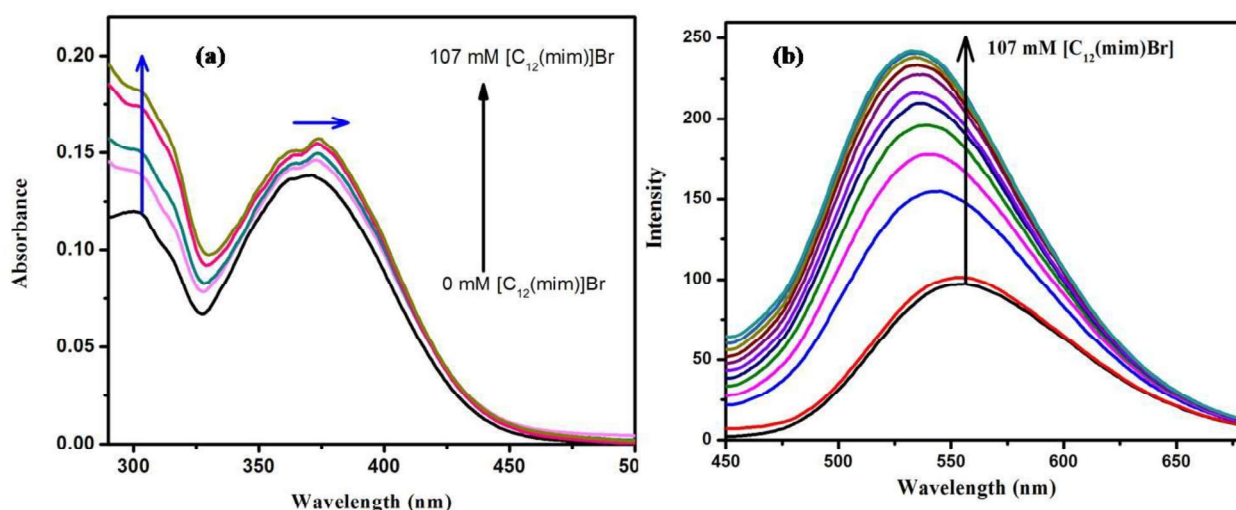


Figure 7.25. Variation of (a) absorption and (b) emission spectra of the colloidal solution of AP with the increasing concentration of the [C₁₂(mim)]Br.

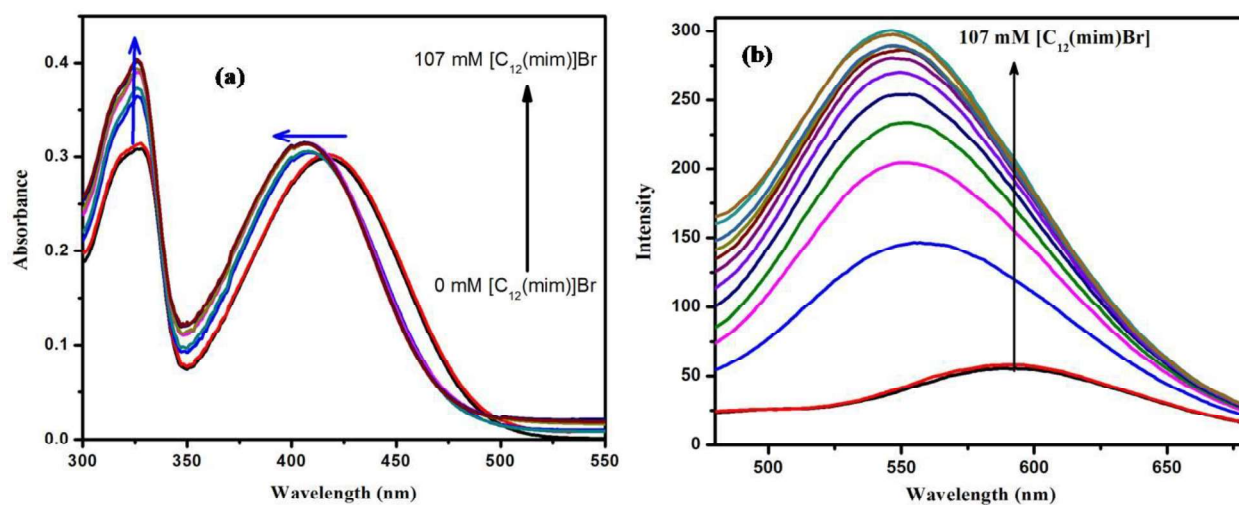


Figure 7.26. Variation of (a) absorption and (b) emission spectra of the colloidal solution of DMP with the increasing concentration of the $[C_{12}(\text{mim})]\text{Br}$.

Table 7.4. Absorption ($\lambda_{\text{max.}}^{\text{abs.}}$) and emission ($\lambda_{\text{max.}}^{\text{em.}}$) maxima of AP and DMP aggregates in presence of $[C_{12}(\text{mim})]\text{Br}$

Systems	$\lambda_{\text{max.}}^{\text{abs.}}(\text{nm})^{\text{a}}$	$\lambda_{\text{max.}}^{\text{em.}}(\text{nm})^{\text{b}}$
AP aggregate	368	551
AP aggregate + $[C_{12}(\text{mim})]\text{Br}$	373	532
DMP aggregate	417	595
DMP aggregate+ $[C_{12}(\text{mim})]\text{Br}$	406	548

^{a,b}Experimental error= $\pm 5\%$

Additionally, the lifetime of both AP and DMP aggregate in presence of longer alkyl chain IL is monitored and data are collected in Table 7.5. The lifetime values of both AP and DMP aggregates are found to increase in presence of $[C_{12}\text{mim}]\text{Br}$ IL (Figure 7.27 and Table 7.5). Please note that lifetime values corresponding to monomers (both AP and DMP) got quenched upon aggregate formation due to aggregation caused quenching. Since in presence of $[C_{12}\text{mim}]\text{Br}$ IL the aggregates dissociate to form monomers, the increase in lifetime values for the current system is expected. The photophysical data reveal that the longer alkyl chain IL,

[C₁₂mim]Br, can be used as a medium for colloidal dissociation of AP and DMP. The outcome of the above study is expected to be helpful in drug delivery methods.

Table 7.5. Fluorescence lifetime (τ) of AP and DMP aggregates in presence of [C₁₂(mim)]Br

Systems	lifetime (ns) ^a	χ^2
AP aggregate	1.13	1.11
AP aggregate + [C ₁₂ (mim)]Br	2.52	1.11
DMP aggregate	0.21	1.23
DMP aggregate + [C ₁₂ (mim)]Br	0.63	1.08

^aExerimental error= $\pm 5\%$

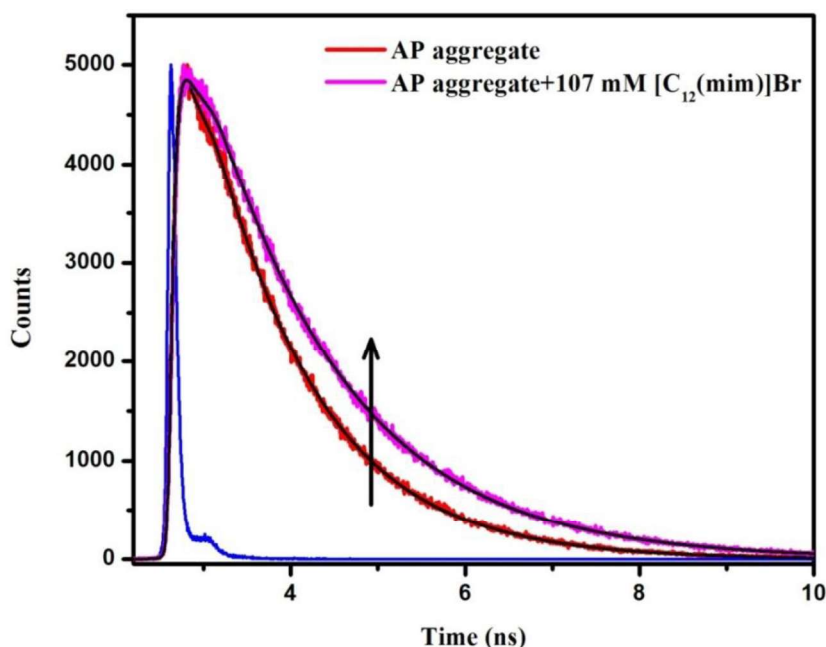


Figure 7.27. Fluorescence decay of AP aggregates in presence and absence of [C₁₂(mim)]Br.

Further, the dissociation of colloidal aggregates in both AP and DMP with addition of long alkyl chain IL has also been confirmed through dynamic light scattering measurements (Figure 7.28). It can be seen from figure, the colloidal particle size is found to decrease in both AP and DMP with addition of long alkyl chain IL. The study demonstrates that long alkyl chain IL dissociates the colloidal aggregates, however short alkyl chain IL does not influence.

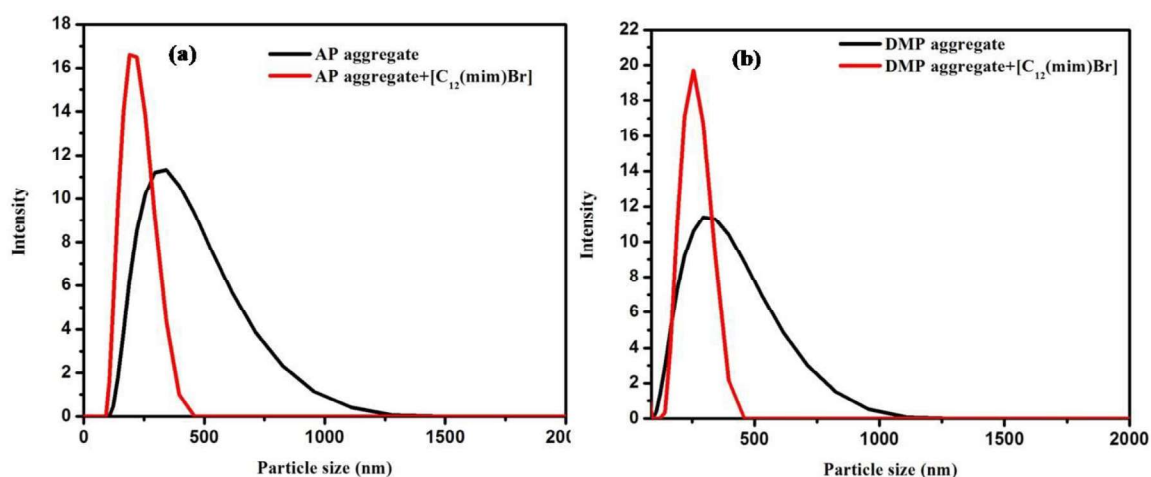


Figure 7.28. The colloidal particle size of (a) AP and (b) DMP aggregates in presence and absence of $[C_{12}(\text{mim})]\text{Br}$.

7.4. Conclusion

In this work, the aggregation behavior of two fluorescent molecules, 4-aminophthalimide (AP) and 4-(N, N-dimethyl)amino-N-methylphthalimide (DMP) have been investigated with the help of photophysical, crystallographic, microscopic and theoretical (DFT) study. Out of the two fluoroprobes, DMP has been synthesized by substituting all the amine hydrogen of AP by methyl groups. These two systems are selected for the present study to basically get an idea about the effect of intermolecular hydrogen bonding interactions (N-H...) on the aggregation behavior of these molecular materials. The aggregates of both AP and DMP are prepared based on standard reprecipitation method without using any external stabilizer. Photophysical behavior on these well characterized systems has been carried out in molecular as well as aggregated forms. Interestingly, AP-aggregate exhibits a blue –shifted absorption band as compared to AP in its molecular form. On the contrary, DMP-aggregate exhibits a red shifted absorption band as compared to its molecular form. These spectral data indicate the formation of H and J aggregates for AP and DMP respectively. Crystal Packing of AP and DMP are analyzed by X-ray crystallographic data to have better idea about the intermolecular interactions that are responsible

for molecular self assembly of AP and DMP. X-ray analysis demonstrates the different modes of aggregation for AP and DMP arises due the varying nature of intermolecular interaction for AP and DMP. Density functional calculations have also been carried out to investigate how different modes of aggregation lead to changes in the UV-VIS spectra of these systems. The outcome of the current IL induced dissociation of organic aggregates is expected to be useful in drug delivery methods.

Summary and Future Prospects

Combined fluorescence, NMR, EPR and FCS studies have been investigated in several mono and dicationic RTILs in order to understand the kinship among intermolecular interaction, structure and dynamics in these media. Several fascinating features in relation to understanding the basics of solute-solvent and solvent-solvent interaction, solute and solvent dynamics have emerged from the present work. The key findings of the present studies are summarised as follows.

(1) Alkyl chainlength on the anionic moiety of RTILs can significantly influence the solute rotation. Existence of void space has been observed in fluid structure of longer alkyl chain containing RTILs. (2) It has been demonstrated that hydroxyl-functionalized RTIL is more heterogeneous and structurally organized than the non-hydroxylic RTIL. (3) The structural organization and dynamical behavior of dicationic RTILs (DILs) are significantly different than MILs. (4) It has been observed that the relatively longer alkyl chain containing imidazolium-based DILs can exist in folded form. (5) The fluorescence of neat RTILs can originate from the molecular aggregates in the bulk ionic liquids and the alkyl chainlength on the anions can play an important role in governing the aggregation behavior of RTILs. (6) The resonance energy transfer (RET) studies (exploiting the fluorescence of neat RTILs) can effectively be used to understand the microscopic structural organization of various RTILs. (7) It has been observed that longer alkyl chain containing surface active ionic liquid (SAIL) can be helpful in dissociating the colloidal organic aggregates.

The present thesis work provides valuable information in understanding the intermolecular interaction, structure and dynamics of various mono and dicationic RTILs. Since, structural organization and dynamical behavior of DILs are significantly different than MILs, it is expected

that solutes reactivity in DILs can be different than MILs. Therefore, investigating the pathway of various organic reactions in DILs could be very interesting. Since, physicochemical properties (such as density, thermal stability etc.) of DILs are found to be more attractive than monocationic RTILs, DILs can be used in several applications. For example, DILs can be used as an electrolyte in lithium-ion/sodium-ion batteries due to its high thermal stability. Moreover, how biomolecules such as proteins, lysozymes etc. can interact with DILs can be an interesting theme of future research.

REFERENCES

- (1) Wilkes, J. S. *Green Chem.*, **2002**, *4*, 73.
- (2) Rogers, R. D.; Seddon, K. R. *Science* **2003**, *302*, 792.
- (3) Wasserscheid, P.; Keim, W. *Angew. Chem. Int. Ed.* **2000**, *39*, 3772.
- (4) Seddon, K. R.; Stark, A.; Torres, M. J. *Pure Appl. Chem.* **2000**, *72*, 2275.
- (5) Welton, T. *Chem. Rev.* **1999**, *99*, 2071.
- (6) Xue, H.; Verma, R.; Shreeve, J. M. *J. Fluorine Chem.* **2006**, *127*, 159.
- (7) Pandey, S. *Anal. Chim. Acta* **2006**, *556*, 38.
- (8) Zhang, J.; Bond, A. M. *Analyst* **2005**, *130*, 1132.
- (9) Buzzeo, M. C.; Evans, R. G.; Compton, R. G. *Chemphyschem* **2004**, *5*, 1106.
- (10) Castner, E. W. Jr.; Wishart, J. F. *J. Chem. Phys.* **2010**, *132*, 120901.
- (11) Weingärtner, H. *Angew. Chem., Int. Ed.* **2008**, *47*, 654.
- (12) Dupont, J. *Acc. Chem. Res.* **2011**, *44*, 1223.
- (13) Seddon, K. R. *J. Chem. Technol. Biotechnol.*, **1997**, *68*, 351.
- (14) Godfrey, D.; Bannock, J. H.; Kuzmina, O.; Welton, T.; Albrecht, T. *Green Chem.*, **2016**, *18*, 1930.
- (15) Hallett, J. P.; Welton, T. *Chem. Rev.* **2011**, *111*, 3508.
- (16) Mahmood, H.; Moniruzzaman, M.; Yusup, S.; Welton, T. *Green Chem.*, **2017**, *19*, 2051.
- (17) Plechkova, N. V.; Seddon, K. R. *Chem. Soc. Rev.* **2008**, *37*, 123.
- (18) Seddon, K. R. *Ionic Liquids, Industrial Applications for Green Chemistry*, American Chemical Society, Washington DC, 2002
- (19) Dupont, J.; de Souza, R. F.; Suarez, P. A. Z. *Chem. Rev.* **2002**, *102*, 3667.
- (20) Rantwijk, F. V.; Sheldon, R. *Chem. Rev.* **2007**, *107*, 2757.

- (21) Giernoth, R. *Angew. Chem. Int. Ed.* **2010**, *49*, 2834.
- (22) Hallett, J. P.; Welton, T. *Chem. Rev.* **2011**, *111*, 3508.
- (23) Wishart, J. F. *Energy Environ. Sci.* **2009**, *2*, 956.
- (24) Kuang, D. B.; Wang, P.; Ito, S.; Zakeeruddin, S. M.; Graätzel, M.; *J. Am. Chem. Soc.* **2006**, *128*, 7732.
- (25) Mazille, F.; Fei, Z. F.; Kuang, D. B.; Zhao, D. B.; Zakeeruddin, S. M.; Gratzel, M.; Dyson, P. J. *Inorg. Chem.* **2006**, *45*, 1585.
- (26) Wasserscheid, P.; Welton, T. *Ionic Liquids in Synthesis*, Wiley-VCH, Weinheim, 2003.
- (27) Golding, J. J.; MacFarlane, D. R.; Spiccia, L.; Forsyth, G. B.; Skelton, B. W.; White, A. H. *Chem. Commun.* **1998**, *18*, 1593.
- (28) Polyakov, O. G.; Ivanova, S. M.; Gaudinski, C. M.; Miller, S. M.; Anderson, O. P.; Strauss, S. H. *Organometallics* **1999**, *18*, 3769.
- (29) Larsen, A. S.; Holbrey, J. D.; Tham, F. S.; Reed, C. A. *J. Am. Chem. Soc.* **2000**, *122*, 7264.
- (30) Xu, W.; Wang, L.-M.; Nieman, R. A.; Angell, C. A. *J. Phys. Chem. B* **2003**, *107*, 11749.
- (31) Rogers, R. D.; Seddon, K. R.; Volkov, S. *Green Industrial Applications of Ionic Liquids*; Kluwer Academic: Dordrecht, Netherlands, 2002.
- (32) Enomoto, T.; Nakamori, Y.; Matsumoto, K.; Hagiwara, R. *J. Phys. Chem. C* **2011**, *115*, 4324.
- (33) Ngo, H. L.; LeCompte, K.; Hargens, L.; McEwen, A. *Thermochim. Acta*, **2000**, *357*, 97.
- (34) Lewandowski, A.; Swiderska-Mocek, A. *J. Power Sources* **2009**, *194*, 601.
- (35) Walden, P. *Bull. Acad. Imper. Sci. St. Petersburg*, **1914**, 1800.
- (36) Wilkes, J. S.; Joseph, A. L.; Robert, A. W.; Charles, L. H. *Inorg. Chem.* **1982**, *21*, 1263.
- (37) Boon, J. A.; Levisky, J. A.; Lloyd Pflug, J.; Wilkes, J. S. *J. Org. Chem.*, **1986**, *51*, 480.

- (38) Chiappe, C.; Pieraccini, D. *J. Phys. Org. Chem.* **2005**, *18*, 275.
- (39) Jeffrey, A. B.; Joseph, A.; Levisky, J.; Lloyd, P.; John, S. W. *J. Org. Chem.* **1986**, *51*, 480.
- (40) Davis, J. H. *Chem. Letter*, **2004**, *33*, 1072.
- (41) Lee, S.-gi. *Chem. Commun.*, **2006**, 1049.
- (42) Surette, J. K. D.; Green, L.; Singer, R. D. *Chem. Commun.* **1996**, 2753.
- (43) Santhosh, K.; Samanta, A. *J. Phys. Chem C* **2012**, *116*, 20643.
- (44) Sankaranarayanan, K.; Sathyaraj, G.; Nair, B. U.; Dhathathreyan, A. *J. Phys. Chem B* **2012**, *116*, 4175
- (45) Ohno, H.; Fukumoto, K. *Acc. Chem. Res.* **2007**, *40*, 1122.
- (46) Shirota, H.; Mandai, T.; Fukazawa, H.; Kato, T. *J. Chem. Eng. Data*, **2011**, *56*, 2453.
- (47) Anderson, J. L.; Ding, R.; Ellern, A.; Armstrong, D. W. *J. Am. Chem. Soc.* **2005**, *127*, 593.
- (48) Lall, S. I.; Mancheno, D.; Castro, S. B.; Cohen J. I.; Engel, R. *Chem. Commun.* **2000**, 2413.
- (49) Engel, R.; Cohen, J. I. *Curr. Org. Chem.* **2002**, *6*, 1453.
- (50) Engel, R.; Cohen, J. I.; Lall, S. I. *Phosphorus, Sulfur Silicon Relat. Elem.* **2000**, *177*, 1441.
- (51) Ito, K.; Nishina, N.; Ohno, H.; *Electrochim. Acta*, **2000**, *45*, 1295.
- (52) Pernak, J.; Skrzypczak, A.; Lota, G.; Frackowiak, E. *Chem. Eur. J.* **2007**, *13*, 3106.
- (53) Dzyuba, S.; Bartsch, R. A. *Chem Phys Chem* **2002**, *3*, 161.
- (54) Carda-Broch, S.; Berthold, A.; Armstrong, D. W. *Anal. Bioanal. Chem.* **2003**, *375*, 191.
- (55) Zhang, S.; Sun, N.; He, X.; Lu, X.; Zhang, X. *J. Phys. Chem. Ref. Data.* **2006**, *35*, 1475.
- (56) Xu, W.; Cooper, E. I.; Angell, C. A. *J. Phys. Chem. B* **2003**, *107*, 6170.
- (57) Hirao, M.; Sugimoto, H.; Ohno, H. *J. Electrochem. Soc.* **2000**, *147*, 4168.
- (58) Fuller, J.; Carlin, R. T.; Long, H. C. D.; Haworth, D. *Chem. Commun.* **1994**, 299.
- (59) Law, G.; Watson, P. R. *Langmuir* **2001**, *17*, 6138.

- (60) Buzzeo, M. C.; Evans, R. G.; Compton, R. G. *Chem Phys Chem* **2004**, *5*, 1106.
- (61) Reichardt, C. *Green Chem.* **2005**, *7*, 339.
- (62) Bonhôte, P.; Dias, A.; Papageorgiou, N.; Kalyanasundaram, K.; Gratzel, M. *Inorg. Chem.* **1996**, *35*, 1168.
- (63) Karmakar, R.; Samanta, A. *J. Phys. Chem. A*, **2002**, *106*, 6670.
- (64) Nishida, T.; Tashiro, Y.; Yamamoto, M. *J. Fluorine Chem.* **2003**, *120*, 135.
- (65) MacFarlane, D. R.; Meakin, P.; Sun, J.; Amini, N.; Forsyth, M. *J. Phys. Chem. B* **1999**, *103*, 4164.
- (66) Aki, S. N. V. K.; Brennecke, J. F.; Samanta, A. *Chem. Commun.* **2001**, 413.
- (67) Ngo, H. L.; LeCompte, K.; Hargens, L.; McEwen, A. *Thermochim. Acta* **2000**, *357*, 97.
- (68) Yadav, A.; Guha, A.; Pandey, A.; Pal, M.; Trivedi, S.; Pandey, S. *J. Chem. Thermodynamics* **2018**, *116*, 67.
- (69) Govinda, V.; Venkatesu, P.; Bahadur, I. *Phys. Chem. Chem. Phys.*, **2016**, *18*, 8278.
- (70) Zhou, Z. B.; Matsumoto, H.; Tatsumi, K. *Chem. Eur. J.* **2005**, *11*, 752.
- (71) Zhou, Z. B.; Matsumoto, H.; Tatsumi, K. *Chem. Lett.* **2004**, *33*, 1636.
- (72) Du, Z. Y.; Li, Z. P.; Guo, S.; Zhang, J.; Zhu, L. Y.; Deng, Y. Q. *J. Phys. Chem. B* **2005**, *109*, 19542.
- (73) Holbrey, J. D.; Turner, M. B.; Reichert, W. M.; Rogers, R. D. *Green Chem.* **2003**, *5*, 731.
- (74) Branco, L. C.; Rosa, J. N.; Ramos, J. J. M.; Afonso, C. A. M. *Chem. Eur. J.* **2002**, *8*, 3671.
- (75) Bagno, A.; Butts, C.; Chiappe, C.; D'Amico, F.; Lord, J. C. D.; Pieraccini, D.; Rastrelli, F. *Org. Biomol. Chem.* **2005**, *3*, 1624.
- (76) Santhosh, K.; Banerjee, S.; Rangaraj, N.; Samanta, A. *J. Phys. Chem. B* **2010**, *114*, 1967.

- (77) Tokuda, H.; Tsuzuki, S.; Susan, M. A.; Hayamizu, K.; Watanabe, M. *J Phys Chem B* **2006**, *110*, 19593.
- (78) Kawai, A.; Hidemori, T.; Shibuya, K. *Chem. Lett.* **2004**, *33*, 1464.
- (79) Kawai, A.; Hirakawa, M.; Abe, T.; Obi, K.; Shibuya, K. *J. Phys. Chem. A* **2001**, *105*, 9628.
- (80) Mandal, P. K.; Samnta, A. *J. Phys. Chem. B* **2005**, *109*, 15172.
- (81) Wakai, C.; Oleinikova, A.; Ott, M.; Weingartner, H. *J. Phys. Chem. B* **2005**, *109*, 17028.
- (82) Köddermann, T.; Wertz, C.; Heintz, A.; Ludwig, R. *Angew. Chem. Int. Ed.*, **2006**, *45*, 3697.
- (83) Carmichael, A. J.; Seddon, K. R. *J. Phys. Org. Chem.* **2000**, *13*, 591.
- (84) Greaves, T. L.; Weerawardena, A.; Fong, C.; Krodkiewska, I.; Drummond, C. J. *J. Phys. Chem. B* **2006**, *110*, 22479.
- (85) Wang, Y.; Voth, G. A. *J. Am. Chem. Soc.* **2005**, *35*, 12192.
- (86) Lopes, J. N. A. C.; Pádua, A. A. H. *J. Phys. Chem. B*, **2006**, *7*, 3330.
- (87) Xiao, D.; Rajian, J. R.; Cady, A.; Li, S.; Bartsch, R.A.; Quitevis, E.L. *J. Phys. Chem. B* **2007**, *111*, 4669.
- (88) Mandal, P. K.; Sarkar, M.; Samanta, A. *J. Phys. Chem. A* **2004**, *108*, 9048.
- (89) Hu, Z.; Margulis, C. J. *Proc. Natl. Acad. Sci. U.S.A.* **2006**, *103*, 831.
- (90) Jin, H.; Li, X.; Maroncelli, M. *J. Phys. Chem. B* **2007**, *111*, 13473.
- (91) Adhikari, A.; Sahu, K.; Dey, S.; Ghosh, S.; Mandal, U.; Bhattacharyya, K. *J. Phys. Chem. B* **2007**, *111*, 12809.
- (92) Dupont, J. J. *Braz. Chem. Soc.* **2004**, *15*, 341.
- (93) Hardacre, C.; Holbrey, J. D.; McMath, S. E. J.; Bowron, D. T.; Soper, A. K. *J. Chem. Phys.* **2003**, *118*, 273.
- (94) Fannin, A. A. Jr.; King, L. A.; Levisky, J. A.; Wilkes, J. S. *J. Phys. Chem.* **1984**, *88*, 2609.

- (95) Abdul-Sada, A. K.; Elaiwi, A. E.; Greenaway, A. M.; Seddon, K. R. *Eur. J. Mass Spectrom.* **1997**, *3*, 245.
- (96) Gozzo, F. C.; Santos, L. S.; Augusti, R.; Consorti, C. S.; Dupont, J.; Eberlin, M. N. *Chem. Eur. J.* **2004**, *10*, 6187.
- (97) Ozawa, R.; Hayashi, S.; Saha, S.; Kobayashi, A.; Hamaguchi, H. *Chem. Lett.* **2003**, *32*, 948.
- (98) Margulis, C. *J. Mol. Phys.* **2004**, *102*, 829.
- (99) Triolo, A.; Russina, O.; Fazio, B.; Triolo, R.; Di Cola, E. *Chem. Phys. Lett.* **2008**, *457*, 362.
- (100) Weingärtner, H.; Merkel, T.; Käshammer, S.; Schröder, W.; Wiegand, S. *Ber. Bunsen-Ges. Phys. Chem.* **1993**, *97*, 970.
- (101) Avent, A. G.; Chaloner, P. A.; Day, M. P.; Seddon, K. R.; Welton, T. *J. Chem. Soc., Dalton Trans.* **1994**, *0*, 3405.
- (102) Every, H. A.; Bishop, A. G.; MacFarlane, D. R.; Oradd, G.; Forsyth, M. *Phys. Chem. Chem. Phys.* **2004**, *6*, 1758.
- (103) Daguenet, C.; Dyson, P. J.; Krossing, I.; Oleinikova, A.; Slattery, J. M.; Wakai, C.; Weingärtner, H. *J. Phys. Chem. B* **2006**, *110*, 12782.
- (104) Weingärtner, H. S.; Sasisanker, P.; Daguenet, C.; Dyson, P. J.; Krossing, I.; Slattery, J. M.; Shubert, T. *J. Phys. Chem. B* **2007**, *111*, 4775.
- (105) Schröder, S.; Annat, G.; MacFarlane, D. R.; Forsyth, M.; Buchner, R.; Hefter, G. *Chem. Commun.* **2006**, 1748.
- (106) Turton, D. A.; Sonnleitner, T.; Ortnew, A.; Walther, M.; Hefter, G.; Seddon, K. R.; Stana, S.; Plechkova, N.; Buchner, R.; Wynne, K. *Faraday Discuss.* **2012**, *154*, 145.
- (107) Weingärtner, H. *Curr. Opin. Colloid Interface Sci.* **2013**, *18*, 183.

- (108) Schröder, U.; Wadhawan, J. D.; Compton, R. G.; Marken, F.; Suarez, P. A. Z.; Consorti, C. S.; de Souza, R. F.; Dupont, J. *New J. Chem.* **2000**, *24*, 1009.
- (109) Wang, Y.; Voth, G. A. *J. Phys. Chem. B* **2006**, *110*, 18601.
- (110) Urahata, S. M.; Ribeiro, M. C. C. *J. Chem. Phys.* **2004**, *120*, 1855.
- (111) Canongia Lopes, J. N.; Costa Gomes, M. F.; Padua, A. A. H. *J. Phys. Chem. B* **2006**, *110*, 16818.
- (112) Santos, L. M. N. B. F.; Canongia Lopes, J. N.; Coutinho, J. A. P.; Esperança, J. M. S. S.; Gomes, L. R.; Marrucho, I. M.; Rebelo, L. P. N. *J. Am. Chem. Soc.* **2006**, *129*, 284.
- (113) Samanta, A. *J. Phys. Chem. Lett.*, **2010**, *10*, 1557.
- (114) Das, S. K.; Sahu, P. K.; Sarkar, M. *RSC Adv.*, **2014**, *4*, 39184.
- (115) Zheng, Z.-P.; Fan, W.-H.; Roy, S.; Mazur, K.; Nazet, A.; Buchner, R.; Bonn, M.; Hunger, J. *Angew. Chem., Int. Ed.* **2014**, *54*, 687.
- (116) Adawiyah, N.; Moniruzzaman, M.; Hawatulailaa, S.; Goto, M. *Med. Chem. Commun.*, **2016**, *7*, 1881.
- (117) Monti, D.; Egiziano, E.; Burgalassi, S.; Chetoni, P.; Chiappe, C.; Sanzone, A.; Tampucci, S. *International Journal of Pharmaceutics*, **2017**, *516*, 45.
- (118) Tanaka, K.; Toda, F. *Chem. Rev.* **2000**, *100*, 1025.
- (119) Kajimoto, O. *Chem. Rev.* **1999**, *99*, 35H.
- (120) Seddon, K. R. *Nature (Materials)* **2003**, *2*, 363.
- (121) Muzart, J. *Adv. Synth. Catal.* **2006**, *348*, 275.
- (122) Shetty, P. H.; Poole, S. K.; Poole, C. F. *Anal. Chim. Acta* **1990**, *236*, 51.
- (123) Kowacz, M.; Mukhopadhyay, A.; Carvalho, A. L.; Esperança, J. M. S. S.; Romão, M. J.; Rebelo, L. P. N. *Cryst Eng Comm*, **2012**, *14*, 4912.

- (124) Takekiyo, T.; Yamazaki, K.; Yamaguchi, E.; Abe, H.; Yoshimura, Y. *J. Phys. Chem. B*, **2012**, *116*, 11092.
- (125) Lewandowski, A.; Swiderska-Mocek, A. *J. Power Sources* **2009**, *194*, 601.
- (126) Armand, M.; Endres, F.; MacFarlane, D. R.; Ohno, H.; Scrosati, B. *Nat. Mater.* **2009**, *8*, 621.
- (127) Ding, J.; Zhou, D.; Spinks, G.; Wallace, G.; Forsyth, S.; Forsyth, M.; MacFarlane, D. *Chem. Mater.* **2003**, *15*, 2392.
- (128) Huie, M. M.; DiLeo, R. A.; Marschlok, A. C.; Takeuchi, K. J.; Takeuchi, E. S. *ACS applied Materials and Interfaces*, **2015**, *7*, 11724.
- (129) MacFarlane, D. R.; Forsyth, M.; Howlett, P. C.; Pringle, J. S.; Annat, G.; Neil, W.; Izgorodina, E. I. *Accounts of Chemical Research*, **2007**, *40*, 1165.
- (130) Qu, J.; Truhan, J. J.; Dai, S.; Luo, H.; Blau, P. J. *Tribol. Lett.* **2006**, *22*, 207.
- (131) Janus, E.; Goc-Maciejewska, I.; Lozynski, M.; Pernak, J. *Tetrahedron Lett.* **2006**, *47*, 4079.
- (132) Huang, K.; Zhang, X. M.; Li, Y. X.; Wu, Y. T.; Hu, X. B. *J. Membr. Sci.* **2014**, *471*, 227.
- (133) Fang, D.; Yang, J. M.; Ni, C. *J. Heteroatom. Chem.* **2011**, *22*, 5.
- (134) Chinnappan, A.; Kim, H. *Chem. Eng. J.* **2012**, *187*, 283.
- (135) Fan, M. M.; Yang, J.; Jiang, P. P.; Zhang, P. B.; Li, S. S. *RSC Adv.* **2013**, *3*, 752.
- (136) Liu, X. F.; Xiao, L. F.; Wu, H. J. T.; Chen, J.; Xia, C. G. *Helv. Chim. Acta* **2009**, *92*, 1014.
- (137) Zeng, Z.; Phillips, B. S.; Xiao, J.-C.; Shreeve, J. M. *Chem. Mater.* **2008**, *20*, 2719.
- (138) Jin, C. M.; Ye, C.; Phillips, B. S.; Zabinski, J. S.; Liu, X. Q.; Liu, W. M.; Shreeve, J. M. *J. Mater. Chem.* **2006**, *16*, 1529.
- (139) Han, X. X.; Armstrong, D. W. *Org. Lett.* **2005**, *7*, 4205.

- (140) Palacio, M.; Bhushan, B. J. *Vac. Sci. Technol. A*, **2009**, *27*, 986.
- (141) Zhang, Z.; Zhoua, H.; Yanga, L.; Tachibana, K.; Kamijima, K.; Xu, J. *Electrochim. Acta*, **2008**, *53*, 4833.
- (142) Hayes, R.; Warr, G. G.; Atkin, R. *Chem. Rev.* **2015**, *115*, 6357.
- (143) Urahata, S. M.; Ribeiro, M. C. C. *J. Chem. Phys.* **2004**, *120*, 1855.
- (144) Castner, E. W. Jr.; Margulis, C. J.; Maroncelli, M.; Wishart, J. F. *Annu. Rev. Phys. Chem.* **2011**, *62*, 85.
- (145) Moosavi, M.; Khasheia, F.; Sedghamiz, E. *Phys. Chem. Chem. Phys.*, **2018**, *20*, 435.
- (146) Hu, Z.; Margulis, C. J. *Proc. Natl. Acad. Sci. U. S. A.* **2006**, *103*, 831.
- (147) Borodin, O. *J. Phys. Chem. B* **2009**, *113*, 12353.
- (148) Kashyap, H. K.; Biswas, R. *J. Phys. Chem. B* **2010**, *114*, 16811.
- (149) Kashyap, H. K.; Biswas, R. *J. Phys. Chem. B* **2008**, *112*, 12431.
- (150) Wang, Y.; Voth, G. A. *J. Am. Chem. Soc.* **2005**, *127*, 12192.
- (151) Henderson, W. A.; Fylstra, P.; De Long, H. C.; Trulovea, P. C.; Parsons, S. *Phys. Chem. Chem. Phys.*, **2012**, *14*, 16041.
- (152) Suarez, P. A. Z.; Einloft, S.; Dullius, J. E. L.; de Souza, R. F.; Dupont, J. *J. Chim. Phys. Phys.-Chim. Biol.*, **1998**, *95*, 1626.
- (153) Canongia Lopes, J. N. A.; Padua, A. A. H. *J. Phys. Chem. B*, **2006**, *110*, 3330.
- (154) Li, S.; Feng, G.; Ban~uelos, J. L.; Rother, G.; Fulvio, P. F.; Dai S.; Cummings, P. T.; *J. Phys. Chem. C*, **2013**, *117*, 18251.
- (155) Palchowdhurya, S.; Bhargava, B. L. *Phys. Chem. Chem. Phys.*, **2015**, *17*, 11627.
- (156) Bhargava, B. L.; Klein, M. L. *J. Phys. Chem. B*, **2011**, *115*, 10439.

- (157) Fakhraee, M.; Zandkarimi, B.; Salari, H.; Gholami, M. R. *J. Phys. Chem. B*, **2014**, *118*, 14410.
- (158) Mandal, P. K.; Samanta, A. *J. Phys. Chem. B*, **2005**, *109*, 15172.
- (159) Patra, S.; Samanta, A. *J. Phys. Chem. B*, **2012**, *116*, 12275.
- (160) Paul, A.; Samanta, A. *J. Phys. Chem. B* **2007**, *111*, 4724.
- (161) Paul, A.; Mandal, P. K.; Samanta, A. *J. Phys. Chem. B*, **2005**, *109*, 9148.
- (162) Werner, J. H.; Baker, S. N.; Baker, G. A. *Analyst* **2003**, *128*, 786.
- (163) Roy, D.; Patel, N.; Conte, S.; Maroncelli, M. *J. Phys. Chem. B* **2010**, *114*, 8410.
- (164) Greaves, T. L.; Drummond, C. *J. Chem. Rev.*, **2015**, *115*, 11379.
- (165) Maroncelli, M.; Zhang, X. X.; Liang, M.; Roy, D.; Ernsting, N. P. *Disc. Faraday Soc.* **2012**, *154*, 409.
- (166) Hunger, J.; Stoppa, A.; Schrödle, S.; Hefter, G.; Buchner, R. *Chem. Phys. Chem.*, **2009**, *10*, 723.
- (167) Zhang, X. X.; Liang, M.; Ernsting, N. P.; Maroncelli, M. *J. Phys. Chem. Lett.* **2013**, *4*, 1205.
- (168) Mandal, S.; Kuchlyan, J.; Banik, D.; Ghosh, S.; Banerjee, C.; Khorwal, V.; Sarkar, N. *Chem Phys Chem*, **2014**, *15*, 3544.
- (169) Banerjee, C.; Kundu, N.; Ghosh, S.; Mandal, S.; Kuchlyan, J.; Sarkar, N. *J. Phys. Chem. B*, **2013**, *117*, 9508.
- (170) Adhikari, A.; Das, D. K.; Sasmal, D. K.; Bhattacharyya, K. *J. Phys. Chem. B*, **2009**, *113*, 3737.
- (171) Das, D. K.; Das, A. K.; Mondal, T.; Mandal, A. K.; Bhattacharyya, K. *J. Phys. Chem. B*, **2010**, *114*, 13159.

- (172) Rao, V. G.; Mandal, S.; Ghosh, S.; Banerjee, C.; Sarkar, N. *J. Phys. Chem. B*, **2012**, *121*, 12021.
- (173) Chowdhury, R.; Chattoraj, S.; Mojumdar, S. S.; Bhattacharyya, K. *Phys. Chem. Chem. Phys.*, **2013**, *15*, 16286.
- (174) Rilo, E.; Vila, J.; Garcí'a-Garabal, S.; Varela, L. M.; Cabeza, O. *J. Phys. Chem. B*, **2013**, *117*, 1411.
- (175) Dutt, G. B.; Ghanty, T. K. *J. Phys. Chem. A*, **2004**, *108*, 6090.
- (176) Carlson, P. J.; Bose, S.; Armstrong, D. W.; Hawkins, T.; Gordon, M. S.; Petrich, J. W. *J. Phys. Chem. B* **2012**, *116*, 503.
- (177) Daschakraborty, S.; Biswas, R. *J. Phys. Chem. B*, **2014**, *118*, 1327.
- (178) Das, S.; Biswas, R.; Mukherjee, B. *J. Phys. Chem. B*, **2015**, *119*, 274.
- (179) Kashyap, H. K.; Biswas, R. *J. Phys. Chem. B* **2010**, *114*, 16811.
- (180) Mukherjee, K.; Das, A.; Choudhury, S.; Barman, A.; Biswas, R. *J. Phys. Chem. B*, **2015**, *119*, 8063.
- (181) Daschakraborty, S.; Biswas, R. *Chem. Phys. Lett.* **2011**, *510*, 202.
- (182) Majhi, D.; Sarkar, M. *Phys. Chem. Chem. Phys.*, **2017**, *19*, 23194.
- (183) Das, S. K.; Sahu, P. K.; Sarkar, M. *J. Phys. Chem. B* **2013**, *117*, 636.
- (184) Majhi, D.; Sahu, P. K.; Seth, S.; Sarkar, M. *Phys. Chem. Chem. Phys.*, **2016**, *18*, 22343.
- (185) Das, S. K.; Majhi, D.; Sahu, P. K.; Sarkar, M. *Chem. Phys. Chem.*, **2017**, *18*, 198.
- (186) Majhi, D.; Pabbathi, A.; Sarkar, M. *J. Phys. Chem. B*, **2016**, *120*, 193.
- (187) Majhi, D.; Seth, S.; Sarkar, M. *Phys. Chem. Chem. Phys.*, **2018**, *20*, 7844.
- (188) Maurya, R.; Naithani, S.; Bandyopadhyay, D.; Choudhury, N.; Dutt, G. B. *J. Phys. Chem. B*, **2017**, *121*, 10965.

- (189) Fruchey, K.; Fayer, M. D. *J. Phys. Chem. B* **2010**, *114*, 2840.
- (190) Mali, K. S.; Dutt, G. B.; Mukherjee, *J. Chem. Phys.* **2008**, *128*, 054504.
- (191) Gangamallaiiah, V.; Dutt, G. B. *J. Phys. Chem. B* **2013**, *117*, 5050.
- (192) Prabhu, S. R.; Dutt, G. B. *J. Phys. Chem. B*, **2015**, *119*, 2019.
- (193) Mali, K. S.; Dutt, G. B.; Mukherjee, T. *J. Chem. Phys.*, **2005**, *123*, 174504.
- (194) Prabhu, S. R.; Dutt, G. B. *J. Phys. Chem. B* **2014**, *118*, 9420.
- (195) Das, S. K.; Sarkar, M. *J. Phys. Chem. B* **2012**, *116*, 194.
- (196) Mali, K. S.; Dutt, G. B.; Mukherjee, T. *J. Chem. Phys.*, **2005**, *123*, 174504.
- (197) Gangamallaiiah, V.; Dutt, G. B. *J. Phys. Chem. B* **2014**, *118*, 13711.
- (198) Dutt, G. B. *J. Phys. Chem. B* **2010**, *114*, 8971.
- (199) Khara, D. C.; Kumar, J. P.; Mondal, N.; Samanta, A. *J. Phys. Chem. B* **2013**, *117*, 5156.
- (200) Das, S. K.; Majhi, D.; Sahu, P. K.; Sarkar, M. *RSC Adv.* **2015**, *5*, 41585.
- (201) Prabhu, S. R.; Dutt, G. B. *J. Phys. Chem. B* **2014**, *118*, 13244.
- (202) Cha, S.; Kim, D. *J. Korean Phys. Soc.* **2012**, *61*, 1555.
- (203) Cha, S.; Shim, T.; Ouchi, Y.; Kim, D. *J. Phys. Chem. B* **2013**, *117*, 10818.
- (204) Das, S. K.; Sahu, P. K.; Sarkar, M. *RSC Adv.* **2014**, *4*, 39184.
- (205) Ito, N.; Arzhantsev, S.; Maroncelli, M. *Chem. Phys. Lett.*, **2004**, *396*, 83.
- (206) Zhang, X.-X.; Liang, M.; Ernsting, N. P.; Maroncelli, M. *J. Phys. Chem. B* **2013**, *117*, 4291.
- (207) Khara, D. C.; Samanta, A. *Phys. Chem. Chem. Phys.* **2010**, *12*, 7671.
- (208) Ito, N.; Arzhantsev, S.; Heitz, M.; Maroncelli, M. *J. Phys. Chem. B*, **2004**, *108*, 5771.
- (209) Sahu, P. K.; Ghosh, A.; Sarkar, M. *J. Phys. Chem. B*, **2015**, *119*, 14221.
- (210) Das, S. K.; Patra, A. S.; Jose, D.; Sarkar, M. *Chem. Phys. Lett.*, **2012**, *528*, 11.

- (211) Sahu, K.; Ghosh, S.; Mondal, S. K.; Ghosh, B. C.; Sen, P.; Roy, D.; Bhattacharyya, K. *J. Chem. Phys.*, **2006**, *125*, 044714.
- (212) Ghosh, A.; De, C. K.; Chatterjee, T.; Mandal, P. K. *Phys. Chem. Chem. Phys.*, **2015**, *17*, 16587.
- (213) Ghosh, A.; Chatterjee, T.; Roy, D.; Das, A.; Mandal, P. K. *J. Phys. Chem. C*, **2014**, *118*, 5051.
- (214) Dhale, R. S.; Sahu, P. K.; Sarkar, M. *J. Phys. Chem. B*, **2017**, *121*, 7934.
- (215) Castiglione, F.; Moreno, M.; Raos, G.; Famulari, A.; Mele, A.; Appetecchi, G. B.; Passerini, S. *J. Phys. Chem. B* **2009**, *113*, 10750.
- (216) Castiglione, F.; Raos, G.; Appetecchi, G. B.; Montanino, M.; Passerini, S.; Moreno, M.; Famulari, A.; Mele, A. *Phys. Chem. Chem. Phys.* **2010**, *12*, 1784.
- (217) Lingscheid, Y.; Arenz, S.; Giernoth, R. *Chem. Phys. Chem.* **2012**, *13*, 261.
- (218) Chiappe, C.; Sanzone, A.; Mendola, D.; Castiglione, F.; Famulari, A.; Raos, G.; Mele, A. *J. Phys. Chem. B* **2013**, *117*, 668.
- (219) Khatun, S.; Castner, E. W. Jr. *J. Phys. Chem. B* **2015**, *119*, 9225.
- (220) Sasmal, D. K.; Mandal, A. K.; Mondal, T.; Bhattacharyya, K. *J. Phys. Chem. B* **2011**, *115*, 7781.
- (221) Strehmel, V.; Laschewsky, A.; Stoesser, R.; Zehl, A.; Herrmann, W. *J. Phys. Org. Chem.* **2006**, *19*, 318.
- (222) Stoesser, R.; Herrmann, W.; Zehl, A.; Laschewsky, A.; Strehmel, V. *Z. Phys. Chem.* **2006**, *220*, 1309.
- (223) Noel, M. A. M.; Allendoerfer, R. D.; Osteryoung, R. A. *J. Phys. Chem. A* **1992**, *96*, 2391.
- (224) Palchowdhury, S.; Bhargava, B. L. *J. Phys. Chem. B*, **2015**, *119*, 11815.

- (225) Sahu, P. K.; Sarkar, M. *Chem. Phys. Lett.* **2016**, *652*, 177.
- (226) Khara, D. C.; Samanta, A. *J. Phys. Chem. B*, **2012**, *116*, 13430.
- (227) Binetti, E.; Panniello, A.; Triggiani, L.; Tommasi, R.; Agostiano, A.; Curii, M. L.; Striccoli, M. *J. Phys. Chem. B*, **2012**, *116*, 3512.
- (228) Majhi, D.; Das, S. K.; Sahu, P. K.; Pratik, Md. S.; Kumar, A.; Sarkar, M. *Phys. Chem. Chem. Phys.*, **2014**, *16*, 18349.
- (229) Thieghi, L. T.; Longo, L. S. Jr.; Licence, P.; Alves, S. **2017**, *657*, 95.
- (230) Shim, Y.; Duan, J. S.; Choi, M. Y.; Kim, H. J. *J. Chem. Phys.* **2003**, *119*, 6411.
- (231) Kobrak, M. N.; Znamenskiy, V. *Chem. Phys. Lett.* **2004**, *395*, 127.
- (232) Znamenskiy, V.; Kobrak, M. N. *J. Phys. Chem. B* **2004**, *108*, 1072.
- (233) Shim, Y.; Choi, M. Y.; Kim, H. J. *J. Chem. Phys.* **2005**, *122*, 044511.
- (234) Bargava, B. L.; Balasubramanian, S. *J. Chem. Phys.* **2005**, *123*, 144505.
- (235) Bargava, B. L.; Balasubramanian, S. *J. Chem. Phys.* **2006**, *417*, 486.
- (236) Nese, C.; Unterreiner, A. N. *Phys. Chem. Chem. Phys.* **2010**, *12*, 1698.
- (237) Kasha, M. *Discuss. Faraday Soc.*, **1950**, *9*, 14.
- (238) Valeur, B.; Weber, G. *Chem. Phys. Lett.* **1977**, *45*, 140.
- (239) Fleming, G. R. *Chemical applications of ultrafast spectroscopy*, Oxford University Press, New York, 1986.
- (240) Demchenko, A. P. *Luminescence*, **2002**, *17*, 19.
- (241) Demchenko, A. P. *In Topics in Fluorescence Spectroscopy*; Lakowicz, J. R., Ed.; Plenum Press: New York, 1991; Vol. 3.
- (242) Lakowicz, J. R.; Nakamoto, S. K. *Biochemistry*, **1984**, *23*, 3013.
- (243) Itoh, K.; Azumi, T. *J. Chem. Phys.* **1975**, *62*, 3431.

- (244) Chattopadhyay, A.; Mukherjee, S. *Biochemistry*, **1993**, 32, 3804.
- (245) Lakowicz, J. R. *Principles of Fluorescence Spectroscopy*, 3rd edition; Springer: New York, 2006.
- (246) Dutt, G. B. *Chem Phys Chem* **2005**, 6, 413.
- (247) Waldeck, D. H. *The Role of Solute-Solvent Friction in Large- Amplitude Motions. In Conformational Analysis of Molecules in the excited States*, Wiley-VCH: New York, 2000, 113.
- (248) Gierer, A.; Wartz, K. *Z. Naturforsch A* **1953**, 8, 532.
- (249) Dote, J. L.; Kivelson, D.; Schwart, R. N. *J. Phys. Chem.* **1981**, 85, 2169.
- (250) Valeur, B. *Molecular Fluorescence Principles and Applications*, Wiley-VCH Verlag GmbH, Weinheim, Germany, 2002.
- (251) Förster, T. *Ann. Phys.*, **1948**, 2, 55.
- (252) Dias, N.; Shimizu, K.; Morgado, P.; Filipe, E.J.M.; Canongia Lopes, J. N.; F. Chavez, V. *J. Phys. Chem. B* **2014**, 118, 5772.
- (254) Damodaran, K. *Annual Reports on NMR Spectroscopy* **2016**, 88, 215.
- (255) Kruk, D.; Meier, R.; Rachocki, A.; Korpala, A.; Singh, R. K.; Rossler, E.A. *J. Chem. Phys.* **2014**, 140, 244509.
- (256) Evans, R. G.; Wain, A. J.; Hardacre, C.; Compton, R. G. *Chem. Phys. Chem.* **2005**, 6, 1035.
- (256) Miyake, Y.; Hidemori, T.; Akai, N.; Kawai, A.; Shibuya, K.; Koguchi, S.; Kitazume, T. *Chem. Lett.* **2009**, 38, 124.
- (257) Stoesser, R.; Herrmann, W.; Zehl, A.; Strehmel, V.; Laschewsky, A. *Chem. Phys. Chem* **2006**, 7, 1106.
- (258) Mladenova, B. Y.; Kattnig, D. R.; Grampp, G. *J. Phys. Chem. B* **2011**, 115, 8183.

- (259) Mladenova, B. Y.; Chumakova, N. A.; Pergushov, V. I.; Kokorin, A. I.; Grampp, G.; Kattnig, D. R. *J. Phys. Chem. B* **2012**, *116*, 12295.
- (260) Birks, J. B. *Photophysics of Aromatic Molecules*; Wiley-Inter-Science: London, 1970.
- (261) Gilbert, A.; Baggott, J.; Wagner, P. J. *Essential of Molecular Photochemistry*; Blackwell science Inc.: Cambridge, USA, 1991.
- (262) Rohatgi-Mukherjee, K. K. *Fundamentals of Photochemistry*; Wiley Eastern Ltd: India, 1986.
- (263) Becker, W. *Advanced time correlated single photon counting technique*; Springer: New York, 2005.
- (264) Demas, J. N. *Excited state lifetime measurement*; Academic press: New York, 1983.
- (265) O'Connor, D. V.; Phillips, D. *Time Correlated Single Photon Counting*; Academic: New York, 1984.
- (266) Ware, W. R. *Creation and detection of the Excited State*; Lamola, A. A., Ed.; Marcel Dekker: New York, 1971; Vol. 1, Part A.
- (267) Bevington, P. R. *Data Reduction and Error Analysis for the Physical Sciences*; McGraw-Hill: New York, 1969.
- (268) McKinnon, A. E.; Szabo, A. G.; Miller, D. R. *J. Phys Chem.* **1977**, *81*, 1564.
- (269) O'Connor, D. V.; Ware, W. R.; Andre, J. C. *J. Phys. Chem.* **1979**, *83*, 1333.
- (270) Ware, W. R.; Doemeny, L. J.; Nemzek, T. L. *J. Phys Chem.* **1973**, *77*, 2083.
- (271) Einstein, A. *Investigations on the Theory of the Brownian Movement*; Dover: New York, 1956.
- (272) Brouwer, A. M. *Pure Appl. Chem.*, **2011**, *83*, 2213.
- (273) Rechthaler, K. *Chem. Phys.* **1984**, *189*, 99.

- (274) Becke, A. D. *J. Chem. Phys.* **1993**, *98*, 5648.
- (275) Zhao, Y.; Schultz, N. E.; Truhlar, D. G. *J. Chem. Theory Comput.*, **2006**, *2*, 364.
- (276) Dorfmler, T.; Pecora, R. *Rotational dynamics of small and macromolecules*, Springer-Verlag, Berlin, 1987.
- (277) Dutt, G. B.; Rama Krishna, G. *J. Chem. Phys.*, **2000**, *112*, 4676.
- (278) Dutt, G. B.; Srivatsavoy, V. J. P.; Sapre, A. V. *J. Chem. Phys.*, **1999**, *110*, 9623.
- (279) Dutt, G. B.; *J. Chem. Phys.*, **2000**, *113*, 11154.
- (280) Dutt, G. B.; Ghanty, T. K. *J. Chem. Phys.*, **2002**, *116*, 6671.
- (281) Dutt, G. B.; Ghanty, T. K. *J. Chem. Phys.*, **2003**, *118*, 4119.
- (282) Chapman, C. F.; Fee, R. S.; Maroncelli, M. *J. Phys. Chem.*, **1995**, *99*, 4811.
- (283) Horng, M. L.; Gardecki, J. A.; Papazyan, A.; Maroncelli, M. *J. Phys. Chem.*, **1995**, *99*, 17311.
- (284) Das, S. K.; Sarkar, M. *Chem. Phys. Lett.*, **2011**, *515*, 23.
- (285) Das, S. K.; Sarkar, M. *J. Fluoresc.*, **2014**, *24*, 455.
- (286) Sahu, P. K.; Das, S. K.; Sarkar, M. *Phys. Chem. Chem. Phys.*, **2014**, *16*, 12918.
- (287) Saha, S.; Samant, A. *J. Phys. Chem. A*, **1998**, *102*, 7903.
- (288) Sension, R. J.; Hochstrasser, R. M. *J. Chem. Phys.*, **1993**, *98*, 2490.
- (289) Small, E. W.; Isenberg, I. *Biopolymers*, **1977**, *16*, 1907.
- (290) Edward, J. T. *J. Chem. Educ.*, **1970**, *47*, 261.
- (291) Amendola, V.; Fabbrizzi, L.; Mosca, L. *Chem. Soc. Rev.*, **2010**, *39*, 3889.
- (292) Balci, M. *Basic ¹H- and ¹³C-NMR spectroscopy*, Elsevier Science, 2005.
- (293) Jalili, A. H.; Rahmati-Rostami, M.; Ghotbi, C.; Hosseini-Jenab, M.; Ahmadi, A. N. *J. Chem. Eng. Data*, **2009**, *54*, 1844.

- (294) Suna, J.; Zhang, S.; Cheng, W.; Ren, J. *Tetrahedron Lett.*, **2008**, *49*, 3588.
- (295) Tang, S.; Baker, G. A.; Zhao, H. *Chem. Soc. Rev.*, **2012**, *41*, 4030.
- (296) Nowicki, J. Dr.; Nosal, H.; Muszyński, M. *Chem Plus Chem*, **2012**, *80*, 648.
- (297) Shinde, S. S.; Chi, H. M.; Lee, B. S.; Chi, D. Y. *Tetrahedron Letters*, **2009**, *50*, 6654.
- (298) Yang, X.; Yan, N.; Fei, Z.; Crespo-Quesada, R. M.; Laurency, G.; Kiwi-Minsker, L.; Kou, Y.; Li, Y.; Dyson, P. J. *Inorg. Chem.*, **2008**, *47*, 7444.
- (299) Holbrey, J. D.; Turner, M. B.; Reichert, W. M.; Rogers, R. D. *Green Chem.*, **2003**, *5*, 731.
- (300) Zhang, S.; Qi, X.; Ma, X.; Lu, L.; Deng, Y. *J. Phys. Chem. B*, **2010**, *114*, 3912.
- (301) Bhattacharyya, K. *J. Phys. Chem. Lett.*, **2010**, *1*, 3254.
- (302) Song, X.; Hamano, H.; Minofar, B.; Kanzaki, R.; Fujii, K.; Kameda, Y.; Kohara, S.; Watanabe, M.; Ishiguro, S.; Umebayashi, Y. *J. Phys. Chem. B*, **2012**, *116*, 2801.
- (303) Amyes, T. L.; Diver, S. T.; Richard, J. P.; Rivas, F. M.; Toth, K. *J. Am. Chem. Soc.* **2004**, *126*, 4366.
- (304) Ziyada, A. K.; Wilfred, C. D.; Bustam, M. A.; Man, Z.; Murugesan, T. *J. Chem. Eng. Data*, **2010**, *55*, 3886.
- (305) Muhammad, N.; Man, Z. B.; Bustam, M. A.; Mutalib, M. I. A.; Wilfred, C. D.; Rafiq, S. *J. Chem. Eng. Data*, **2011**, *56*, 3157.
- (306) Muhammad, N.; Man, Z.; Ziyada, A. K.; Bustam, M. A.; Mutalib, M. I. A.; Wilfred, C. D.; Rafiq, S.; Tan, I. M. *J. Chem. Eng. Data*, **2012**, *57*, 737.
- (307) Gu, Z.; Brennecke, J. F. *J. Chem. Eng. Data*, **2002**, *47*, 339.
- (308) Smith, T. A.; Bajada, L. M.; Dunstan, D. E. *Macromolecules*, **2002**, *35*, 2736.
- (309) Li, B.; Qiu, M.; Long, S.; Wang, X.; Guo, Q.; Xia, A. *Phys. Chem. Chem. Phys.*, **2013**, *15*, 16074.

- (310) Karmakar, R.; Samanta, A. *Chem. Phys. Lett.*, **2003**, 376, 638.
- (311) Sarkar, A.; Trivedi, S.; Baker, G. A.; Pandey, S. *J. Phys. Chem. B*, **2008**, 112, 14927.
- (312) Sarkar, A.; Trivedi, S.; Pandey, S. *J. Phys. Chem. B*, **2009**, 113, 7606.
- (313) Moog, R. S.; Bankert, D. L.; Maroncelli, M. *J. Phys. Chem.* **1993**, 97, 1496.
- (314) Kim, J. Y.; Kim, T. H.; Kim, D. Y.; Park, N.-G.; Ahn, K.-D. *J. Power Sources*, **2008**, 175, 692.
- (315) Ishida, T.; Shirota, H. *J. Phys. Chem. B*, **2013**, 117, 1136.
- (316) Sahu, P. K.; Das, S. K.; Sarkar, M. *J. Phys. Chem. B*, **2014**, 118, 1907.
- (317) Li, S.; Zhang, P.; Fulvio, P. F.; Hillesheim, P. C.; Feng, G.; Dai, S.; Cummings, P. T. *J. Phys.: Condens. Matter*, **2014**, 26, 284105.
- (318) Patil, R. A.; Talebi, M.; Xu, C.; Bhawal, S. S.; Armstrong, D. W. *Chem. Mater.*, **2016**, 28, 4315.
- (319) Ding, Y.-S.; Zhaa, M.; Zhang, J.; Wang, S.-S. *Colloids Surf. A*, **2007**, 298, 201.
- (320) Pitawala, J.; Matic, A.; Martinelli, A.; Jacobsson, P.; Koch, V.; Croce, F. *J. Phys. Chem. B*, **2009**, 113, 10607.
- (321) Lee, M.; Niu, Z.; Slebodnick, C.; Gibson, H. W. *J. Phys. Chem. B*, **2010**, 114, 7312.
- (322) Persson, K.; Bales, B. L. *J. Chem. Soc., Faraday Trans.*, **1995**, 91, 2863.
- (323) Dzyuba, S. V.; Bartsch, R. A. *Tetrahedron Lett.*, **2002**, 43, 4657.
- (324) Persson, K.; Bales, B. L. *J. Chem. Soc., Faraday Trans.*, **1995**, 17, 2863.
- (325) Bales, B. L.; Stenland, C. *J. Phys. Chem.*, **1993**, 97, 3418.
- (326) Bales, B. L. *J. Magn. Reson.*, **1982**, 48, 418.
- (327) Costa, A. J. L.; Esperanca, J. M. S. S.; Marrucho, I. M.; Rebelo, L. P. N. *J. Chem. Eng. Data*, **2011**, 56, 3433.

- (328) Lovelock, K. R. J.; Ejigu, A.; Loh, S. F.; Men, S.; Licence, P.; Walsh, D. A. *Phys. Chem. Chem. Phys.*, **2011**, *13*, 10155.
- (329) Habasaki, J.; Ngai, K. L. *J. Chem. Phys.*, **2008**, *129*, 194501.
- (330) Tsuzuki, S. *Chem. Phys. Chem.*, **2012**, *13*, 1664.
- (331) Burrell, A. K.; Del Sesto, R. E.; Baker, S. N.; McCleskey, T. M.; Baker, G. A. *Green Chem.* **2007**, *9*, 449.
- (332) Tang, F.; Wu, K.; Ding, Li.; Yuan, J.; Liu, Q.; Nie, L.; Yao, S. *Sep. Purif. Technol.* **2008**, *60*, 245.
- (333) LaPlante, R. S.; Carson, R.; Gillard, J.; Aubry, N.; Coulombe, R.; Bordeleau, S.; Bonneau, P.; Little, M.; O'Meara, J.; Beaulieu, P. L. *J. Med. Chem.* **2013**, *56*, 5142.
- (334) Zheng, Z. P.; Fan, W. H.; Roy, S.; Mazur, K.; Nazet, A.; Buchner, R.; Bonn, M.; Hunger, J. *Angew. Chem., Int. Ed.* **2014**, *53*, 1.
- (335) Perrin, F. *J. Phys. Radium.* **1936**, *7*, 1.
- (336) Youngren, G. K.; Acrivos, A. *J. Chem. Phys.* **1975**, *63*, 3846.
- (337) Rilo, E.; Domínguez-Pérez, M.; Vila, J.; Varela, L. M.; Cabeza, O. *J. Chem. Thermodynamics*, **2012**, *49*, 165.
- (338) Rilo, E.; Varela, L. M.; Cabeza, O. *J. Chem. Eng. Data* **2012**, *57*, 2136.
- (339) Varela, L. M.; Carrete, J.; García, M.; Gallego, L. J.; Turmine, M.; Rilo, E.; Cabeza, O. *Fluid Phase Equilibria* **2010**, *298*, 280.
- (340) Ghosh, J. C. *J. Chem. Soc., Trans.* **1918**, *113*, 449.
- (341) Frank, H. S.; Thomson, P. T. *The Structure of Electrolyte Solutions*, Wiley, New York, 1939.
- (342) Triolo, A.; Russina, O.; Bleif, H.-J.; Cola, E. D. *J. Phys. Chem. B* **2007**, *111*, 4641.

- (343) Castner, E. W. Jr.; Wishart, J. F.; Shirota, H. *Acc. Chem. Res.* **2007**, *40*, 1217.
- (344) Russina, O.; Gontrani, L.; Fazio, B.; Lombardo, D.; Triolo, A.; Caminiti, R. *Chem. Phys. Lett.* **2010**, *493*, 259.
- (345) Mele, A.; Tran, C. D.; Lacerda, S. H. D. P. *Angew. Chem., Int. Ed.* **2003**, *42*, 4364.
- (346) Dávila, M. J.; Aparicio, S.; Alcalde, R.; García, B.; Leal, J. M. *Green Chem.*, **2007**, *9*, 221.
- (347) García-Garabal, S.; Vila, J.; Rilo, E.; Domínguez-Pérez, M.; Segade, L.; Tojo, E.; Verdía, P.; Varela, L.M.; Cabeza, O. *Electrochimica Acta*, **2017**, *231*, 94.
- (348) Ajayaghosh, A.; Praveen, V. K.; Vijayakumar, C. *Chem. Soc. Rev.*, **2008**, *37*, 109.
- (349) Izawa, H.; Wakizono, S.; Kadokawa, J.-i. *Chem. Commun.*, **2010**, *46*, 6359.
- (350) Horn, D.; Rieger, J. *Angew. Chem., Int. Ed.*, **2001**, *40*, 4330, and references therein.
- (351) Alivistos, P. A. *Science*, **1996**, *271*, 933.
- (352) Peng, X.; Michael, C. S.; Andreas, V. K.; Alivisatos, A. P. *J. Am. Chem. Soc.*, **1997**, *119*, 7019.
- (353) Silinsh, E. A. *Organic Molecular Crystals: Their Electronic States*, Springer-Verlag, Berlin, 1980.
- (354) Li, D.; Guo, J. L. *J. Phys. D: Appl. Phys.*, **2008**, *41*, 105115.
- (355) Varghese, S.; Das, S. *J. Phys. Chem. Lett.*, **2011**, *2*, 863.
- (356) Babu, S. S.; Prasanthkumar, S.; Ajayaghosh, A. *Angew. Chem., Int. Ed.*, **2012**, *51*, 1766.
- (357) Wang, H.; Xu, X.; Kojtari, A.; Ji, H.-F. *J. Phys. Chem. C*, **2011**, *115*, 20091.
- (358) Ibanez, A.; Maximov, S.; Guiu, A.; Chaillout, C.; Baldeck, P. L. *Adv. Mater.*, **1998**, *10*, 1540.
- (359) Balzer, F.; Rubahn, H. *Nano Lett.*, **2002**, *2*, 747.

- (360) Kietzke, T.; Neher, D.; Landfester, K.; Montenegro, R.; Guntner, R.; Scherf, U. *Nat. Mater.*, **2003**, *2*, 408.
- (361) Zhao, L.; Yang, W.; Luo, Y.; Zhai, T.; Zhang, G.; Yao, J. *Chem.-Eur. J.*, **2005**, *11*, 3773.
- (362) Mas-Torrent, M.; Hadley, P. *Small*, **2005**, *1*, 806.
- (363) Onodera, T.; Kasai, H.; Okada, S.; Oikawa, H.; Mizuno, K.; Fujitsuka, M.; Ito, O. *Opt. Mater.*, **2002**, *21*, 595.
- (364) Oikawa, H.; Mitsui, T.; Onodera, T.; Kasai, H.; Nakanishi, H.; Sekiguchi, T. *Jpn. J. Appl. Phys.*, **2003**, *42*, L111.
- (365) Takahashi, S.; Miura, H.; Kasai, H.; Okada, S.; Oikawa, H.; Nakanishi, H. *J. Am. Chem. Soc.*, **2002**, *124*, 10944.
- (366) Fu, H. B.; Yao, J. N. *J. Am. Chem. Soc.*, **2001**, *123*, 1434.
- (367) Fu, H.; Loo, B. H.; Xiao, D.; Xie, R.; Ji, X.; Yao, J.; Zhang, B.; Zhang, L. *Angew. Chem., Int. Ed.*, **2002**, *41*, 962.
- (368) Xiao, D.; Xi, L.; Yang, W.; Fu, H.; Shuai, Z.; Fang, Y.; Yao, J. *J. Am. Chem. Soc.*, **2003**, *125*, 6740.
- (369) An, B.-K.; Kwon, S.-K.; Jung, S.-D.; Park, S. Y. *J. Am. Chem. Soc.*, **2002**, *124*, 14410.
- (370) Li, S.; He, L.; Xiong, F.; Li, Y.; Yang, G. *J. Phys. Chem. B*, **2004**, *108*, 10887.
- (371) Patra, A.; Venkatram, N.; Rao, D. N.; Radhakrishnan, T. P. *J. Phys. Chem. C*, **2008**, *112*, 16269.
- (372) Patra, A.; Hebalkar, N.; Sreedhar, B.; Radhakrishnan, T. P. *J. Phys. Chem. C*, **2007**, *111*, 16184.
- (373) Karunakaran, V.; Prabhu, D. D.; Das, S. *J. Phys. Chem. C*, **2013**, *117*, 9404.

- (374) Mazumdar, P.; Das, D.; Sahoo, G. P.; Salgado-Mora'n, G.; Misra, A. *Phys. Chem. Chem. Phys.*, **2014**, *16*, 6283.
- (375) Hamley, I. W. *Angew. Chem., Int. Ed.*, **2003**, *42*, 1692.
- (376) Olenyuk, B.; Whiteford, J. A.; Fechtenkotter, A.; Stang, P. J. *Nature*, **1999**, *398*, 796.
- (377) Huang, X.; Jeong, Y.; Moon, B. K.; Zhang, L.; Kang, D. H.; Kim, I. *Langmuir*, **2013**, *29*, 3223.
- (378) Patra, A.; Hebalkar, N.; Sreedhar, B.; Sarkar, M.; Samanta, A.; Radhakrishnan, T. P. *Small*, **2006**, *2*, 650.
- (379) Birks, J. B. *Photophysics of Aromatic Molecules*, Wiley, London, 1970.
- (380) Kazunori, K.; Glenn, S.; Masayuki, K. Y.; Teruo, O.; Yasuhisa, S. *J. Controlled Release*, **1993**, *24*, 119.
- (381) Rapoport, N. *Prog. Polym. Sci.*, **2007**, *32*, 962.
- (382) Kataoka, K.; Harada, A.; Nagasaki, Y. *Adv. Drug Delivery Rev.*, **2001**, *47*, 113.
- (383) Pool, R.; Bolhuis, P. G. *Phys. Chem. Chem. Phys.*, **2010**, *12*, 14789.
- (384) Paul, B. K.; Ray, D.; Guchhait, N. *J. Phys. Chem. B*, **2012**, *116*, 9704.
- (385) Ghosh, S.; Ghatak, C.; Banerjee, C.; Mandal, S.; Kuchlyan, J.; Sarkar, N. *Langmuir*, **2013**, *29*, 10066.
- (386) Mandal, S.; Kuchlyan, J.; Ghosh, S.; Banerjee, C.; Kundu, N.; Banik, D.; Sarkar, N. *J. Phys. Chem. B*, **2014**, *118*, 5913.
- (387) Geng, F.; Liu, J.; Zheng, L.; Yu, L.; Li, Z.; Li, G.; Tung, C. *J. Chem. Eng. Data*, **2010**, *55*, 147.
- (388) Shi, L.; Zheng, L. *J. Phys. Chem. B*, **2012**, *116*, 2162.
- (389) Reichardt, C. *Chem. Rev.*, **1994**, *94*, 2319.

- (390) Riedl, J.; Pohl, R.; Ernsting, N. P.; Orsag, P.; Fojta, M.; Hocek, M. *Chem. Sci.*, **2012**, *3*, 2797.
- (391) Stambasky, J.; Hocek, M.; Kocovsky, P. *Chem. Rev.*, **2009**, *109*, 6729.
- (392) Wetzler, D. E.; Chesta, C.; Ferná'ndez-Prini, R.; Aramendi'a, P. F. *J. Phys. Chem. A*, **2002**, *106*, 2390.
- (393) Mandal, D.; Datta, A.; Pal, S. K.; Bhattacharyya, K. *J. Phys. Chem. B*, **1998**, *102*, 9070.
- (394) Sajadi, M.; Oberhuber, T.; Kovalenko, S. A.; Mosquera, M.; Dick, B. N.; Ernsting, P. *J. Phys. Chem. A*, **2009**, *113*, 44.
- (395) Sen, S.; Sukul, D.; Dutta, P.; Bhattacharyya, K. *J. Phys. Chem. A*, **2001**, *105*, 10635.
- (396) Noukakis, D.; Suppan, P. *J. Lumin.*, **1991**, *47*, 285.
- (397) Wang, R.; Hao, C.; Li, P.; Wei, N. G.; Chen, J.; Qiu, J. *J. Comput. Chem.*, **2010**, *31*, 2157.
- (398) Ware, W. R.; Lee, S. K.; Brant, G. J.; Chow, P. P.; *J. Chem. Phys.*, **1971**, *54*, 4729.
- (399) Soujanya, T.; Fessenden, R. W.; Samanta, A. *J. Phys. Chem.*, **1996**, *100*, 3507.
- (400) Dupont, J.; Consorti, C. S.; Suarez, P. A. Z.; de Souza, R. F.; Fulmer, S. L.; Richardson, D. P.; Smith, T. E.; Wolff, S. *Org. Synth.*, **2002**, *79*, 236.
- (401) Kasha, M.; Rawls, H. R.; El-Bayoumi, M. A. *Pure Appl. Chem.*, **1965**, *11*, 371.
- (402) Datta, A.; Pati, S. K. *J. Chem. Phys.*, **2002**, *118*, 8420.
- (403) Yuning, H.; Jacky, W. Y.; Ben, Z. T. *Chem. Commun.*, **2009**, 4332.
- (404) Yuning, H.; Jacky, W. Y.; Ben, Z. T. *Chem. Soc. Rev.*, **2011**, *40*, 5361.
- (405) Durantini, A. M.; Falcone, R. D.; Anunziata, J. D.; Silber, J. J.; Abuin, E. B.; Lissi, E. A.; Correa, N. M. *J. Phys. Chem. B*, **2013**, *117*, 2160.
- (406) Li, T.; Ayers, P. W.; Liu, S.; Swadley, M. J.; Clare, A.-M. *Chem. Eur. J.*, **2009**, *15*, 361.
- (407) Sarkar, M. *Acta Crystallogr., Sect. E: Struct. Rep. Online*, **2008**, *64*, O1654.
- (408) Panda, A.; Mugesh, G.; Singh H. B.; Ray, J. B. *Organometallics*, **1999**, *18*, 1986.

- (409) Zhao, Y.; Schultz, N. E.; Truhlar, D. G. *J. Chem. Theory Comput.*, **2006**, *2*, 364.
- (410) Zhao, Y.; Truhlar, D. G. *Acc. Chem. Res.*, **2008**, *41*, 157.
- (411) Abraham, S. A.; Jose, D.; Datta, A. *Chem Phys Chem*, **2012**, *13*, 695.
- (412) Jissy, A. K.; Ashik, U. P. M.; Datta, A. *J. Phys. Chem. C*, **2011**, *115*, 12530.
- (413) Jose, D.; Datta, A. *Cryst. Growth Des.*, **2011**, *11*, 3137.
- (414) Stratmann, R. E.; Scuseria, G. E.; Frisch, M. J. *J. Chem. Phys.*, **1998**, *109*, 8218.
- (415) McGaughey, G. B.; Gagne, M.; Rappe, A. K. *J. Biol. Chem.*, **1998**, *273*, 15458.
- (416) Martinez, C. R.; Iverson, B. L. *Chem. Sci.*, **2012**, *3*, 2191.
- (417) Datta, A.; Pati, S. K. *Chem. Eur. J.*, **2005**, *11*, 4961.
- (418) Datta, A.; Tarenziani, F.; Painelli, A. *Chem Phys Chem*, **2006**, *7*, 2168.
- (419) Datta, A.; Pati, S. K. *J. Chem. Phys.*, **2003**, *118*, 8420.
- (420) Datta, A.; Pati, S. K. *J. Phys. Chem. A*, **2004**, *108*, 320.
- (421) Datta, A.; Pati, S. K. *Chem. Soc. Rev.*, **2006**, *35*, 1305.
- (422) Ghatak, C.; Rao, V. G.; Mandal, S.; Ghosh, S.; Sarkar, N. *J. Phys. Chem. B*, **2012**, *116*, 3369.

APPENDIX

Table APPX1. Crystal data and structure refinement for DMP

Empirical formula	C11 H12 N2 O2
Formula weight	204.23
Temperature	296(2) K
Wavelength	0.71073 Å
Crystal system	Monoclinic
Space group	P21/n
Unit cell dimensions	a = 7.7124(4) Å
	b = 8.9272(4) Å
	c = 14.9003(7) Å
	$\alpha = 90^\circ$.
	$\beta = 97.869(3)^\circ$.
	$\gamma = 90^\circ$.
Volume	1016.23(8) Å ³
Z	4
Density (calculated)	1.335 Mg/m ³
Absorption coefficient	0.094 mm ⁻¹
F(000)	432
Crystal size	0.12 x 0.09 x 0.07 mm ³
Theta range for data collection	2.67 to 29.21°.
Index ranges	-10 ≤ h ≤ 10, -12 ≤ k ≤ 12, - 20 ≤ l ≤ 20
Reflections collected	17324
Independent reflections	2735 [R(int) = 0.0363]
Completeness to theta = 29.21°	99.1 %
Absorption correction	Empirical
Max. and min. transmission	0.9935 and 0.9888
Refinement method	Full-matrix least-squares on F ²
Data / restraints / parameters	2735 / 0 / 136
Goodness-of-fit on F ²	1.042
Final R indices [I > 2σ(I)]	R1 = 0.0531, wR2 = 0.1471
R indices (all data)	R1 = 0.0712, wR2 = 0.1591

Largest diff. peak and hole	0.303 and -0.256 e.Å ⁻³
-----------------------------	------------------------------------

Table APPX2. Bond lengths [Å] and angles [°] for DMP

Bond lengths [Å]		Bond angles [°]		Torsion angles [°]	
C(1)-C(2)	1.386(2)	C(2)-C(1)-C(6)	119.23(14)	C(6)-C(1)-C(2)-C(3)	-0.1(2)
C(1)-C(6)	1.3904(19)	C(2)-C(1)-C(8)	132.28(14)	C(8)-C(1)-C(2)-C(3)	-179.96(17)
C(1)-C(8)	1.468(2)	C(6)-C(1)-C(8)	108.49(14)	C(1)-C(2)-C(3)-C(4)	0.0(3)
C(2)-C(3)	1.376(2)	C(3)-C(2)-C(1)	118.82(14)	C(2)-C(3)-C(4)-N(2)	179.60(16)
C(3)-C(4)	1.415(2)	C(2)-C(3)-C(4)	122.46(15)	C(2)-C(3)-C(4)-C(5)	0.0(2)
C(4)-N(2)	1.365(2)	N(2)-C(4)-C(3)	121.08(15)	N(2)-C(4)-C(5)-C(6)	-179.44(15)
C(4)-C(5)	1.417(2)	N(2)-C(4)-C(5)	121.03(14)	C(3)-C(4)-C(5)-C(6)	0.1(2)
C(5)-C(6)	1.367(2)	C(3)-C(4)-C(5)	117.89(14)	C(4)-C(5)-C(6)-C(1)	-0.3(2)
C(6)-C(7)	1.490(2)	C(6)-C(5)-C(4)	118.33(13)	C(4)-C(5)-C(6)-C(7)	179.10(14)
C(7)-O(1)	1.205(2)	C(5)-C(6)-C(1)	123.27(14)	C(2)-C(1)-C(6)-C(5)	0.3(2)
C(7)-N(1)	1.388(2)	C(5)-C(6)-C(7)	129.10(13)	C(8)-C(1)-C(6)-C(5)	-179.83(14)
C(8)-O(2)	1.215(2)	C(1)-C(6)-C(7)	107.62(13)	C(2)-C(1)-C(6)-C(7)	-179.22(14)
C(8)-N(1)	1.397(2)	O(1)-C(7)-N(1)	125.23(15)	C(8)-C(1)-C(6)-C(7)	0.67(16)
C(9)-N(2)	1.444(2)	O(1)-C(7)-C(6)	128.89(15)	C(5)-C(6)-C(7)-O(1)	-0.9(3)
C(10)-N(2)	1.450(2)	N(1)-C(7)-C(6)	105.87(12)	C(1)-C(6)-C(7)-O(1)	178.60(17)
C(11)-N(1)	1.453(2)	O(2)-C(8)-N(1)	123.60(16)	C(5)-C(6)-C(7)-N(1)	179.89(15)
		O(2)-C(8)-C(1)	130.24(16)	C(1)-C(6)-C(7)-N(1)	-0.65(16)
		N(1)-C(8)-C(1)	106.15(13)	C(2)-C(1)-C(8)-O(2)	0.0(3)
		C(7)-N(1)-C(8)	111.86(13)	C(6)-C(1)-C(8)-O(2)	-179.87(17)
		C(7)-N(1)-C(11)	124.05(14)	C(2)-C(1)-C(8)-N(1)	179.42(17)
		C(8)-N(1)-C(11)	124.10(14)	C(6)-C(1)-C(8)-N(1)	-0.44(17)
		C(4)-N(2)-C(9)	121.17(15)	O(1)-C(7)-N(1)-C(8)	-178.91(16)
		C(4)-N(2)-C(10)	120.48(15)	C(6)-C(7)-N(1)-C(8)	0.38(17)
		C(9)-N(2)-C(10)	118.07(15)	O(1)-C(7)-N(1)-C(11)	1.3(3)
				C(6)-C(7)-N(1)-C(11)	-179.42(14)
				O(2)-C(8)-N(1)-C(7)	179.49(16)
				C(1)-C(8)-N(1)-C(7)	0.02(18)
				O(2)-C(8)-N(1)-C(11)	-0.7(3)
				C(1)-C(8)-N(1)-C(11)	179.82(14)

				C(3)-C(4)-N(2)-C(9)	173.92(17)
				C(5)-C(4)-N(2)-C(9)	-6.5(3)
				C(3)-C(4)-N(2)-C(10)	0.2(3)
				C(5)-C(4)-N(2)-C(10)	179.73(15)

Symmetry transformations used to generate equivalent atoms

Table APPX3. Distance [Å] of each atom from the mean plane in DMP and AP molecules (generated by Diamond 3.1e software)

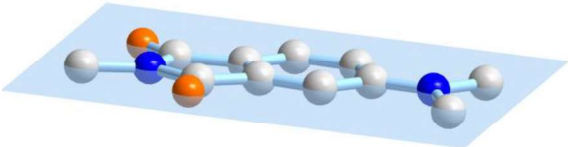
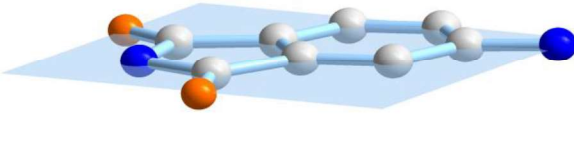
DMP		AP	
			
Atoms	Distance from mean plane [Å]	Atoms	Distance from mean plane [Å]
C11	-0.0106	O1	0.0007
N1	-0.0034	C1	0.0160
O1	0.0313	N1	0.0315
O2	-0.0091	C6	0.0053
C8	-0.0095	O2	-0.0388
C7	0.0055	C7	0.0136
C6	-0.0041	C8	0.0010
C1	-0.0035	C2	-0.0285
C5	-0.0025	C3	-0.0318
C2	0.0050	C4	0.0034
C3	0.0094	C5	0.0108
C4	0.0060	N2	0.0374
N2	0.0194		
C9	-0.1149		
C10	0.0336		

Table APPX4. Angle between two planes in DMP molecule (generated by Diamond 3.1e software)

Value	3.355(71)°		
Plane normal	m1=-0.9085(3) m2=0.2701(6) m3=-0.3188(6)		
Dist. from origin	d=-0.5511(26) Å		
Const. atoms	d [Å]	s [Å]	(d/s) ²
C5	-0.0010	0.0015	0.4181
C6	0.0014	0.0014	0.9229
C1	-0.0010	0.0015	0.4917
C2	0.0001	0.0016	0.0054
C3	0.0004	0.0016	0.0758
C4	0.0000	0.0015	0.0002
Plane normal	m1=-0.9133(4) m2=0.3039(11) m3=-0.2713(11)		
Dist. from origin	d=-0.4024(40) Å		
Const. atoms	d [Å]	s [Å]	(d/s) ²
C9	-0.0205	0.0023	77.6338
N2	0.0278	0.0015	324.0431
C4	-0.0091	0.0015	37.4456
C10	-0.0193	0.0023	72.1807

Table APPX5. Angle between two planes of AP molecule (generated by Diamond 3.1e software)

Value	5.20(8)°		
Plane normal	m1=-0.4073(17) m2=-0.0265(18) m3=-0.9129(8)		
Dist. from origin	d=-7.4363(230) Å		
Const. atoms	d [Å]	s [Å]	(d/s) ²
C4	0.0093	0.0045	4.3219
C3	-0.0050	0.0041	1.4363
C2	-0.0024	0.0048	0.2534
C8	0.0056	0.0041	1.7996
C7	-0.0025	0.0042	0.3488
C5	-0.0051	0.0045	1.3076
Plane normal	m1=-0.3376(595) m2=-0.0789(202) m3=-0.9380(198)		
Dist. from origin	d=-7.4652(2836) Å		
Const. atoms	d [Å]	s [Å]	(d/s) ²
H2A	0.0780	0.0727	1.1515
N2	-0.0011	0.0051	0.0465
C4	0.0002	0.0045	0.0021
H2B	0.0906	0.0727	1.5566